STRUCTURAL AND OPTOELECTRONIC PROPERTIES OF COPPER, ZINC, CADMIUM AND LEAD CHALCOGENIDE NANOCRYSTALLINE THIN FILMS DEPOSITED AT THE WATER-TOLUENE INTERFACE

A thesis submitted to the Department of Chemistry, College of Science

Kwame Nkrumah University of Science and Technology, Kumasi,

in partial fulfillment

for the award of the Degree of

DOCTOR OF PHILOSOPHY (INORGANIC CHEMISTRY)

By

Noah Kyame Asare-Donkor

B.Sc (Hons) KNUST-Kumasi), M.Sc Inorganic Chemistry (KNUST-Kumasi)

November, 2013

CERTIFICATION

I hereby declare that this submission is my own work towards the Ph.D and that, to the best of my knowledge, it contains no material previously published by another person nor material which has been accepted for the award of any other degree of the Kwame Nkrumah University of Science and Technology, Kumasi or any other university or other institution of learning except where due acknowledgement has been made in the text.

N. K. ASARE-DONKOR	……	……..
(PG 4050709)	Signature	Date
Student Name & ID		

Certified by

PROF A.A ADIMADO	……	……..
Supervisor	Signature	Date

Certified by

Dr. J.A.M. AWUDZA	……	……..
Supervisor	Signature	Date

Certified by

DR. R. B. VOEGBORLO	……	……..
Head of Department	Signature	Date

SUMMARY OF THESIS

The use of nanotechnology to develop a suite of sustainable energy production scheme is one of the most important scientific challeges of the 21st century. The challenge is to design, to synthesize and characterize new functional nanomaterials with controllable sizes, shapes and/or structures. The work described in this thesis deals with the exploitation of the unique properties pertaining at the water-toluene interface for the synthesis of functional zinc, copper, cadmium and lead chalcogenide nanomaterials at temperatures below 100 °C. These semiconductor materials had hitherto been synthesized by sophisticated methods at high temperatures and/or under quite difficult conditions such as high vacuum or high pressure or salt solvent mediated high temperature conditions. The metal chalcogenides are important semiconductor nanomaterials which have found many applications in optoelectronics and solar cell technology. Metal chalcogenides as thin films and nanocrystals have also received considerable interest in low cost photovoltaic devices.

In the first part of this work a series of copper, zinc, cadmium and lead alkyldithiocarbamate complexes were prepared with variations of the carbon chains of the alkyl moiety from two to four. In addition to copper, zinc, cadmium and lead cupferronates were also prepared. These precursors were characterized by FTIR as well as elemental analyses.

In the second part of the work the as-synthesised organometallic complexes were used as precursors for the deposition of zinc, copper, cadmium and lead chalcogenide thin films nanoparticles at the water-toluene interface. The as-deposited thin films nanoparticles were characterised by XRD, SEM, TEM and energy dispersive X-ray (EDAX) analyses. Although the self-assembly of colloidal particles at a curved fluid interface has been reported for about 100 years, the self-assembly at a flat fluid interface to form functional films is just a burgeoning field. Compared with previous solution-based self-assembly routes, the advantages of this self-

assembly strategy are evident in their universality, simplicity, high efficiency and the high quality of the as-assembled film. The binary metal chalcogenides were successfully prepared using cheap, low temperature and environmentally friendly methods. Easy manipulation of the processes at the water-toluene interface has led to the syntheses of particles with controlled sizes and morphologies. The variation of the deposition parameters such as concentrations of the precursors, deposition times, temperatures of the deposition and other rheological parameters has led to the synthesis of nanomaterials with varied optical and electrical properties based on the quantum-size effects. With the appropriate choice of metal precursors and reducing agents, this work has led to the fabrication of a variety of nanocrystalline thin films.

This thesis is made up of the following chapters:

1. Chapter one presents a general discussion on semiconductors, band structure, quantum size effects, classification of nanocrystals, methods of synthesis of nanomaterials, the liquid-liquid interface method-assembly at fluid interface, growth process of nanocrystals and applications of semiconductors (thin films and nanocrystals). Additionally, literature report about metal chalcogenide nanocrystals and their applications is also presented.
2. Chapters two to five describe the deposition of zinc, copper, cadmium and lead chalcogenide nanomaterials/thin films at the water-toluene interface and their characterization by XRD, SEM and TEM.
3. Chapter six describes the methodology and other physical measurements.
4. Chapter seven gives a short summary of the results and conclusions drawn from this research work and based on these conclusions provides an outlook to future research.

TABLE OF CONTENTS

Chapter 7 Outlook and conclusion

LIST OF FIGURES

Chapter 1

Chapter 2

Apendix B

LIST OF TABLES

COPYRIGHT

ACKNOWLEDGEMENT

I wish to express many thanks to my supervisors, Prof. A. A. Adimado, Prof. Paul O'Brien (F.R.S.) and Dr. J. A. M. Awudza for their support, kindness, guidance, efficient supervision and many invaluable suggestions during the course of this study.

I am also thankful to Dr. John Thomas formerly a lecturer at the School of Chemistry University of Manchester and now of Bangor University, Wales, for his commendable assistance, advice, immense contribution towards the success of this work and giving me space to work in his laboratory.

I would like to thank Dr. Chris Wilkins and Mike Faulkner for spending long hours assisting me with SEM and EDAX analyses, and for their patient encouragement and support. Sincere thanks also go to Alan Harvey for training and assistance with the TEM analysis.

I would like to thank Judith Shackleton and Gary Harrison all of Material Science Centre of School of Materials University of Manchester for their training and expert assistance in X-ray diffraction and the use of the X-ray diffractometer.

I would like to thank The School of Chemistry, University of Manchester, UK for appointing me as an honorary staff to facilitate my laboratory work.

I am thankful to all my research colleagues of the POB group and Dr. John Thomas's research group especially Enteisar Albrasi, Hanan Al Chaghouri, Khadijat Abdulwahab and Gemma Stansfield all of The School of Chemistry University of Manchester, UK.

I would also like to thank Christine Taylor, The School manager of The School of Chemistry, The University of Manchester, UK for her assistance and encouragement.

I acknowledge with gratitude financial support from the Leverhulme Trust-Royal Society Africa award scheme and The Teaching and Innovation Fund (TALIF) of Government of Ghana.

Finally, I am thankful for the unconditional support from my family, especially my wife and children whose constant support and encouragement made me to undertake this study.

DEDICATION

To my loving parents, Mr. J. K. Donkor and Madame Beatrice Asabea whose cheerful memories have been sources of inspiration to me.

ABBREVIATIONS

AACVD	Aerosol-assisted chemical vapour deposition
AFM	Atomic force microscopy
BSE	Back scattered electrons
CB	Conduction band
CBD	Chemical beam deposition
CCD	Charged couple device
CSE	Classical-size effects
CVD	Chemical vapour deposition
DCE	1, 2-dichloroethane
DOS	Density of states
E_c	Conduction band
EDAX	Energy dispersive X-ray analysis
EELS	Energy electron loss spectroscopy
EELS	Electron energy loss spectrum
EFTEM	Energy filtered transmission electron microscopy
Eg	Band gap energy
Eq	Equation
ESEM	Environmental scanning electron microscope

Et	Ethyl group
Ethex	Ethylhexyl group
E_v	Valence band
FESEM	Field emission scanning electron microscopy
FET	Field effect transistors
FT-IR	Fourier transform infrared spectroscopy
FWHM	Full width at half maximum
GSED	Gaseous secondary detector
GSEM	Gaseous secondary electron detector
HOMO	Highest occupied molecular orbital
HRTEM	High resolution transmission electron microscopy
HTMA	Hexadecyltrimethylammonium
^{i}Bu	Iso-butyl group
ICDD	International centre for diffraction data
ICP	Inductively coupled plasma
ICP-OES	Inductively coupled plasma-optical emission spectroscopy
IM	Image mode
^{i}Pr	Iso-propyl group
JCPDS	Joint committee for powder diffraction standards

LB	Langmuir-Blodgett
LCAO	Linear combination of atomic orbitals
LED	Light emitting diode
LUMO	Lowest unoccupied molecular orbital
Me	Methyl group
MEG	Multiple exciton generation
MHT	Modified hydrothermal
mmol	Millimole
MOT	Molecular orbital theory
MPB	Modified Poisson-Boltzmann
MWCNT	Multi-walled carbon nanotube
NB	Nitrobenzene
NB	Nitrobenzene
NCs	Nanocrystal(s)
NWs	Nanowire(s)
Ph	Phenyl group
PL	Photoluminescence
PLA	Pressure limiting apertures
PLQY	Photoluminescence quantum yield

ppm	Parts per million
Pr	Propyl group
QELS	Quasi-electron laser scattering
QELS	Quasi-electron laser scattering
QHE	Quantum hall effect
QSE	Quantum size effects
SAED	Selected area electron diffraction
SE	Secondary electrons
SEM	Scanning electron microscopy
SM	Spectra mode
STEM	Scanning-transmission electron microscope
TAA	Thioacetamide
TE	Tunnelling effect
TEM	Transmission electron microscopy
TMS	Tetramethylsilane
TOP	Trioctylphosphene
UV/Vis	Ultra-violet/visible
VB	Valence band
VPSEM	Variable pressure scanning electron microscope

WD	Working distance
WZ	Wurtzite
XRD	X-ray diffraction
XRD	X-ray deffractogram
ZB	Zinc blende

CHAPTER ONE

GENERAL INTRODUCTION

In this chapter, a general discussion about semiconductors, band structure, quantum size effects, classification of nanocrystals, methods of syntheses of nanomaterials, the liquid-liquid interface method-assembly at fluid interface, growth process of nanocrystals and applications of semiconductors (thin films and nanocrystals) is described. Additionally, literature about metal chalcogenide nanocrystals and their applications is also presented.

1.1 Introduction

The natural world artfully harnesses the interface between immiscible liquids to carry out vital processes such as growing bones and contracting muscles (Volkov *et al*., 1998). In contrast, synthetic chemists generally regard such an interface as an intractable barrier to be circumvented by the use of phase transfer reagents. A small number of studies have explored the use of the water–oil interface to synthesize inorganic nanostructures, materials that have assumed great significance in recent times (Faraday, 1857; Brust *et al.*, 1994; Rao *et al.*, 2005; Fan *et al*., 2007a,b; Rao and Kalyanikutty, 2008; Stansfield *et al.*, 2010). In these studies, the use of the interface has led to remarkably simple and straightforward routes to complex solids. Careful consideration of current understanding of the structure and properties of the water-oil interface suggests the interface and its immediate environs possess features well suited for synthesis of solids with reduced dimensions.

The interface introduces steep gradients in ionic concentration with critical lengths of the order of nanometres, owing to limited mixing of the liquids around the original interface (Birdi, 1997). With appropriate precursors, these gradients can create a spatially confined region of supersaturation for the growth of low-dimensional crystallites. These crystallites can then be

quickly extracted from the interface to yield a dispersion of nanocrystals (Faraday, 1857). This method, originally due to Faraday, has been very successfully adapted by Schiffrin as well as others for the synthesis of metal nanocrystals such as Au (Brust *et al*., 1994), Ag (Kang and Kim, 1998), Pt (Horswell *et al*., 1999) and Pd (Chen *et al*., 2000). However, this technique has remained largely unexplored for the synthesis of semiconductor nanocrystals.

Nanostructured materials are not only in the forefront of the hottest fundamental materials research nowadays, but they are also gradually intruded into our daily life (Fang *et al*., 2008; Zhai *et al*., 2010; Fang *et al*., 2009). ‘‘There’s plenty of room at the bottom, the principles of physics, as far as I can see, do not speak against the possibility of manoeuvring things atom by atom, put the atoms down where the chemist says, and so you make the substance...’’, this famous statement of legendary Richard Feynman made in 1959 with immense foresight has been realized in less than half a century by consistent efforts and significant contributions from the scientific community across the globe (Kuchibhatla *et al*., 2007).

Nanostructured materials are a new class of materials, having dimensions in the 1–100 nm range, which provide one of the greatest potentials for improving performance and extended capabilities of products in a number of industrial sectors (Xia *et al.*, 2003). There is a large number of new opportunities that could be realized by down-sizing currently existing structures into the nanometer scale (<100 nm), or by making new types of nanostructures. The most successful examples are seen in microelectronics, where ‘‘smaller’’ has always meant a greater performance ever since the invention of transistors: e.g. higher density of integration, faster response, lower cost, and less power consumption (Fang *et al*., 2008).

Inorganic semiconductor nanomaterials like CdS, ZnS, CdSe, ZnSe etc. are proven to be versatile materials because of their applications in optoelectronic devices due to large variation of band gap as a function of particle size. Cadmium sulphide (CdS) and zinc sulphide (ZnS)

nanomaterials have attracted considerable interest in recent years. CdS is a wide band gap semiconducting material having band gap energy 2.4 eV and widely used because of its size dependent photophysical, photochemical and non-linear optical properties etc. (Alivisatos, 1996; Soloviev *et al.*, 2001; Zhang *et al.*, 2003). ZnS (band gap energy 3.6 eV) is also most widely used nanomaterial in solar cells, electroluminescent devices for the cathode ray tube, field emission display and scintillators as one of the most frequently used phosphors (Ghrayeb *et al.*, 1997; Barton and Ranby, 1997).

Recently, CdS and CdSe nanocrystals have been obtained by employing cadmium myristate in toluene and aqueous thio- or selenourea, in an autoclave (Pan *et al.*, 2004, 2005). Core-shell nanocrystals such as CdS/CdSe have been obtained by alternating the two reactions (Pan *et al.*, 2008). Crucially, the semiconductor nanocrystals exhibited band-edge, size-tunable emission, which is characteristic of crystallites with low defects (Murray *et al.*, 1993; Lazell and O'Brien, 1999; Malik *et al.*, 2001; Peng & Peng, 2001; Battaglia and Peng, 2002; Nair *et al*., 2002; Yu and Peng, 2002; Li *et al*., 2003; Pradhan *et al.*, 2003; Park *et al.*, 2004; Mohamed *et al.*, 2005). Such band-edge emission which is critical for these applications had hitherto been achieved using only non-facile methods that usually involve high temperatures (Murray *et al.*, 1993; Lazell and O'Brien, 1999; Malik *et al.*, 2001; Peng and Peng, 2001; Nair *et al.*, 2002; Park *et al.*, 2004).

Various morphologies of lead chalcogenide (PbS, PbSe and PbTe) nanocrystal have been reported including spheres (Murray *et al.*, 2001), cubes (Lu *et al*., 2005) rings (Cho *et al*., 2005), tubes (Tong *et al.*, 2006), wires (Wang *et al.*, 1998; Afzaal and O'Brien, 2006), dendrides (li *et al.*, 2008), and spongelike structures (Kerner *et al*., 2001). In addition some groups have also reported shape evolution in PbSe nanocrystals from cubes to truncated octahedral (Cheng *et al.*, 2009), spheres to cubes (Lee *et al.*, 2002) and star shape to cubes (Jdanov *et al.*, 2004). The shape evolution for the lead chalcogenides can be affected by temperature, growth time, solvent and

precursor delivery. The synthesis of such nanocrystals has involved methods that include sputtering (Ge and Li, 2003), ultrasonic synthesis (Kumar *et al*., 2009), the injection of a solution of lead salt and tri-octylphosphinechalcogenide (TOP-E, E=S, Se, Te) into a hot solvent (Trindade *et al.*, 1999; Akhtar *et al.*, 2010), thermolysis of single source precursors (Lee *et al*., 2002; Trindade *et al.*, 1997; Moloto *et al.*, 2005; Berhanu *et al.*, 2006; Du *et al.*, 2008; Rhodes *et al.*, 2011) or hydrothermal synthesis (Rhodes *et al.*, 2011; Ziqubu *et al.*, 2010). These methods generally involve high temperatures and/or quite difficult conditions such as high vacuum or high pressure or salt solvent mediated high temperature.

In contrast to the other techniques, the liquid-liquid interface method is a one-step process that enables syntheses of nanoparticle arrays at the interface under ambient conditions. Thus, interfacial schemes hold out the promise of producing high-quality crystallites under mild conditions (Pan *et al*. 2004, 2008), since the systematic tuning of nanocrystallites size and shape remains a key objective in realizing both functionality and assembly. The liquid-liquid interface is therefore considered a new route to semiconductor nanocrystals, reliant on the barrier provided by the water-oil interface, to be a worthy addition to the arsenal of available techniques. Nanoparticles anchored to surfaces in the form of film are considered to be important because of their potential use in nanodevices. A liquid-liquid interface offers potential to synthesize nanoparticles, as well as casting them into films. At a liquid-liquid interface, the particles are highly mobile and rapidly achieve an equilibrium assembly (Russell *et al.*, 2003). This method involves the reaction of a metal precursor dissolved in the organic layer with a reducing, a chalcogenide, or an oxidising agent in the aqueous layer. The material formed at the interface corresponds to an ultrathin nanocrystalline film consisting of closely-packed nanocrystals coated with the organic species present at the interface.

The novelty of this method is that it involves a finite growth rate of the ultrathin nanocrystalline film with controllable parameters such as temperature and concentration. The nanocrystals in the

films can be readily extracted to aqueous or organic layers by adding suitable capping agents. Further, the nanocrystalline film obtained at the interface can be easily transferred onto a solid support such as mica, glass, quartz or a polymer film. With appropriate choice of metal precursors and reducing agents, a variety of nanocrystalline films can be fabricated. Unlike the air-water interface, the liquid–liquid (organic-aqueous) interface has not been investigated sufficiently, and it is only recently that there has been concerted efforts to understand the structure of the liquid-liquid interface. The liquid-liquid surface possesses unique thermodynamic properties such as viscosity and density. A liquid-liquid interface is a nonhomogeneous region having a thickness of the order of a few nanometres. The interface is not sharp, since there is always a little solubility of one phase in the other.

Metal chalcogenide materials with critical dimensions in the nanometer range have been of considerable interests lately because of their unique physical and chemical properties, and the potential for use in a diverse range of applications. Zinc chalcogenide semiconductors are well-established photo-conductors with several current and many potential uses. It is also a promising material for use in solar cells and in non-linear optical devices. CuSe is a p-type semiconductor material with potential application in solar cells, superionic conductors, thermoelectric devices and microwave shield coating. It also has potential application in optical filters, nanoswitches, thermoelectric and photoelectric transformers and superconductors. Copper and indium based nanocrystals have been utilized as mid to low band gap photovoltaic materials (Braunger *et al.*, 1996; Wu *et al*., 2008). Lead chalcogenides (PbS, and PbSe) are frequently studied for their optoelectronic properties and represent promising components for a wide range of applications from near-infrared photodetectors to biological labelling materials (Konstantatos *et al.*, 2006).

Low-temperature cadmium based nanocrystals, CdS, CdSe, CdTe, are being explored for a variety of applications including light-emitting diodes, lasers, biological labelling and photovoltaic devices. Since size and shape drastically affect their electronic properties, there

have been significant advances in achieving strict morphological control. However, most low-temperature synthetic methods of CdS, CdSe and CdTe produce only ill-defined, highly agglomerated nanocrystals (Wang *et al.*, 1999a; Wang *et al.*, 1999b; Wang *et al*., 2000; 2002).

1.1.1 Objectives of research and justification

While the examples described in the previous section represent the most successful attempts towards low-temperature solution-phase synthesis of metal chalcogenide nanocrystals, high-temperature routes remain the most dependable and popular methods to produce monodispersed, high-quality nanocrystals. Most low-temperature synthetic methods rely on poorly reactive reagents, such as thiourea and selenourea among others to serve as the chalcogenide source which often results in small, ill-defined, polydispersed nanocrystals. In addition, reaction conditions whereby controlled anisotropic growth is favoured at lower temperatures are rare. Since the demand for nanocrystal-based technologies is steadily growing, there is a strong need for dependable and versatile synthetic strategies that avoid high-temperatures, thus decreasing the energy and costs required to create nanocrystals.

Inspired by the above, this research project seeks to explore the unique properties of the liquid-liquid interface to synthesize semiconductor nanomaterials. It will also contribute to the development of the liquid-liquid interface as a full-fledged, generic, benign soft-chemical medium for the growth and deposition of thin films and nanoscopic material.

The specific objective of this work is to synthesize nanomaterials of zinc, cadmium, copper and lead chalcogenide at the water-toluene interface using metal-dithiocarbamates and metal-cupferronates precursors and characterize them. Dithiocarbamates and cupferronates belong to families of compounds whose chemistry is well known and analogues are readily available, making the present benign method potentially generic (Hogarth, 2005). The chalcogenide source

would either be a sulphide or selenide or telluride ion obtained by the borohydride reduction of sulphur or selenium or tellurium powder in ultrapure water.

The justification of these objectives lie in the fact that the project is going to exploit the simple and unique properties of the water-toluene interface to synthesize these semiconductor materials which had hitherto been synthesized by sophisticated methods at high temperatures and/or quite difficult conditions such as high vacuum or high pressure or salt solvent mediated high temperature. Easy manipulation of the processes at the liquid-liquid interface would lead to the synthesis of particles with controlled sizes and morphologies. The variation of the deposition parameters such as concentrations of the precursors, deposition times, temperatures of the deposition and other rheological parameters will lead to the synthesis of nanomaterials with varied optical and electrical properties based on the quantum-size effects. With the appropriate choice of metal precursors and reducing agents, this work is also going to lead to the fabrication of a variety of nanocrystalline films.

1.2 Inorganic materials

Inorganic materials can be classified in a number of ways. One of the most common method is according to their ability to conduct electricity namely, conductors, insulators, and semiconductors (Singh, 2006, Brus, 1984). A material that has much lower resistance to the flow of electricity can be classified as a conductor. Common examples of conductors include copper (Cu), zinc (Zn), silver (Ag) and sodium (Na). In all these examples, there is a partially filled outermost band. For instance each copper atom has one 4s electron and so the 4s band is half filled. Electrons in this band are free to move when an electric field is applied. An insulator on the other hand offers more resistance to the flow of the electric current. All the electrons are held within the valence band and the conduction band remains completely empty. Due to large band gap it is energetically unlikely for an electron in the valence band to be promoted to the empty

conduction band. A semiconductor on the other hand, shows resistance to the flow of electric current in between those of insulators and conductors. They have completely filled band separated by a small band gap from an empty conduction band. As a result, electrons can obtain enough energy to move into the conduction band. The electrical conduction in semiconductors depends on temperature, illumination and magnetic field. Another way of defining a semiconductor is on the basis of free carrier concentration at room temperature. Semiconductors have moderate carrier density while conductors have rather large carrier density, and insulators have negligible carrier density. Table 1.1 shows the classification of inorganic solids on the basis of resitivity (ρ), energy gap (E_g), and carrier density (n)

Table 1.1 Classification of inorganic materials according to electrical conductivity (Grahn, 1999)

Type	Resistivity (Ohm/cm)	E_g (eV)	n (cm^{-3})	Examples
Conductor	10^{-5} to 10^{-8}	nil	10^{22}	Copper, silver, tungsten, gold, carbon
Semiconductor	10^{-2} to 10^{9}	$0 < E_g < 4$	$< 10^{17}$	Lead sulphide, lead telluride, lead selenide, copper sulphide, copper selenide, zinc sulphide, zinc selenide, Cadmium sulphide, cadmium selenide
Insulator	$< 10^{12}$ to 10^{22}	$4 \leq E_g$	$<< 1$	Sulphur, glass, quartz

1.3 Electronic structure of semiconductors

Semiconductors are made up of individual atoms bonded together in a regular, periodic structure to form an arrangement whereby each atom is surrounded by 8 electrons. An individual atom consists of a nucleus made up of a core of protons (positively charged particles) and neutrons (particles having no charge) surrounded by electrons. The number of electrons and protons is equal, making the atom electrically neutral. The electrons occupy certain energy levels, based on the number of electrons in the atom, which is different for each element in the Periodic Table. The structure of a typical semiconducting material, silicon, is shown in Figure 1.1 below.

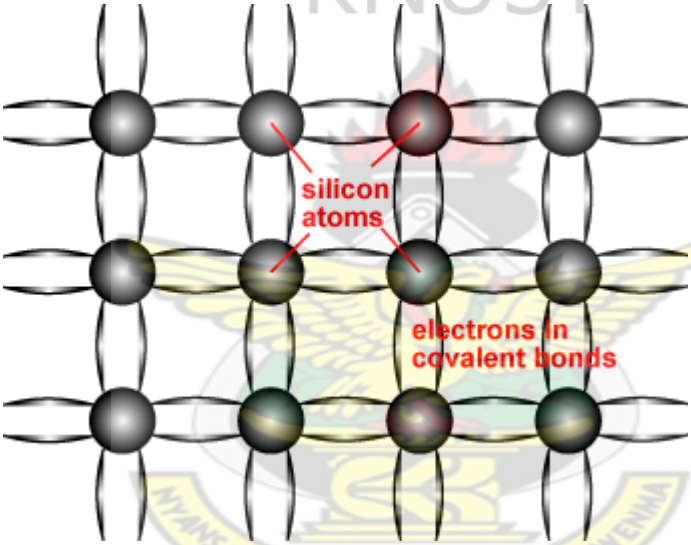

Figure 1.1: Schematic representation of covalent bonds in a silicon crystal lattice *(Honsberg* and *Bowden, 1999)*.

The atoms in a semiconductor are materials from either group IV of the Periodic Table, or from a combination of group III and group V (called III-V semiconductors), or of combinations from group II and group VI (called II-VI semiconductors). Silicon is the most commonly used semiconductor material as it forms the basis for integrated circuit (IC) chips. Most solar cells are also silicon based. Figure 1.2 shows a section of the Periodic Table where the elements (either in single forms or in compound forms or alloyed forms) are semiconductors. A semiconductor

can be either of a single element, such as Si or Ge, a compound, such as GaAs, INP or CdTe, or an alloy, such as $Si_xGe_{(1-x)}$ or $Al_xGa_{(1-x)}$ as, where x is the fraction of the particular element and ranges from 0 to 1.

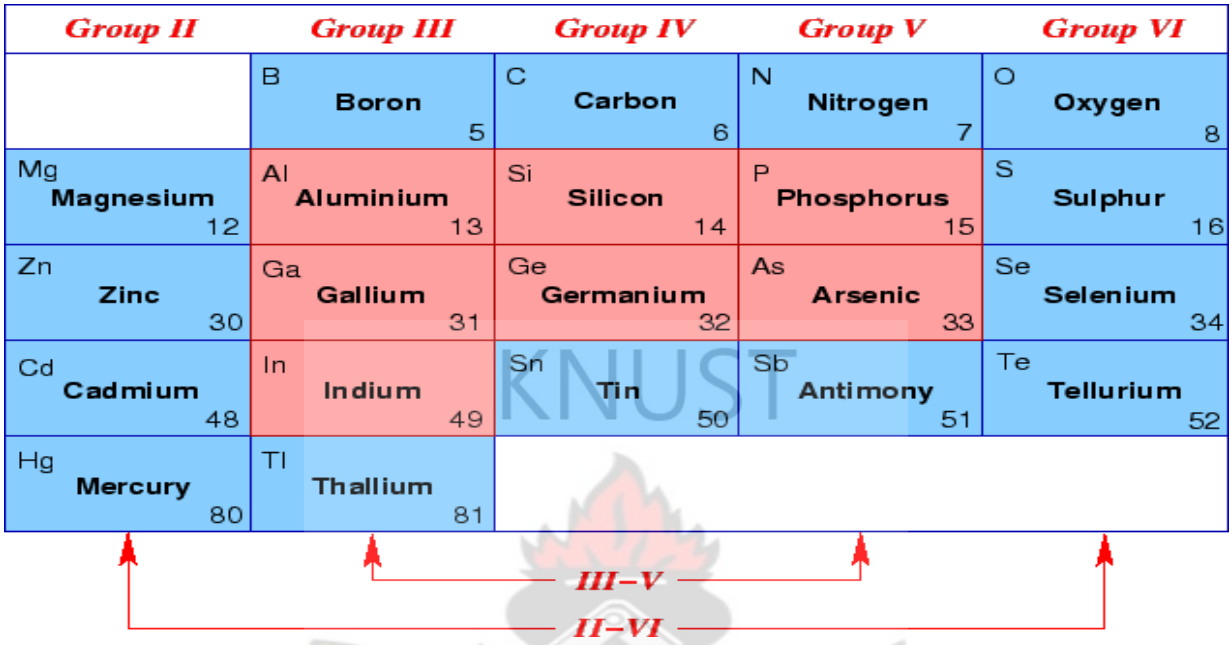

Figure 1.2: Part of the Periodic Table showing the elements involved in the formation of semiconductors (Liu, 1999).

The bond structure of a semiconductor determines the material properties of a semiconductor. One of the key effects is that it limits the energy levels which the electrons can occupy and how they move about in the crystal lattice. The electrons surrounding each atom in a semiconductor are part of a covalent bond. A covalent bond consists of two atoms "sharing" a single electron, such that each atom is surrounded by 8 electrons (octet rule). The electrons in the covalent bond are held in place by this bond and hence they are localised to the region surrounding the atom. Since they cannot move or change their energy, electrons in a bond are not considered "free" and cannot participate in current flow, absorption or other physical processes which require presence of free electrons. However, it is only at absolute zero temperature that all electrons are in a bonded arrangement. At elevated temperatures, the electron can gain enough energy to escape

from its bond, and when this happens, the electron is free to move about the crystal lattice and participate in conduction. At room temperature, a semiconductor material has enough free electrons to allow it to conduct current, while at, or close to absolute zero temperatures, a semiconductor behaves like an insulator.

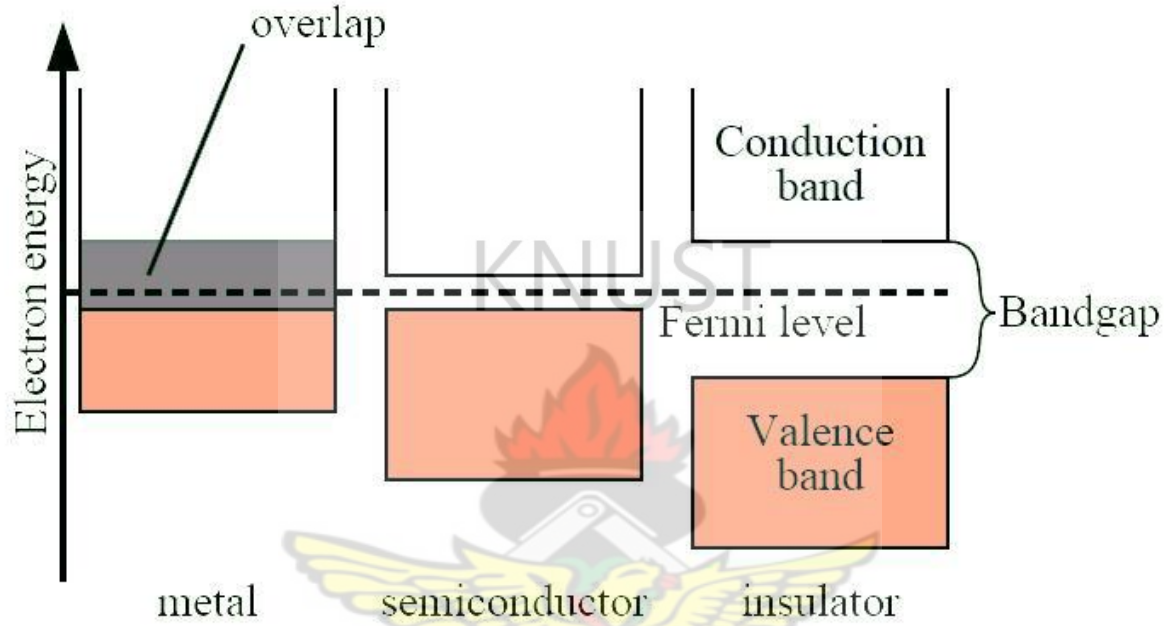

Figure 1.3: Simplified diagram of the electronic band structure of metals, semiconductors, and insulators (Gong and Barron, 2012).

The presence of the bond introduces two distinct energy states for the electrons. The lowest energy position for the electron is to be in its bound state. However, if the electron has enough thermal energy to break free of its bond, then it becomes free. The electron cannot attain energy values intermediate to these two levels; it is either at a low energy position in the bond, or it has gained enough energy to break free and therefore has a certain minimum energy. This minimum energy is called the band gap of a semiconductor. The number and energy of the free electrons is basic to the operation of electronic devices.

The space left behind by the electrons allows a covalent bond to move from one electron to another, thus appearing to be a positive charge moving through the crystal lattice. This empty space is commonly called a "hole", and is similar to an electron, but with a positive charge.

The most important parameters of a semiconductor material for its operation in electronic devices and solar cells are: the band gap, the number of free carriers available for conduction, and the "generation" and recombination of free carriers in response to the electric field, temperature and light shining on the material.

The band structure of a semiconductor gives the energy of the electrons on the y-axis and is referred to as a "band diagram". The lower energy level of a semiconductor is referred to as the "valence band" (E_v) and the energy level at which an electron can be considered free is called the "conduction band" (E_c). The band gap (E_g) is the distance between the conduction band and valence band. Figure 1.3 shows a simplified diagram of the electronic band structure of metals, semiconductors and insulators.

Once the electron is in the conduction band, it is free to move about the semiconductor and participate in conduction. However, the movement of an electron to the conduction band leaves behind an empty space for another electron. Therefore, an electron from a neighbouring atom can move into this empty space creating behind another space. The continuous movement of the space for an electron, "hole", can be illustrated as the movement of a positively charged particle through the crystal structure. Consequently, the movement of an electron to the conduction band results not only in an electron in the conduction but also a hole in the valence band. Hence both the electron and hole can participate in conduction and are known as "carriers". The thermal excitation of a carrier from the valence band to the conduction band creates free carriers in both bands.

In order to understand the physics and application of semiconductors, there is the need to study the band theory. Band theory is basically derived from the molecular orbital theory (MOT) (James, 2008). According to the MOT the linear combination of atomic orbitals approximation (LCAO) results in the formation of molecular orbitals on the basis of interaction of wave functions as shown in Figure 1.4. Hydrogen molecule (H_2) is a typical example in which the single s electron wave functions of two hydrogen atoms (commonly represented as $\chi_A + \chi_B$) interact with all possible linear combinations to generate a bonding and antibonding orbital (ψ_1 and ψ_2) respectively.

$$\psi_1 = \chi_A + \chi_B \qquad \text{and} \qquad \psi_2 = \chi_A - \chi_B$$

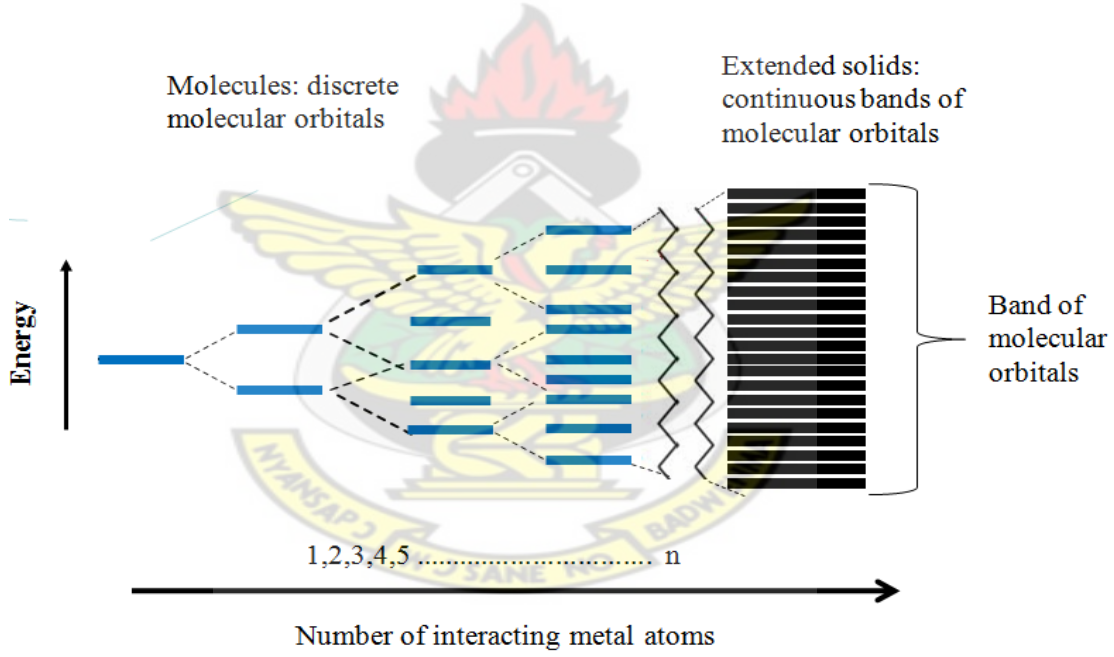

Figure 1.4: Schematic diagram of molecular orbitals in inorganic solids on the basis of linear combination of atomic orbitals (LCAO) (Daintith, 2004).

The molecular orbitals thus formed thus have different energy levels than the corresponding overlapping atomic s orbitals. The bonding orbitals have lower energy while the antibonding orbitals are higher in energy than the original atomic orbitals. The two s electrons from hydrogen

atoms in each case occupy the lowest possible energy configuration therefore populating the bonding orbitals whereas the antibonding orbitals remain unoccupied (Daintith, 2004). In a similar way, due to large number of combining atomic orbitals in materials (conductors, insulators and semiconductors) these energy levels merged together and form energy bands as shown in Figure 1.3. Each band has a different energy and the electrons fill these bands from the lowest energy to the highest, similar to the way electrons occupy the orbitals in a single atom. The band gap is the difference in energy between the valence and conduction bands. The laws of quantum mechanics forbid electrons from being in the band gap; thus, an electron must always be in one of the bands (Singh, 2006).

Electrons are unable to occupy the region between energy bands and this region is termed as the band gap (E_g). Absorption of energy results in transition of an electron from the valence band that crosses the band gap and shifts to the conduction band. The energy required for this transition is a characteristic of the particular material in question. These unique band gaps are usually measured in electron-volts. In a metal (Cu, Ag), the valence band is only partially filled with electrons. This means that the electron can access empty areas within the valence band, and move freely across all atoms that make up the solid as shown in Figure 1.5 (a). A semiconductor Figure 1.5 (b) is a special case in which the band gap is small enough for electrons in the valence band to be able to jump into the conduction band using thermal energy. Thus an important property of semiconductors is that their conductivity increases as they heat up and more electrons fill the conduction band. In an electrical insulator, there is no possibility for electron transition (Figure 1.5 (c)), because the valence band is completely filled with electrons, and the conduction band is too far away in terms of energy to be accessed by these electrons.

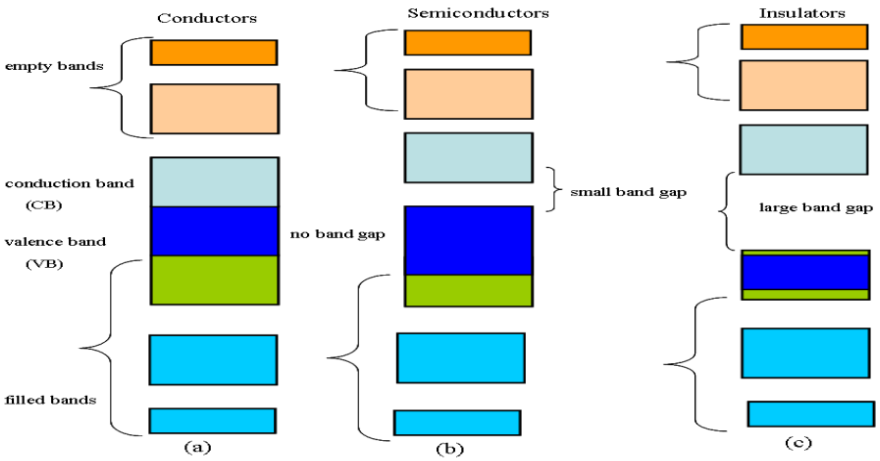

Figure 1.5. Schematic diagram of electronic band structure of (a) conductor (b) semiconductor and (c) insulator (Anthony, 1999)

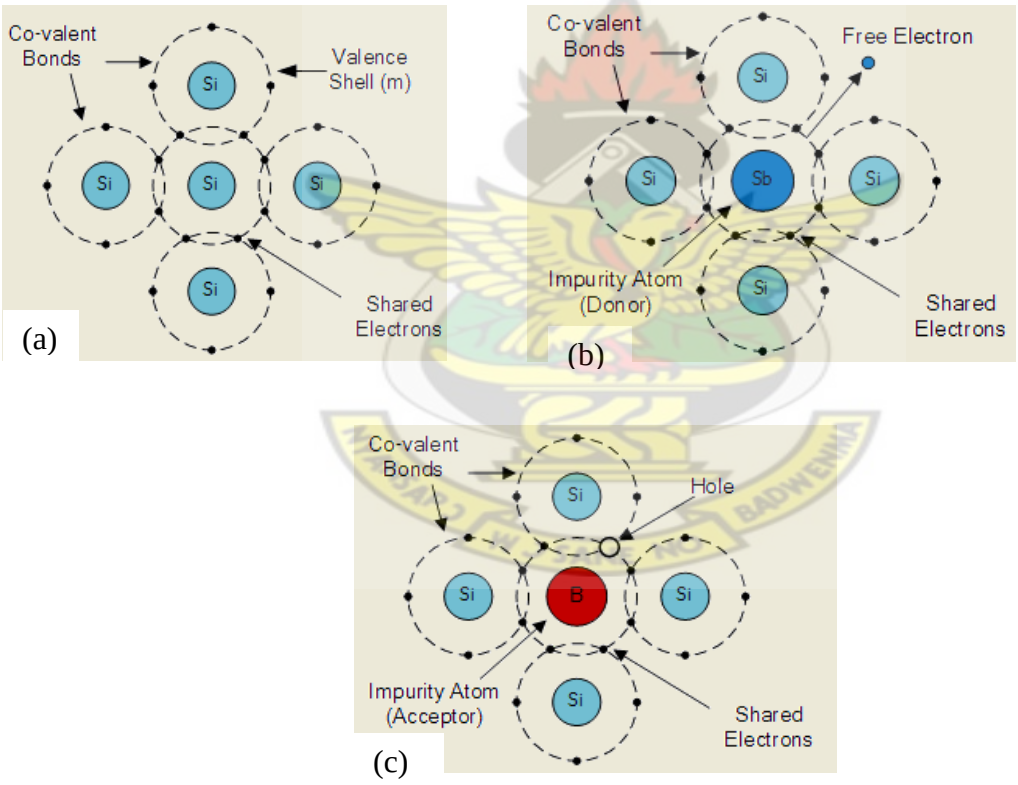

Figure 1.6. Electronic diagram of (a) Si semiconductor crystal showing the distribution of electrons in the outer shell of each Si atom; (b) n-type doping, the fifth electron does not contribute to the bonding, free to move inside he Si crystal; (c) p-type doping (Anthony, 1999).

1.4 Extrinsic and intrinsic semiconductors

Extrinsic semiconductors have their electrical properties based on impurities, also known as dopants. They have considerably higher conductivity compared to intrinsic semiconductors. The commercially available semiconductors belong to this type. The process of addition of controlled impurities is known as doping which can tailor the electronic and conductivity properties. The addition of impurity atoms into a semiconductor material produces new energy levels within the band gap. When a semiconductor is doped with atoms having more valence electrons (doping of silicon with phosphorus), the materials are termed as n-type as shown in Figure 1.6 (b). The extra non-bonded electron remains bonded to phosphorus atom. When this electron is promoted to the conduction band by utilizing thermal energy at room temperature, a positive charge on each phosphorus atom is created. This positive charge is attached to the phosphorus nuclei and does not act as mobile hole. Under the charge imbalance, the Fermi level shifts towards the conduction band and a new energy level is thus formed as shown in Figure 1.7 (a).

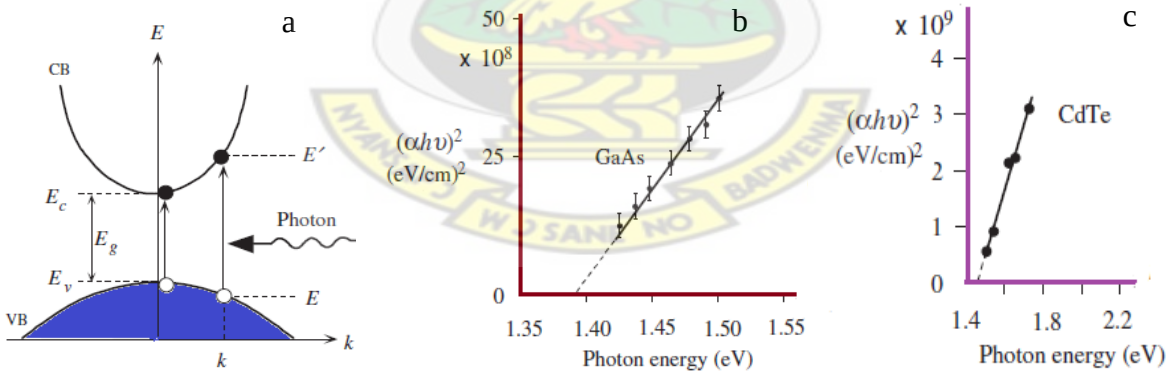

Figure 1.7. (a) A direct transition from the valence band (VB) to the conduction band (CB), (b) and (c) fundamental absorption of photon of GaAs (Kudman and Seided, 1962) and CdTe (Rakhshani, 1997) respectively.

However, when doping is created with such atoms which have one less valence electron than the host (e.g. doping of silicon with boron) as shown in Figure 1.6 (c), the impurity atoms act as electron acceptors and create holes (positive charge) in the host materials. They are known as p-type and the Fermi level shifts close to the valence band as in Figure 1.7 (b) (Anthony, 1999). Besides, a number of compound semiconductors can act as n-type or p-type materials based on defects within the crystal lattice. These defects arise due to vacant sites in the lattice points corresponding to the stoichiometry of the compounds. For example, in PBS, due to excess of sulphur vacancies it acts as n-type or p-type due to excess of Pb sites.

1.5 Direct and indirect band gap semiconductors

The band gap of a semiconductor is always one of two types, a direct band gap or an indirect band gap. The band gap is said to be "direct" if the momentum of electrons and holes is the same in both the conduction band and the valence band; an electron can directly emit a photon. In an "indirect" band gap, a photon cannot be emitted because the electron must pass through an intermediate state and transfer momentum to the crystal lattice. The minimal-energy state in the conduction band and the maximal-energy state in the valence band are each characterized by a certain crystal momentum (k-vector) in the Brillouin zone. If the k-vectors are the same, it is called a "direct gap". If they are different, it is called an "indirect gap". Band- to- band absorption occurs due to the photo excitation of an electron from the valence band to the conduction band. In crystalline solids, the band structures depend on the electron wave vector K. On the basis of transition between band to band, semiconductors can be grouped as direct and indirect band gap semiconductors (Kudman and Seided, 1962, Rakhshani, 1997).

In direct band gap semiconductors (e.g. GaAs, PbS or ZnO), the process does not involve phonons. Since phonon momentum is negligible compared with electron momentum, the K-vector does not change. A direct transition on the E-K diagram is a vertical transition from an

initial energy E and wave vector K in the VB to the final energy E' and wave vector K' in the CB where K' = K as shown in Figure 1.8 (a) (Singh, 2006). The energy ($E-E_c$) is the kinetic energy of the electron with an effective mass Q, and E_v-E is the kinetic energy of the hole left behind in the VB. The E_g is band gap energy (E_c-E_v) (Singh, 2006). Figure 1.7 (b) and (c) represents the direct band gap of GaAs and CdTe semiconductors, the extrapolation to zero phonon energy provides band gap E_g which is 1.40 eV for GaAS and 1.46 eV for CdTe.

In indirect band gap semiconductors, absorption of phonons requires the absorption thick layer or emission of phonons as illustrated in Figure 1.8 (a). For indirect band gap semiconductor like silicon, an electron cannot be directly excited to the conduction band with energy E_g. Additional energy is required as a phonon, the electron undergoes a change in momentum obtain an indirect transition with energy $E_v = E_g + E_{phonon}$ is obtained. The phonon energy, E_{ph}, is very small compared to E_g.

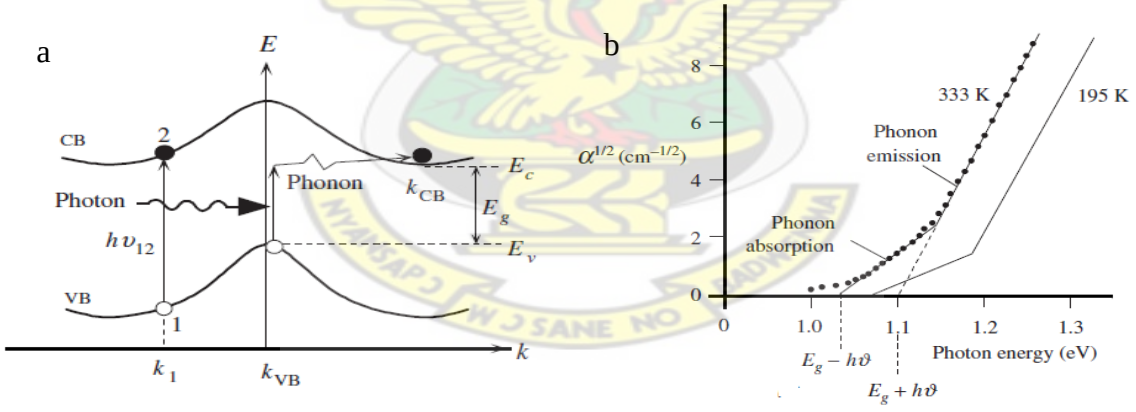

Figure 1.8 (a) Indirect transition across the band gap involve phonons; (b) Fundamental absorption in Si at two temperatures (Singh, 2006).

Figure 1.8 (b) shows fundamental absorption of Si at two temperatures. Since indirect transition require the participation of phonon (lattice vibrational energy) and hence are unambiguously dependent on temperature. The absorption coefficient for indirect semiconductors is smaller than for direct semiconductors; in essence light absorption is less efficient process for indirect

semiconductors. Indirect band gap semiconductors have lower absorption co-efficient for example, 99 % of light photons with energy equal to the band gap of CdTe (1.45 eV) are absorbed by a 1 μm. By comparison, crystalline silicon (indirect band gap material) requires 20 μm thickness layers.

Similarly, in the case of light emission, a direct band gap material is also more likely to emit a phonon than an indirect band gap material. Indirect band gap materials are occasionally used for some LEDs; they result in low conversion efficiency. Direct band gap materials are used exclusively for semiconductor laser diodes. Table 1.2 shows band gaps and other important parameters of selected semiconducting materials (Grahn, 1999).

1.6 Applications of semiconductors

Semiconductors form the basis of the modern information processing devices. In essence the current technological modern life would not be possible without the semiconductor industry. The fabrication of the first semiconductor device in 1948 at Bell laboratories stimulated scientists to prepare improved technological devices. To date, these tiny structures are integral components of CD/DVD players, cellular phones and computers. In addition, they have also been used to prepare diodes, bi-polar junction transistors and field effect transistors. The fabrication of modern optoelectronic devices such as laser diodes, modulators and detectors is very much indebted to them. Semiconductors also provided a platform to explore fundamental questions of physics.

Table 1.2: Physical properties of commonly used semiconducting materials (Grahn, 1999)

Semiconductors	Bang gap (eV)	Band gap type	Lattice Parameters (A)	Crystal Structure
IV - IV				
Ge	0.66	Indirect	5.846	Cubic
Si	1.12	Indirect	5.437	Cubic
II - IV				
ZnS	3.68	Direct	5.420	Cubic
CdS	2.42	Direct	5.832	Cubic
	2.51	Direct	6.710	Hexagonal
ZnSe	2.70	Direct	5.669	Cubic
	4.00	Direct	6.54	Hexagonal
CdSe	1.70	Direct	6.050	Cubic
	1.75	Direct	7.010	Hexagonal
CdTe	1.56	Direct	6.482	Zinc blend
III - V				
GaAs	1.42	Direct	5.653	Cubic
InP	1.35	Direct	5.869	Cubic
InAs	0.36	Direct	6.058	Cubic
AlAs	2.16	Indirect	5.661	Cubic
IV – VI				
PbTe	0.29	Direct	6.439	Cubic
PbSe	0.27	Direct	6.12	Cubic
PbS	0.41	Direct	5,9	Cubic

Table 1.3: Applications of some important semiconductors (Jones and O'Brien, 1997).

Materials	Devices	Applications
GaAs/AlGaAS	Detectors, infrared LEDs, lasers	Remote control TV, video disk players, rang findings, optical fibre communication
InP/InGaP	Infrared LEDs, lasers (1.6 μm)	Optical fibre communication
InP/InGaAs	1-1.6 m detectors	Optical fibre communication, Displays, laser
InGaAlAs/InGaAS	1.67-2 m LEDs	Printers/scanners
GaInAlP	LEDs and lasers	Watches, calculators
Si	Detectors, solar cells	Detectors
SiC	Blue LEDs	Displays
GaSb/GaAlSb/InSb	Long wavelength detector	Infrared imaging, night vision sights, missile seekers
PbS	IR-detectors, photodetectors	Optical fibre communication, sensors, lasers
PbSe	IR-detectors, photodetectors	Optical fibre communication, sensors
PbTe	Thermoelectric devices	Heating devices

Quantum Hall Effect (QHE), tunnelling effect (TE) and multiple exciton generation (MEG) are some noteworthy processes that have been studied in semiconductor structures. Table 1.3 shows the main application of semiconductors (Jones and O'Brien, 1997).

1.7 Semiconductor nanoparticles

Nanocrystalline particles represent a state of matter in the transition region between bulk solid and single molecule. As a consequence, their physical and chemical properties gradually change from solid state to molecular behaviour with decreasing particle size. The band structure gradually evolves with increasing particle size, i. e., molecular orbital convert into delocalised band states. Figure 1.9, shows the size quantization effect responsible for the transition between a bulk metal or semiconductor, and cluster species. In a metal, the quasi-continuous density of states in the valence and the conduction bands splits into discrete electronic levels, the spacing between these levels and the band gap increasing with decreasing particle size (Schön and Simon, 1995). Also for semiconductors the band gap increases when the particle size is decreased and the energy bands gradually convert into discrete molecular electronic levels (Weller, 1993). By judiciously choosing the size of the semiconductor nanoparticles one can alter the energy width of the band gap and consequently tune the optical and electrical response of the material.

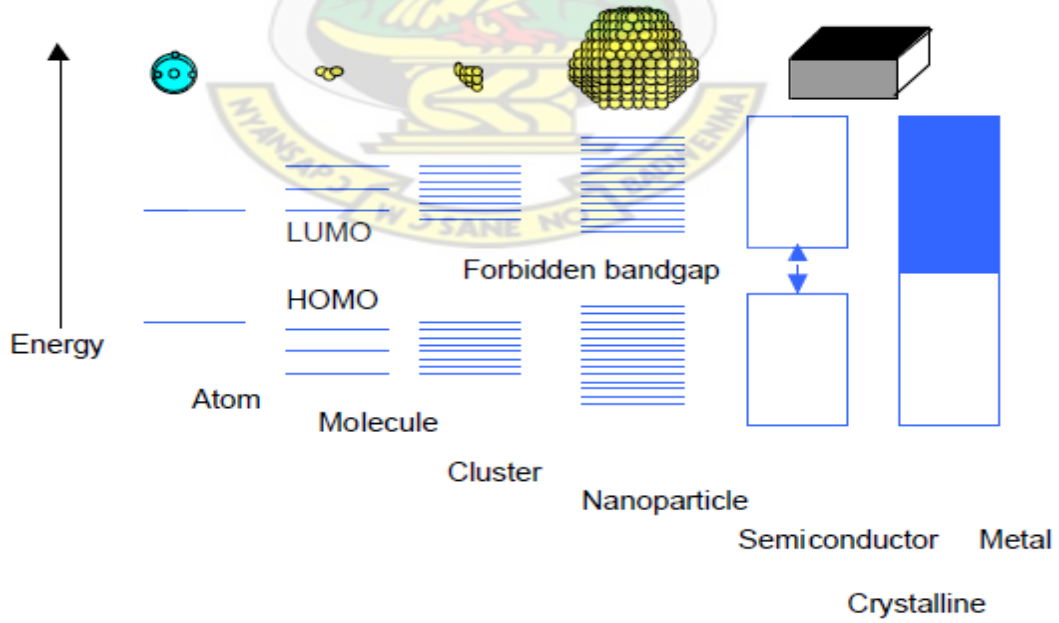

Figure 1.9. Size quantization effect. Electronic state transition from bulk metal/semiconductor to small cluster (Alivisatos, 1996b).

One fact that should not be forgotten in all of these is that the chemical compound (material) remains in essence the same and therefore has effectively the same composition and chemistry. The nanomaterials are considered as artificial atoms and occupy a unique position as a bridge between atoms and bulk solids as shown in Figure 1.10. This is a major advantage that therefore arises from the use of materials at the nanometre scale as any chemical modification that has been successfully applied to one size (colour) can be further applied to any other. This is unlike the case for dye stuffs, where the optically active centres are molecular and where to change the optical properties one must engineer the molecule. This is by its very nature a more challenging prospect and once achieved still only allows one characteristic absorption and emission profile. On the other hand by stopping the growth of nanoparticles at a particular size one can effectively pre-select the part of the spectrum that one wishes the material to be active in. By removing portions of the growth mixture at different times one can obtain the material at a number of different sizes and therefore, where the different fractions are optically active, obtain material which has been tuned to be active in a number of different regions of the spectrum.

One of the most important criteria that one must consider when dealing with the "quality" of a sample of nanoparticles is the polydispersity i.e. the range of sizes present in the sample. It makes sense of course that if the properties of the material are determined by the size then having a wide range of sizes present will lead to a situation where the required property is smeared out or hidden due to the range of size determined properties present in the sample. This makes it difficult to determine accurately the extent of the property of interest or at the very least the material becomes more difficult to characterize. An added advantage to being able to achieve monodisperse samples is the tendency of such systems to self-assemble giving access to secondary (monolayer) and even tertiary (multilayer) levels of organisation.

The properties of bulk materials are determined by intramolecular bonding forces as their strength is much stronger than intermolecular binding forces therefore, electronic, optical

properties of such materials are independent of the size of the crystal (Brus, 1984). On the other hand, inorganic semiconductors and metals consist of network of ordered atoms, where electronic excitations from valence band to conduction band results in the formation of loosely bound electron-hole pair usually delocalized over a length longer than the lattice constant of the material. As the size of the semiconductor crystallite approaches this exciton Bohr diameter, electronic properties start to change. This effect is known as the quantum size effect (QSE).

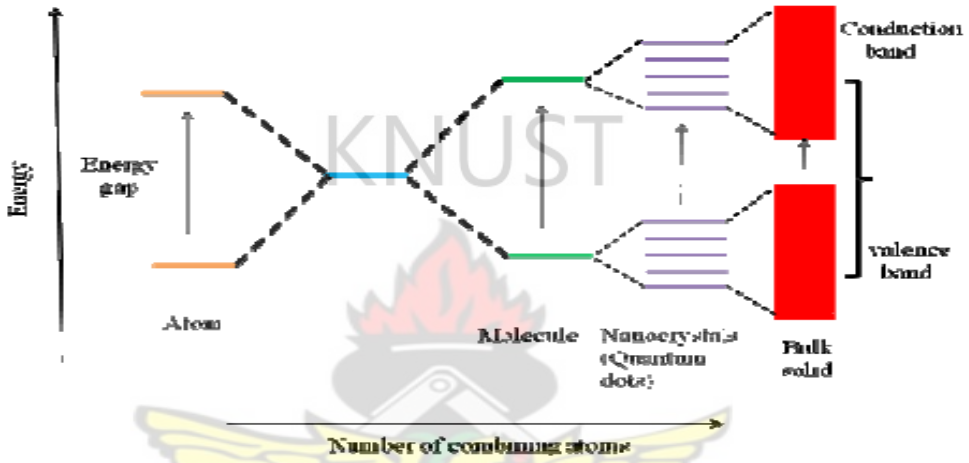

Figure1.10. Schematic diagram to show energy levels in an isolated atom, molecule, nanocrystal and bulk solid (Roduner, 2006).

1.8 Quantum size effects

Quantum size effects are unusual properties of extremely small crystals that arise from confinement of electrons to small regions of space in one, two, or three dimensions. Figure 1.11 shows quantum confinement and corresponding increase in band gap whereas Figure 1.12 shows the density of states for a free electron gas in various dimensions. In a metal thin film of a semiconductor, the conduction electrons are confined in a quantum-size region bound by the vacuum on one side and the metal semiconductor interface on the other, which produces quantum levels or sub-bands known as quantum well states. Such quantum-size effect can influence the

stability of metal thin films on a supporting substrate. Their model contains three central ingredients: (i) quantum confinement, (ii) charge spilling, and (iii) interface-induced Friedel oscillations. Electronic confinement within the metal over layer can mediate an effective repulsive force between the interface and the metal surface, acting to stabilize the over layer. Electron transfer from the over layer to the substrate leads to an attractive force between the two interfaces, acting to destabilize the flat over layer. Interface-induced Friedel oscillatory modulation in electron density can further impose an oscillatory modulation on to the two previous interfaces. These three competing actors, all of electronic nature, can make a flat metal over layer critically or marginally stable or totally unstable against roughening.

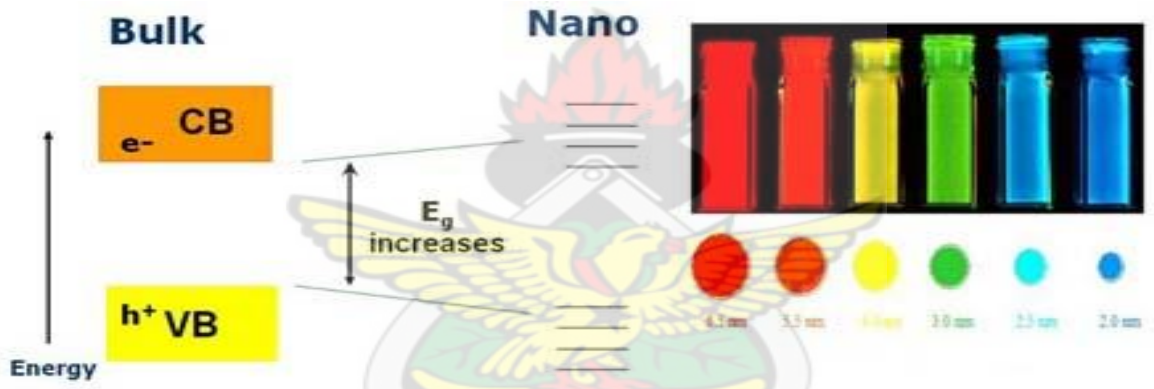

Figure 1.11 Quantum confinement – Increase in band gap (Rao *et al.*, 2007).

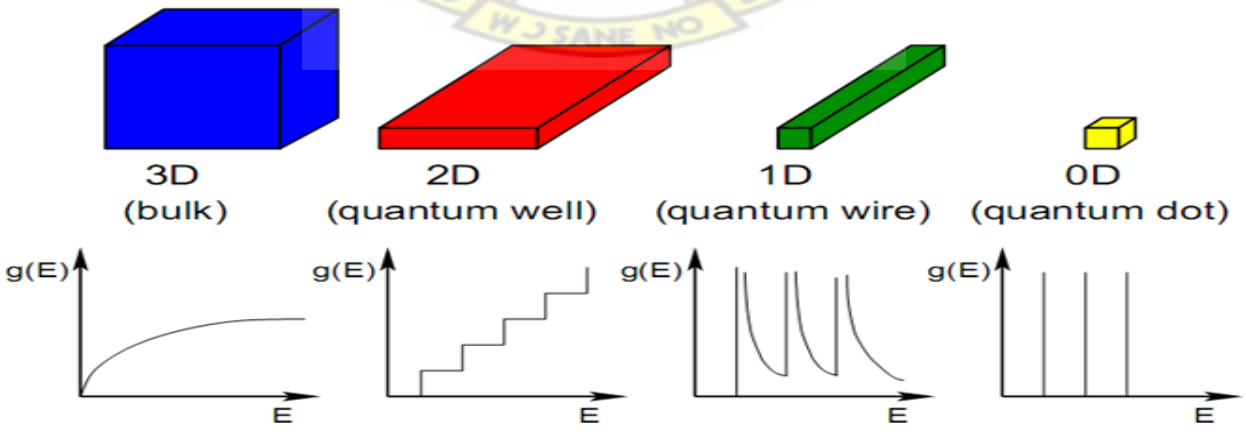

Figure 1.12: Density of states for a free electron gas in various dimensions (general trend) (Arregui, 2004).

When the system size achieves the same order of its components, a transition from the scalable to the non-scalable regime occurs because the strength of the interaction between the particles is of the same order as the total energy of the system. This new emergent nature can be triggered by different processes that compete or complement with each other to give peculiar properties to the system. When the size of the system achieves the electron wavelength the role of Quantum Mechanics is crucial. Nevertheless, even from the classical point of view, if the system size is of the same order of the atomic scale, the addition or subtraction of one atom produces non-scalable, discontinuous and eventually qualitative changes. Finally, a third one that is closely related to the previous ones is the reduction of the dimensionality (i.e., the system becomes very small in 1, 2 or 3 dimensions of the space).

The effect of the dimensionality on quantum mechanical properties is shown in Figure1.9, where the density of states (DOS) of an electron gas is plotted. For zero-dimensional systems the DOS are delta functions located at the energies of the allowed electronic states. In a one-dimensional system the DOS still has divergences at the energy positions of the confined states. For the two-dimensional electron gas the stepped DOS is quite similar to the 3-dimensional or bulk continuous function.

When the size is comparable to the mean free path of the conduction electrons, the mesoscopic transport regime is entered leading to so-called finite-size effects (FSE) or classical-size effects (CSE). These effects include additional electron scattering processes both at the surface of the structure and at inner grain boundaries. When the structure size even reaches the Fermi-wavelength λ_F and, hence, the electronic wave function becomes confined, quantum-size effects (QSE) are expected to occur which involve a change of the density of states and, thus, affect the transport properties as well as the optical properties.

The quantum size effect describes the physics of electron properties in solids with great reductions in particle size. This effect does not come into play by going from macro to micro dimensions. However, it becomes dominant when the nanometer size range is reached. Quantum effects can begin to dominate the behaviour of matter at the nanoscale – particularly at the lower end (single digit and low tens of nanometers) – affecting the optical, electrical and magnetic behaviour of materials. Materials can be produced that are nanoscale in one dimension (for example, very thin surface coatings), in two dimensions (for example, nanowires and nanotubes) or in all three dimensions (for example, nanoparticles and quantum dots).

The causes of these drastic changes stem from the weird world of quantum physics. The bulk properties of any material are merely the average of all the quantum forces affecting all the atoms that make up the material. As things are made smaller and smaller, eventually a point would be reached where the averaging no longer works and specific behaviour of individual atoms or molecules have to be dealt with - the behaviour that can be very different from when these atoms are aggregated into a bulk material.

Materials reduced to the nanoscale can suddenly show very different properties compared to what they show on a macro scale. For instance, opaque substances become transparent (copper); inert materials become catalysts (platinum); stable materials turn combustible (aluminium); solids turn into liquids at room temperature (gold); insulators become conductors (silicon).

Quantum size effects (QSE) can be defined as the increase in band gap of a metal or semiconductor material with increase in the size of the particle. It results in the formation of discrete energy levels of the electrons and holes. The QSE can be observed as a blue shift in the optical absorption spectrum of the NCs. For example, in CdS, QSE occurs when the crystallite diameter is comparable or below the exciton diameter of 50-60 Å (3000-4000 atoms), however, in PbS this size effect can be observed for a crystallite as large as 180 Å, which contains over

10^5 atoms. In confinement regime, electrons and holes are trapped in a small area, leading to novel physical and chemical properties. Quantum confinement of holes and electrons takes place in two-dimensions (2-D), one-dimensions (1-D) or zero-dimensions (0-D) (Wise, 2000). The nanocrystals are promising and ideal materials for applications in devices from optoelectronics, single electron transistors and light emitters, nonlinear optical devices, catalysis, solar energy conversions, photonic band gap materials to biomedical applications.

1.9 Properties of nanoparticles (NPs)

1.9.1 Electronic properties

The size-dependent properties of nanoparticles can be attributed to two main factors: their small size and extremely large surface-to-volume (S/V) ratio. These two are interrelated since the S/V ratio increases as the size decrease, for example, S/V = 3/r for a spherical particle. In general, the density of electronic states (DOS) decreases and the energy level spacing increases as a consequence of reducing the dimensionality, which means that a charge carrier in nanoparticles is no longer solvated in an effectively infinite medium. From a quantum mechanical point of view, it is due to the spatial confinement of the wave function of charge carriers, which is termed quantum size confinement and result in the quantization of energy states.

1.9.2 Metallic nanoparticles

The energetic band structures in a metallic atom, a metallic nanoparticle and a bulk metal are compared in Figure 1.13. The bulk metal has a band structure that consists of a large number of electronic levels with very similar energy. In a metallic atom, the electronic structure features a series of discrete energetic levels with a highest occupied molecular orbital (HOMO) and a lowest unoccupied molecular orbital (LUMO). However, in a nanoparticle consisting of a few tens or hundreds of atoms, the structured s- and d-bands are beginning to be split and disappear

and discrete energy levels are appearing but not truly forming. There is no sharp borderline between these two fundamental situations, but this transition is continuous. The description of bulk metals is made in terms of the laws of classical physics. And quantum mechanics is a well-established theory for describing the electronic situation in molecules and atoms. So far, there is nothing new, however, in relation to nanoparticles. The model of the "electron in a box", normally used for atoms, helps to describe simply the situation in small metal particles when size restriction begin to influence electronic behaviour.

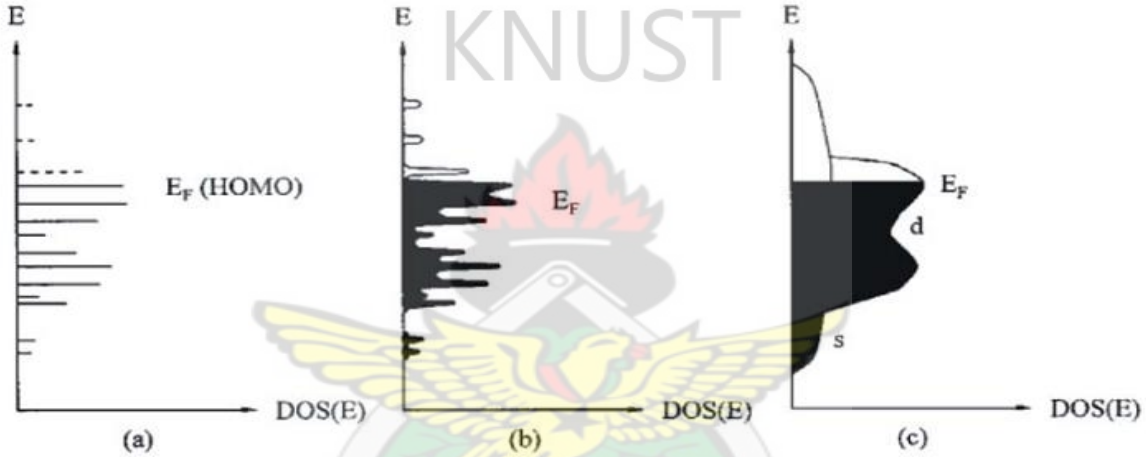

Figure 1.13 Comparison of the electronic band structure of a metallic atom (a), a metallic nanoparticle (b) and a bulk metal (c). E_F = Fermi energy; DOS = density of states (Alivisatos, 1996b).

The most important property of a metal is its conductivity. For example, in d^{10} elements such as palladium, platinum, or gold, the s-bands can function as unoccupied bands for transfer of electrons located in the fully occupied d-bands. The conductivity in the bulk metal follows the classic Ohm's law. However, as a metal particle becomes small enough, discrete energy levels finally dominate and, as a consequence, ohms law is no longer valid. Indeed, small gold nanoparticles consisting of less than 200 gold atoms do not show a linear current response with

respect to the potential but a successive single electron transfer behaviour even at room temperature (Chen *et al*., 1998).

1.9.3 Size dependent effects of nanoparticles

According to the theory of energy levels in solid-state physics, the electronic properties of a bulk semiconductor are determined by the energy band gap (E_g) between valence band (VB) and conduction band (CB):

$$E_g = E_{CB} - E_{VB} \quad (1.1)$$

As particles become smaller, their electronic structure changes, and eventually the charge carriers produces discrete energy states in the valence and conduction bands due to local confinement: there is no sufficient space for electron-hole pairs to form. The electronic and optical properties of such small particles are hence more like those of a molecule than an extended solid. Size dependent effects are expected to occur when the particle size become smaller than the Bohr radius of the first exciton in the bulk semiconductor. The Bohr radius is defined as:

$$r_B = \frac{h^2 \varepsilon_0 \varepsilon_r}{\pi e^2 m^* m_0} \quad (1.2)$$

Where h is the Plank constant, ε_0 and ε_r are the dielectric constants of the vacuum and the semiconducting material, respectively; e, m^* and m_0 are the elementary charge, the effective mass of the charge carriers and the electron mass, respectively. In general, semiconducting NPs with physical dimensions smaller than r_B are termed quantum dots. In quantum dots, the band gap energy becomes size-dependent (Brus, 1984):

$$E_g(QDs) = E_g(bulk) + \frac{h^2}{8r^2}\left(\frac{1}{m_e^* m_0} + \frac{1}{m_h^* m_0}\right) - \frac{1.82e^2}{4\pi\varepsilon_0\varepsilon r} - \frac{0.124e^4}{h^2(4\pi\varepsilon_0\varepsilon_r)^2}\left(\frac{1}{m_e^* m_0} + \frac{1}{m_h^* m_0}\right)^{-1} \quad (1.3)$$

The first term is the band gap energy of the bulk semiconductor, r is the particle radius, m_e^* and m_h^* are the effective mass of the electron and hole, respectively. The third term shifts $E_g(QDs)$ to smaller energy as r, while the second term shifts $E_g(QDs)$to higher energy asr^2. The fourth term is generally very small. Thus the apparent band gap energy will always increase for small enough r.

1.9.4 Surface effect and nanoparticle stability

With decreasing the size of metal particles, the percentage of surface atoms increases. This is an important point to be considered when one discusses the properties of nanoparticles. The influence of surface atoms becomes more important the smaller the particle is. Strictly speaking, only the inner-core atoms represent a minute piece of the bulk with strong quantum size effects. Physical measurements that give averaged information on the total particle are therefore always to be considered in this light. Another surface effect is equally important: nanoparticles in general are provided with a protective shell of ligand molecules. Otherwise, one would not be able to prepare them by chemical methods and especially to isolate and to investigate them as individual particles. Nanoparticles can be stabilized electrostatically in solutions. Basically, the repulsive interaction of the diffuse layers around nanoparticles offsets the van der Waals interactions. The sum of these two energies determines the particle stability. High diffuse layer potentials and low electrolyte concentrations, which increase the range of repulsion, are necessary for nanoparticles stability. A typical example is the stabilization of gold nanoparticles prepared by citrate reduction following the Turkevich method (Enustun and Turkevich, 1963). In this case, gold nanoparticles are stabilized by an electric double layer composed of bulky citrate ions, chloride ions and the cations attached to them. In contrast to the charge-stabilization of nanoparticles, the stabilization of nanoparticles by ligands which form chemical bonds with or chemisorb onto the particle surface are an effective method, which also enable nanoparticles

use for a variety of purposes. A typical example is the stabilization of gold nanoparticles by molecules with mercaptan groups, which have a very strong affinity for gold surfaces and ensure the formation of a dense monolayer on the surface. The merit of this approach is that the stabilized nanoparticles can be repeatedly isolated from and dissolved in the dispersing solvent without irreversible aggregation or decomposition. Importantly, further functionalization is possible by ligand-exchange reactions.

1.9.5 Optical properties

1.9.5.1 Optical absorption of nanoparticles

According to Lambert-Beer law, for a dilute colloidal solution, if the particles are much smaller than the incident light wavelength, the electric dipole absorption is predominant:

$$A = \log\left(\frac{I_0}{I}\right) = \frac{N\sigma l}{2.303} \quad (1.4)$$

Where l in cm is the light path in a spectrophotometer, N in cm^{-3} is the number density of the particle, σ is the extinction cross-section of a single particle in cm^{-2} and I_0 and I are the initial and final intensities of the light. For a metallic nanoparticle, σ is given by:

$$\sigma = \frac{24\pi^2 r^2 \varepsilon_m^{3/2} \varepsilon_2}{\lambda(\varepsilon_1 + 2\varepsilon_m)^2 + \varepsilon_2^2} \quad (1.5)$$

where λ is the wavelength of the incident light, r is the particle radius, ε_m is the dielectric function of the medium, ε_1 and ε_2 are the real and imaginary parts of the complex dielectric function of the particle ($\varepsilon = \varepsilon_1 + i\varepsilon_2$). Considering the motions of electrons in a spherical metal nanoparticle under the effect of an electric field vector of the light, it is possible to get:

$$\varepsilon_1 = \varepsilon^{\infty} - \frac{\omega_p^2}{\omega^2 + \omega_d^2} \quad (1.6)$$

$$\varepsilon_2 = \frac{\omega_p^2 \omega_d}{\omega(\omega^2 + \omega_d^2)} \quad (1.7)$$

Where ω is the frequency of the incident light, ε^{∞} is the high-frequency dielectric constant, ω_d is the relaxation or damping frequency and ω_p is the bulk plasma frequency.

For a semiconductor nanoparticle, if the optical transitions are far from the strong resonance and far from the band edges where the density of states could be approximated as a continuum, its extinction cross-section can be formalized to the sum of the absorption (σ_{abs}) and scattering (σ_{scat}) cross sections (van de Hulst, 1957,1981):

$$\sigma_{ex} = \sigma_{abs} + \sigma_{scat} \quad (1.8)$$

For particles with radii much smaller than the light wavelength, σ_{abs} is much larger than σ_{scat} . Therefore, the latter can be neglected. Then for the absorbing particles with isotropic polarizability, σ_{abs} can be evaluated from:

$$\sigma = 4\pi k \mathrm{Re}\,(i\alpha) = \frac{8\pi^2 m_2}{\lambda} Re(i\alpha) \quad (1.9)$$

Where k is the wave vector and λ the light wavelength, α is the polarizability of the dielectric sphere:

$$\alpha = \frac{m_1^2 - m_2^2}{m_1^2 + 2m_2^2} a^3 \quad (1.10)$$

Where a is the radius of the particle, $m_1 = n_1 - ik_1$ and $m_2 = n_2 - ik_2$ are the complex refractive indices of the particle and the solvent. Thus, σ_{abs} is given by:

$$\sigma_{abs} = \frac{8\pi^2 m_2}{\lambda} \times \frac{(2n_1k_1 - 2n_2k_2)(n_1^2 - k_1^2 + 2n_2^2 - 2k_2^2) - (n_1^2 - k_1^2 - n_2^2 + k_2^2)(2n_1k_1 + 4n_2k_2)}{(n_1^2 - k_1^2 + 2n_2^2 - 2k_2^2)^2 + (2n_1k_1 + 4n_2k_2)^2} \quad (1.11)$$

1.9.5.2 Size dependent optical properties

For a bulk metal, there is:

$$\omega_d = \frac{v_F}{r_\infty} \qquad (1.12)$$

Where v_F is the electron velocity at Fermi level and r_∞ the mean free path of the electron in the bulk metal. When the particle radius, r, is smaller than r_∞, the mean free path, R, becomes size-dependent with:

$$\frac{1}{R} = \frac{1}{r} + \frac{1}{r_\infty} \qquad (1.13)$$

It can be seen that a decrease in the particle size leads to an increase inω_d, causing the band to broaden and the maximum intensity to decrease. The peak position is virtually unaffected by small changes of ω_d, but for large damping frequencies, a slow shift to lower energies occurs. For rather small particles (< 1-2 nm), quantization of the energy levels within the conduction band takes place as the metal character of the particles begins to disappear, and the Plasmon band characteristic of the delocalized electrons breaks up into discrete bands due to single electron optical transitions.

For semiconducting nanoparticles, the fundamental absorption edge is related to the band gap energy via:

$$\lambda_g(nm) = \frac{1240}{E_g(eV)} \qquad (1.14)$$

Since in quantum dots the effective band gap increases with decreasing size of the particles, accordingly, a blue shift in the band edge absorption will be observed.

1.9.5.3 Luminescence properties

For a d^{10} metallic nanoparticle, absorption of light by the d-band electrons leads to interband transitions of these electrons to the empty sp-conduction band above the Fermi level. Both electrons and holes can relax by scattering with phonons then recombine radiatively to give rise to the visible luminescence (Huang and Murray, 2001). Light excitation of a semiconducting nanoparticle with an energy higher than that of the band gap leads to an electron-hole pair in the nanoparticle. The recombination lifetime of this excitation is usually small (in the picosecond to microsecond range) depending on the recombination pathway. Ideally, the luminescence of semiconducting nanoparticles should be size dependent as that of the excitation, but it is not the case. First, the nature of the nanoparticle surface strongly influences the luminescence through the surface trap states, which may result from a lot of factors, such as structural defects, atomic vacancies, dangling bonds, and adsorbates at the interface. For well-passivated surfaces, the luminescence of the nanoparticles is indeed very strong and is blue-shifted when the nanoparticle size is decreased. The luminescence is attributed to the radiative band-gap or near-band-gap (shallow trap states) recombination. However, if the electrons and/or holes are able to crossover into traps of various energy levels, the possibility of radiative recombination is decreased. A weak, broad, and substantially red shifted luminescence band is usually observed, indicating the loss of the radiationless recombination (Rogach *et al*., 1999; Gao *et al.,* 1998). Second, if the holes or electrons are preferentially scavenged by a reducing or oxidizing species, the nanoparticle is left with electrons (or holes) solely. As electrons and holes are separated into two different phases, the lifetime of the charge carriers in the nanoparticle can be relatively long (Germeau *et al.*, 2003). Third, electrons can be injected into semiconducting nanoparticles using strong reducing species. The oxidized species form then the positive counter charge, compensating the charge of the electrons in the nanoparticles (Wang *et al.*, 2001; Shim and Guyot-Sionnest, 2000).

1.10 The Liquid-liquid interface method assembly at fluid interface

The self-assembly of nanoparticles at fluid interfaces (liquid–vapour and liquid–liquid) has enabled the preparation of high quality two-dimensional crystals. In particular Langmuir trough techniques provide a means to tune the interparticle distances and facilitate the transfer of the crystal monolayers to solid substrates (Fendler, 1996). Particles adsorbed at interfaces also play an important role in industrial processes concerned with foams and emulsion (Aveyard and Clint, 1995; Binks, 2002). Among the interfacial assembly methods, such as liquid-air interface, the liquid-liquid (water-oil) interface possess unique thermodynamic properties such as viscosity, density and also the interface is not sharp since there is always the solubility of one phase in the other (Burdi, 1997). There have been remarkable experimental developments on the assembly of metallic nanoscopic materials at the liquid-liquid interface, with the particular mention of the assembly of gold monolayers at the water-oil interface driven by the reduction of particle's hydrodynamic radius (Vanmaekelbergh *et al*., 2004). Vanmaekelbergh *et al* (2004) have reported that citrate capped, hydrophilic gold nanoparticles can be assembled into two dimensional arrays at liquid-liquid interface, induced by the destabilization with the addition of a low-dielectric solvent to an aqueous colloidal solvent. Möhwald *et al* (2005) also directed the assembly of hydrophobic and hydrophilic nanoparticles at water-oil interface by capping the nanoparticles with appropriate ligands.

1.10.1 Water-air interface

Monolayers of insoluble amphiphiles assembled at the water/air interface are considered traditional means of assembly. They have played a huge role in providing an insight into fundamental aspects of two dimensional assemblies at interfaces, and have been a cornerstone of modern colloid chemistry and interface science (Böker *et al.*, 2007; Avouris *et al*., 2009). The generation of Langmuir monolayers involves, firstly, the formation of a single layer of molecules

(a monolayer), on a water surface. The interaction on the surfaces of the water molecules is strong and two dimensional, which ensures that the molecules are bound to the surface and have no tendency to form a layer more than one molecule thick. The existence of strong anisotropic interaction between the molecules and the liquid or sub-phase is critical. This factor necessitates the use of water in this technique, so that the molecules in the monolayer have no tendency to prefer their own kind and thus crystallize (Böker *et al.,* 2007; Avouris *et al*., 2009; Golberg *et al.,* 2009) Also to achieve the necessary 2-D interaction, one end of the molecule must be substituted with a group capable of interacting strongly with water (hydrophilic) via its dipole moment or hydrogen bonding, while the other end must be a hydrophobic chemical group large enough to ensure that the molecule as a whole is insoluble (Böker *et al*., 2007; Avouris *et al*., 2009; Golberg *et al.,* 2009). The formed layer is initially quite loosely packed and inhomogeneous, but by reducing the area of the water surface the molecules are forced together, thus eliminating voids. In a second step, the now uniform layer can be transferred onto a solid substrate as a material known as Langmuir-Blodgett film. An illustration of a transfer for a Langmuir-Blodgett thin film to the substrate is shown in Figure 1.14. In this method the particles are mostly prepared prior to their dispersion and assembly into films (Waser and Aono, 2007).

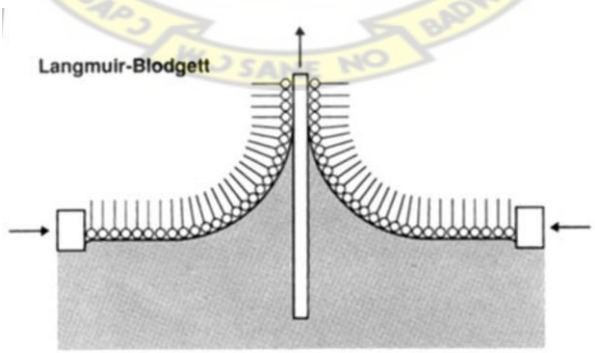

Figure 1.14. A schematic diagram showing how a Langmuir-Blodgett monolayer can be transferred from the surface of the solvent to a hydrophilic solid by raising the substrate through the water air interface (Golberg *et al*., 2010).

1.10.2 Oil–water interfacial self-assembly

Most recently, an oil–water planar interface has been considered as an ideal template for self-assembly of various nanostructures into functional nanofilms, and has received intensive attention (Rao and Kalyanikutty, 2008; Ariga *et al*., 2009; Vanmaekelbergh *et al*., 2004; Wang and Möhwald, 2004; Möhwald et *al.*, 2004; Möhwald et *al*., 2006; Xia and Wang, 2008; Möhwald et *al.*, 2005; Wang *et al*., 2010). Au, Ag, Pt, SiO_2 and $CoPt_3$ nanoparticles have been successfully self-assembled at the oil–water interface (Park *et al*., 2007; Park and Park, 2008; Park *et al*., 2008; Sun *et al*., 2006; Rotello *et al*., 2008). 1-D nanostructures and 2-D nanoplatelets and exfoliated nanosheets have also been successfully self-assembled at the oil–water interface (Rotello *et al*., 2008; Miyashita *et al*., 2007; Miyashita *et al.*, 2008; Miyashita *et al*., 2009; Niu *et al*., 2008; Kane *et al*., 2006; Park *et al.*, 2007; Park *et al.*, 2009; Yu *et al.*, 2010; Sasaki *et al*., 2008; Sasaki *et al*., 2009; Biswas and Drzal, 2009; Wang *et al.*, 2010). This novel assembly strategy effectively opens the door for the self-assembly of hydrophilic nanostructures into closely-packed nanofilms. More importantly, this self-assembly has been developed as a novel and facile strategy to fabricate nanofilm-based devices, such as photodetectors, electrical resistive switching device (Langmuir *et al*., 2010; Fang *et al*., 2011).

1.10.3 Discovery and mechanism of oil–water planar interfacial self-assembly

The self-assembly of colloidal particles at the curved liquid interface has been studied for a century since it was pioneered by Pickering (Pickering, 1907; Nagayama *et al.*, 1996; Weitz *et al*., 2002; Binks, 2002; Clint *et al*., 2003). Emulsions stabilized by colloidal particles are known as Pickering emulsions. Similar to the curved liquid interfacial self-assembly, the planar interfaces between two immiscible fluids have also been employed as an ideal template to produce 2-D self-assemblies with long-range orders. In 2004, Vanmaekelbergh *et al.* first observed a surprising result that gold nanocrystals can spontaneously form a monolayer film at

the oil–water interface by the addition of some inducer (Vanmaekelbergh *et al.,* 2004). Upon addition of ethanol to the gold sol, a blue layer of gold nanocrystal immediately appears at the heptane–water interface. The as-formed film at the interface is very stable and does not collapse into multilayers. Instead, the film creeps up the glass wall of the vial to a height of a few centimetres without breaking into pieces. According to Pieranski's thermodynamics model, the self-assembly of particles at a curved oil–water interface can be regarded as the reduction in the total interfacial energy of the system (Pieranski, 1980; Binks and Clint, 2002,). Analogously, the fundamental mechanism of the self-assembly at the planar oil–water interface can also be understood by Pieranski's theory. Concretely, before assembly, the hydrophilic nanoparticles are dispersed in the water phase and the initial interfacial energy is the energy between the oil and water phases. After the entrapment of one spherical crystallite at the oil–water interface, a proportion of initial oil–water interface is replaced by the nanoparticle-oil interface (as shown in Figure 1.14), and thus there are three contributions for the total energy change for this process, respectively arising from the particle–oil, particle–water and nanoparticle–water interfaces. Combined with the Young's equation (Pieranski, 1980), the total energy (Helmholtz free energy) change ΔE can be expressed as follows (Russell *et al.*, 2003):

$$\Delta E = -\pi R^2 [\gamma OW - (\gamma PW - \gamma PO)]^2/\gamma OW < 0 \qquad (1.1)$$

Where γPO, γPW, and γOW represent the interfacial tensions between the particle and oil, the particle and water, the oil and water, respectively. R is the radius of a spherical nanoparticle.

From eqn (1.1), one can see that the total energy change ΔE is negative after the entrapment of the nanoparticles at the oil–water interface. Thus the interfacial assembly of nanoparticles is dictated by a minimization of the Helmholtz free energy. Here, ΔE is mainly dominated by two factors, the size of particle and the wettability of the particle surface. Because ΔE is directly proportional to R^2, the energy gain is larger and the assembly is more stable for larger

nanoparticles than for smaller ones (Russell *et al*., 2003; Russell *et al*., 2003; Russell *et al.*, 2005): For large-sized particles, the decrease in the total energy per particle is much larger than the thermal energy, k_BT, (where k_B is the is the Boltzmann constant and T is the temperature) so the particles are strongly held on the liquid–liquid interface.

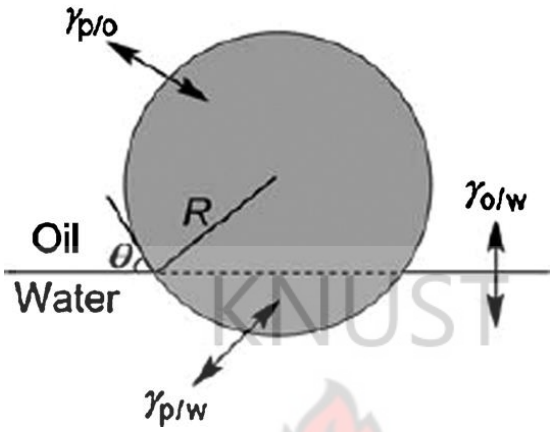

Figure 1.15. An isotropic particle at the oil–water interface, showing the interfacial tensions between the particle and oil, the particle and water, the oil and water, respectively (Wang *et al*., 2010).

For small-sized nanoparticles, thermal energy is sufficient to induce a displacement of the particles from the interface, and the assembly is dynamic with particles adsorbing to and desorbing from the oil–water interface. Therefore, this liquid–liquid interfacial self-assembly is quite size-dependent. In fact, Russell *et al*. (2003) have observed that thermal fluctuation makes no droplet stabilization at a curved liquid–liquid interface when the diameter of the particles is less than 1.6 nm. In their study, a~20 mm-diameter water droplet was dispersed in toluene containing CdSe nanoparticles. The nanoparticles segregated to the toluene–water interface, forming a monolayer at the interface. By addition of water to the dispersion of nanoparticles in toluene, nanoparticle-coated water droplets with diameters from 10 to 100 mm were obtained. Subsequently, they introduced 4.6 nm CdSe particles in toluene to a dispersion containing water

droplets in toluene that had been stabilized with 2.8 nm particles. Interestingly, the 4.6 nm particles assembled on the surface of an existing stabilized droplet, displacing the smaller 2.8 nm particles. However, displacement of larger nanoparticles with smaller ones did not occur. This result confirms the reliability of eqn (1.1), and thus the self-assembly of the particles should be attributed to the decrease in total interfacial energy. Wang and co-workers found an essential role of the contact angle of 90º for the interface entrapment of nanoparticles (Möhwald *et al.*, 2004; Möhwald *et al*., 2006; Xia and Wang, 2008; Möhwald *et al*., 2005). They transferred the as-assembled film at the oil–water interface onto solid substrates, and then the contact angle of the nanoparticles with the oil–water interface could be determined by resting a water droplet covered with toluene on the surface of the as-assembled film. As shown in Figure 1.15, the position of nanoparticles at the oil–water interface is determined by their contact angle: for a hydrophilic particle with a contact angle smaller than 90º, its larger fraction resides in the water bulk phase, or vice versa. When its contact angle is around 90º, the particle prefers to reside at the interface. Furthermore, the profile of the calculated partition of 10 nm particles in oil–water two-phase systems shows that when the contact angle slightly deviates from 90º, the nanoparticles prefer to go to the bulk phase, further suggesting that the contact angle of 90º should play a pivotal role for the interface entrapment of nanoparticles (Russell *et al*., 2005). Wang *et al*. (2006) and Binks, (2003) also studied the effect of the surface charge of particles on their interfacial entrapment at an oil–water interface. They observed the interfacial assembly of nanoparticles at a low pH value when the surface charge density of the nanoparticles was reduced by the protonation of the carboxylic acid groups on the surfaces. Then the de-protonation of the carboxylic acid groups at a high pH value caused the detachment of the nanoparticles from the interfaces and redispersion in bulk water phase. This result suggests that the increase of the surface charge density not only reduces the interfacial activity of the particles but also enlarges the electrostatic repulsion between the charged particles.

Although the nanoparticles are readily self-assembled at an oil–water interface, the entrapment does not occur with the absence of an inducer. Vanmaekelbergh *et al*. (2004) pointed out that the surface charge of the nanoparticles dispersed in a water phase was decreased by the addition of an inducer, such as ethanol. They speculated that the decreasing surface charge reduced the interfacial energy of the nanoparticles and caused the contact angle of nanoparticles to approach to 90º. This has been also confirmed by Miyashita's experiment by examining the ζ-potential of an aqueous dispersion of carbon nanotubes. The ζ-potential of the carbon nanotubes gradually decreases with addition of ethanol to the dispersion, due to the adsorption of ethanol molecules to the multi-walled carbon nanotube (MWCNT) surface (Miyashita *et al*., 2007). The hydroxyl groups of ethanol molecules form hydrogen bonds with carboxyl anions, which compensate the negative charge at the MWCNT surface. Vanmaekelbergh *et al*. (2004) considered this self-assemble process in terms of a thermodynamic evaluation of charged nanoparticles. In their model, the chemical potential of the nanoparticles in the bulk phase and the oil water interface were considered by taking into account the interfacial energies, van der Waals interactions and the electrostatic interactions. They derived an equation by setting the chemical potential for charged nanoparticles at the interface to be equal to one in the bulk phase, showing an isotherm of the interfacial particle coverage as a function of the surface charge density of nanoparticles. The surface coverage of the nanoparticles at the interface increased with decreasing surface charge density of the particles. When an inducer such as ethanol was added, the surface charge density of the nanoparticles decreased, and the liquid–liquid interface became completely filled with nanoparticles (Möhwald *et al*., 2006; Böker *et al*., 2007). Combined with the aforementioned Wang's results one can conclude that addition of an inducer decreases the surface charge density of the particles, increases the interfacial activity of the particles, and finally leads to the attachment of particles at the oil–water interface. Although the surface charge of nanoparticles is apparently decreased by the addition of an inducer, Park *et al*. supposed that

there exists a limiting point for the surface charge that can be achieved by adding an inducer (Park *et al*., 2007; Park and Park, 2008; Park *et al*., 2008). It is easily understood that the complete removal of the electrostatic repulsive force should lead to the irreversible coagulation of nanoparticles at the interface. Since the as-assembled film is very stable at the interface, the entrapped nanoparticles at the interface should retain a certain electrostatic repulsive force, which prevents the formation of closely-packed aggregations by counteracting the van der Waals interaction. In fact, the voids among the nanoparticles were usually observed in the as-assembled film by this strategy (Vanmaekelbergh *et al*., 2004; Wang and Möhwald , 2004; Möhwald *et al*., 2004; Möhwald *et al*., 2006; Xia and Wang, 2008; Möhwald *et al*., 2005; Wang *et al*., 2010; Park *et al*., 2007; Park and Park, 2008; Park *et al*., 2008; Sun *et al*., 2006), also demonstrating the presence of residual surface charge of the nanoparticles assembled at the interface.

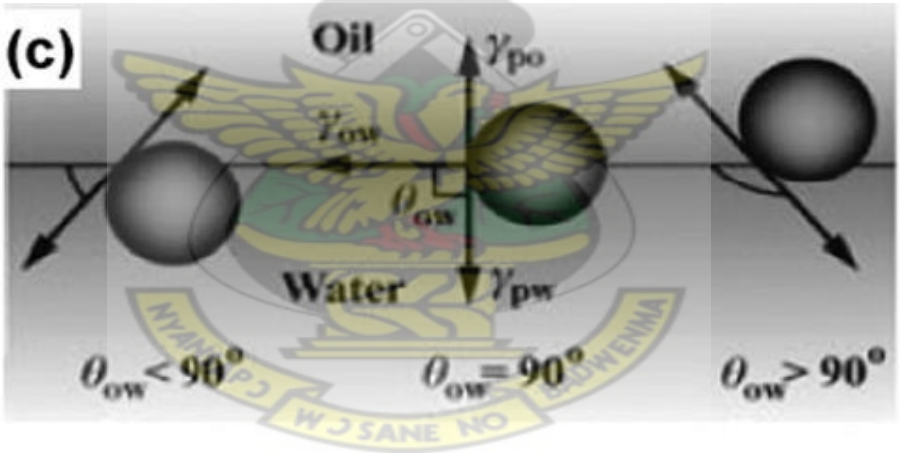

Figure 1.16 Schematic representation of the position of a particle at an oil–water interface for a contact angle with the interface less than 90º (left), equal to 90º (centre), and larger than 90º (right) (Möhwald *et al*., 2004).

The liquid-liquid interface techniques have the advantages of being simple, scalable, low cost, low temperature deposition, no additives are necessary and films produced independent of substrate.

Figure 1.17: Schematic diagram showing thin film nanoparticles formed at the liquid-liquid interface (Rao and Kalyanikutty, 2008).

The method primarily involves a metal precursor dissolved in the organic layer and a reducing, a precipitating, or an oxidizing agent in the aqueous layer. The reaction occurs at the interface giving rise to a film at the interface with several interesting features. The interface has a dual role in controlling charge transport and directing the structure of the deposit. This method has been employed in the preparation of nanocrystalline films of gold and in generating ultrathin polycrystalline, as well as single-crystaline, films of some metal chalcogenides at the interface (Figure 1.17). The formation of single-crystalline films is indeed a noteworthy feature and it is believed that this method can be adopted not only for generating nanocrystalline films of various materials but also to study processes occurring at the liquid–liquid interface.

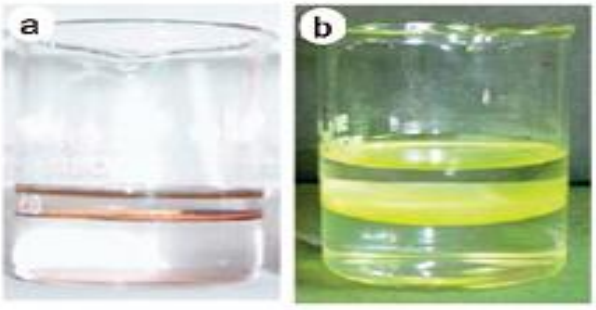

Figure 1.18: Nanocrystalline films of (a) Au and (b) CdS formed at the water-toluene interface (Rao and Kalyanikutty, 2008).

When toluene solution containing the metal precursor was mixed with aqueous solution containing NaHE (E= S, Se, Te), the colour of the interfacial layer changes immediately indicating the nucleation process has started. After the container was left under ambient laboratory conditions for some time a thin film was formed at the interface. Figure 1.19 shows the interface formation and subsequently reaction occurring in both phases. The overall reaction is given below

$$M(S_2CNR_2)_2 + 2NaHE \longrightarrow ME + 2R_2CNS_2Na + H_2E$$

Where M = a metal; E = a chalcogenide

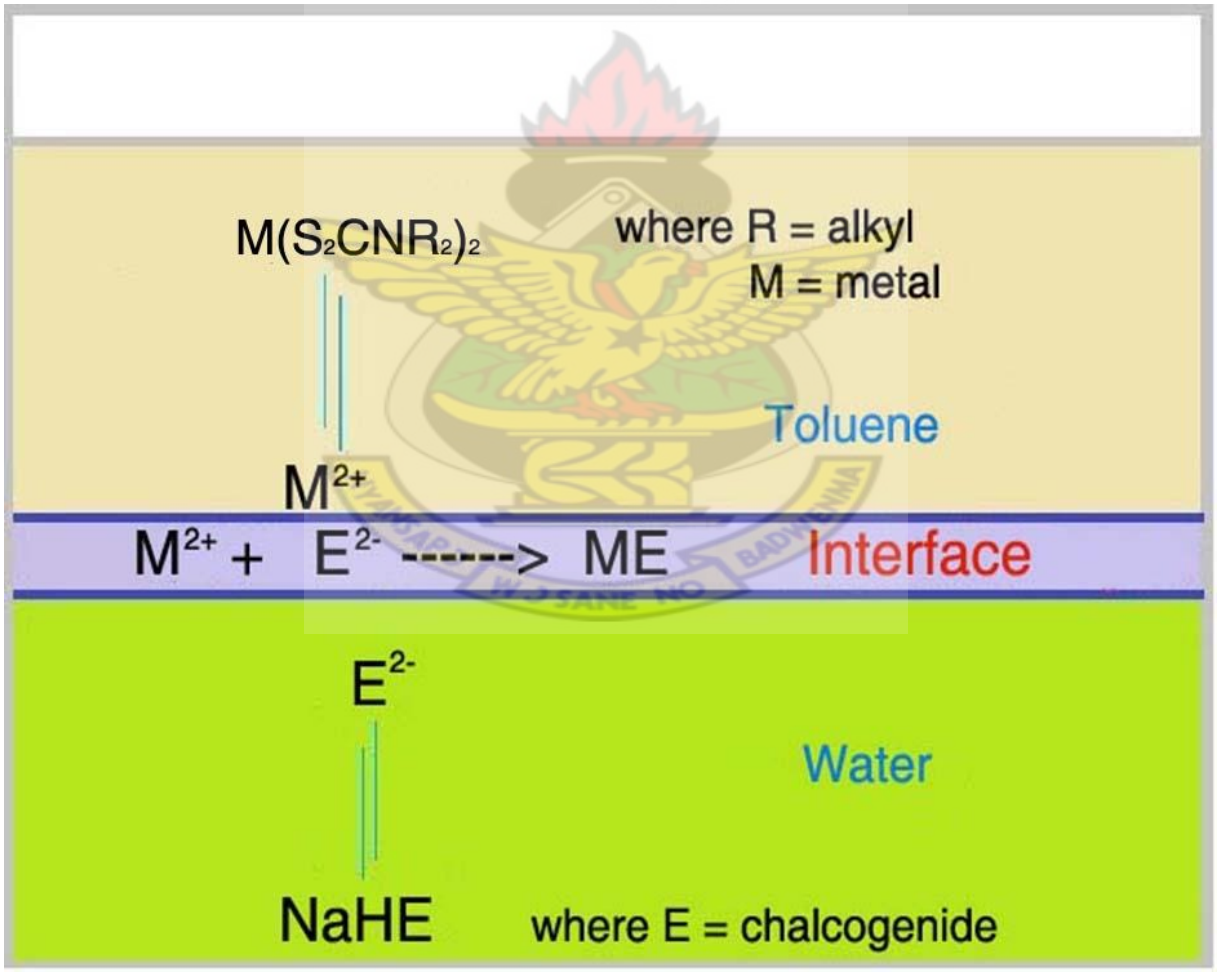

Figure 1.19. Schematic diagram showing the formation of interfacial layer on mixing toluene/water and movement of ions.

1.11 Growth process of nanocrystals

According to classical model of crystallization a crystal is formed via addition of atom by atom or monomer by monomer to an inorganic or organic temperate or alternatively by dissolution of unstable phases and precipitation of the more thermodynamically stable phase (Lamer and Dineger, 1950; Kim and Kim, 2003). Extensive research has been carried out to understand these processes and factors affecting them aiming to get an insight to prepare nanocrystals of desired shape and size. Interestingly for a specific solute there is certain limit of solubility in a particular solvent and addition of excess solute will result in precipitation and formation of nanocrystals. Broadly two stages can be identified during growth of nanocrytals namely nucleation and growth (Lamer and Dinegar's model) (Lamer and Dineger, 1950). For the nucleation stage, solution should be supersaturated either by directly dissolving the solute at a higher temperature and subsequently cooling to room temperature or by introduction of reactants to yield supersaturating solution during the reaction. Nucleation stage is followed by particle growth stage. Growth occurs either by diffusion or coalescence. In diffusion growth, monomers in solution interact with the solid seeds to form a bigger particle, whereas in coalescence nuclear merge into a bigger particle. The coalescence mechanism creates defects and grain boundaries in resulting nanocrystals due to utilization of energy process (Figure 1.20).

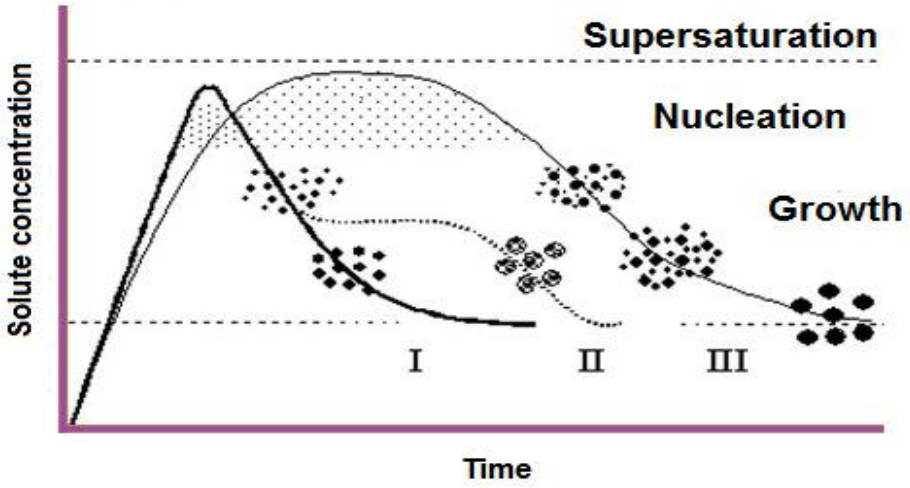

Figure 1.20. A schematic representation of the mechanism during the growth of nanocrystals according to Lamer and Dinegar's model of variation of concentration versus time (Lamer and Dineger, 1950).

Curve I represents formation of uniform particles by diffusion, curve II is for bigger size particle formation by aggregation of smaller subunits, while curve III represents formation of large particles by Ostwald ripening. (Lamer and Dineger, 1950).

With the passage of time when the reactants are depleted due to particle growth, size defocusing or Ostwald ripening will take place, where larger nuclei continue to grow and smaller ones get smaller and finally dissolve. Stopping the reaction at this stage will result in the particles having broad size distribution. Thus, it is difficult to get monodisperse particles unless the reaction time is extended to deplete the supersaturation and the smaller nuclear. Thus by rapid injection of precursors in solvent which generates sudden burst of nuclei simultaneously followed by self-sharpening growth process nearly monodisperse sized particles can be obtained by stopping the reaction.

1.12 References

Acharya, S., Hill, J. P. & Ariga, K. (2009). "Soft Langmuir-Blodgett technique for hard nanomaterials". *Adv. Mater*., 21: 2959-2981.

Afzaal, M. & O'Brien, P. (2006). "Silica coated PbS nanowires". *J. Mater. Chem*., 16: 1113-1115.

Akhtar, J., Malik, M. A., O'Brien, P. & Helliwell, M. (2010). "Controlled synthesis of PbS nanoparticles and the deposition of thin films by Aerosol-Assisted Chemical Vapour Deposition (AACVD)". *J. Mater. Chem*., 20: 6116-6124.

Alivisatos, A. P. (1996a). Semiconductor Clusters, Nanocrystals, and Quantum Dots. *Science*, 271: 933-937.

Alivisatos, A.P. (1996b). Perspectives on the physical chemistry of semiconductor nanocrystals, Journal of Physical Chemistry, 100, 31, 13226-13239.

Anthony, R.W., (1999). "Basic solid state chemistry, John Wiley & Son.

Ariga, K., Hill, J. P., & Ji, Q. M. (2007). "Layer-by-layer assembly as a versatile bottom-up nanofabrication technique for exploratory research and realistic application," *Phys. Chem.*, 9(19): 2319-2340.

Armstrong, A. J., Mockler, & Osullivan, W. J. (1989). "Isothermal-expansion melting of two-dimensional colloidal monolayers on the surface of water". *J. Phys. Condens, Matt*., 1707-1730.

Arregui, E. O. (2004). Quantum size effects and stability of nanostructures, Doctoral Thesis, University of the Basque Country.

Arumugam, P., Patra, D., Samanta, B., Agasti, S. S., Subramani, C. & Rotello, V. M. (2008). "Self-Assembly and Cross-linking of FePt Nanoparticles at Planar and Colloidal Liquid-Liquid Interfaces" *J. Am. Chem. Soc.*, 130: 10046-10047.

Asuri, P., Karajanagi, S. S., Sellitto, E., Kim, D. Y., Kane, R. S. & Dordick, J. S. (2006). "Water-soluble carbon nanotube-enzyme conjugates as functional biocatalytic formulations". *Biotechnol Bioeng*, 95(5): 804-811.

Aveyard, A., Binks, B. P. & Clint, J. H. (2003). "Emulsions stabilised solely by colloidal particles". *Adv. Colloid Inter. Sci*., 100: 503-546.

Aveyard, R. & Clint, J. H. (1995). Liquid droplets and solid particles at surfactant solution interfaces. *J. Chem. Soc. Faraday Trans.* 91: 2681-2697.

Bain, C. & Whistides, G. M. (1989). "Modeling Organic Surfaces with Self-Assembled. Monolayers". *Angew. Chem. Int. Ed. Engl*., 28: 506-516.

Barton, J. C. & Ranby, P. W. (1977). Zinc sulphide scintillator with faster decay *J. Phys. E*: *Sci. Instrum*., 10: 437-438.

Basu, J. K. & Sanyal, M. K., (2002). Ordering and Growth of Langmuir-Blodgett films: X-ray Scattering Studies. *Phys Reports*, 363(1): 1-84.

Battaglia, D. & Peng, X. (2002). "Formation of high quality InP and In As nanocrystals in a noncoordinating solvent". *Nano Lett*., 2: 1027-1030.

Benjamin, I. (1996). "Chemical Reactions and Solvation at Liquid Interfaces: A Microscopic Perspective". *Chem. Rev*., 96: 1449-1475.

Benkoski, J., Jones, R. L., Doughlas, J. F. & Karim, A. (2007). "Photo curable Oil/Water Interfaces as a Universal Platform for 2-D Self-Assembly". *Langmuir*., 23: 3530-3537.

Berhanu, D., Govender, K., Boyle, D. S., Archbold, M., Halliday, D. P. & O'Brien, P. (2006). "A novel soft hydrothermal (SHY) route to crystalline PbS and CdS nanoparticles exhibiting diverse morphologies". *Chem. Commun*., 417: 4709-4711.

Binder, W. H. (2005). "Supramolecular Assembly of Nanoparticles at Liquid-Liquid Interfaces". *Angew. Chem. Int. Ed*., 44: 2-5.

Binks, B. P. & Clint, J. H. (2002). "Solid Wettability from Surface Energy Components: Relevance to Pickering Emulsions". *Langmuir*, 18: 1270-1273.

Binks, B. P. & Clint, J. H. (2002). "Solid wettability from surface energy components: relevance to Pickering emulsions". *Langmuir*, 18: 1270-1273.

Binks, B. P. (2002). "Particles as surfactants - similarities and differences". *J. Colloid Interface Sci.*, 7: 21-41.

Binks, B. P. (2003). "Particles as surfactants-similarities and differences". *Curr. Opin. Colloid Interface Sci*., 100: 503-546.

Binks, B. P., Lumsdon, S. O. (2000). "Influence of particle wettability on the type and stability of surfactant-free emulsions". *Langmuir*, 16: 8622-8631.

Birdi, K. S. (ed.) (1997). Handbook of surface and colloid chemistry. Boca Raton, FL: CRC Press.

Biswas, S. & Drzal, L. T. (2009). "A Novel Approach to Create a Highly Ordered Monolayer Film of Graphene Nanosheets at the Liquid-Liquid Interface". *Nano Lett*., 9: 167-172.

Boker, A., He, J., Emrick, T., Russell, T. P. (2007). "Self-assembly of Nanoparticles at. Interfaces". *Soft Matter*, 3; 1231-1248.

Braunger, D., Hariskos, D., Walter, T. & Schock, H. W. (1996). "An 11.4 % Efficient Polycrystalline Thin Film Solar Cell Based on $CuInS_2$ with Cd-Free Buffer Layer". *Sol. Energy Mater. Sol Cells*, 40: 97-102.

Bresme, F. & Ottel, M. (2007). "Nanoparticles at fluid interfaces". *J. Phys*.: *Condens. Matter*, 19: 413101.

Brus, L. E. (1984). "The size dependence of the lowest excited electronic state". *J. Chem. Phys*., 80: 4403-4409.

Brus, L. E., (1984). "Electron–electron and electron-hole interactions in small semiconductor crystallites: The size dependence of the lowest excited electronic state". *J. Chem. Phys*., 80: 4033-4409.

Brust, M., Walker, M., Bethell, D., Schiffrin, D. J. & Whyman, R. (1994). "Synthesis of thiol derivatised gold nanoparticles in a two-phase liquid–liquid system". *J. Chem. Soc. Chem. Commun.*, 7: 801-802.

Buess-Hermann, C. (1994). Self-assembled monolayers at electrode metal surfaces. *Progr. Surf. Sci*., 46: 335-337.

Burdi, K. S. (1997). *Handbook of Surface and Colloid Chemistry*, CRC Press, New York, 2nd Ed.

Chen, M., Hu, L. F., Xu, J. X., Liao, M. Y., Wu, L. M. & Fang, X. S. (2011). "ZnO Hollow-Sphere Nanofilm Based High-Performance and Low-Cost Photo detector". *Small*, 7: 2449-2453.

Chen, S. W., Huang, K. & Stearns, J. A. (2000). "Alkanethiolate-protected palladium nanoparticles". *Chem. Mater.*, 12: 540-547.

Chen, S., Ingrma, R. S., Hostetler, M. J., Pietron, J. J., Murray, R. W., Schaaff, T.G., Khoury, J. T., Alvarez, M. M. & Whetten, R. L (1998). "Gold Nanoelectrodes of Varied Size: Transition to Molecule-Like Charging". *Science*, 280: 2098-2101.

Cheng, C., Hu, G., Zhang, H. (2009). "Facile solvothermal synthesis of nanostructured PbSe with anisotropic shape: Nanocubes, submicrometer cubes and truncated octahedron". *J. Cryst. Growth*, 311: 1285-1290.

Cho, K., Talapin, D. V., Gaschler, W., Murray, C. B. & Designing, J. (2005). "PbSe Nanowires and Nanorings through Oriented Attachment of Nanoparticles". *Am. Chem. Soc*., 127: 7140-7147.

Cho, Y. -H., Cho, G. & Lee, J.-S. (2004). "Two-Dimensional, Open-Pored, Mesoscopic Titania Layers Using Polymeric Nanoparticle Monolayers as a Template". *Adv. Mater*., 16: 1814.

Klayman, D. L. & Griffin, T. S. (1973). "Reaction of selenium with sodium borohydride in protic solvents. A facile method for the introduction of selenium into organic molecules". *J. Am Chem. Soc*., 95: 197-199.

Daintith, J., (2004). *Oxford Dictionary of Chemistry*, New York: Oxford University Press.

Dinsmore, A. D., Hsu, M. F., Nikolaides, M. G., Marquez, M., Bausch, A. R., Weitz, D. A. (2002). "Colloidosomes: Self-Assembled, Selectively-Permeable Capsules Composed of Colloidal Particles". *Science*, 298: 1006-1009.

Dryfe, R. A. W. (2006). "Modifying the liquid/liquid interface: pores, particles and deposition". *Phys. Chem. Chem. Phys*., 8: 1869-1883.

Du, M., Wang, Y., Xu, J., Yang, P. & Du, Y. (2008). "PbSe quantum dots: Preparation in a high boiling point solvent and characterization". *Colloid J*., 70: 720.

Duan, H. W., Wang, D. Y., Kurth, D. G., Möhwald, H. (2004). "Directing self-assembly of nanoparticles at water/oil interfaces". *Angew. Chem. Int. Ed.*, 43: 5639-5642.

Enustun, B. V. & Turkevich, J. (1963). "Coagulation of Colloidal Gold". *J. Am. Chem. Soc*., 85: 3317-3328.

Fan, D., Thomas, P. J. & O'Brien, P. (2007a). "Deposition of CdS and ZnS thin films at the water/toluene interface". *J. Mater. Chem*., 17: 1381-1386.

Fan, D., Thomas, P. J. & O'Brien, P. (2007b). "The synthesis of inorganic materials at the water– toluene interface". *J. Nanosci. Nanotechnol.* 7: 1689-1694.

Fan, D., Thomas, P. J. & O'Brien, P. (2008a). "Pyramidal lead sulphide crystallites with high energy {113} facets". *J. Am. Chem. Soc*., 130: 10892-10894.

Fan, D., Thomas, P. J. & O'Brien, P. (2008b). Synthesis and assembly of Bi_2S_3 nanoparticles at the water–toluene interface. *Chem. Phys. Lett*., 465: 110-114.

Fang, X. S., Bando, Y, Gautam, U. K., Ye, C. H. & Golberg, D. (2008). Inorganic semiconductor nanostructures and their field-emission applications. *J. Mater Chem*., 18: 509-522.

Fang, X. S., Bando, Y., Gautam, U. K., Zhai, T. Y., Liao, M. Y. & Golberg, D. (2009). "ZnO and ZnS nanostructures: ultraviolet-light emissions", lasers and sensors, *Crit. Rev. Mater. Sci*. 34: 190-223.

Fang, X. S., Bando, Y., Gautam, U. K., Zhai, T. Y., Liao, M. Y. & Golberg, D. (2010). "An efficient way to assemble ZnS nanobelts as ultraviolet-light sensors with enhanced photocurrent and stability", *Adv. Funct. Mater.* 20(3): 500-508.

Fang, X.S., Bando, Y., Gautam, U.K., Zhai, T.Y., Zeng, H.B. & Xu, X.J. (2009). "ZnO and ZnS nanostructures: ultraviolet-light emitters, lasers and sensors". *Crit. Rev. Solid State Mat. Sci*., 34: 190-223.

Faraday, M. (1857). "The Bakerian lecture: experimental relations of gold (and other metals) to light". *Phil. Trans. R. Soc. Lond. B*, 147: 145-181.

Fendler, J. H. (1996). "Nanoparticles at air/water interfaces". *Curr. Opin. Colloid Interface Sci.* 1: 202-207

GAO, M., Richter, B., Kirstein, S. & Möhwald, H. (1998) Electroluminescence studies on self-assembled films of PPV and CdSe nanoparticles, *J. Phys. Chem. B*, 102: 4096-4103.

Gautam, U. K., Ghosh, M. & Rao, C. N. R. (2004). "Template-free chemical route to ultrathin Single crystalline films of CuS and CuO employing the liquid–liquid interface". *Langmuir*, 20: 10776-10778.

Ge, J. E. & Li, Y. D. (2003). "Ultrasonic synthesis of nanocrystals of metal selenides and tellurides". *J. Mater. Chem*., 13: 911-918.

Germeau, A., Roest, A. L., Vanmaekelbergh, D., Allan, G., Delerue, C. & Meulenkamp, E. (2003). "Optical Transitions in Artificial Few-Electron Atoms Strongly Confined inside ZnO Nanocrystals". *A. Phys. Rev. Lett*., 90: 097401/1-097401/4.

Ghrayeb, J., Jackson, T. W., Daniels, R. & Hopper, D. G. (1997). "Review of Field Emission Display Potential as a Future (Leap-Frog) Flat Panel Technology". *Proc. SPIE,* 3057: 237-248.

Goldenberg, L. M., Wagner, J., Stumpe, J., Paulke, B. R., Gornitz, E. (2002). "Ordered arrays of large latex particles organized by vertical deposition". *Langmuir*, 18: 3319-3323.

Gong, Y. and Barron, A. (2012). "Band Gap Measurement". *Connexions.*

Grahn, H. T. (1999). Introduction to Semiconductor Physics. World Scientific: Singapore.

Ha, K., Lee, Y. J., Lee, H. J. & Yoon, K. B. (2000). "Micro patterning of Oriented Zeolite Monolayers on Glass by Covalent Linkages". *Adv. Mater*., 12: 1114-1117.

Hogarth, G. (2005). "Transition metal dithiocarbamates: 1978-2003". *Prog. Inorg. Chem*. 53: 71-561.

Honsberg, C and Bowden, S. (1999) Photovoltaics: Photovoltaic devices, Volume 1. University New York: Wiley. of New South Wales Photovoltaics Centre.

Horswell, S. L., Kiely, C. J., O'Neil, I. A., David, J. & Schiffrin, D. J. (1999). "Alkyl isocyanide derivatized platinum nanoparticles". *J. Am. Chem. Soc.,* 121: 5573-5574.

Hu, L. F., Ma, R. Z., Ozawa, T. C. & Sasaki, T. (2009). "Oriented monolayer film of Gd_2O_3:0.05 Eu crystallites: quasi-topo tactic transformation of the hydroxide film and drastic enhancement of photoluminescence properties". *Angew. Chem. Int. Ed.*, 48: 3846-3849.

Hu, L. F., Wu, L. M., Liao, M. Y. & Fang, X. S. (2011). "ZnS nanostructure arrays: a developing material star". *Adv. Mater*., 23: 1988-1992.

Hu, L., Ma, R., Ozawa, T., Geng, F., Iyi, N., Sasaki, T. (2008). "Oriented Films of Layered Rare-Earth Hydroxide Crystallites Self-Assembled at the Hexane/Water Interface". *Chem. Commun.* 47, 4897-4899.

Huang, T. & Murray, R. W. (2001). "Visible Luminescence of Water-Soluble Monolayer-Protected Gold Clusters". *J. Phy. Chem. B*, 105: 12498-12502.

Hurd, A. J. & Schaefer, D. W. (1985). "Diffusion-limited aggregation in 2 dimensions". *Phys. Rev. Lett.*, 54: 1043-1046.

Iijima, S. (1991). "Helical microtubules of graphitic carbon". *Nature*, 354, 56-58.

James, E. H. (2008). Inorganic chemistry, Amsterdam: Elsevier.

Jdanov, A., Pelleg, J., Dashevsky, Z. & Shneck, R. (2004). "Growth and characterization of PbTe films by magnetron sputtering". *Mater. Sci. Eng. B*, 106, 89-94.

Jones, A. C. and O'Brien, P. (1997) CVD of compound semiconductors: precursor synthesis, development and applications; Germany, Cambridge.

Kang, S. Y. & Kim, K. (1998). "Comparative study of dodecanethiol-derivatized silver nanoparticles prepared in one-phase and two-phase systems". *Langmuir*, 14, 226-230.

Kerner, R., Pelchik, O. & Gedanken, A., (2001). "Sonochemical and Microwave-Assisted Preparations of PbTe and PbSe. A Comparative Study". *Chem. Mater*., 13, 1413.

Kim, B., Tripp, S. L. & Wei, A. (2001). "Self-Organization of Large Gold Nanoparticle Arrays". *J. Am. Chem. Soc*., 123: 7955-7956.

Kim, K. D. & Kim, H. T. (2003). "Comparison of the effect of reaction parameters on particle size in the formation of SiO_2, TiO_2, and ZrO_2 nanoparticles". *Mater. Let*. 57, 3211-3216.

Kleitz, F., Marlow, F., Stucky, G. D. & Schuth, F. (2001). "Mesoporous Silica Fibres: Synthesis, Internal Structure, and Growth Kinetics". *Chem. Mater*., 13, 3587-3595.

Konstantatos, G., Howard, I., Fisher, A., Hoogland, S., Clifford, J., Klem, E., Levina, L. & Sargent, E. H. (2006). "Ultrasensitive Solution-Cast Quantum Dot Photodetectors". *Nature*, 442: 180-183.

Kuchibhatla, S. V. N. T., Karakoti, A. S., Bera, D. & Seal, S. (2007). "One dimensional nanostructured materials". *Prog. Mater. Sci*. 52: 699-913.

Kumar, U., Sharma, S. N., Singh, S., Ka, M., Singh, V. N., Mehta, B. R. & Kakar, R. (2009). "Size- and shape-controlled synthesis and properties of colloidal PbSe nanocrystals". *Mater. Chem. Phys*., 113(1): 107114.

Kutuzov, S., He, J., Tangirala, R., Emrick, T., Russell, T. P., Boker, A. (2007). "On the kinetics of nanoparticle self-assembly at liquid/liquid interfaces". *Phys. Chem. Chem. Phys*, 9: 6351-6358.

Lamer, V. K. & Dineger, R. H. (1950). "Theory, Production, and. Mechanism of Formation of Monodispersed Hydrolysis". *J. Am. Chem. Soc*., 72: 4847-4854.

Lan, G. Y., Lin, Y. W., Huang, Y. F. & Chang, H. T. (2007). "Photo-assisted synthesis of highly fluorescent ZnSe quantum dots in aqueous solution". *J. Mater. Chem*., 17: 2661-2666.

Langmuir, I. (1917). "The constitution and fundamental properties of solids and liquids. II Liquids. *J. Am. Chem. Soc*., 39: 1848-1906.

Langmuir, I. (1920). "The mechanism of the surface phenomena of flotation". *Irving. Trans. Faraday Soc*., 15: 62-74.

Lazell, M. & O'Brien, P. (1999). "Synthesis of CdS nanocrystals using cadmium dichloride and trioctylphosphinesulphide". *J. Mater. Chem.,* 9: 1381-1382.

Lee, J. S., Lim, H., Ha, K., Cheong, H. & Yoon, K. B. (2006). "Facile Monolayer Assembly of Fluorophore-Incorporating Zeolite Rods in Uniform Orientations for Anisotropic Photoluminescence". *Angew. Chem., Int. Ed*., 45: 5288-5292.

Lee, S. M., Jun, Y., Cho S. N. & Cheon, J. (2002). "Single-crystalline star-shaped nanocrystals and their evolution: programming the geometry of nano-building blocks". *J. Am. Chem. Soc.,* 124: 11244-11245.

Li, G. R., Yao, C. Z., Lu, X. H., Zheng, F. L., Feng, Z. P., Yu, X. L., Su, C. Y., Tong, Y. X. (2008). Facile and Efficient Electrochemical Synthesis of PbTe Dendritic Structures. *Chem. Mater*., 20: 3306-3314.

Li, J. J., Wang, Y. A., Guo, W., Keay, J. C., Mishima, T. D., Johnson, M. B. & Peng, X. (2003). "Large-scale synthesis of nearly monodisperse CdSe/CdS core/shell nanocrystals using air-stable reagents via successive ion layer adsorption and reaction". *J. Am. Chem. Soc*., 125: 12567-12575.

Li, Y. J., Huang, W. J. & Sun, S. G. (2006). "A universal approach for the self-assembly of hydrophilic nanoparticles into ordered monolayer films at a toluene/water interface". *Angew. Chem. Int. Ed*., 45(16): 2537-2539.

Lin, Y., Böker, A., Skaff, H., Cookson, D., Dinsmore, A. D., Emrick, T. & Russell, T. P. (2005). *Langmuir*, 21: 191-194.

Lin, Y., Skaff, H., Boeker, A., Dinsmore, A. D., Emrick, T., Russell, T. P. (2003). "Ultrathin Cross-Linked Nanoparticle Membranes". *J. Amer. Chem. Soc. Commun.,* 125: 12690-12691.

Lin, Y., Skaff, H., Emrick, T. S., Dinsmore, A. D. & Russell, T. P. (2003). "Nanoparticle Assembly and Transport at Liquid-Liquid Interfaces". *Science,* 299: 226-229.

Liu, W. (1999) *Fundamentals of III-V Devices: HBTs, MESFETs, and HFETs/HEMTs*.

Lu, W., Fang, J., Ding, Y., Wang, Z. L. (2005). "Formation of PbSe Nanocrystals: A Growth toward Nanocubes". J. *Phys. Chem. B*, 109: 19219-19222.

Malik, M. A., O'Brien, P. & Revaprasadu, N. (2001). "Synthesis of TOPO-capped Mn-doped ZnS and CdS quantum dots". *J. Mater. Chem.*, 11: 2382-2386.

Mao, Z. W., Xu, L. H. & Wang, D. Y. (2010). Molecular Mimetic Self-Assembly of Colloidal Particles. Advanced Functional Materials. *Adv. Funct. Mater*. 20: 1053-1074.

Matsui, J., Iko, M., Inokuma, N., Orikasa, H., Kyotani, T. & Miyashita, T. (2006). "Simple Fabrication of Carbon Nanotube Monolayer Film". *Chem. Lett*., 35: 42-43.

Matsui, J., Yamamoto, K. & Miyashita, T. (2009). "Assembly of untreated single-walled carbon nanotubes at a liquid-liquid interface". *Carbon*, 47, 1444-1450.

Matsui, J., Yamamoto, K., Inokuma, N., Orikasa, H., Kyotani, T. & Miyashita, T. (2008). "Multi-Walled Carbon Nanotube Ultrathin Film Using a Liquid-Liquid Interface: Effect of Alcohol Type to the Film Property". *Mol. Cryst. Liq. Cryst.*, 491: 9-13.

Miyashita, T., Yamamoto, K., Inokuma, N., Orikasa, H., Kyotani, T. & Matsui, J. (2007). "Fabrication of densely packed multi-walled carbon nanotube ultrathin films using a liquid-liquid interface". *J. Mater. Chem.*, 17: 3806-3811.

Mlondo, S. N., Thomas, P. J. & O'Brien, P. (2008). "Deposition of hierarchical Cd $(OH)_2$ anisotropic nanostructures at the water–toluene interface and their use as sacrificial templates for CdO or CdS nanostructures". *Chem. Commun*., 28(24): 2768-2770.

Mlondo, S. N., Thomas, P. J. & O'Brien, P. (2009). "Facile deposition of nanodimensional ceria particles and their assembly into conformal films at liquid–liquid interface with a phase transfer catalyst". *J. Am. Chem. Soc*., 131: 6072-6073.

Mohamed, M. B., Tonti, D., Al-Salman, A., Chemseddine, A. & Chergui, M. (2005). "Synthesis of high quality zinc blende CdSe nanocrystals". *J. Phys. Chem. B,* 109: 10533-10537.

Möhwald, H. (1988). "Controlling the Microstructure of Monomolecular Layers". *Adv. Mater*. 100: 750-756.

Moloto, M. J., Revaprasadu, N., Kolawole, G. A., O'Brien, P. & Malik, M. A. (2005). "The synthesis and characterization of Cu_xS_y and PbS nanoparticles from alkylthiourea lead and copper complexes". *S. Afr. J. Sci*. 101: 463-465.

Murray, C. B., Norris, D. J. & Bawendi, M. G. (1993). "Synthesis and characterization of nearly monodisperse CdE (E = sulphur, selenium, tellurium) semiconductor nanocrystallites". *J. Am. Chem. Soc.*, 115: 8706-8715.

Murray, C. B., Sun, S., Gaschler, W., Doyle, H., Betley, T. A., Kagan, C. R., (2001). "Colloidal synthesis of nanocrystals and nanocrystal superlattices". *IBMJ. Res. Dev*., 45: 47-56.

Nair, S., Radhakrishnan, T., Revaprasadu, N., Kolawole, G. & O'Brien, P. (2002). "A single-source route to CdS nanorods". *Chem. Commun*., 6: 564-565.

Pan, D. C., Ji, X. L., an, L. J. & Lu, Y. F. (2008) "Observation of nucleation and growth of CdS nanocrystals in a two-phase system". *Chem. Mater*., 20: 3560-3566.

Pan, D. C., Wang, Q., Jiang, S. C., Ji, X. L. & an, L. J. (2005) "Synthesis of extremely small CdSe and highly luminescent CdSe/CdS core-shell nanocrystals via a novel two-phase thermal approach". *Adv. Mater*., 17: 176-179.

Pan, D., Jiang, S., An, L. & Jiang, B. (2004). "Controllable synthesis of highly luminescent and monodisperse CdS nanocrystals by a two-phase approach under mild conditions". *Adv. Mater.*, 16: 982-985.

Park, J., An, K., Hwang, Y., Park, J.-G., Noh, H.-J., Kim, J.-Y., Park, J.-H., Hwang, N.-M. & Hyeon, T. (2004). "Ultra-large-scale syntheses of mono-dispersed nanocrystals". *Nat. Mater*. 3: 891-895.

Park, Y.-K. & Park, S. (2008). "Directing Close-Packing of Mid-nanosized Gold Nanoparticles at a Water/Hexane Interface". *Chem. Mater*., 20: 2388-2393.

Park, Y.-K., Yoo, S. H. & Park, S. (2007). "Assembly of highly ordered nanoparticle monolayers at a water/hexane interface". *Langmuir*, 23: 10505-10510.

Park, Y.-K., Yoo, S.-H. & Park, S. (2008). "Three-dimensional Pt-coated Au nanoparticle arrays: applications for electro catalysis and surface-enhanced Raman scattering". *Langmuir*, 24: 4370-4375.

Peng, Z. & Peng, X. (2001). "Formation of high-quality CdTe, CdSe, and CdS nanocrystals using CdO as precursor". *J. Am. Chem. Soc*. 123: 183-184.

Pickering, S. (1907). "Separation of Solids in the Surface-layers of Solutions and Suspensions". *J. Chem. Soc*., 91: 2001-2021.

Pieranski, P. (1980). "Two-dimensional interfacial colloidal crystals". *Phys. Rev. Lett*., 45: 569-572.

Pradhan, N., Katz, B. & Efrima, S. (2003). "Synthesis of high-quality metal sulphide nanoparticles from alkyl xanthate single precursors in alkyl amine solvents". *J. Phys. Chem. B,* 107: 843-854.

Rao, C. N. R. & Kalyanikutty, K. P. (2008). "The Liquid-Liquid Interface as a Medium to Generate Nanocrystalline Films of Inorganic Materials". *Acc. Chem. Res*., 41: 489-499.

Rao, C. N. R., Kulkarni, G. U., Agrawal, V. V., Gautam, U. K., Ghosh, M. & Tumkurkar, U. (2005). "Use of the liquid–liquid interface for generating ultrathin nanocrystalline films of metals, chalcogenides, and oxides". *J. Colloid Interface Sci*. 289: 305-318.

Rao, C. N. R., Thomas, P. J., Kulkarni, G. U. (2007) Nanocrystals: Synthesis, Properties, and Applications. New York: Springer-Verlag.

Rhodes, R., O'Brien, P., Saunders, B. R. (2011). "Triggered aggregation of PbS nanocrystal dispersions; towards directing the morphology of hybrid polymer films using a removable bidentate ligand". *J. Colloid Interface Sci*. 358: 51.

Rogach, A. L., Kornowski, A., Gao, M., Eychmueller, A. & Weller, H. (1999). "Synthesis and Characterization of a Size Series of Extremely Small Thiol-Stabilized CdSe Nanocrystals". *J. Phys. Chem. B,* 103: 3065-3069.

Russell, T. P., Lin, Y., Skaff, H., Emrick, T. Russell, T. P. & Dinsmore, A. D. (2003). "Nanoparticle Assembly and Transport at Liquid-Liquid Interfaces". *Science,* 299: 226-229.

Schön, G., Simon, U. (1995). A fascinating new field in colloid science: Small ligand-stabilized metal clusters and their possible application in microelectronics. *Colloid Polym. Sci.* 273, 10, 202-218.

Shim, M. & Guyot-Sionnest, P. (2000). "N-Type Colloidal Semiconductor Nanocrystals," *Nature*, 407: 981-983.

Singh, J., (2006). Optical Properties of Condensed Matter and Applications, John Wiley and Sons, Ltd.

Soloviev, V. N., Eichhofer, A., Fenske, D. & Banin, U. (2001). "Size-dependent optical spectroscopy of a homologous series of CdSe cluster molecules". *J. Am. Chem. Soc*., 123: 2354-2364.

Song, J. M.; Zhu, J. H. & Yu, S. H. (2006). "Crystallization and Shape Evolution of Single-Crystalline Selenium Nanorods at Liquid-Liquid Interface: From Monodisperse Amorphous Se Nanospheres toward Se Nanorods". *J. Phys. Chem. B*, 110: 23790-23795.

Stansfield, G. L., Vanitha, P. V., Johnston, H. M., Fan, D., AlQahtani, H., Hague, L., M. Grell, M. & Thomas, P. J. (2010). "Growth of nanocrystals and thin films at the water–oil interface". *Phil. Trans. R. Soc. A*, 368: 4313-4330.

Stansfield, G. L., Vanitha, P. V., Johnston, H. M., Fan, D., Alqahtani, H., Hague, I., Grell, Tang, Z., Zhuang, J. & Wang, X. (2010). "Exfoliation of graphene from graphite and their self- assembly at the oil-water interface". *Langmuir*, 26: 9045.

Tong, H., Zhu, Y. J., Yang, L. X., Li, L. & Zhang, L. (2006). "Lead Chalcogenide Nanotubes Synthesized by Biomolecule-Assisted Self-Assembly of Nanocrystals at Room Temperature". *Angew. Chem.*, 118: 7903-7906.

Trindade, T., Monteiro, O. C., O'Brien, P. & Motevalli, M. (1999). "Synthesis of PbSe nanocrystallites using a single-source method. The X-ray crystal structure of lead (II) diethyldiselenocarbamate". *Polyhedron*, 18: 1171-1175.

Trindade, T., O'Brien, P., Zhang, X. M., Motevalli, M. (1997). "Synthesis of PbS nanocrystallites using a novel single molecule precursors approach: x-ray single-crystal structure of Pb (S_2CNE_t-^{i}Pr)$_2$". *J. Mater. Chem.*, 7: 1011-1016.

Van de Hulst, H. C. (1957, 1981). Light Scattering by Small Particles. Dover Publications, Inc., New York. Unbridged and corrected republication of the work originally published in 1957.

Vanmaekelbergh, D., Reincke, F., Hickley, S. G., Kegel, W. K. (2004). "Spontaneous Assembly of a Monolayer of charged Gold Nanocrystals at the water/oil Interface". *Angew. Chem., Int. Ed.*, 43: 458-462.

Volkov, A. G., Deamer, D. W., Tanelian, D. L. & Markin, V. S. (Eds) (1998). Liquid Interfaces in Chemistry & Biology. New York, NY: Wiley-Interscience.

Wang, C. Y., Mo, X., Zhou, Y., Zhu, Y. R., Liu, H. T. & Chen, Z. Y. (2000). "A Convenient Ultraviolet Irradiation Technique for In Situ Synthesis of CdS Nanocrystallites at Room Temperature". *J. Mater. Chem.*, 10: 607-608.

Wang, C., Shim, M. & Guyot-Sionnest, P. (2001). "Electrochromic Nanocrystal Quantum Dots". *Science*, 291: 2390-2392.

Wang, J., Wang, D. Y., Sobal, N. S., Giersig, M., Jiang, M., Möhwald, H. (2006). "Stepwise directing of nanocrystals to self-assemble at water/oil interfaces". *Angew. Chem. Int. Ed.*, 45: 7963-7966.

Wang, Q., Russell, T. P. & Niu, Z. (2010). "Synthesis of Nano/Microstructures at Fluid Interfaces". *Angew. Chem., Int. Ed.*, 49: 10052-10066.

Wang, W., Geng, Y., Qian, Y., Ji, M. & Liu, X. (1998). "A Novel Pathway to PbSe Nanowires at Room Temperature". *Advanced Materials*, 10: 1479-1481.

Wang, W., Geng, Y., Yan, P., Liu, F., Xie, Y. & Qian, Y. (1999). "A Novel Mild Route to Nanocrystalline Selenides at Room Temperature". *J. Am. Chem. Soc.*, 121: 4062-4063.

Wang, W., Germanenko, I. & El-Shall M. S. (2002). "Room-Temperature Synthesis and Characterization of Nanocrystalline Cd, ZnS, and $Cd_xZn_{1-x}S$". *Chem. Mater*.14: 3028-3033.

Waser, R. & Aono, M., (2007). "Nanoionics-based resistive switching memories". *Nat. Mater*. 6: 833-840.

Weller, H., (1993). Quantized semiconductor Particles: A novel state of matter for materials science. *Adv. Mater*. 5, 2, 88-95.

Weller, H., Eychmüller, A. (1996). Semiconductor Nanoclusters; Elsevier Science;Amsterdam,

Wise, F. W. (2000). Lead salt Quantum Dots: the limit of string Quantum Confinement. *Acc. Chem. Res.*, 33: 773-780.

Wu, Y., Wadia, C., Ma, W., Sadtler, B. & Alivisatos, A. P. (2008). "Synthesis and photovoltaic application of copper (I) sulphide nanocrystals". *Nano Letters*, 8: 2551-2555.

Xia H. B. & Wang, D. Y. (2008). "Fabrication of Macroscopic Freestanding Films of Metallic Nanoparticle Monolayers by Interfacial Self-Assembly". *Adv. Mater*., 20: 4253.

Xia, Y. N., Yang, P. D., Sun, Y. G., Wu, Y. Y., Mayers, B., Gates, B., Yin, Y., Kim, F. & Yan, H. (2003). "One-dimensional nanostructures: synthesis, characterization, and applications". *Adv. Mater*. 15: 353-389.

Yu, W. W. & Peng, X. (2002). "Formation of high-quality CdS and other II–VI semiconductor nanocrystals in noncoordinating solvents: tunable reactivity of monomers". *Angew. Chem. Int. Ed.,* 41: 2368-2371.

Zhai, T.Y., Fang, X.S., Li, L., Bando, Y., Golberg, D. (2010). "One-dimensional CdS nanostructures: synthesis, properties, and applications". *Nanoscale*, 2: 168-187.

Ziqubu, N., Ramasamy, K., Rajasekhar, P. V. S. R., Revaprasadu, N. & O'Brien, P. (2010). "Simple Route to Dots and Rods of PbTe Nanocrystals". *Chem. Mater.*, 22: 3817.

CHAPTER TWO

DEPOSITION OF COPPER CHALCOGENIDE NANOMATERIALS AT THE WATER-TOLUENE INTERFACE

This chapter describes the syntheses of Copper chalcogenide nanoparticles. The work was carried out at the School of Chemistry, and characterization of nanomaterials by XRD and SEM was performed in the School of Materials Science, The University of Manchester, UK.

Deposition of copper chalcogenide nanomaterials at the water/toluene interface

Abstract

Nanostructured thin films of CuE (E=S, Se, Te) have been prepared at the water-toluene interface by reacting toluene solutions of copper cupferronates with aqueous chalcogenide ions obtained by the borohydride reduction of sulphur, selenium and tellurium powder. The thin film deposits were characterized by powder X-ray crystallography, scanning electron microscopy and absorption spectroscopy. The influence of deposition conditions such as precursor concentrations, temperature as well as deposition times were studied. The average crystallite sizes of the as-prepared nanoparticles at different temperatures, concentrations and deposition times ranged from 3.4 to 4.3 nm for CuS, 5.1 to 5.7 nm for CuSe and 1.4 to 4.5 nm for CuTe. The dislocation densities ranged from 5.46 to 8.85 x 10^{17} lines/m for CuS and 2.32 to 3.86 x 10^{17} lines/m for CuSe, 5.0 to 47.91 x 10^{17} lines/m for CuTe. The shape of the as-prepared nanoparticles at different temperatures was studied by SEM and gave morphologies from cubes to rods. The band gaps obtained for CuS ranged from 3.6 to 3.9 eV and CuSe ranged from 3.53 to 3.96 eV.

2.1 Introduction

The potential for the use of the interface between two liquids to synthesize materials of importance is at present being realized (Rao *et al*., 2003, 2005). There have been some reports on deposition of nanocrystals and thin films at the interface of two essentially immiscible liquids (Rao *et al.,* 2003; 2005; Gautam *et al.,* 2004; 2003; Platt *et al.,* 2004). In this method, a metal precursor dissolved in a solvent such as toluene is held in contact with an aqueous layer containing a reducing or oxidizing agent. The reaction proceeds at the interface of the liquids and results in deposits suspended in the interfacial region. The products of such reactions are typically thin continuous films or aggregates of nanocrystals. The macroscopic structure of the

deposit at the interface is reflective of the structure of the interface. The interface has a dual role of controlling charge transport and directing the structure of the deposit. The former role has recently received much attention due to its ability to cast preformed nanocrystals into thin layers (Duan *et al*., 2004; Dryfe, 2006; Lin *et al*., 2003; Reincke *et al.*, 2004; Su *et al*., 2005). Different methods have been employed for the synthesis of II-VI semiconductor nanocrystals. These include solution-based methods, solvothermal and sonochemical procedures, precursor decomposition, and the use of confined media such as zeolites and micelles (O'Brien and Green, 1999; Catarina *et al*., 2002; Murray *et al*., 1999; Wang *et al*., 2002; Gedanken, 2004).

The method of interfacial deposition shares many of the advantages of conventional chemical bath deposition. It provides a simple, convenient and inexpensive route to thin films. Films can be deposited at low temperatures and on a variety of substrates. The thickness and other characteristics of the deposited layers may be controlled by variation of the deposition parameters such as deposition time, temperature or reagent concentrations. The process is potentially easily adaptable to large area processing with low fabrication cost. Further, unlike other methods that use templates, little or no effort is required to remove the template at the end of deposition.

Currently research on the controlled synthesis of semiconductor nanocrystals is not only geared towards high quality, but also attempts the use of facile "green" low cost environmentally friendly precursors and solvents in addition to low temperatures. This is because there are environmental concerns that limit the application of current nanocrystals containing heavy metals such as Cd, Hg, and Pb which are essentially toxic (Shen *et al.*, 2010). In addition those containing the rare metals (such as in) are threatened by potential shortages due to their limited abundances. The use of pyrophoric, toxic and expensive reagents is increasingly becoming inappropriate for industrial synthesis or application in the near future. In order to address this situation attention is now being directed towards, non-toxic and inexpensive nanocrystals such

as those of Copper chalcogenides. Recently various methods have been reported on the synthesis of chalcogenide nanomaterials due to their excellent chemical and physical properties (Qin *et al.,* 2005).

A considerable amount of interest has been focused on copper sulphides owing to their special properties arising from their varied nonstoichiometric composition, valence states, nanocrystal morphologies, complex structures among others. The stoichiometry of copper sulphides varies starting from CuS_2 at the copper-deficient side to Cu_2S at the copper-rich side (Zhang *et al.,* 2008). At least five stable phases of the copper sulphur system are known to exist in nature and these are *covellite* ($Cu_{1.00}S$), *anilite* ($Cu_{1.75}S$), *digenite* ($Cu_{1.80}S$), *djurleite* ($Cu_{1.97}S$), and *chalcocite* ($Cu_{2.00}S$) (Panthan and Lokhande, 2004, Evans, 1981). Other phases that exist include *yarowite* ($Cu_{1.12}S$) and *spionkopite* ($Cu_{1.14}S$) (Goble, 1985). The crystal structures of the Cu_xS such as hexagonal, orthorhombic, pseudo cubic and tetragonal is determined by the value of *x*. XRD diffractogram have shown that varying the deposition temperature for the films grown by spray CuS, one of the important semiconductor transition metal chalcogenides, transforms into a superconductor at 1.6 K (Yao *et al.,* 2007) and has potential application as p-type semiconductor, sensor, solar energy converter, cathode material, catalyst, optical filter, and nonlinear optical material (Li *et al.,* 2009, Mao *et al.,* 2009, Wan *et al.,* 2004). In the form of thin film, CuS has been used in photo thermal conversion, electrodes, solar cell devices, coatings for microwave shields, and solar control (Zhang *et al.,* 2005, Sigman *et al.,* 2003, Chen *et al.,* 2003).

Different morphologies of CuS have been fabricated using different methods in recent times (Saunders *et al.,* 2006, Du *et al.,* 2007). Many methodologies have been explored which include solventless and solution thermolysis, sacrificial templating, solution phase reactions, hydrothermal or solvothermal method, ultrasonic and microwave irradiation, template-assisted methods, micro emulsion, electro deposition, chemical vapour deposition, and so on

(Nagarathinam *et al.,* 2009, Yan *et al.,* 2008, Feng *et al.,* 2007). Nicolini *et al.* (2005) have directly synthesized CuS nanoparticles in the polymer matrix using carboxylic groups of the polymer as nucleation centres and H_2S as sulphide source. Ying *et al*. (2008) have fabricated hierarchical CuS nanoparticles employing $CuCl_2$ and thioacetamide (TAA) in ionic liquid, Yu and co-workers have synthesized complex CuS micro tubes using $CuCl_2$ and TAA in acetic acid (Yu *et al.,* 2006). In solution phase, syntheses of transition metal chalcogenides, TAA is a commonly used sulphide source (Yao *et al.,* 2007). Lone pair of electrons on nitrogen and sulphur of TAA coordinate to form a metal complex. In case of Cu (II) complex, TAA suffers decomposition to form CuS because of the strong affinity of sulphide ion with Cu (II) (Nagarathinam *et al.,* 2009). The TAA assisted CuS syntheses have inspired us to explore a facile method to prepare CuS nanoparticles in large-scale under mild modified hydrothermal (MHT) (Sinha *et al.,* 2009) condition at the liquid-liquid interface. The CuS nanoparticles at the liquid-liquid junction emerge as stacked plates and efficient photo catalyst.

Photocatalysis has many merits in terms of the removal of harmful organic compounds, wastewater treatment, and clean-up measures of polluted air (Vinu and Madras, 2009). Dyes constitute a major class of organic compounds, which find a multitude of applications in our daily life (Kar *et al.,* 2009). The preparation of submicrometer size covellite CuS crystals in liquid-liquid interface via a simple MHT method at a relatively lower temperature without using any stabilizing agent has been reported (Basu *et al.,* 2010). CuS being a nontoxic, inexpensive, and stable under ambient conditions, would be ideal to use it in clean technology. The morphology of the CuS plates is habitually stacked and the plates show an effective catalytic property under visible light for mineralization of varied dye molecules in water.

CuSe is also a p-type semiconductor material with potential application in solar cells, superionic conductors, thermoelectric devices and microwave shield coating (Lakshmikvmar, 1994, Mane *et al.,* 2006, Bhuse *et al.,* 2003, Grozdanov, 1994). It also has potential application in optical

filters, nanoswitches, thermoelectric and photoelectric transformers and superconductors (Bhuse *et al.,* 2003). Micro- and nanocrystallites with various morphologies such as particles (Zhang *et al.,* 2000), tubes (Xu *et al.,* 2008), cages (Cao *et al.,* 2006) and flake-like structures (Xie *et al.,* 2002) have been reported. Thin films of CuSe prepared chemical bath deposition (CBD) (Dhanam *et al.,* 2005, Pai *et al.,* 2005).and CuSe with p-type semiconducting behaviour have been also been reported by Zainal *et al* using a combination of chemical precipitation and dip coating technique (Zainal *et al.,* 2005). There have been few reports of the synthesis of one dimensional (1D) nanomaterials of copper selenides like $Cu_{2-X}Se$ nanowires (Hsu *et al.,* 2006). Arrays of copper selenide nanowires of mixed compositions with Se/Cu/ in various proportions for example $Cu_3Se_2/Cu_{2-X}Se$ or $Cu_{2-X}Se/Cu$ have been reported (Jagminas *et al.,* 2006). 1-D snake-like CuSe nanomaterial based on biomolecule-assisted synthesis by Munoz-Rojas *et al* (2008) and bovine serum albumen-assisted copper selenide nanosnakes by Cui *et al*. (2010) have also been reported.

Several methods of synthesis have been employed for the synthesis of CuSe including the thermolysis of copper and selenium powder mixtures between 400-700 ^oC under argon, mechanical alloying of selenium and copper in a high energy ball mill (Ohtani and Motoki, 1995), reaction of selenium with elemental copper in liquid ammonia (Henshaw *et al.,* 1996, 1997). Synthesis of nanocrystalline $Cu_{2-X}Se$ using a solvothermal method in which CuI and Se were heated at 90 ^oC in an autoclave with ethylenediammine as solvent has also been reported (Wang *et al.,* 1998).

Most of the synthetic techniques employed for the synthesis have been reported to be tedious and yield polycrystalline films. Polycrystalline films are associated with having defects and grain boundaries which create trap states which act as carrier scattering centres reducing the carrier mobility and transparency of the films. It is therefore desirable to develop techniques that

would easily yield these materials with relative ease and at the same time reduce the polycrystalline nature of the film.

Interfaces between immiscible liquids are known to be ideal for assembling of colloidal particles (Lin *et al.,* 2003). Brust *et al*., (1994) used immiscible water-organic solvent mixtures in the presence of phase-transferring reagents to prepare metal organosols. Preliminary experiments have revealed that it was indeed possible to prepare nanocrystals of metals and other materials at the liquid-liquid interface through the reaction of a metal precursor taken in the organic layer with an appropriate reagent in the aqueous layer (Rao *et al.,* 2003, 2003).

The potential for the use of the interface between two liquids to synthesize materials of importance is at present being realized (Rao *et al.,* 2003, 2005). There have been several recent reports on deposition of nanocrystals and thin films at the interface of two essentially immiscible liquids (Gautam *et al.,* 2004, Platt *et al.,* 2004, Duan *et al.,* 2004, Dryfe, 2006, Lin *et al.,* 2003, Reincke *et al.,* 2004, Su *et al.,* 2005). In this method, a metal precursor dissolved in a solvent such as toluene is held in contact with an aqueous layer containing a reducing or oxidizing agent. The reaction proceeds at the interface of the liquids and results in deposits suspended in the interfacial region. The products of such a reaction are typically thin continuous films or aggregates of nanocrystals. The macroscopic structure of the deposit at the interface is reflective of the structure of the interface. The interface has a dual role of controlling charge transport and directing the structure of the deposit. The former role has recently received much attention due to its ability to cast preformed nanocrystals into thin layers (Shen *et al.,* 2010).

Rao *et al* (2004) have reported the synthesis and significant features of the ultrathin films of CuS and CuO obtained at the liquid-liquid interface and demonstrated the utility and potential of the liquid-liquid interface in generating such novel materials. This was remarkable considering that the procedure is so simple, basically involving the dissolution of copper cupferronate in the

organic layer and Na_2S or NaOH in the aqueous layer to produce the metal sulphide or the oxide film at the interface. Extensive investigations carried out since indicated that the nanocrystalline CuS and CuO films obtained at the interface were essentially single crystalline in nature.

In this chapter, the synthesis of thin films/ nanomaterials of CuS, CuSe and CuTe by the use of copper cupferronate ($Cu(cup)_2$)/copper dithiocarbamate as copper source and the borohydride reduction sulphur, selenium and tellurium powders as sulphide, selenide and telluride sources respectively are being reported.

2.2 Deposition of copper chalcogenide thin film nanomaterials

Briefly 30 ml of degassed water containing 0.1 mmol of NaHE (E= S, Se, Te) was transferred into a 100 ml beaker and 30 ml of toluene containing the 0.1 mmol of the copper dialkyldithiocarbamate/cupferronate precursor was layered on top of the solution in the beaker. The reaction vessel was placed in an oven preheated to the desired temperature for 4 hours. The deposits formed at the interface were isolated by gently lifting the film from the interface onto glass substrates. The reaction was repeated by varying the reaction conditions such as temperature, time and the reacting species (details of the deposition are given in chapter 6 section 6.4). The reactions were carried out in a 100 ml beaker with the height of the liquid column at 4 cm. The nature and characteristics of the as-prepared thin film nanoparticles were studied by X-ray diffraction, scanning electron microscopy, and, UV-visible spectroscopy.

2.3 Results and Discussions

2.3.1 Copper sulphide

2.3.1.1 Structural characterization and morphology

Figure 2.1shows the XRD diffractogram of the as-prepared of CuS nanoparticles obtained at the liquid-liquid interface at room temperature, 50 °C after 4 to 6 hours, respectively. These are fairly continuous films and extend over wide areas. All the reflections are attributed to pure

hexagonal phase CuS covellite. The entire diffraction patterns match with the data reported in the literature (JCPDS card no. 06-0464). The diffraction peaks at 2θ of 29.45, 31.82, 48.10 and 59.18 correspond to the 102,103, 110 and 116 peaks of hexagonal CuS respectively. Hexagonal CuS crystallite has space group P63/mmc and primitive unit cell with cell constants a= 3.792 Å and c=16.34 Å which contains twelve atoms, six for Cu and S each. No impurities such as CuO and other nonstoichiometric copper sulphides were detected. The XRD peaks were quite broad indicating these samples were composed of nanocrystalline particles. Peak intensity increases with an increase in deposition time and indicates increase in the crystallinity of the material shown in Figure 2.1. The peak broadening at lower angle is more meaningful for the calculation of particle size; therefore size of the nanocrystals has been calculated using Debye-Scherrer formula (Guinier, 1963) using reflections from the XRD pattern.

The Debye-Scherrer formula for crystallite size determination is given by:

$$D = \frac{0.94\,\lambda}{\beta\,Cos\,\theta}$$

Where D is the crystallite size, λ is the wavelength of X-ray, β is the full width at half maximum (FWHM) after correcting for the instrument for peak broadening (β is expressed in radians), θ is

the Bragg's angle. The calculated crystallite sizes of the CuS nanoparticles range from 3.36 to 4.28 nm as calculated by the Debye-Scherrer formula (Table 2.1).

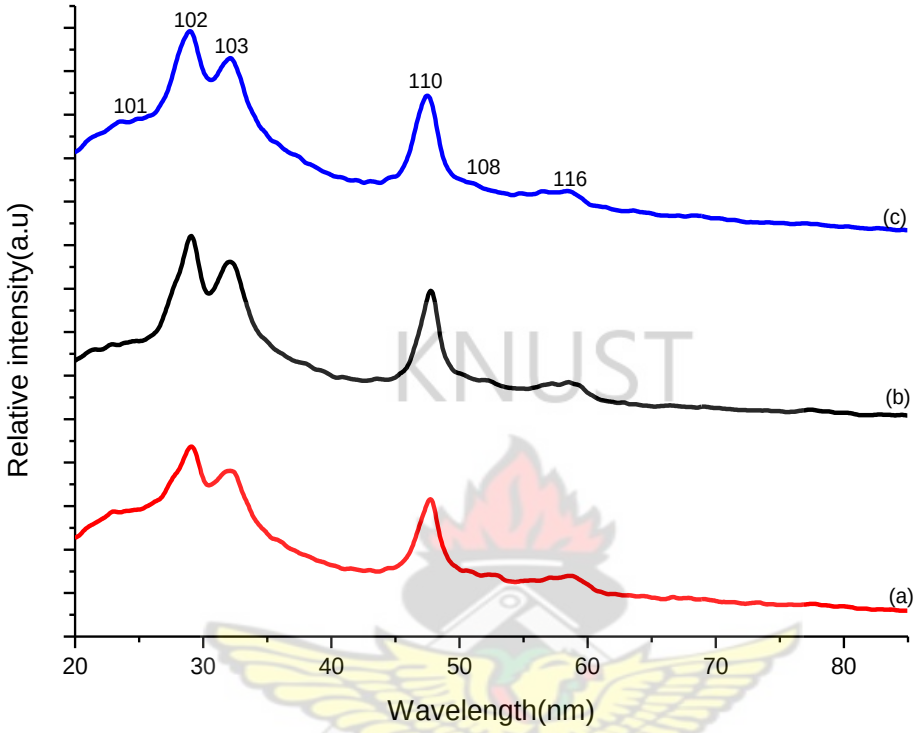

Figure 2.1: XRD of different as-prepared CuS samples (a) for 4 hours (b) for 5 hours and (c) 6 hours at 50 °C.

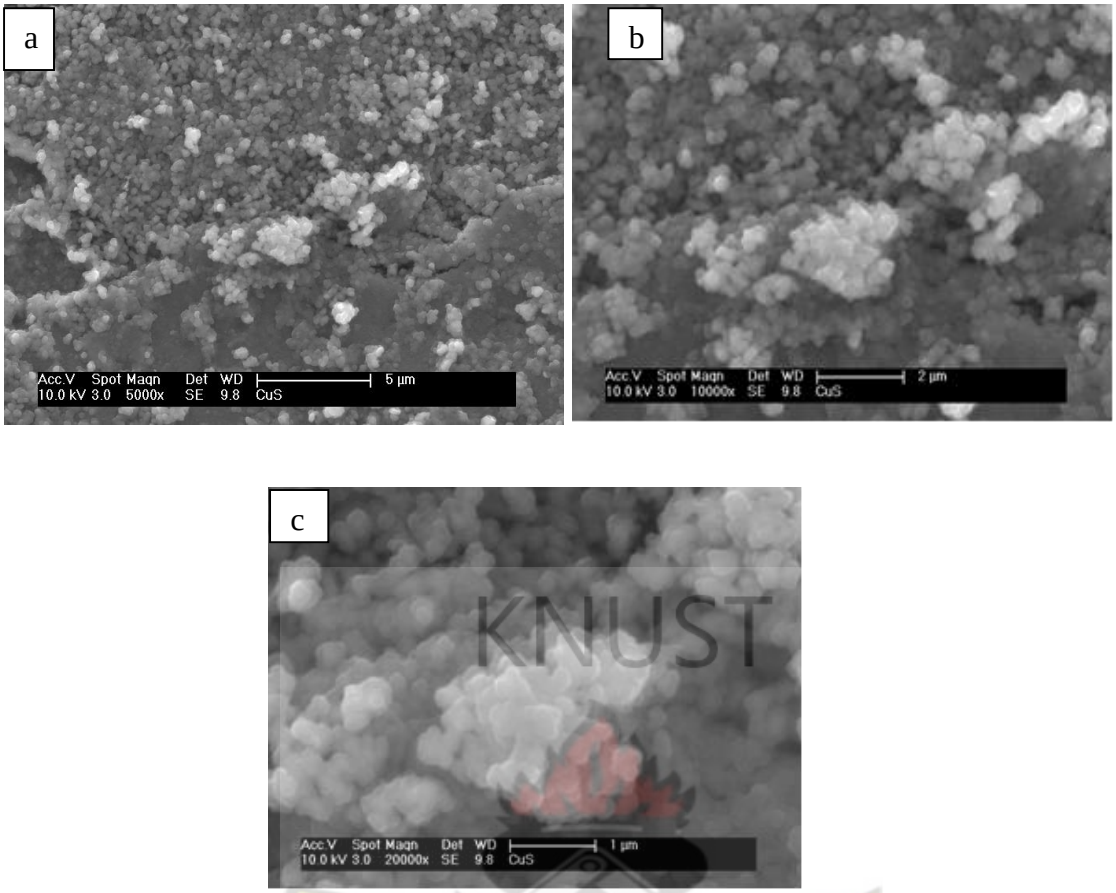

Figure 2.2: Scanning electron microscopy (SEM) image of CuS nanomaterial formed at 50 ^{o}C for 5 hours at different magnifications (a-5000x, b-10000x and c-20000x).

The Scanning electron microscopy (SEM) images of CuS nanomaterials/thin films formed at the water-toluene interface by reacting 30 ml of toluene solution of 0.10 mM copper cupferronate and 30 ml of 0.10 mM NaHS for 5 hours at 50 ^{o}C with different magnifications.

2.3.1.2 Optical analyses

The optical absorption spectra of the nanocrystals were measured using CARY 5000 UV-Vis-NIR spectrophotometer. The optical absorption spectra have been measured at room temperature over a range of 250 to 600 nm.

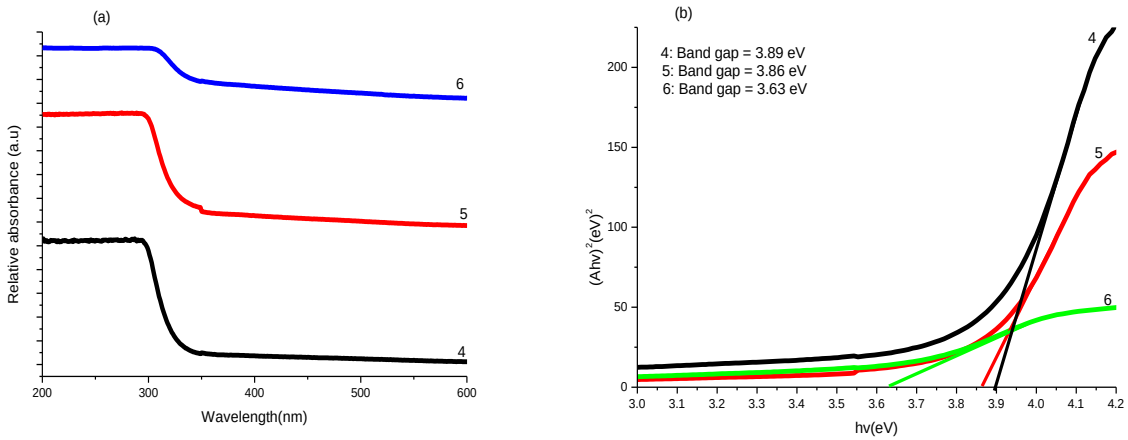

Figure 2.3: (a) Optical absorption spectra and (b) optical band gap of the as-prepared CuS samples for 4, 5 and 6 hours at 50 °C.

The fundamental absorption corresponds to the electron excitation from the valence band to the conduction band and can be used to determine the optical band gap. The relationship between the absorbance (A) and the incident photon energy (hυ) is given by the Stern relationship of near-edge absorption (Stern and Kim, 1981):

$$A = [k(h\upsilon - E_g)]^{1/n}/h\upsilon$$

Where υ is the frequency, h is the constant, k is a constant and carries a value of either 1 or 4. The value of n is 1 for direct transition and 4 for indirect transition respectively. The optical band gap is determined by a plot of $(Ah\upsilon)^{2/n}$ as a function of hυ extrapolation of the line to the hυ axis where $(Ah\upsilon)^{2/n}$ is zero gives the band gap E_g. The plots of $(Ah\upsilon)^2$ versus hυ is a straight line indicating that CuS is a direct band gap material. The plots of $(Ah\upsilon)^2$ versus hυ for the different nanocrystallites obtained at 50 ^oC are given in the Figure 2.3b.

Table 2.1 Optical parameters and crystalline sizes of CuS nanoparticles

Precursor	Deposition Temperature/^{o}C	Deposition time (hours)	Band gap of nanoparticle (eV)	Particle size (nm)	
				U.V	XRD
$Cu(Cup)_2$: S/$NaBH_4$	50	4	3.9	1.79	3.36
		5	3.85	1.82	4.28
		6	3.6	2.0	3.95

Band gap of bulk CuS = 1.75 eV

The optical band gap of the CuS nanocrystalline thin films was in the range between 3.6 and 3.9 eV, exhibiting considerable blue shift due to quantum size effects.

2.3.2 Copper selenide

2.3.2.1 Structural characterization and morphology

Figures 2.4 to 2.7 displays the powder X-ray patterns of the nanoparticles/thin films obtained by the reaction of 0.1 mmols of $Cu(cup)_2$ in 30 ml of toluene with 0.1 mmol of selenide ion generated by the reduction of selenium powder with $NaBH_4$ in an ice bath at room temperature, at 50 ^{o}C and at 70 ^{o}C respectively. Figure 2.8 also gives the XRD diffractogram of different as-prepared CuSe samples (a) for 8 hours and (b) for 10 hours at 50 ^{o}C when selenosulphate was used as the selenide source.

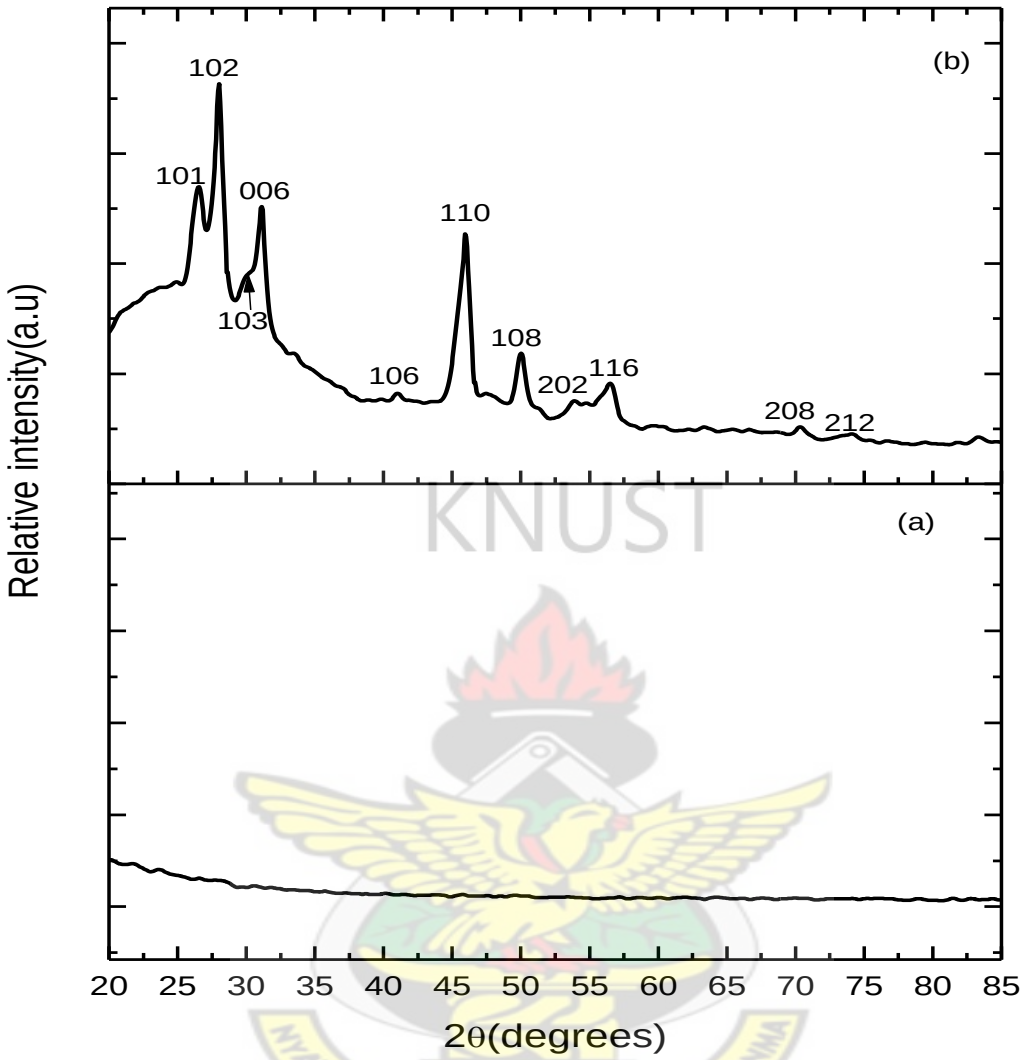

Figure 2.4: XRD of different as-prepared CuSe samples (a) for 5 hours and (b) 6 hours at room temperature using copper cupferronate.

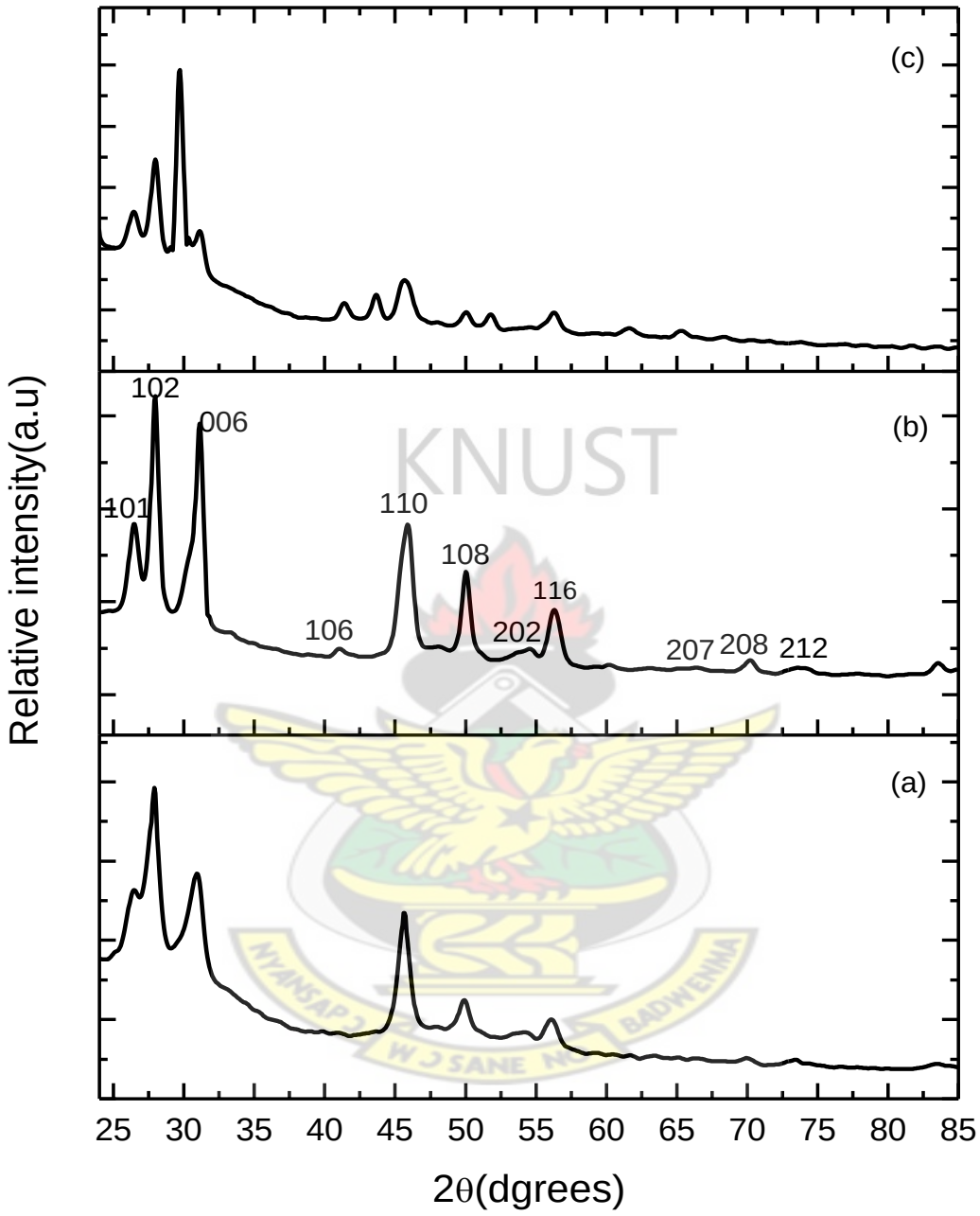

Figure 2.5: XRD of different as-prepared CuSe samples (a) for 4 hours (b) for 5 hours and (c) for 6 hours at 50 ^{o}C using copper cupferronate.

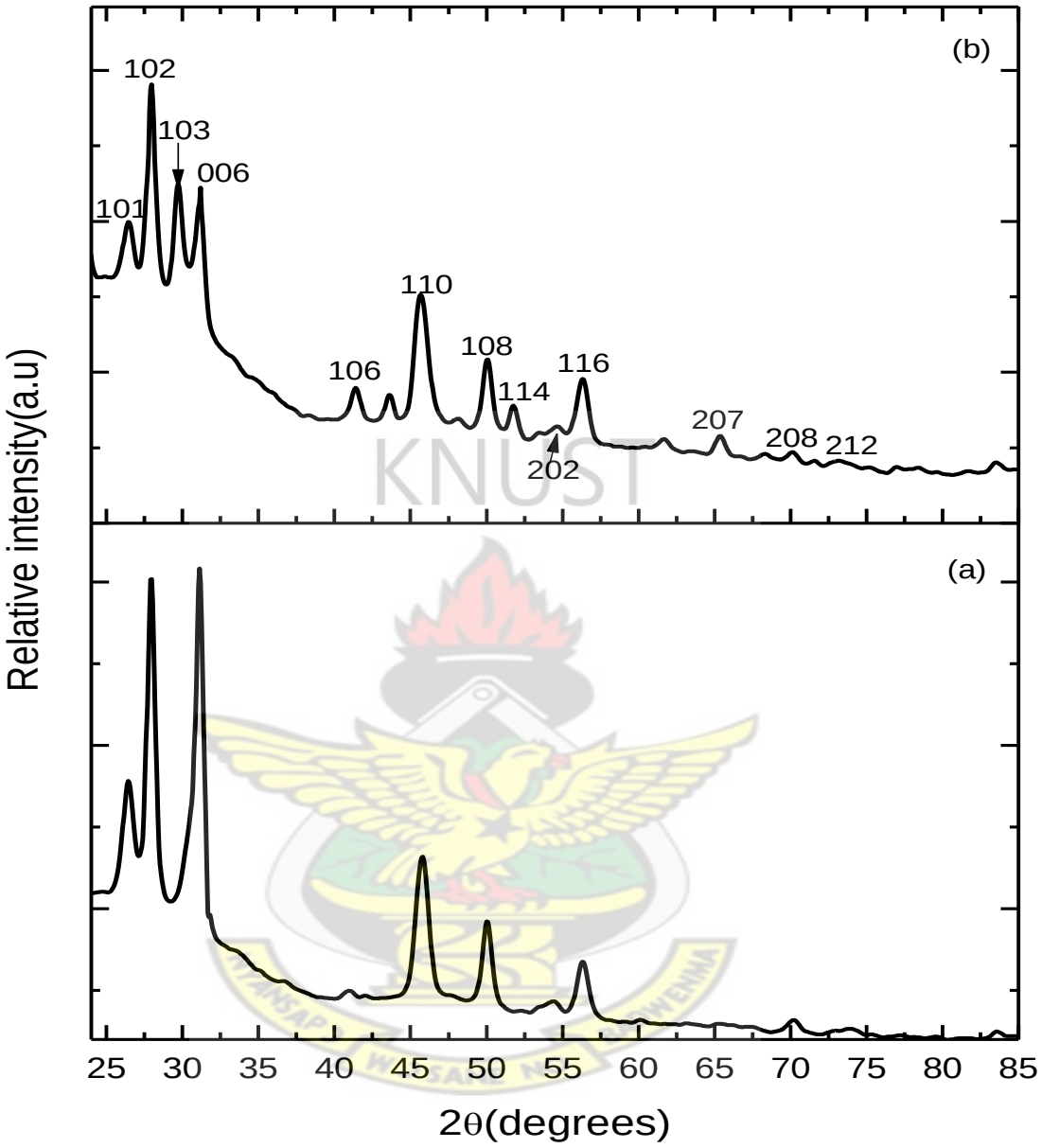

Figure 2.6: XRD of different as-prepared CuSe samples (a) for 5 hours and (b) for 6 hours at 70 ^{o}C using copper cupferronate.

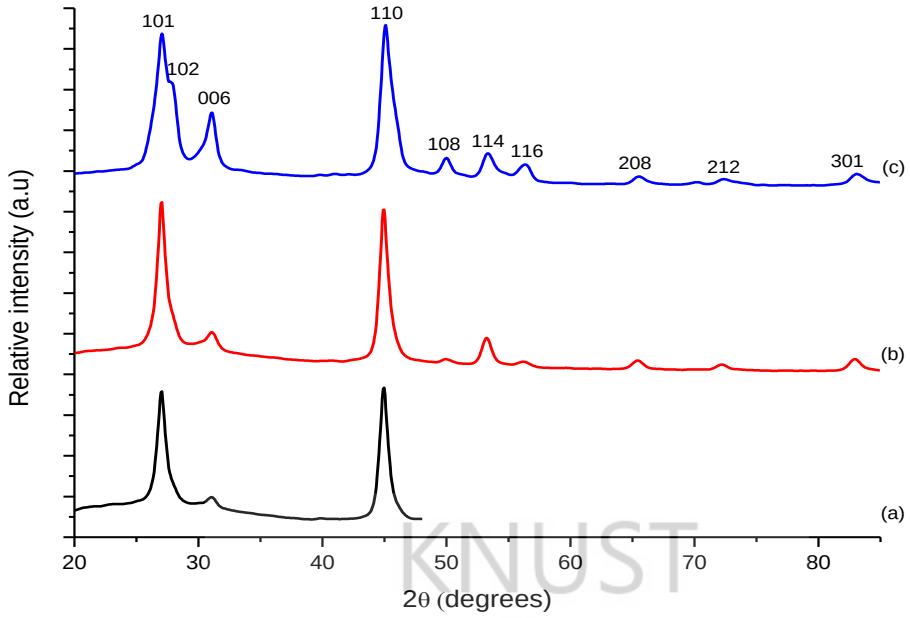

Figure 2.7: XRD of different as-prepared CuSe samples (a) for 4 hours, (b) for 5 hours at and (c) for 6 hours at 50 ^{o}C using copper cupferronate.

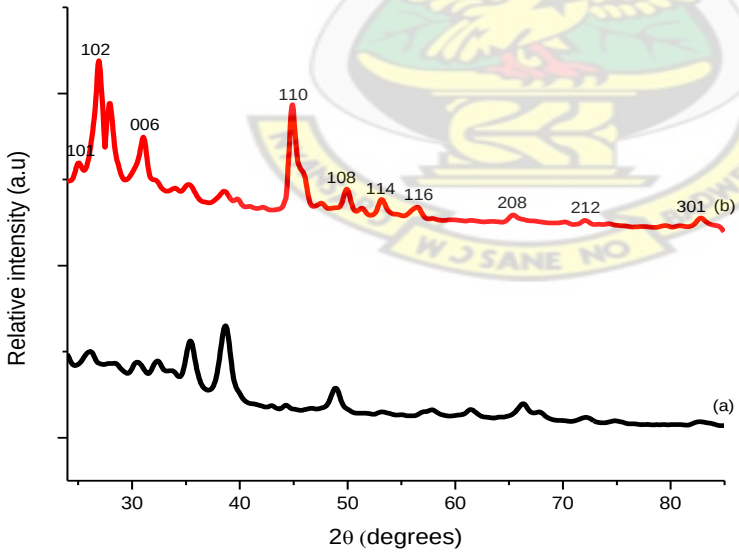

Figure 2.8: XRD of different as-prepared CuSe samples (a) for 8 hours and (b) for 10 hours at 50 ^{o}C using selenosulphate as the selenide source and copper cupferronate.

The diffraction peaks observed at 26.6^{o}, 33.1^{o}, 45.8^{o} and 50.6^{o} could be indexed to 101, 002, 201 and 003 of the hexagonal structure of CuSe (ICDD 00-020-1020) with orientation along the 101 plane. The broadening of the XRD peaks pattern clearly indicates the formation of CuSe nanocrystalline materials. Peak intensity was observed to increase with an increase in deposition time and temperature. This indicates increase in the crystallinity of the material shown in Figures 2.4 to 2.7. The XRD pattern for the as prepared CuSe at room temperature for 5 hours show no peak at all and clearly indicates that the thin film formed was amorphous. The particle sizes calculated by the Debye-Scherrer formula ranged from 1.3 nm to 6.6 nm as indicated in Table 2.2.

The Scanning electron microscopy (SEM) images of CuSe nanomaterials/thin films formed at the water-toluene interface by reacting toluene solution of copper cupferronate and aqueous solution of NaHSe obtained by the borohydride reduction of selenium powder for 5 hours at 50 ^{o}C and 70 ^{o}C are shown in Figure 2.9. Figure 2.9 (d) shows that for CuSe formed at 70 ^{o}C the predominant morphology of the particles were flakes. The energy dispersive X-ray analysis (EDAX) spectra as shown in Figure 2.10 indicate the elemental composition of the CuSe nanomaterial/thin film formed at 50 ^{o}C for 5 hours at water-toluene interface. Analysis by energy dispersion analytical X-ray (EDAX) in the electron microscope showed the presence of Cu and Se with atomic weight percentage ratio of 52.31: 47.69 within the limitations of the experimental conditions.

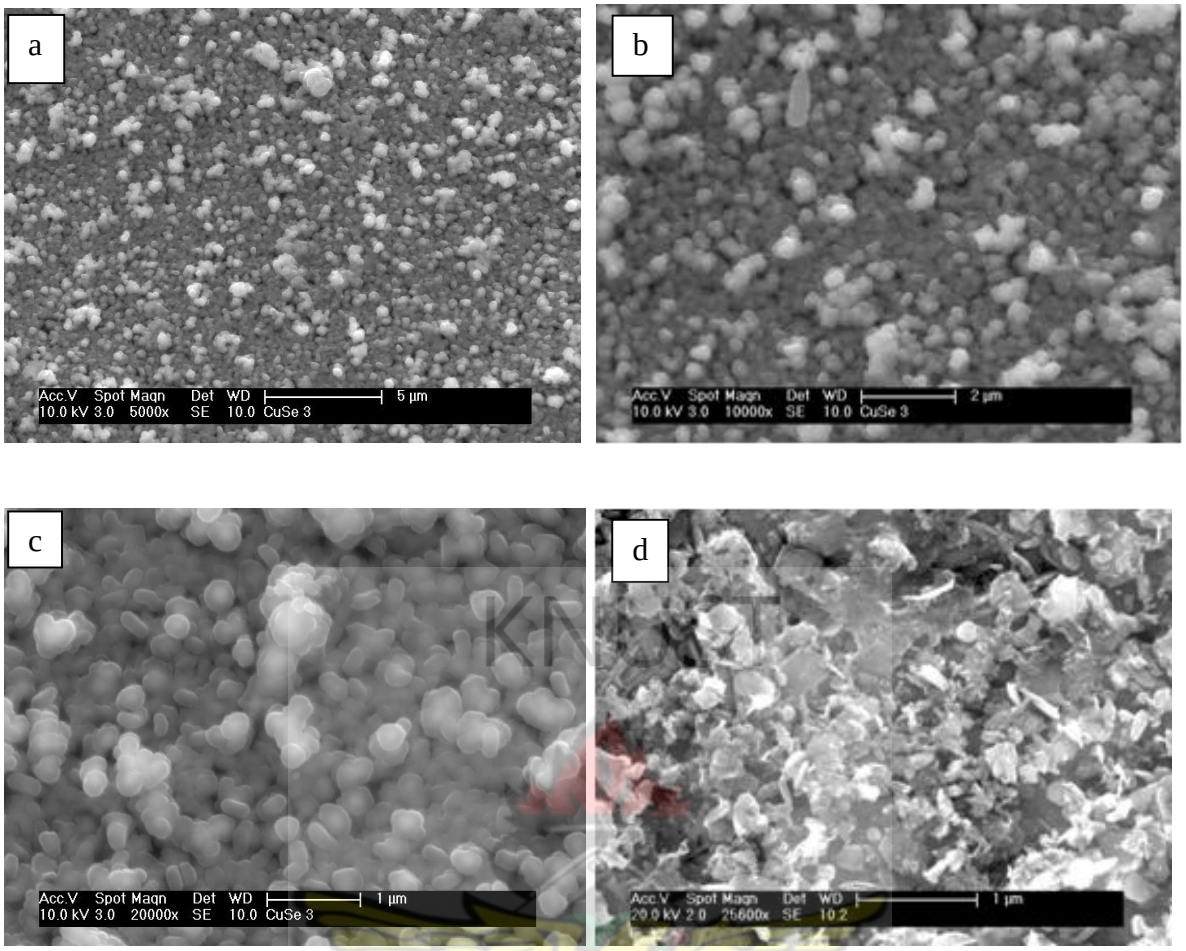

Figure 2.9: (a), (b), (c), Scanning electron microscopy (SEM) image of CuSe nanomaterial formed at 50 ^{o}C for 5 hours at different magnifications (a-5000x, b-10000x, c-20000x) and (d) SEM image of CuSe nanomaterial formed at 70 ^{o}C for 5 hours.

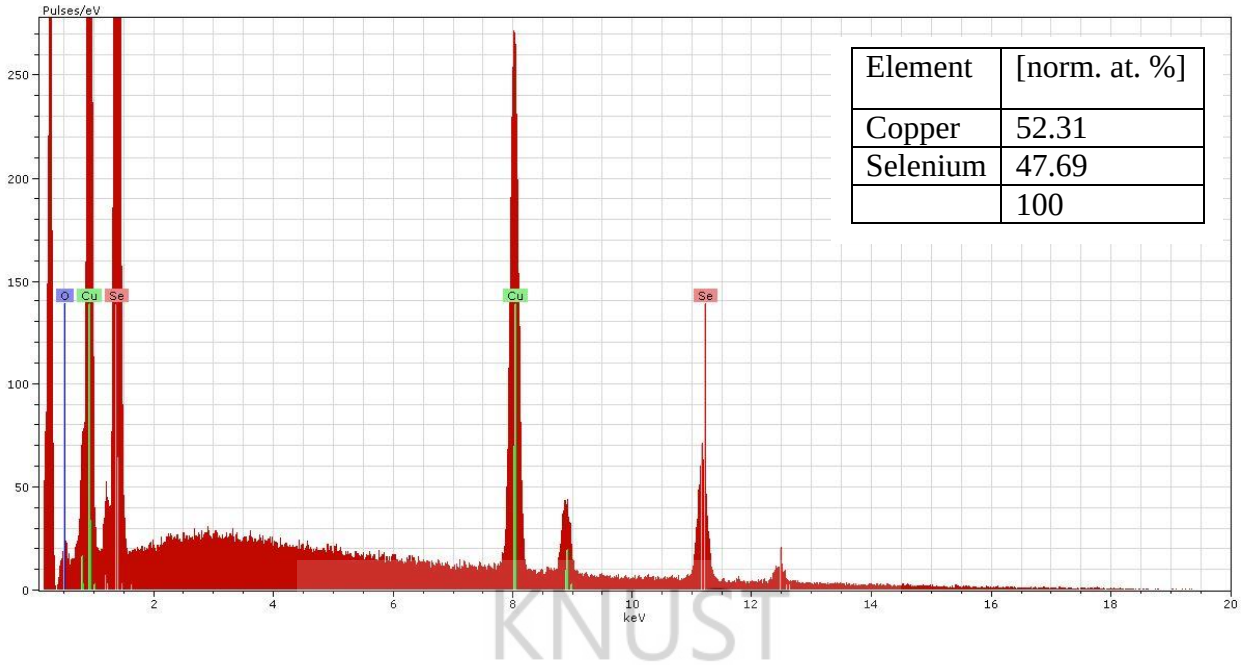

Element	[norm. at. %]
Copper	52.31
Selenium	47.69
	100

Figure 2.10: Quantitative EDAX analysis of CuSe nanomaterial formed at the water-toluene interface at 50 ºC for 5 hours

It is believed that the following steps are responsible for the formation of the copper selenide structures indicated. Initially the two liquids (water and toluene) mix to a limited extent at the interface, leading to the formation of spherical granules which are adsorbed at the interface to form a "pickering" emulsion. The formation of this emulsion lowers the interfacial tension promoting the diffusion of selenide ions. Further growth at the interface is autocatalytic. It is suggested that the interfacial copper selenide films grow in three stages as suggested for ceria (O'Brien *et al.,* 2009; Zhang *et al.,* 2005) and shown in Figure 2.11 for ceria.

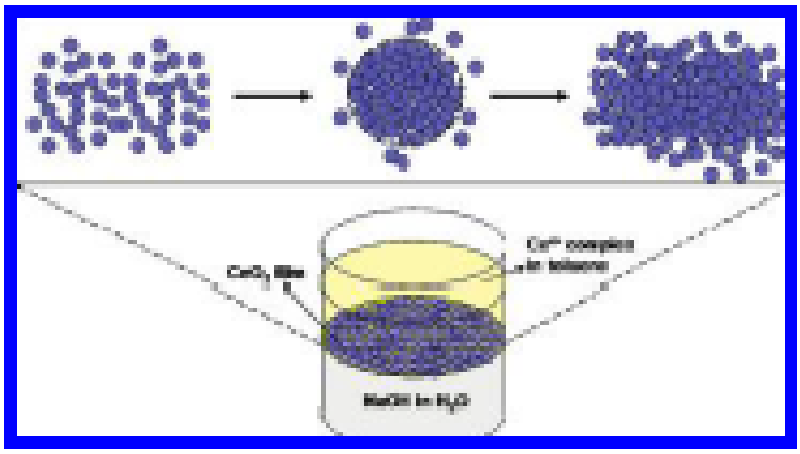

Figure 2.11. Schematic diagram illustrating the growth and agglomeration mechanism for CeO_2 nanoparticles (O'Brien *et al.*, 2009; Zhang *et al.*, 2005)

The first stage involves the growth of the primary nanoparticles, these then aggregate into larger mesoscopic discs or spheres. The voids between the spheres are filled by the smaller particles; which with the passage of time form the flakes as indicated in the SEM image (Figure 2.9). Presumably the formation of large spherical aggregates further lowers the interfacial tension, permitting diffusion of selenide ions that aids the generation of the flaky deposits in the Figure 2.9d. The large spherical aggregates are probably held together by weak van der Waals forces: whilst the platelet structures are more likely to be due to stronger chemical bonds between the particulates (Tsantilis *et al.*, 2004; Kammler *et al.*, 2005).

2.3.2.2 Optical analyses

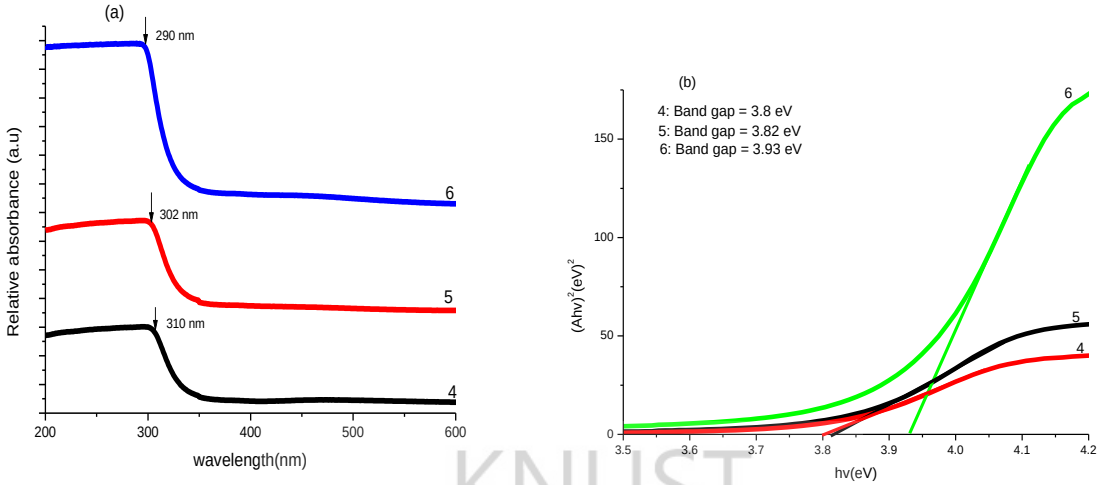

Figure 2.12: (a) Optical absorption spectra and (b) optical band gap of the as-prepared CuSe samples for 4, 5 and 6 hours at 50 ^{o}C

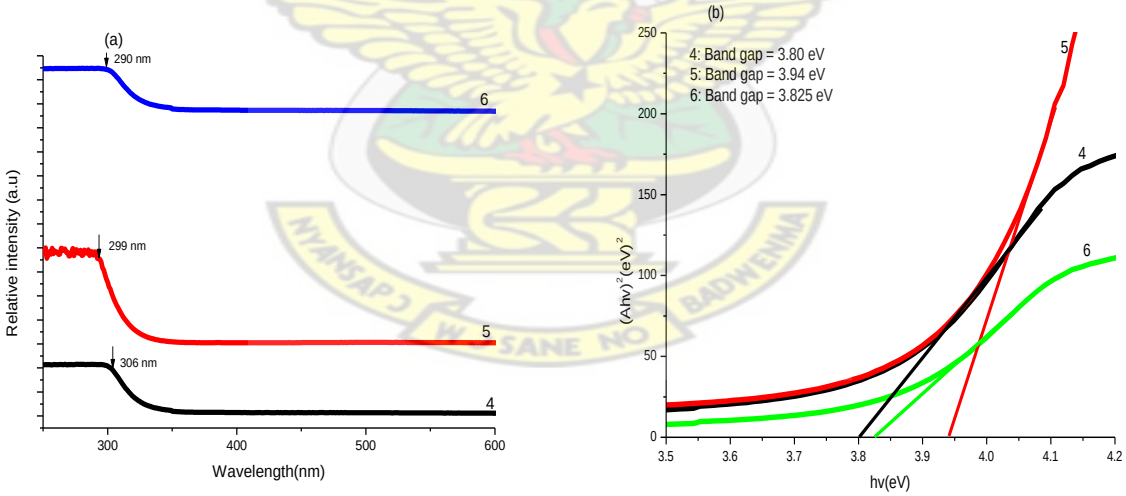

Figure 2.13: (a) Optical absorption spectra and (b) optical band gap of the as-prepared CuSe samples for 4, 5 and 6 hours at 70 ^{o}C

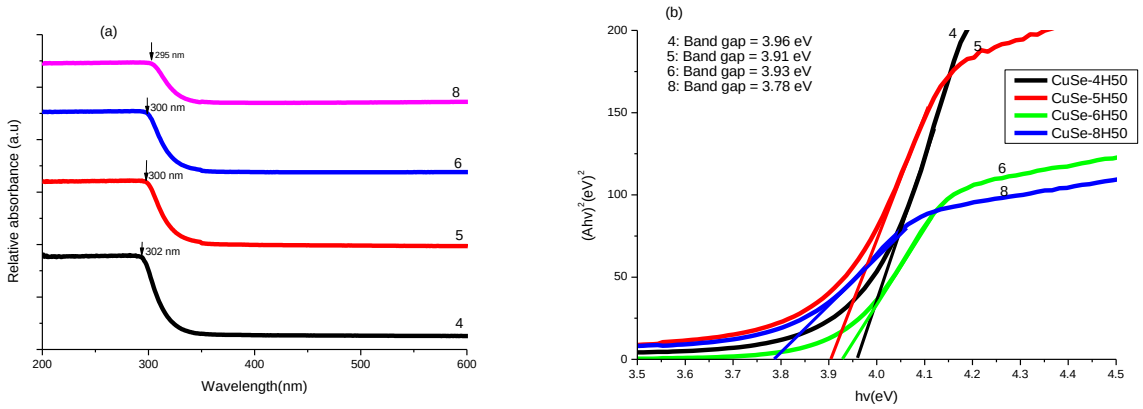

Figure 2.14: (a) Optical absorption spectra and (b) optical band gap of the as-prepared CuSe sample for 4, 5, 6 and 8 hours at 50 ^{o}C

Figures 2.12b–2.14b show the optical absorption spectra and the plots of $(Ah\upsilon)^2$ versus $h\upsilon$ for the different nanocrystallites of different as-prepared CuSe nanoparticles with deposition times ranging from 4 to 6 hours and deposition temperatures of 50 ^{o}C and 70 ^{o}C . The optical absorption spectra have been measured at room temperature over a range of 250 to 600 nm using the CARY 5000 UV-Vis-NIR spectrophotometer.

Table 2.2 Optical parameters and crystallite sizes of CuSe nanoparticles

Precursor	Deposition Temperature/^{o}C	Deposition time (hrs)	Band gap of nanoparticle (eV)	Particle size (nm)	
				U.V	XRD
$Cu(Cup)_2$: Se/$NaBH_4$	RT	6			5.091
$Cu(Cup)_2$: Se/$NaBH_4$		4	3.96	1.95/2.82	6.56
	50	5	3.91	1.98/2.89	5.37
		6	3.53	2.29/3.67	5.69
		8	3.78	2.08/3.11	
$Cu(Cup)_2$: Se/$NaBH_4$		4	3.80	2.05/3.07	5.51
	70	5	3.94	1.96/2.85	-
		6	3.82	2.05/3.04	5.31
$Cu(Cup)_2$: Selenosulphate	50	8	-	-	1.265
$Cu(Cup)_2$: Selenosulphate	50	10	-	-	1.274

Band gap of bulk CuSe = 2.0/2.8 eV

The CuSe nanocrystals show a considerable increase in band gap. The broad absorption edge with an excitonic peak at 320 nm observed for all the nanocrystalline thin films suggests a decrease in the particle size and a narrow size distribution. The absorption band edges fitted to a direct transition for the nanocrystalline thin films as shown in Figures 2.12b -2.14b. The average

particle size of CuSe ranged from 1.27 to 6.56 nm and the band gap ranged from 3.78–3.94 eV as indicated in Table 2.2. This change in size is reflected as a shift in the absorption spectra

2.3.3 Copper telluride

2.3.3.1 Structural characterization and morphology

Figure 2.15 displays the powder X-ray pattern of the nanoparticles/thin films obtained by the reaction of 0.1 mmols of $Cu(cup)_2$ in 30 ml of toluene with 0.1 mmol of telluride ion generated by the reduction of tellurium powder with $NaBH_4$ at 50 ^oC (a) and at 70 ^oC (b). The diffraction peaks observed at 22.9^o, 27.5^o, 40.5^o and 50.7^o could be indexed to 111, 112, 106 and 108 of the hexagonal structure of CuTe. The particle sizes ranged from 1.4 nm to 4.5 nm as indicated in Table 2.3.

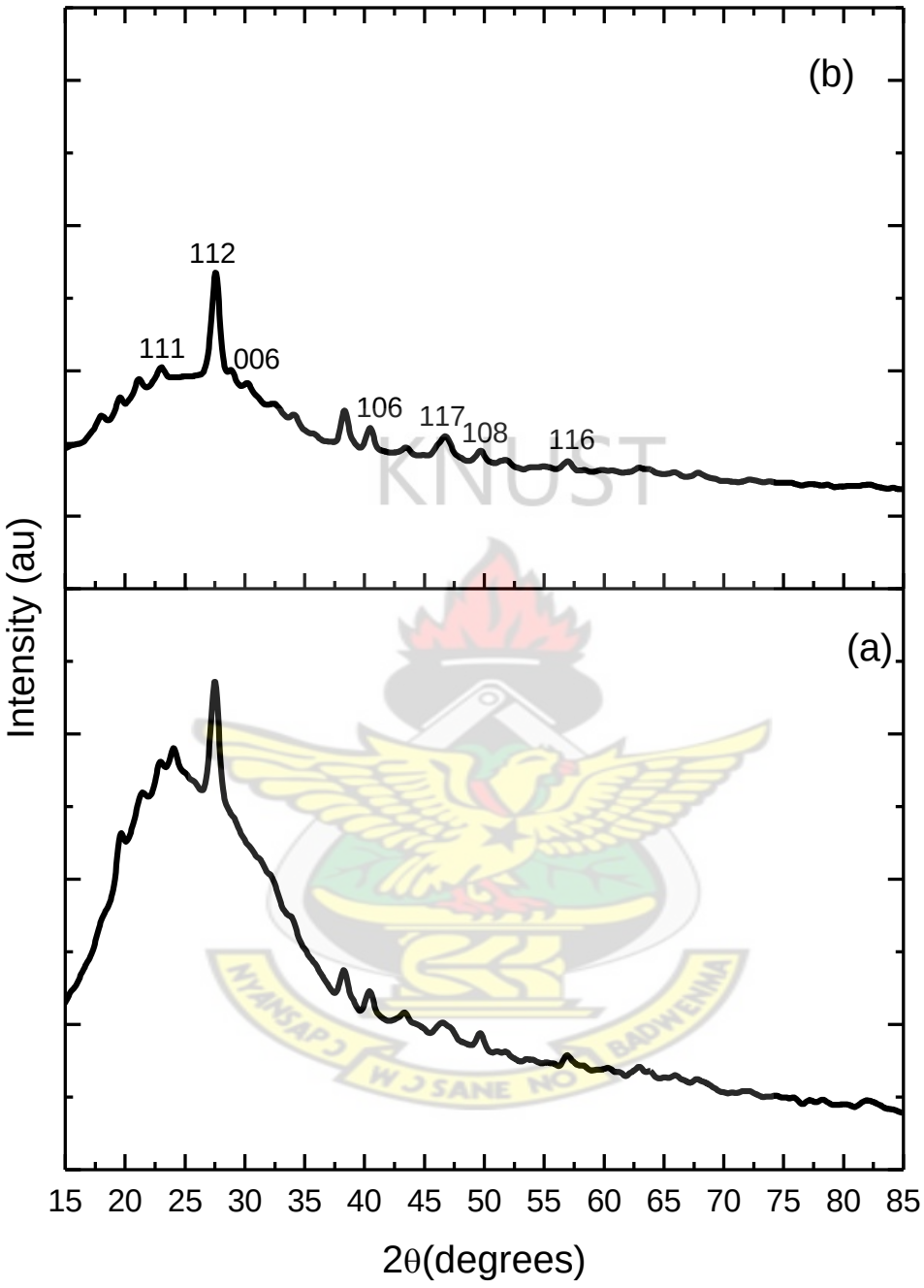

Figure 2.15: XRD of different as-prepared CuTe sample at (a) 50 ºC and (b) 70 ºC

Table 2.3 Crystallite sizes of CuTe nanoparticles

Precursors	Deposition Temperature/^{o}C	Deposition time (hrs)	Particle size (nm)
$Cu(Cup)_2$: $Te/NaBH_4$	50	6	1.4
$Cu(Cup)_2$: $Te/NaBH_4$	70	6	4.5

2.4 Conclusions

The present study shows how the liquid-liquid interface provides a unique way to produce single-crystalline ultrathin films/nanomaterials of inorganic materials. This has been demonstrated by the preparation of CuS, CuSe and CuTe at the water-toluene interface by a simple technique involving the reaction of copper cupferronate [$Cu(cup)_2$]/copper *bis*-(diethyldithiocarbamate) [$Cu(dtc)_2$] dissolved in toluene and sulphide, selenide or telluride ions in water generated by the $NaBH_4$ reduction of sulphur/selenium/tellurium powder. Unlike chemical methods such as the LB technique where non-single-crystalline films are obtained by assembling nanocrystals or CVD and related techniques where stringent conditions as well as substrates are required, the interface method described here is simple and can also be extended for use with a variety of materials. The average crystallite sizes of the as-prepared nanoparticles at different temperatures, concentrations and deposition times ranged from 3.4 to 4.3 nm for CuS, 5.1 to 5.7 nm for CuSe and 1.4 to 4.5 nm for CuTe. The dislocation densities ranged from 5.46 to 8.85 x 10^{17} lines/m for CuS, 2.32 to 3.86 x 10^{17} lines/m for CuSe and 5.0 to 47.91 x 10^{17} lines/m for CuTe. The band gaps obtained for CuS ranged from 3.6 to 3.9 eV and CuSe ranged from 3.53 to 3.96 eV. These show significant increases from the band gaps of the bulk materials.

2.5 References

Alivisatos, A. P., Rockenberger, J., Scher, E. C. (1999). "A new nonhydrolytic single precursor approach to surfactant-capped nanocrystals of transition metal oxides". *J. Amer. Chem. Soc*., 121: 11595-11596.

Bhuse, V. M., Hankare, P. P., Garadkar, K. M. & Khomane, A. S. (2003). "A simple, convenient, low temperature route to grow polycrystalline copper selenide thin films". *Mater. Chem. Phys*., 80: 82-88.

Brust, M., Walker, M., Bethell, D., Schiffrin, J. D. & Whyman, R. (1994). "Synthesis of Thiol Derivatised Gold Nanoparticles in a Two Phase Liquid/Liquid System". *Chem. Commun*. 7: 801-802.

Cao, H. L., Qiam, X. F., Zai, J. T., Yiu, J. & Zhu, Z. K. (2006). Conversion of Cu_2O nanocrystals into hollow Cu_2−xSe nanocages with the preservation of morphologies. *Chem. Commun*., 43: 4548-4550.

Catarina, A., Esteves, C. & Trinidale. T. (2002). "Synthetic studies on II/VI semiconductor quantum dots". *Curr. Opin. Solid State Mater. Sci*., 6: 347-353.

Chen, G. Y., Deng, B., Cai, G. B., Dong, W. F., Zhang, W. X. & Xu, A. W. (2008). "Synthesis, characterization, and formation mechanism of copper sulphide-core/carbon-sheath cables by a simple hydrothermal route". *Cryst. Growth Des.* 8: 2137-2143.

Cui, D., Huang, P., Kong, Y., Li, Z., Gao, F. (2010). Copper selenide nanosnakes: bovine serum albumin-assisted room temperature controllable synthesis and characterization. *Nanoscale Res. Lett*. 8: 949-956.

Dhanam, M, Manoj, P. K, Prabhu, R. R. (2005). "High-temperature conductivity in chemical bath deposited copper selenide thin films". *J. Cryst. Growth,* 280: 425-435.

Dryfe, R. A. W. (2006). "Modifying the liquid/liquid interface: pores, particles and deposition". *Phys. Chem. Chem. Phys*., 16: 1869-1883.

Du, W., Qian, X., Ma, X., Gong, Q., Cao, H. & Yin, J. (2007). "Controlled hydrothermal synthesis and growth mechanism of various nanostructured films of copper and silver tellurides". *Chem. Eur. J*., 13: 3241-3247.

Duan, H., Wang, D., Kurth, D. G. & Möhwald, H. (2004). "Directing Self-Assembly of Nanoparticles at Water/Oil Interfaces". *Angew. Chem., Int. Ed*., 43: 5639-5642.

Evans, H. T. (1981). "Copper coordination in low chalcocite and djurleite and other copper-rich sulphides". *American Mineralogist,* 66: 807-818.

Feng, X., Li, Y., Liu, H., Li, Y., Cui, S., Wang, N., Jiang, Li., Liu, X. Yuan, M. (2007). "Controlled growth and field emission properties of CuS nanowalls". *Nanotechnology*, 18(14): 145706.

Gautam, U. K., Ghosh, M. & Rao, C. N. R. (2004). "A template-free chemical route to ultrathin single crystalline films of CuS and CuO employing the liquid-liquid interface". *Langmuir*, 20: 10775-10778.

Gedanken, A. (2004). "Using sonochemistry for the fabrication of nanomaterials". *Ultrason Sonochem*, 11: 47-55.

Goble, R. J. (1985). "The relationship between crystal structure, bonding and cell dimensions in the copper sulphides". *Canadian Mineralogist,* 23: 61-76.

Grozdanov, I. (1994). "Electroconductive copper selenide films on transparent polyester sheets". *Synthetic Met*. 63, 213-216.

Guinnier, A. (1963). X-ray Diffraction in Crystals, Imperfect Crystals and Amorphous Bodies, 2: 46.

Hanshaw, G., Parkin, J. P., Shaw, G. (1996). Convenient, low-energy synthesis of metal sulphides and selenides; PbE, Ag_2E, ZnE, CdE (E = S, Se). *Chem. Commun.*, 10: 1095-1096.

Henshaw, G., Parkin, J. P., Shaw, G. (1997). Convenient, room-temperature liquid ammonia routes to metal chalcogenides. *J. Chem. Soc, Dalton Trans.*, 231-236.

Hsu, Y. J., Jiang, C. M., Lin, Y. F., Liaw, B. J., Lobana, T. S., Lu, S. Y. & Liu, C. W. (2006). "$[Cu_4\{Se_2P(O^iPr)_2\}_4]$: A Novel Precursor Enabling Preparation of Nonstoichiometric Copper Selenide ($Cu_{2-x}Se$) Nanowires". *Chem. Mater*. 18: 3323-3329.

Huang, P., Kong, Y., Li, Z., Gao, F. & Cui, D. (2010). "Copper selenide nanosnakes: bovine serum albumin-assisted room temperature controllable synthesis and characterization". *Nanoscale Res. Lett.*, 5(6): 949-956.

Jagminas, A., Juskenas, R., Gailiute, I., Statkuteb, G. & Tomasiunas, R. (2006). "Electrochemical synthesis and optical characterization of copper selenide nanowire arrays within the alumina pores". *J. Cryst. Growth*, 294: 343-348.

Kar, A., Smith, Y. R. & Subramanian, V. (2009). "Improved photo catalytic degradation of textile dye using titanium dioxide nanotubes formed over titanium wires". *Environ. Sci. Technol.*, 43: 3260-3265.

Lakshmikvmar, S. T. (1994). "Selenization of Cu and in thin films for the preparation of selenide photo absorber layers in solar cells using Se vapour source". *Mater. Solar Cells,* 32: 7-19.

Li, F., Bi, W., Kong, T. & Qin, Q. (2009). "Optical, photo catalytic properties of novel CuS Nanoplate-based architectures synthesized by a solvothermal route." *Cryst. Res. Technol*., 44, 729-735.

Lin, Y., Skaff, H., Emrick, T., Dinsmore, A. D. & Russell, T. P. (2003). "Nanoparticle assembly and transport at liquid-liquid interfaces". *Science,* 299: 226-229.

Basu, M., Sinha, A. K., Pradhan, M., Sarkar, S., Negishi, Y. & Govind, T. P. (2010). "Evolution of Hierarchical Hexagonal Stacked Plates of CuS from Liquid-Liquid Interface and its Photo catalytic Application for Oxidative Degradation of Different Dyes under Indoor Lighting". *Environ. Sci. Technol.,* 44:6313-6318

Mane, R. S., Kajve, S. P., Lokhande, C. D. & Han, S. (2006). "Studies on p-type copper (I) selenide crystalline thin films for hetero-junction solar cells". *Vacuum,* 80(6): 631-635.

Mao, J., Shu, Q., Wen, Y., Yuan, H., Xiao, D. & Choi, M. M. F. (2009). "Facile fabrication of porous CuS Nanotubes using well-aligned [Cu(tu)]Cl.1/2H_2O nanowire precursors as self-sacrificial templates". *Cryst. Growth Des*. 9: 2546-2548.

Muñoz-Rojas, D., Oró-Soté, J. & Gómez-Romero, P. (2008). "From nanosnakes to nanosheets: a matrix-mediated shape evolution". *J. Phys. Chem. C,* 112(5): 20312-20318.

Nagarathinam, M., Chen, J., Vittal, J. J. (2009). "From self-assembled Cu(II) coordination polymer to shape-controlled CuS nano- crystals". *Cryst. Growth Des*. 9(5): 2457-2463.

Murray, C. B., Norris, D. J. & Bawendi, M. G., (1999). "Synthesis and characterization of nearly monodisperse CdE (E = sulphur, selenium, tellurium) semiconductor nanocrystallites". *J. Am. Chem Soc.,* 115: 8706-8715.

Nicolini, C. A., Narizzano, R. & Erokhin, V., (2005). "Heterostructure composed of conjugated polymer and copper sulphide nano- particles." *J. Phys. Chem. B,* 109: 15798-15802.

O'Brien, P. and Green, M. (1999). 'The synthesis of cadmium phosphide nanoparticles using cadmium diorganophosphide precursors' J. Mater. Chem., 1999, 9, 243-247

Ohtani, T., Motoki, M. (1995). Synthesis of binary copper chalcogenides by mechanical alloying. *Material Research Bulletin,* 30, 1495-1504.

Pai, R. R., John, T. T, Lakshmi, M., Vijayakumar, K. P. & Kartha, C. S. (2005). "Observation of phase transitions in chemical bath deposited copper selenide thin films through conductivity studies". *Thin Solid Films,* 473: 208-212.

Pathan, H. M., Lokhande, C. D. (2004). "Deposition of metal chalcogende thin films by successive ionic layer absorption and reaction (SILAR) method". *Bull. Mater. Sci*., 27: 85-111.

Platt, M., Dryfe, R. A. W. & Roberts, E. P. L. (2004). "Structural and electrochemical characterisation of Pt and Pd nanoparticles electrodeposited at the liquid/liquid interface". *Electrochim. Acta,* 49: 3937-3945.

Qin, A. M., Fang, Y. P., Ou, H. D., Liu, H. Q. & Su, C. Y. (2005). "Formation of various morphologies of covellite copper sulphide submicron crystals by a hydrothermal method without surfactant". *Cryst. Growth Des*. 5: 855-860.

Rajamathi, M. & Seshadi, R. (2002). "Oxide and chalcogenide nanoparticles from hydrothermal/solvothermal reactions". *Curr. Opin. Solid State Mater. Sci*. 6(4), 337-345

Ramasamy, K., Nejo, A. O., Ziqubu, N., Rajasekhar, P. V. S. R., Nejo, A. A., Revaprasadu, N. & O'Brien, P. (2011). "A New Route to Lead Chalcogenide Nanocrystals". *Eur. J. Inorg. Chem.*, 33: 5196-5201.

Rao, C. N. R., Gautam, U. K. & Ghosh, M. (2004). "Template-Free Chemical Route to Ultrathin Single-Crystalline Films of CuS and CuO Employing the Liquid-Liquid Interface". *Langmuir*, 20, 25: 10775-10778.

Rao, C. N. R., Kulkarni, G. U., Agrawal, V. V., Ujjal, K., Goutam, M. G. & Tumkurkar, U. (2005). "Use of the liquid–liquid interface for generating ultrathin nanocrystalline films of metals, chalcogenides, and oxides". *Journal of Colloid and Interface Science* 289: 305-318.

Rao, C. N. R., Kulkarni, G. U., Thomas, P. J., Agrawal, V. V. & Saravanan, P. (2003). "Films of Metal Nanocrystals Formed at Aqueous-Organic Interfaces". *J. Phys. Chem. B,* 107: 7391-7395.

Rao, C. N. R., Kulkarni, G. U., Thomas, P. J., Agrawal, V. V., Ujjal, K., Goutam, M. G. & Ghosh, M. (2003). "Nanocrystals of metals, semiconductors and oxides: Novel synthesis and applications". *Current Science,* 85: 1041-1045.

Reincke, F., Hickey, S. G., Kegel, W. K. & Vanmaekelbergh, D. (2004). "Spontaneous Assembly of a Monolayer of Charged Gold Nanocrystals at the Water/Oil Interface". *Angew. Chem., Int. Ed.,* 43: 458-462.

Saunders, A. E., Ghezelbash, A., Smilgies, D. M., Sigman, M. B. & Korgel, B. A. (2006). "Columnar self-assembly of colloidal nanodisks". *Nano Lett.,* 6: 2959-2963.

Shen, H., Niu, J. Z., Wang, H., Li, X., Li, L. S. & Chen, X. (2010). "Size- and shape-controlled synthesis of ZnSe nanocrystals using SeO_2 as selenium precursor". *Dalton Trans*. 39: 11432-11438.

Sigman, M. B., Ghezelbash, A., Hanrath, T., Saunders, A. E., Lee, F. & Korgel, B. A. (2003). "Solventless synthesis of monodisperse CuS nanorods, nanodisks, and nanoplatelets". *J. Am. Chem. Soc.,* 125: 16050-16057.

Sinha, A. K., Jana, S., Pande, S., Sarkar, S., Pradhan, M., Basu, M., Saha, S., Pal, A. & Pal, T. (2009). "New Hydrothermal process for hierarchical TiO_2 nanostructures". *Cryst. Eng. Comm,* 11: 1210-1212.

Su, B., Fermin, D. J., Abid, J.-P., Eugster, N. & Girault, H. H. (2005). "Adsorption *and* Photo reactivity of CdSe Nanoparticles at. Liquid|Liquid Interfaces". *J. Electroanal. Chem*., 583: 241-247.

Vinu, R. & Madras, G. (2009). "Kinetics of sonophotocatalytic degradation of anionic dyes with nano-TiO_2". *Environ. Sci. Technol*., 43: 473-439.

Wan, S., Guo, F., Shi, L., Peng, Y., Liu, X., Zhang, Y. & Qian, Y. (2004). "Single-step synthesis of copper sulphide hollow spheres by a template interface reaction route". *J. Mater. Chem.,* 14: 2489-2491.

Wang, W., Germanenko, I. & El-Shell, M. S. (2002). "Room-temperature synthesis and characterization of nanocrystalline CdS, ZnS and $Cd_xZn_{1-x}S$". *Chem. Mater.,* 14: 3028-3033.

Wang, W., Yan, P., Liu, F., Geng, Y. & Qian, Y. (1998). "Preparation and nanocrystallites". *J. Mater. Chem.* 8: 2321-2322.

Xie, Y., Zheng, X. W., Jiang, X. C., Lu, J. & Zhu, L. Y. (2002). "Sonochemical synthesis and mechanistic study of copper selenides". *Inorg Chem*, 41: 387-392.

Xu, J., Zhang, W. X., Yang, Z. H. & Yang, S. H. (2008). "Lithography inside $Cu(OH)_2$ nanorods: A general route to controllable synthesis of the arrays of copper chalcogenide nanotubes with double walls". *Inorg. Chem.*, 47, 699-704.

Yan, H., Wang, W. & Xu, H. (2008). "A micro-interface route to CuS superstructure composed of intersectional nanoplates". *J. Cryst. Growth*, 310: 2640-2643.

Yao, Z., Zhu, X., Wu, C., Zhang, X. & Xie, Y. (2007). "Fabrication of micrometer-scaled hierarchical tubular structures of CuS assembled by nanoflake-built microspheres using an *in situ* formed Cu(I) Complex as a self-sacrificed template". *Cryst. Growth Des.* 7: 1256-1259.

Ying, T. K., Xu, C., Wang, L. & Zou, D. B. (2008). "Synthesis and optical properties of CuS nanowires fabricated by electrodeposition with anodic alumina membrane". *Mater. Lett*. 62: 3181-3184.

Yu, S. H., Wu, C., Chen, S., Liu, G. & Liu, B. (2006). "Large Scale Synthesis of uniform CuS nanotubes in ethylene glycol by a sacrificial templating method under mild conditions". *J. Mater. Chem.*, 16: 3326-3331.

Zainal, Z., Nagalingam, S. & Loo, T.C. (2005). "Copper selenide thin films prepared using combination of chemical precipitation and dip coating method". *Mater. Lett*. 59, 1391-1394.

Zhang, H. T., Wu, G., Chen, X. H., Zhang, H. T., Wu, G. & Chen, X. H. (2005). "Large-scale synthesis and self-assembly of monodisperse hexagon Cu_2S nanoplates". *Langmuir*, 21: 4281-4282.

Zhang, H., Zhang, Y., Yu, J. & Yang, D. (2008). "Phase-selective synthesis and self-assembly of monodisperse copper sulphide nanocrystals". *J. Phys. Chem. C*, 112: 13390-13394.

Zhang, W. X., Zhang, X. M., Zhang, L., Wu, J. X., Hui, Z. H., Cheng, Y. W., Liu, J. W., Xie, Y. & Qian, Y.T. (2000). "A Redox Reaction to Synthesize Nanocrystalline $Cu_{2-x}Se_x$ in Aqueous Solution". *Inorg. Chem.*, 39: 1838-1839.

Ziqubu, N. Rasamy, K., Rajasekhar, P. V. S. R., Revaprasadu, N. & O'Brien, P. (2010). *Chem Mater*. 22: 3817-3819.

CHAPTER THREE

DEPOSITION OF ZINC CHALCOGENIDE NANOMATERIALS AT THE WATER-TOLUENE INTERFACE

This chapter describes the syntheses of Zinc chalcogenide nanoparticles and nanorods. The work was carried out at the School of Chemistry, and characterization of nanomaterials/ nanowires by XRD, SEM and TEM was performed in the School of Materials Science, The University of Manchester, UK.

Deposition of zinc chalcogenide nanomaterials at the water-toluene interface

Abstract

Nanostructured thin films of ZnE (E=S, Se, Te) have been prepared at the water-toluene interface by reacting toluene solutions of alkyldithiocarbamates with aqueous chalcogenide ions obtained by the borohydride reduction of sulphur, selenium and tellurium powder. The thin film deposits were characterized by powder X-ray crystallography, scanning and transmission electron microscopy and absorption spectroscopy. The influence of deposition conditions such as precursor concentrations, temperature as well as deposition times were studied. The average crystallite sizes of the as-prepared nanoparticles at different temperatures, concentrations and deposition times ranged from 1.3 to 6.9 nm for ZnS, 2.0 to 7.1 nm for t-Se and 1.8 to 6.7 nm for t-Te. The dislocation densities ranged from 1.14 to 9.33 x 10^{17} lines/m for ZnS, 2.0 to 8.7 x 10^{17} lines/m for t-Se and 2.22 to 6.5 x 10^{17} lines/m for t-Te. The shape of the as-prepared nanoparticles at different temperatures was studied by SEM and gave morphologies from flowers to nanowires. The band gaps obtained for ZnS ranged from 3.6 to 3.88 eV, t-Se ranged from 2.86 to 3.91 eV and for t-Te from 3.6 to 3.9 eV.

3.1 Introduction

Zinc sulphide (ZnS) is one of the first semiconductors discovered (Davidson, 1948) and it has traditionally shown remarkable fundamental properties versatility and a promise for novel diverse applications, including light-emitting diodes (LEDs), electroluminescence, flat panel displays, infrared windows, sensors, lasers, and biodevices, etc. Its atomic structure and chemical properties are comparable to more popular and widely known ZnO. However, certain properties pertaining to ZnS are unique and advantageous compared to ZnO. ZnS has a larger band gap of 3.72 eV and 3.77 eV (for cubic zinc blende (ZB) and hexagonal wurtzite (WZ) ZnS, respectively) as compared to ZnO (3.4 eV) and therefore it is more suitable for visible-blind ultraviolet (UV)-

light based devices such as sensors/photodetectors. ZnS is also traditionally the most suitable candidate for electroluminescence devices.

The nanostructures of ZnS have not been investigated in much detail as compared to ZnO nanostructures. Using various facile techniques, nanoparticles, nanorods, nanowires, nano-belts/nanoribbons, nanosheets, nanotubes, core/shell nanostructures, hierarchical nanostructures, complex nanostuctrues and heterostructures of ZnS have been synthesized under specific growth conditions so far. The recent progress on the improvement of their properties and finding novel potential applications, such as the latest achievements in using various ZnS nanostructures as field emitters, field effect transistors (FETs), p-type conductors, catalyzators, UV-light and chemical sensors (including gas sensors), biosensors, and nanogenerators cannot be overemphasized.

Two crystallographic modifications are commonly found for ZnS (Wang *et al*., 2006; Wu *et al*., 2005; Wright and Gale, 2004; Gardner and Pang, 1988). Both contain close-packed sulphur layers with zinc atoms occupying one half of the tetrahedral interstices. The low temperature, cubic polymorph, ZnS, is known as sphalerite or zincblende, while the high temperature, hexagonal polymorph, ZnS, is known as wurtzite (Figure 3.1). The ΔH° of the sphalerite to wurtzite phase transition has recently been reported to be *ca.* -2.5 + 1.5 kJmo1^{-1} (Gardner and Pang, 1988).

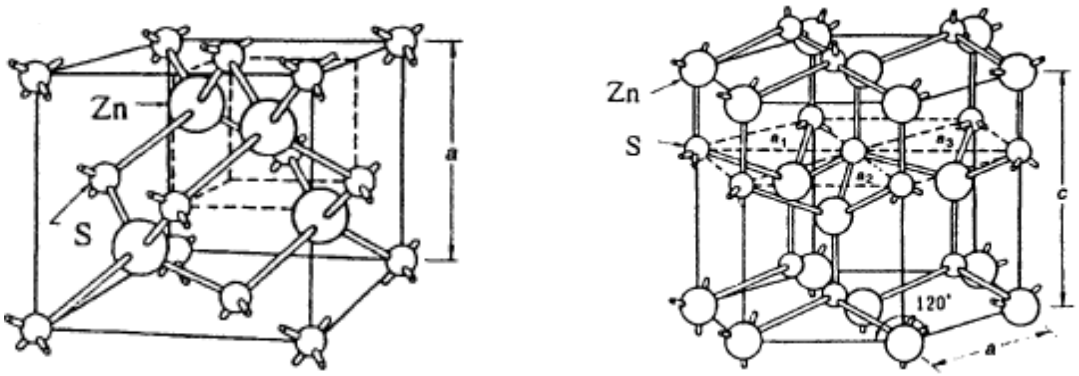

a b

Figure 3.1.The sphalerite or zinc blend crystal structure of ZnS (a) and the wurtzite structure of ZnS (b).

At elevated temperatures, bulk ZnS can undergo a phase transformation from the cubic structure to the hexagonal wurtzitic form (Moore and Wang, 2006; Fang and Zhang, 2006; Wang *et al*., 2006; Wu *et al*., 2005; Wright and Gale, 2004; Gardner and Pang, 1988). The hexagonal form has more desirable optical properties than the cubic form.

Another important characteristic of ZnS is its polar surface. The most common polar surface is the basal plane. The oppositely charged ions produce positively charged Zn(0001) and negatively charged S(0001) polar surfaces, resulting in a normal dipole moment and polarization along the c-axis as well as a divergence in surface energy (Moore and Wang, 2006; Fang and Zhang, 2006).

Zinc selenide (ZnSe) has a structure which is closely related to that of ZnS but is a narrower band gap semiconductor material with bulk band gap of 2.7 eV (Xinhua *et al*., 2005). It emits in the violet-blue window when the size is reduced to below the Bohr excitonic radius (Hines *and* Guyot-Sionnest, 1998). In recent developments, ZnSe has been targeted as an efficient semiconductor host to dope different transition metal ions extending its emission window from violet blue to the red end of the visible spectrum (Norris *et al*., 2008; 2001; Pradhan *et al*., 2005; Chin *et al.*, 2009; Erwin *et al*., 2005).

Zinc selenide (ZnSe) is a light yellow binary compound (II-VI) semiconductor and like most of its counterparts is generally produced as an n-type semiconductor (Yenkatachalam *et al*., 2006). The properties such as large band gap, low resistivity and high photosensitivity make this semiconducting material highly attractive. As a photoelectronic semiconductor material, ZnSe, has been extensively studied as single crystals and also as epitaxial and polycrystalline thin films prepared by different techniques to unearth other properties with the hope of exploring potentialities for fabrication of new scientific and technological devices.

Among the II-VI compound semiconductors, ZnSe has drawn considerable interest due to its direct and large band gap which makes it appropriate for use in optoelectronics as detectors as well as emitters. It is useful for optical components in high power laser window and multispectral applications where it provides good imaging characteristics (Deutsch, 1973; Chu *et al*., 1996). It is also used as an infrared optical material because of its wide transmission wavelength range (200 nm - 2000 nm) (Masetti *et al*., 1993), and commonly used as a transmission window in IR spectroscopy, right vision application and Attenuated total reflection (ATR) prism. ZnSe is also useful in high resolution thermal imaging systems where it is used to correct for colour distortion inherent in other lenses used in the systems. ZnSe exists in two crystallite forms: wurtzite (Hexagonal) and zinc blende (cubic) of which the cubic phase is believed to be stable. The ZnSe has the electron affinity of 4.09 eV and electron mobility of 530 $Cm^2V^{-1}S^{-1}$ at room temperature (Tamarso, 2002). Some groups have reported the syntheses of high quality ZnSe and related Cu-, Mn-doped ZnSe nanocrystals with an emitting window of from 400-610 nm (Pradhan *et al*., 2007; 2005; Pradhan and Peng, 2007; Hines and Guyot-Sionnest, 1998; Santangelo *et al.*, 2007; Zu *et al*., 2006; Norberg *et al.*, 2006; Panda *et al*., 2007; Cozzoli, 2005; Pradhan *et al.*, 2004; Dai *et al*., 2008; Shen *et al*., 2009; 2010). These features indicate that ZnSe nanocrystals with or without dopant have the potential of replacing nanocrystals of heavy metal ions (such as Cd, Hg and Pb), and those containing rare metals (such as Indium). However the synthetic procedures

so far employed have involved temperatures above 300 ^{o}C and other drastic conditions such as high pressure and long residence times.

In recent years, research on zinc telluride (ZnTe) has gained momentum due to its potential applications in different optoelectronic devices and solar cell technology. While most II–VI semiconductors such as ZnO, ZnS, and CdS exhibit n-type characteristics (Johnson *et al*., 2003, Ding *et al*., 2004), zinc telluride (ZnTe) is a p-type II-VI semiconductor with applications in various optoelectronic devices, such as green light-emitting diodes, solar cells, etc. (Wu *et al*., 1996, Bose and Bhunia, 1998). ZnTe has a direct band gap of ~2.26 eV at 300 K. P-type characteristics of ZnTe offer great potential in fabricating p-type FETs (Zhang *et al.*, 2008) or in forming p–n junctions with other n-type II–VI semiconductors (Schrier *et al*., 2007). ZnTe films are well suited for use in thin-film optoelectronic devices due to their high-absorption-coefficient and p-type conductivity (Nisho *et al*., 2001). Polycrystalline ZnTe films and its alloys such as CdTe, CdSe, and CdS are successfully utilized in the fabrication of tandem solar cells and quantum well structures (Kim *et al*., 1999).

ZnTe films are usually prepared by techniques such as thermal evaporation (Aquili *et al*., 2000), hot-wall evaporation (Mondal *et al.*, 1987), radio frequency (rf) sputtering (Bellakhder *et al.*, 2001), liquid-phase epitaxy (Fujita *et al.*, 1975), molecular beam epitaxy (Lee *et al.*, 1990), and electrodeposition (Bozzini *et al*., 2000). Among these techniques, electrodeposition seems to be the most promising, especially for large-scale use. It has been shown that smooth, uniform, and good quality ZnTe films could be obtained from inexpensive raw materials by low-cost techniques such as electrodeposition (Bozzini *et al.*, 2000). ZnTe nanorods, nanowires, and nanoribbons have been synthesized by the pulsed electrochemical deposition technique (Li *et al*., 2005), solvothermal synthesis (Yong *et al.*, 2007; Li *et al*., 1999), molecular beam epitaxy (Janik *et al*., 2006), and thermal evaporation or the sublimation method (Huo *et al*., 2006).

However, there are few reports on heterostructures of ZnTe nanowires and their properties (Dong *et al*., 2007).

In this chapter, the synthesis of ZnS, ZnSe and ZnTe nanomaterial/thin films at water-toluene interface at temperatures below 100 ^{o}C by the use of zinc diethyldithiocarbamate (ZDTC) as zinc source and the borohydride reduction of Sulphur/Selenium/Tellurium as sulphide/selenide/telluride sources are reported.

3.2 Deposition of zinc chalcogenide thin film nanomaterials

Briefly 30 ml of degassed water containing 0.1 mmol of NaHE (E = S, Se, Te) was transferred into a 100 ml beaker. 30 ml of toluene containing the 0.1mmol of the zinc dialkyldithiocarbamate precursor was layered on top of the solution in the beaker. The reaction vessel was placed in an oven preheated to the desired temperature for 4 hours. The deposits formed at the interface were isolated by gently lifting the film from the interface onto glass substrates. The reaction was repeated by varying the reaction conditions such as temperature, time and the reacting species (details of the deposition are given in chapter 7 section 7.4). The reactions were carried out in a 100 ml beaker with the height of the liquid column at 4 cm. The nature and characteristics of the thin films obtained were studied by X-ray diffraction, transmission electron microscopy, scanning electron microscopy, and, UV-visible spectroscopy

3.3 Results and discussions

3.3.1 Zinc sulphide

3.3.1.1 Structural characterization and morphology

The reaction of 0.1 mM of zinc diethyldithiocarbamate in 30 ml of toluene with 0.1 mM NaHS generated by the borohydride reduction of sulphur powder in 30 ml of water at 50 ^{o}C for 4, 5 and

6 hours yielded cubic (zinc blende) ZnS nanomaterial at the water-toluene interface as shown by the X-ray diffraction measurements. Figures 3.2 and 3.3 show the XRD pattern of ZnS film with reflections corresponding to those of the cubic ZnS (ICDD 01-080-0020, cell constant a = 1.54056 Å) (Yeh *et al*., 1992).

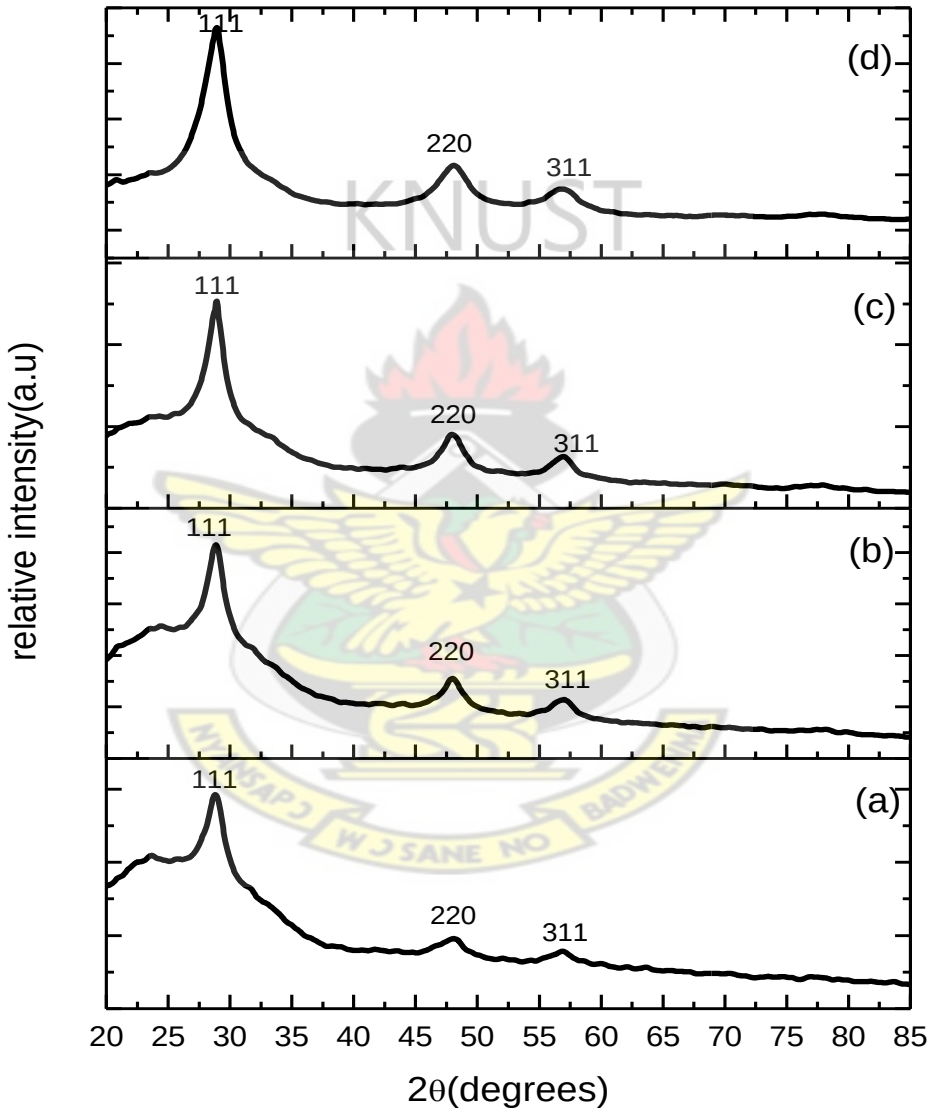

Figure 3.2. XRD of different as-prepared ZnS samples (a) for 4 hrs (b) for 5 hrs, (c) for 6 hrs and (d) for 8 hrs at 50 °C.

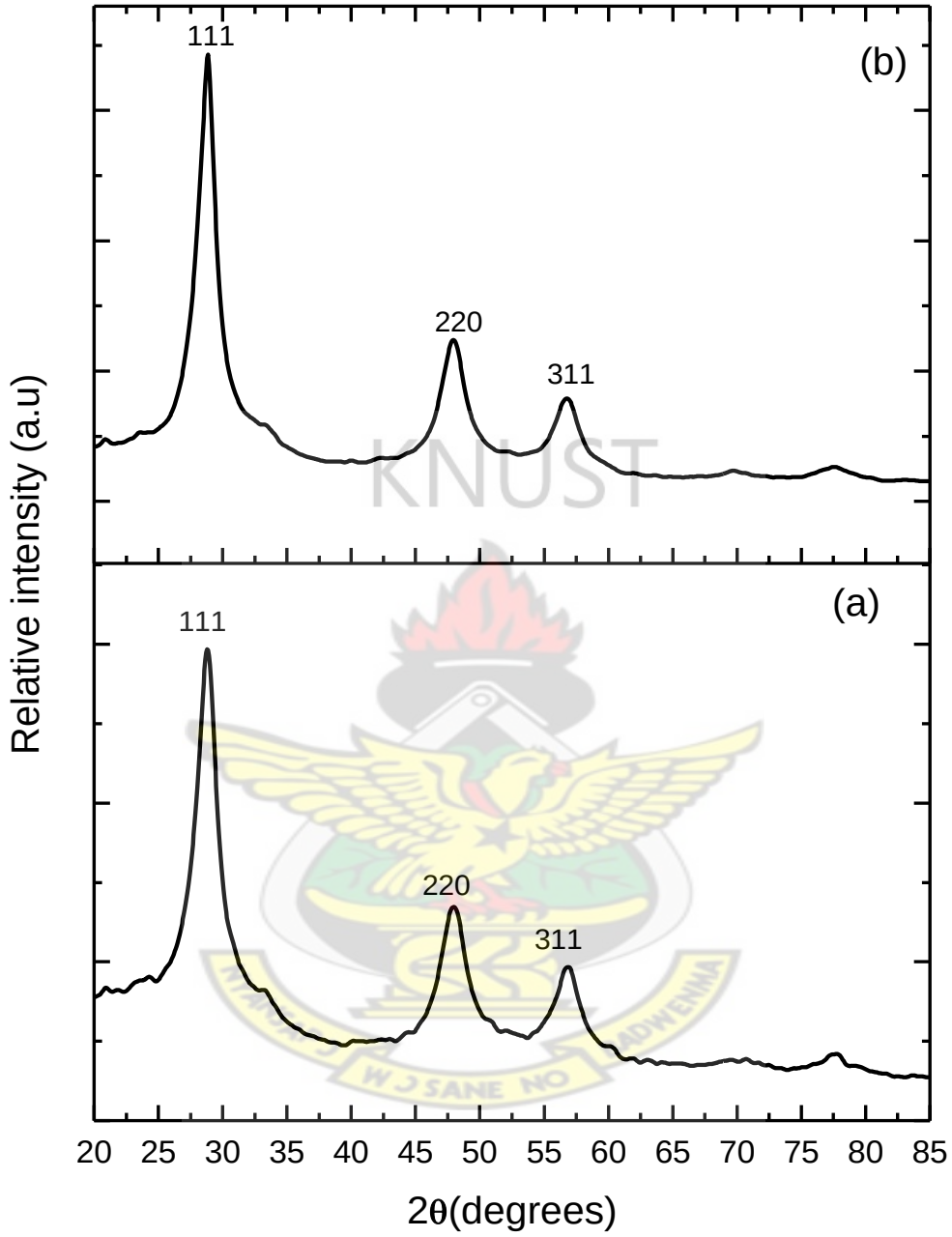

Figure 3.3. XRD of different as-prepared ZnS samples (a) for 5 hrs and (b) for 6 hrs at 70 °C.

Broadening of the diffraction peaks were observed implying that the size of the ZnS particles was small. Due to size effects the peaks broaden and the widths become larger as the crystal becomes smaller (Lu *et al*., 2001; Ghosh *et al*., 2004; Hu *et al*., 2005; Warad *et al*., 2005; Lan *et al*., 2003). Gosh *et al* (2004) have reported that the broadening of the peak may also occur due

to micro strains of the crystal structure arising from defects like dislocation and twinning etc. They have considered these defects to be associated with the chemically synthesized spontaneously growing nanocrystals. But in this work since the nanocrystals grew in a controlled manner at the interface there is no possibility of having considerable defects. The broadening of the peaks may arise due to insufficient energy that is needed for the atom to move to the proper site in forming the crystallite as reported. Small crystallites have relatively few lattice planes that contribute to the broadening. The observed diffraction peaks correspond to the (111), (220) and (311) planes of the cubic crystalline ZnS and are reported as identifying peaks of ZnS by earlier workers. Using the Bragg equation

$$d_{hkl} = \frac{n\lambda}{2sin\,\theta}, \qquad (3.1)$$

Where d is the spacing, *hkl* are the miller indices, λ is the wavelength of X-ray, θ is the Bragg angle and n is an integer determined by the order given. The d-spacing has been calculated and the estimated values are in good agreement with ICDD 10-080-0020. Peak intensity was observed to increase with increase in deposition time and temperature indicating increase in the crystallinity of the material shown in Figures 3.2 and 3.3.

The peak broadening at lower angle is more meaningful for the calculation of particle size; therefore size of the nanocrystals has been calculated using Debye-Scherrer formula (Guinier, 1963) using reflections from the XRD pattern.

The calculation gave particle sizes ranging from 1.4 to 5.5 nm with dislocation densities estimated from X-ray diffraction ranging from 1.13 to 9.32 x 10^{17} lines per metre. The dislocation density is a measure of the number of dislocations in a unit volume of a crystalline material. Dislocations in semiconductors are a nuisance for device developers since they introduce states which trap electrical charge, reducing the number of available carriers. By getting charged they

introduce electric fields, locally affecting device performance by scattering the electrons. Their states act as non-radiative recombination centers for electrons and holes, therefore reducing the efficiency of opto-electronic devices. They may also cause current leakages by jumping of the electrons from state to state.

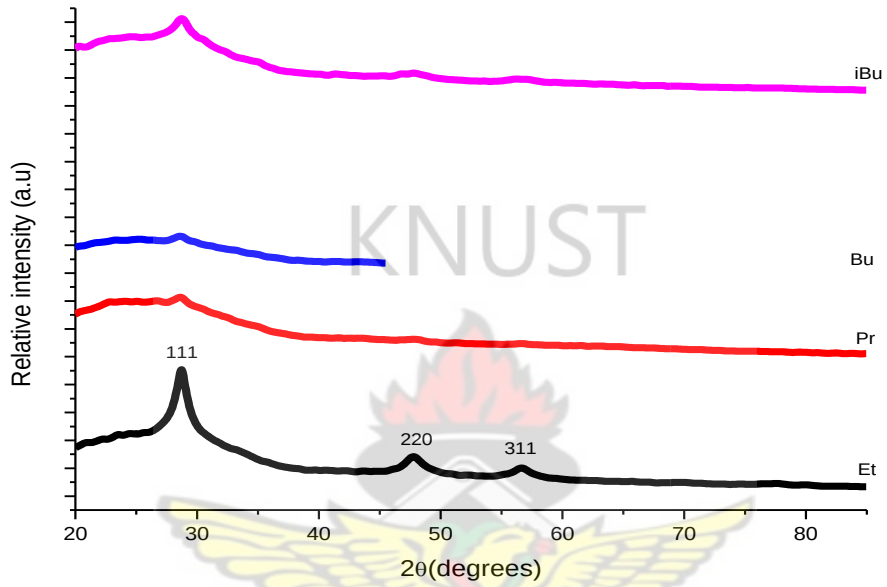

Figure 3.4: XRD of different as-prepared ZnS samples using different chain lengths of the alkyl group in the dithiocarbamate precursors at 50 °C for 6 hours. (Et = ethyl, Pr = propyl, Bu = butyl, ^{i}Bu = isobutyl)

The effect of the length of the alkyl chain length on the size of the crystallites and morphology of the nanoparticle was also investigated by varying the alkyl chain from ethyl to butyl and isobutyl in the dithiocarbamate precursor. The XRD diffractogram is shown in Figure 3.4 and the structural parameters given in table 3.2. The crystallite sizes as calculated by the Debye-Scherrer relation increase with increasing chain length (i.e. from Et=ethyl through Pr= propyl to Bu= butyl). However there was a reduction in size from Bu to ^{i}Bu. In another experiment when

zinc cupferronate was used as the precursor under the same experimental conditions as the zinc dialkyldithiocarbamate no thin film nanoparticle was formed.

The Scanning electron microscopy (SEM) images of ZnS nanomaterials/thin films formed at the water-toluene interface by reacting toluene solution of zinc diethyldithiocarbamate and aqueous solution of NaHS for 5 hours at 50 ^{o}C is shown in Figure 3.5.

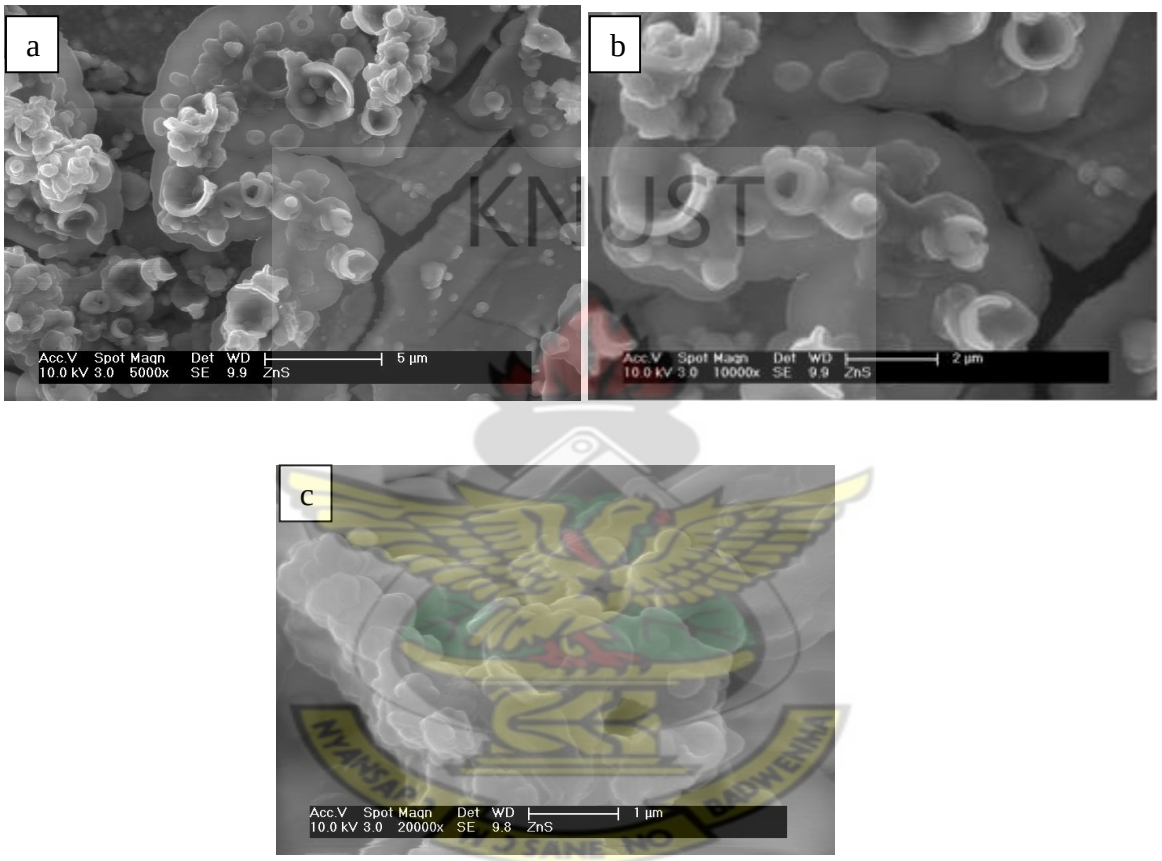

Figure 3.5: Scanning electron microscopy (SEM) image of ZnS nanomaterial formed at the water-toluene interface at 50 ^{o}C for 5 hours at different magnifications (a-5000x, b-10000x and c-20000x).

The compositional analysis of ZnS was done by energy dispersive X-ray analysis (EDAX) as shown in Figures 3.6. The ratio between zinc and sulphide peaks should be nearly stoichiometric. From the graph it is noted that for a deposition time of 5 hours and temperature of 50 ^{o}C the

atomic percentage of zinc was 48.41 while that of sulphur was 51.59. The composition ratio is affected by the cumulative effect of ionic transport, discharge, nucleation and growth during the higher deposition time and temperature.

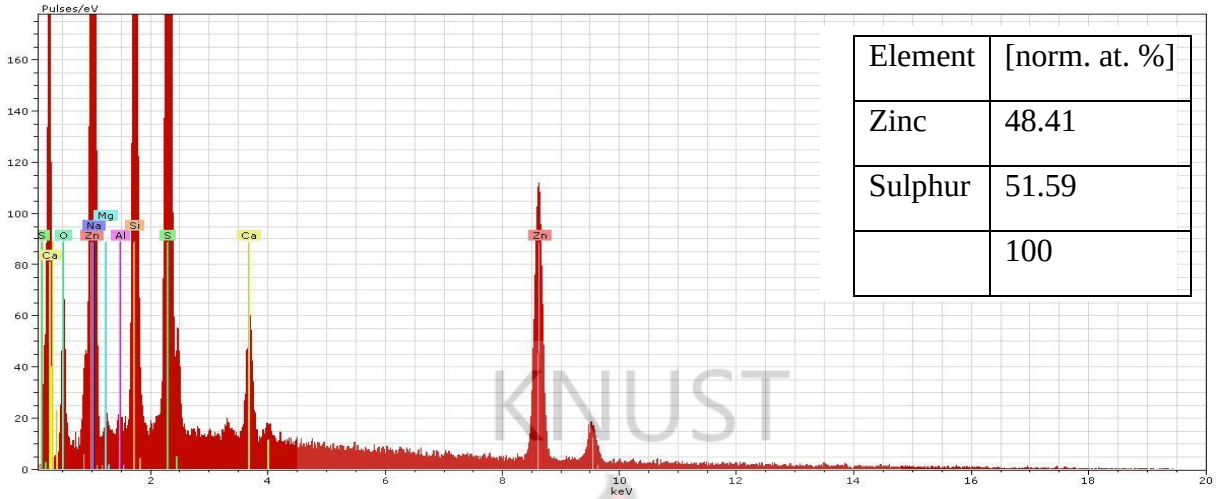

Element	[norm. at. %]
Zinc	48.41
Sulphur	51.59
	100

Figure 3.6: EDAX analysis of ZnS nanomaterial formed at the water-toluene interface at 50 ^{o}C for 5 hours

3.3.1.2 Optical analysis

In order to examine the quantum confinement effect of the synthesized nanoparticles, UV-VIS absorption spectra was employed. The optical absorption spectra of the nanocrystals were measured using CARY 5000 UV-Vis-NIR spectrophotometer. The optical absorption spectra have been measured at room temperature over a range of 250 to 600 nm (Figures 3.7-3.10). The peak of the UV absorption is indicative of the band gap of the semiconductor ZnS nanoparticles.

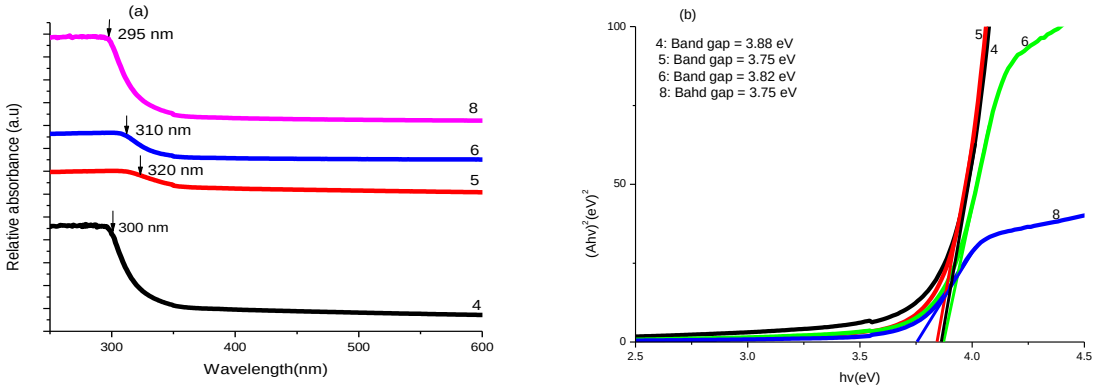

Figure 3.7: (a) Optical absorption spectra and (b) optical band gap of the as-prepared ZnS samples for 4, 5, 6 and 8 hrs at 50 °C.

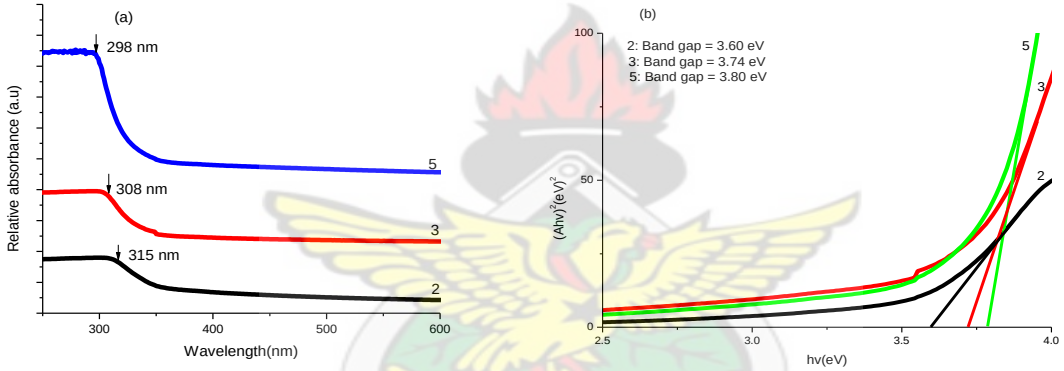

Figure 3.8: (a) Optical absorption spectra and (b) optical band gap of the as-prepared ZnS samples for 2, 3, and 5hrs at 50 °C.

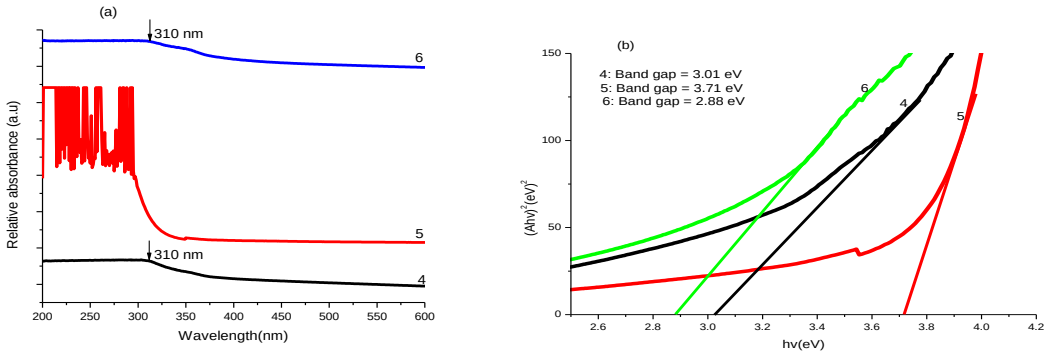

Figure 3.9: (a) Optical absorption spectra and (b) optical band gap of the as-prepared ZnS samples for 4, 5, and 6 hrs at 70 °C.

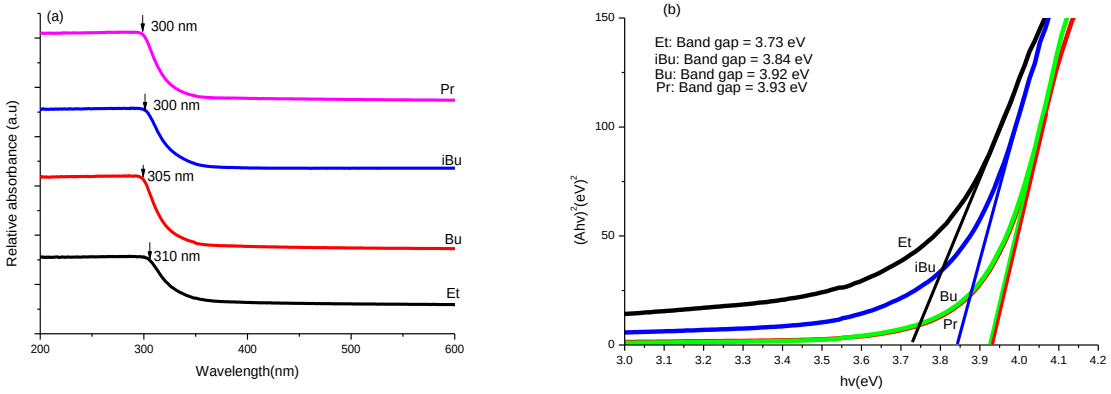

Figure 3.10: (a) Optical absorption spectra and (b) optical band gap of as-prepared ZnS samples using different chain lengths of the alkyl group in the dithiocarbamate precursors and lead cupferronate precursor at 50 °C for 6 hrs. (Et = ethyl; Pr = propyl; Bu = butyl; ^{i}Bu = isobutyl).

The fundamental absorption corresponds to the electron excitation from the valence band to the conduction band and can be used to determine the optical band gap. The relationship between the absorbance (A) and the incident photon energy (hυ) is given by the Stern relationship of near-edge absorption (Stern and Kim, 1981):

$$A = [k(h\upsilon - E_g)]^{1/n}/h\upsilon$$

Where υ is the frequency, h is the constant, k is a constant and carries a value of either 1 of 4. The value of n is 1 for direct transition and 4 for indirect transition. The optical band gap is determined by a plot of $(Ah\upsilon)^{2/n}$ as a function of hυ, extrapolation of the line to the hυ axis where $(Ah\upsilon)^{2/n}$ is zero gives the band gap E_g. The plots of $(Ah\upsilon)^2$ versus hυ is a straight line indicating that ZnS is a direct band gap material. The plots of $(Ah\upsilon)^2$ versus hυ for the different nanocrystallites obtained at various temperatures are also given in the Figures 3.7-3.10. Using the estimated band gap values of the nanoparticles in the Brus equation (Brus, 1984) (eq 3.1), the particle size can be calculated from the optical spectra. The Brus equation is the theoretical calculation for semiconductor nanoparticles based on "effective mass approximation" (EMA).

In this approximation, an exciton is considered to be confined to a spherical volume of the crystallite and the mass of electron and hole is replaced with effective masses (m_e and m_h) to define the wave function.

$$E_{np} = E_g + \frac{h^2}{8r^2}\left[\frac{1}{m_e^*} + \frac{1}{m_h^*}\right] - \frac{1.8e^2}{4\pi\varepsilon\varepsilon_0 r} \qquad (3.2)$$

Where, E_{np} = band gap energy of nanoparticle, E_g(bulk) = band gap energy of bulk semiconductor, r = radius of nanoparticle, m*e = effective mass of excited electron, m*h = effective mass of excited hole, h = Planck's constant and e = electronic charge.

Table 3.1 Optical parameters and crystallite sizes of ZnS nanoparticles

Precursor	Deposition Temperature /°C	Deposition time (hrs)	Band gap of nanoparticle (eV)	Particle size (nm)	
				U.V	XRD
$Zn(S_2CNEt_2)_2$: $S/NaBH_4$		2	3.60	-	2.962*
	50	3	3.74	10.5	2.123
		4	3.88	5.70	
		5	3.75	9.72	1.335
		6	3.82	6.84	1.687
		8	3.75	9.72	1.988
$Zn(S_2CNEt_2)_2$: $S/NaBH_4$	70	4	3.69/3.01	-	2.274
		5	3.71	14.88	1.981
		6	3.73	5.70	1.624
$Zn(S_2CNPr_2)_2$: $S/NaBH_4$	50	6	3.84	6.39	6.877
$Zn(S_2CNBu_2)_2$: $S/NaBH_4$	50	6	3.92	5.19	6.793
$Zn(S_2CN^iBu_2)_2$: $S/NaBH_4$	50	6	3.93	5.08	5.267

Band gap of bulk ZnS = 3.68 eV; * X-ray measured radius above Bohr exciton bulk radius of 2.5 nm.

Table 3.1 shows optical parameters and crystallite sizes of ZnS nanoparticles. The XRD measurements showed that the average radii of the nanoparticles in this study are below the excitonic Bohr radius of bulk ZnS (2.5 nm). The calculated band gap values ranging from 3.74 to 3.93 eV are higher than the bulk value of 3.68 eV because of quantum confinements of the ZnS nanoparticle thin films. The absorption spectra reveal that the excitonic absorption peaks for the nanoparticles are blue shifted compared to the bulk band gap of 3.68 eV (corresponding to the absorption edge at 336 nm) and clearly indicate strong quantum size effects. Size

quantization of carriers in a small volume crystallite is well known to cause the blue shift. The shift of band gap have been utilized in determining the crystallite radius using the effective mass approximation relation and the particle sizes obtained in this work are also given in Table 3.1. These values are significantly above the estimates based on X-ray diffraction measurements because of the assumption that the confining potentials for the electron and hole are infinite.

3.3.2 t-Selenium nanorods

The reaction of toluene solution of zinc diethyldithiocarbamate with NaHSe generated by the borohydride reduction of selenium powder in water at 50 ^{o}C for 5 hours yielded t-Selenium nanorods contaminated with cubic (zinc blende) ZnSe nanomaterial at the water-toluene interface as shown by the X-ray diffraction measurements. Selenium shows interesting properties such as high photoconductive and catalytic properties and has commercial use in photocopiers and rectifiers (Zingaro and Cooper, 1974). Nanorods of *t*-selenium have been synthesized by using a simple solution-based method (Rao *et al*., 2003), where selenium powder is first reduced with $NaBH_4$ to yield NaHSe (Klayman and Griffin, 1973) in aqueous solution to obtain amorphous selenium. The selenium dissolves in water in 60 min giving rise to a clear colourless solution. The reaction mechanisms involved are:

$$4NaBH_4 + 2Se + 7H_2O \longrightarrow 2NaHSe + Na_2B_4O_7 + 14H_2 \quad \ldots\ldots(3.3)$$

$$Na_2B_4O_7 + 2NaHSe + 2Se + 5H_2O \longrightarrow 2Na_2Se + 4H_3BO_3 \quad \ldots\ldots(3.4)$$

$$Na_2Se + 2H_2O \longrightarrow 2a\text{-}Se + 2NaOH + H_2 \quad \ldots\ldots(3.5)$$

$$a\text{-}Se \longrightarrow t\text{-}Se \quad \ldots\ldots(3.6)$$

The selenide ion acts as the source of Se in this method. The nascent selenium produced in step (3) imparts a wine red colour to the aqueous solution. On standing for a few hours, the solution

transforms into amorphous Se in colloidal form. A small portion of the dissolved selenium precipitates as t-Se nanoparticles which act as nuclei to form one-dimensional nanorods (Gautam *et al*., 2005).

In the water-toluene interface method which is the method for this study the mechanism is quite similar to the simple solution-based method but with a slight variation. The dissolved selenide ion migrated to the water-toluene interface. The expectation was that Zn^{2+} ions which were obtained through the decomposition of the zinc diethyldithiocarbamate would also migrate to the water-toluene interface where it would react with the selenide ions to form ZnSe nanoparticles. However, the results indicate that there were two processes at the water-toluene interface. The first process is the reaction between the Zn^{2+} ions and the Se^{2-} anions to form ZnSe as expected i.e.

$$Zn^{2+} + Se^{2-} \longrightarrow ZnSe \qquad (3.7)$$

The second process involves the transformation of the selenide ion into amorphous Se in colloidal form a small portion of which precipitates as t-Se nanoparticles which acts as nuclear to form one-dimensional nanorods according to equation (3.6). The predominance of the t-Se nanorods points to the fact that the conditions and energetics at the water-toluene interface was more favourable towards the second process.

3.3.2.1 Structural characterization and morphology

Figures 3.11 and 3.12 show the X-ray diffraction patterns of as-prepared t-Se nanowires. The diffraction peaks at 2θ (degrees) of 23.57°, 29.73°, 41.28°, 43.68°, 45.43°, 51.72°, 56.07°, 61.62°. 65.24° and 71.60° are respectively indexed as the (100), (101), (110), (102), (111), (201), (112), (103), (210) and (113) planes of t-Se. All the diffraction peaks in the 2θ range measured correspond to the trigonal structure of t-Se with lattice constants a = 4.35 Å and c = 4.93 Å are

in good agreement with those on the standard card (JCPDS card No. 06-0362). The sharpness of the diffraction peaks suggests that the product is well crystallized. The crystallite size of t-selenium is calculated using Debye-Scherrer formula. Peak intensity was observed to increase with increase in deposition time and temperature. This indicates increase in the crystallinity of the material with increase in deposition time and temperature.

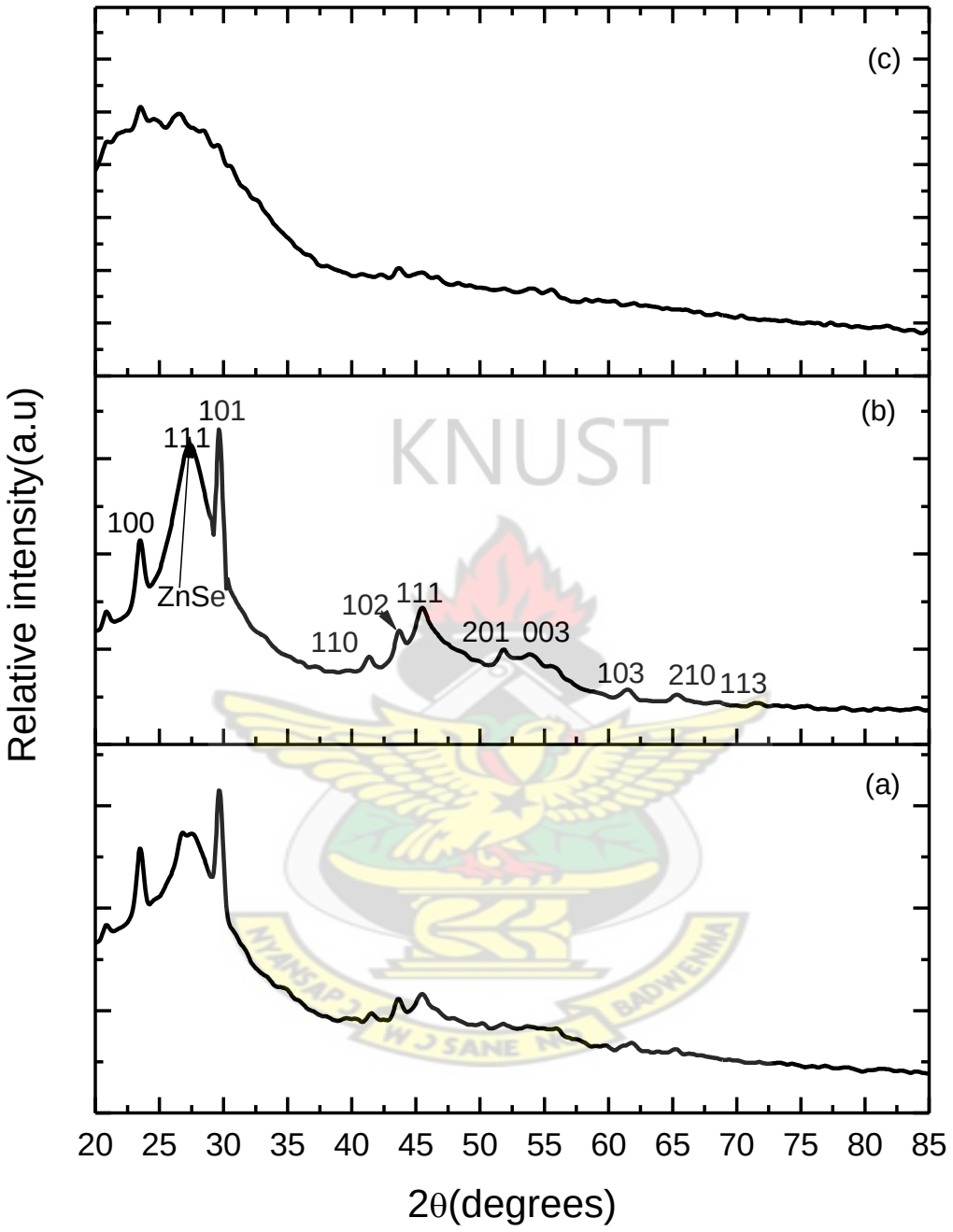

Figure 3.11: XRD of different as-prepared t-Se nanorods (a) for 4 hrs (b) for 5 hrs and (c) for 6 hrs at 50 ^{o}C.

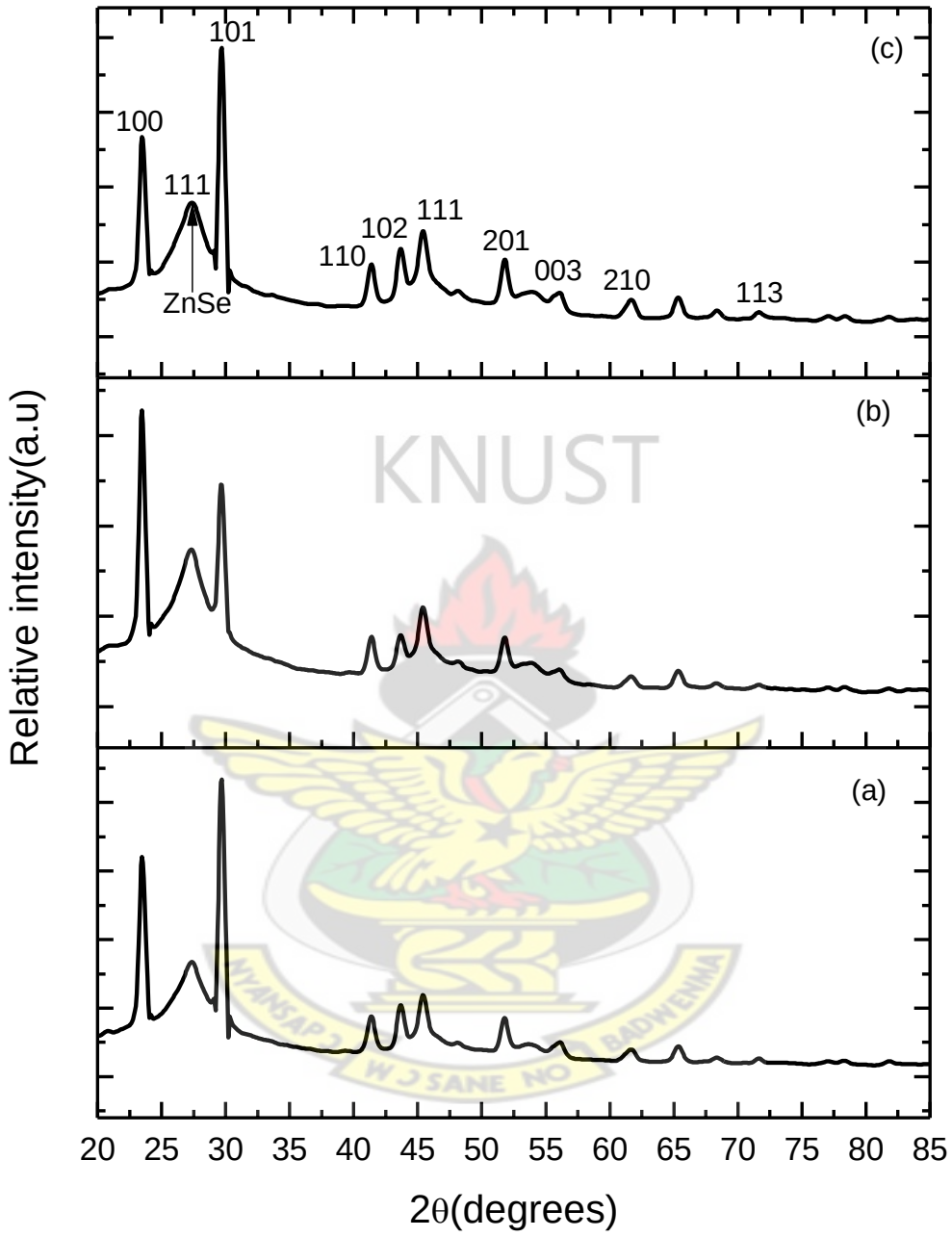

Figure 3.12: XRD of different as-prepared t-Se nanorods (a) for 4 hrs (b) for 5 hrs and (c) for 6 hrs at 70 ^{o}C.

As in the case of ZnS the effect of the length of the alkyl chain length on the size of the crystallites and morphology of the nanoparticle was also investigated. The XRD diffractogram is shown in Figure 3.13 and the structural parameters given in Table 3.5.

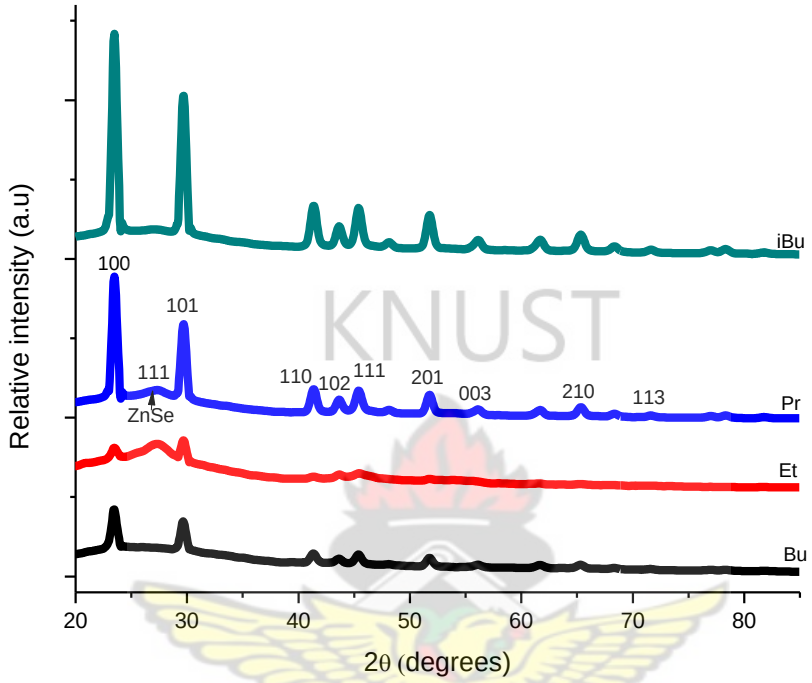

Figure 3.13: XRD of different as-prepared t-Se nanorods using different chain lengths of the alkyl group in the Zinc dithiocarbamate precursors at 50 °C for 6 hrs. (Et = ethyl; Pr = propyl; Bu = butyl; ^{i}Bu = isobutyl).

The Scanning electron microscopy (SEM) images of t-Se nanowires formed at the water-toluene interface by reacting 30 ml of toluene solution of 0.56 mM zinc diethyldithiocarbamate and aqueous solution of NaHSe generated by the borohydride reduction of selenium powder for 5 hours at 50 ^{o}C and 70 ^{o}C are shown in Figure 3.14. These images show the formation of some hexagonal rods structures. The high resolution transmission electron microscopy (HRTEM) image at high magnification of t-Se nanorods formed at water-toluene interface by reacting toluene solution zinc diethyldithiocarbamate and aqueous solution of NaHSe at 50 ^{o}C for 5 hours

is also given by Figure 3.15 with the Fresnel fringes indicating the formation of crystalline material. The energy dispersive X-ray analysis (EDAX) spectra shown in Figure 3.16 indicate the elemental composition of the nanomaterial/thin film formed at 50 ^{o}C for 5 hours. Quantitative EDAX spectra of t-Se nanomaterial formed at water-toluene interface 50 ^{o}C for 5 hours gave a composition ratio of 1:7.33 within the limitations of the experimental conditions (Figure 3.16) indicating that the nanorods formed were predominantly that of t-Se.

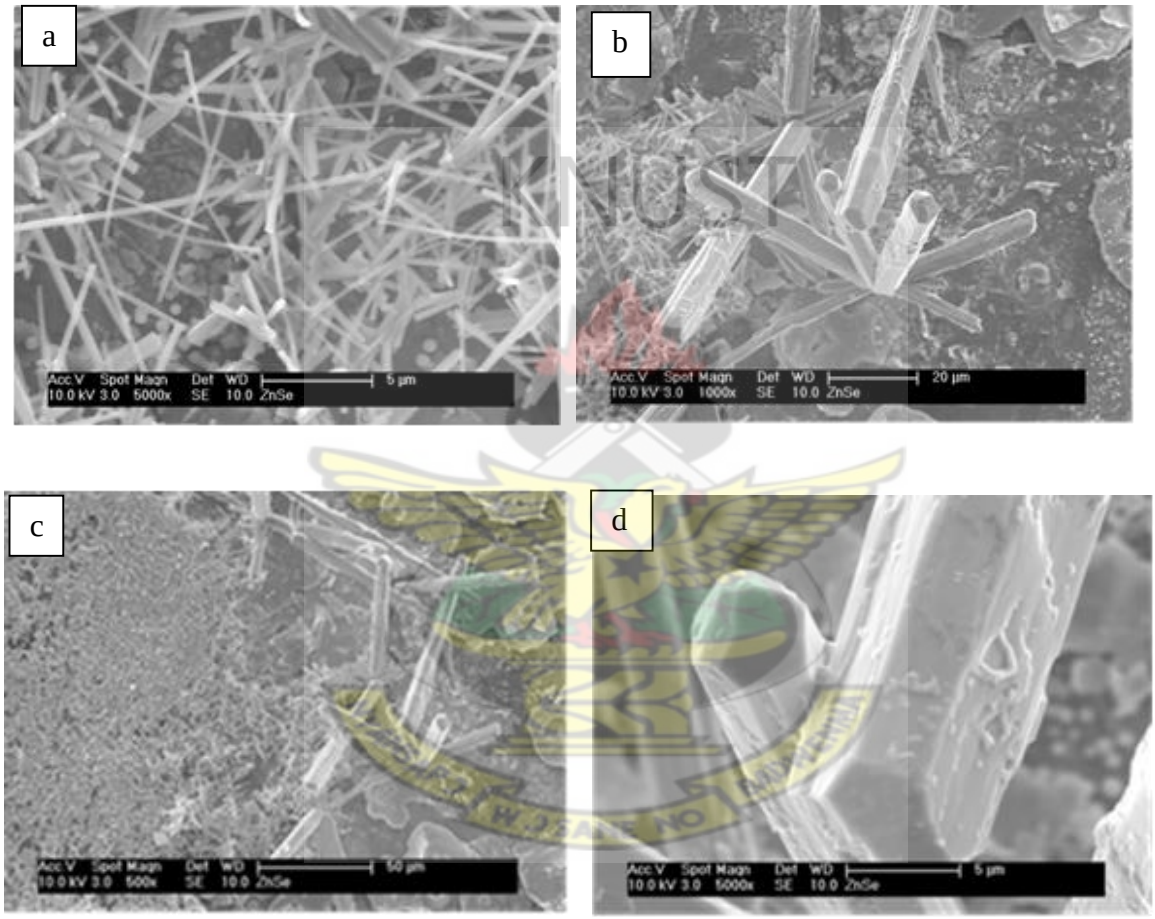

Figure 3.14: Scanning electron microscopy (SEM) image of t-Se nanorods formed at the water-toluene interface at 50 ^{o}C for 5 hours at different magnifications (a-5000x, b-10000x and c-20000x).

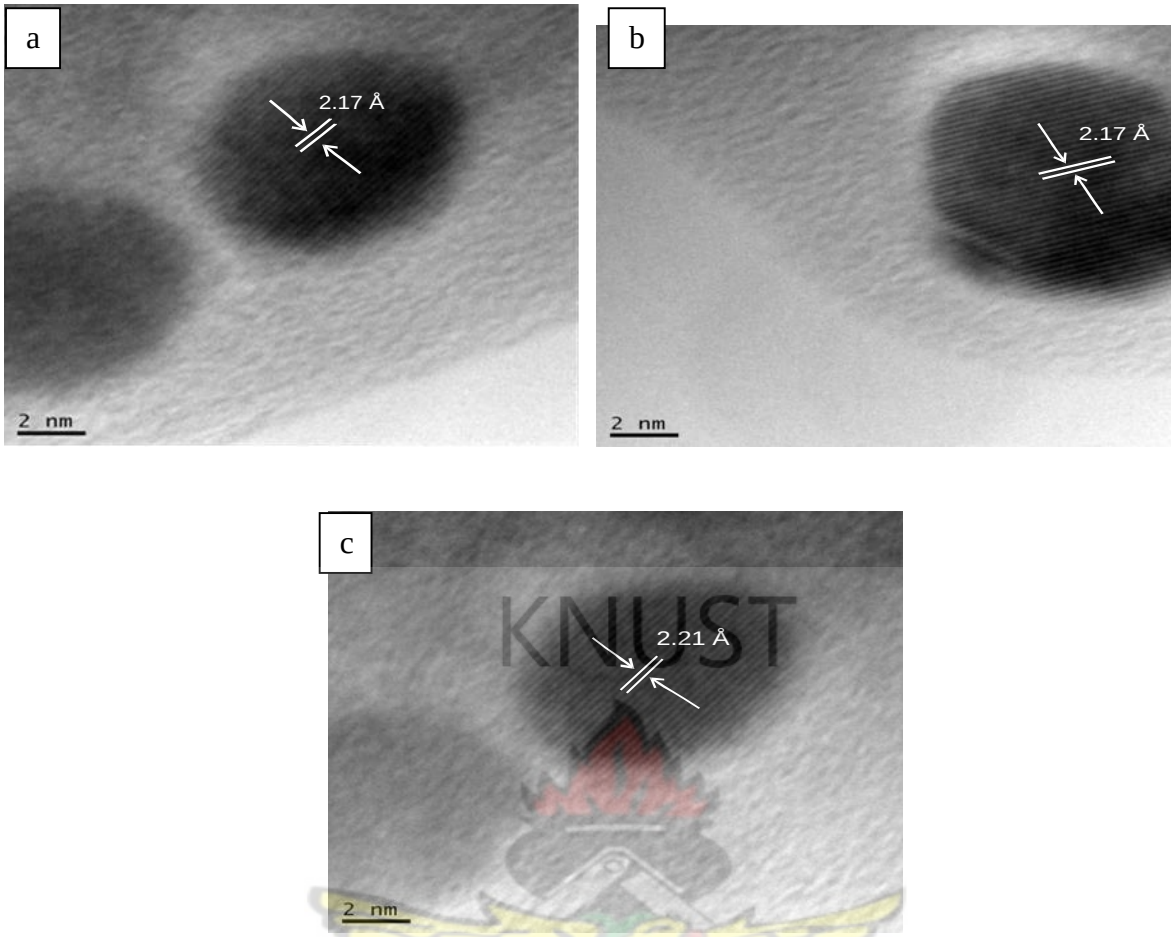

Figure 3.15: High resolution transmission electron microscopy (HRTEM) image at high magnification of t-Se nanorods formed at water-toluene interface by reacting toluene solution of zinc diethyldithiocarbamate and aqueous solution of NaHSe at 50 ˚C for 5 hours

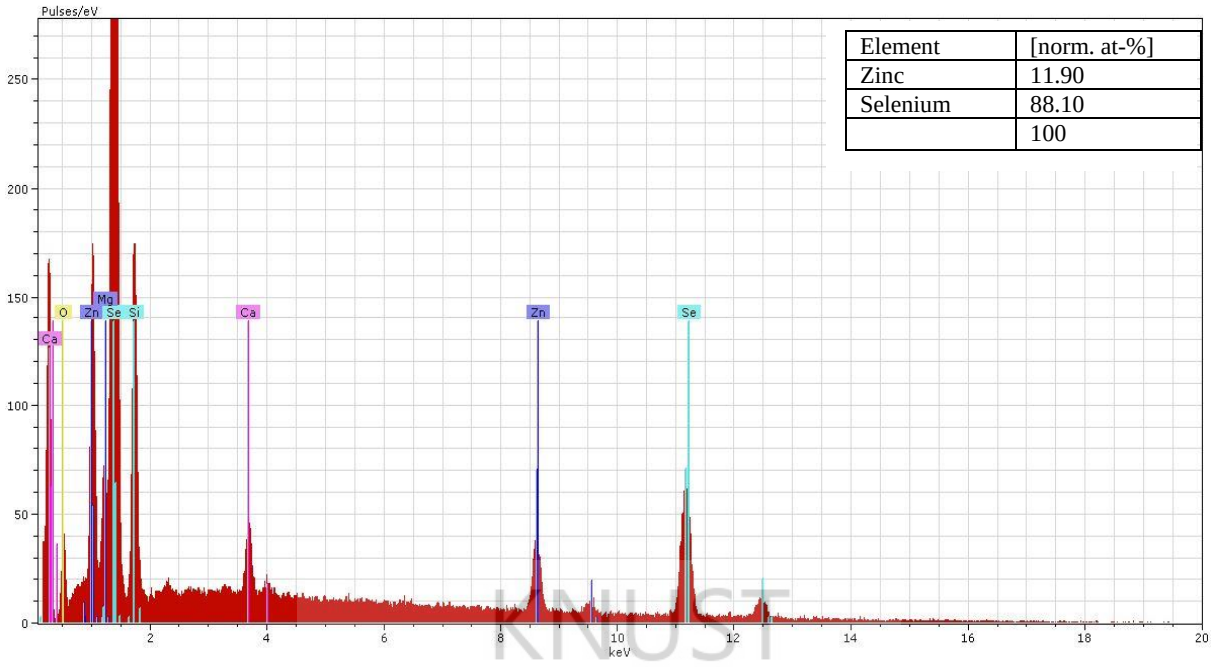

Figure 3.16: EDAX spectra of t-Se nanorods formed at water-toluene interface by reacting at 50 ^{o}C for 5 hours.

3.3.2.2 Optical analyses

The optical absorption spectra of the nanorods were also measured using CARY 5000 UV-Vis-NIR spectrophotometer. The optical absorption spectra were measured at room temperature over a range of 250 to 600 nm (Figures 3.17-3.20).

The plots of $(Ah\upsilon)^2$ versus $h\upsilon$ is a straight line indicating that t-Se is a direct band gap material. The plots of $(Ah\upsilon)^2$ versus $h\upsilon$ for the different nanocrystallites obtained at 50 ^{o}C are given in the Figures 3.17–3.20. Using the estimated band gap values of the nanoparticles in the Brus equation the particle size were calculated from the optical spectra.

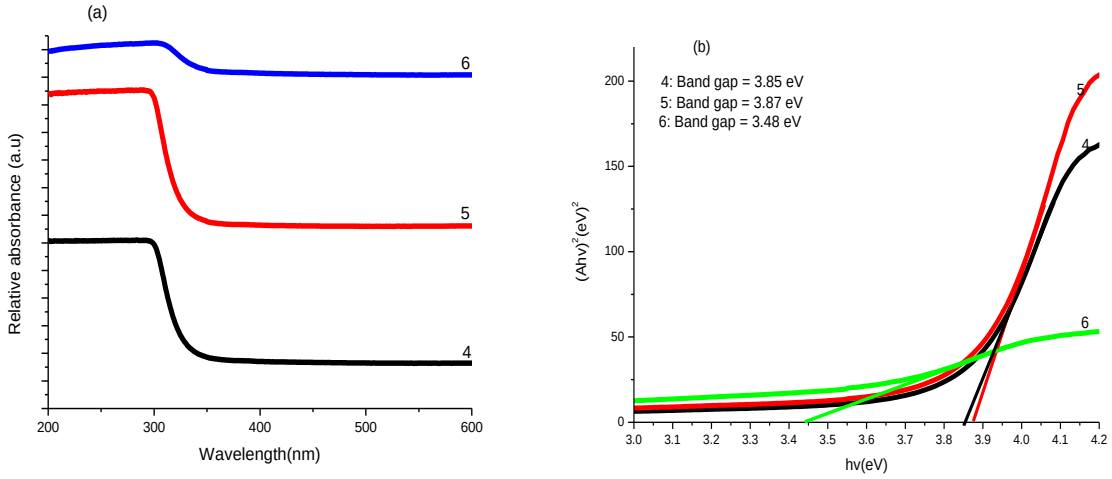

Figure 3.17: (a) Optical absorption spectra and (b) optical band gap of the as-prepared t-Se nanorods for 4, 5 and 6 hours at room temperature.

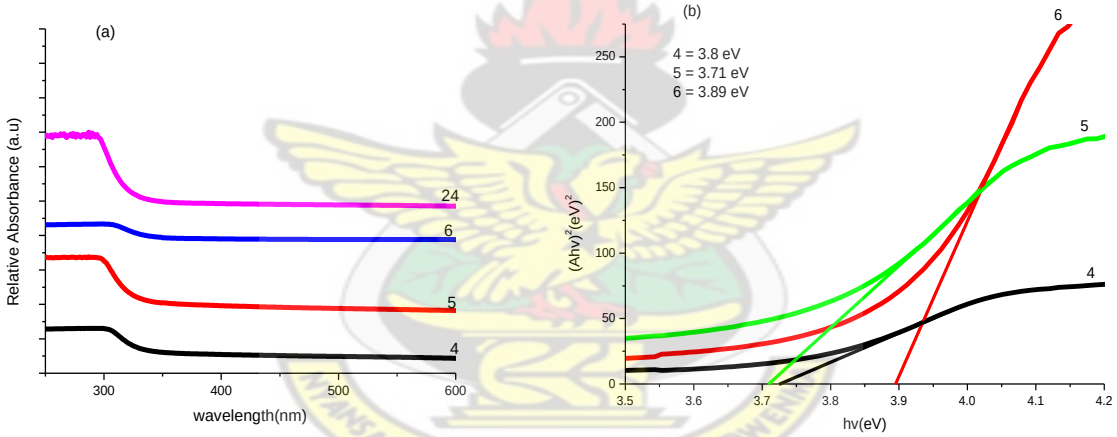

Figure 3.18: (a) Optical absorption spectra and (b) optical band gap of as-prepared t-Se nanorods for 4, 5, 6 and 24 hours at 50 ^{o}C.

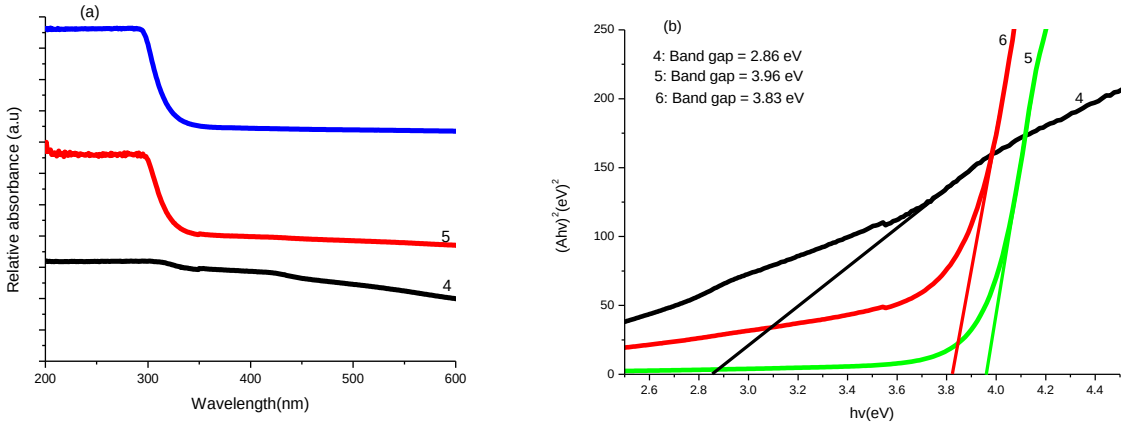

Figure 3.19: (a) Optical absorption spectra and (b) optical band gap of the as-prepared t-Se nanorods for 4, 5 and 6 hours at 70 ^{o}C

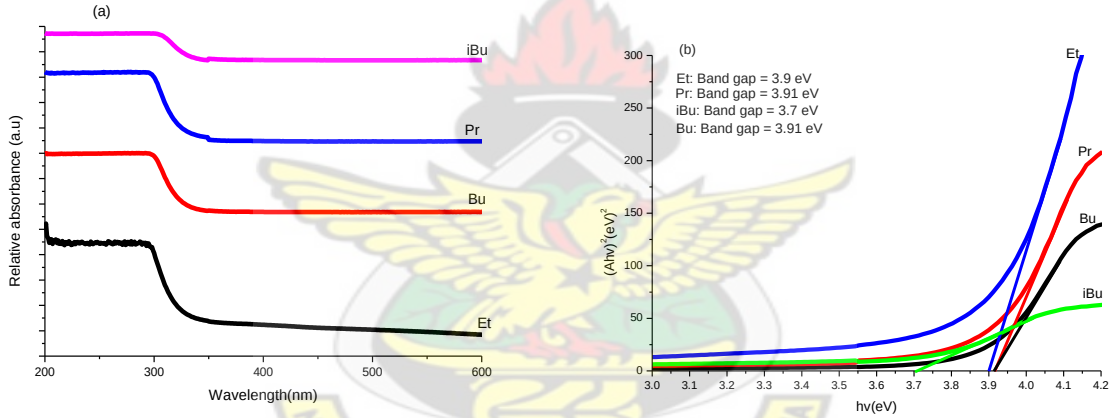

Figure 3.20: (a) Optical absorption spectra and (b) optical band gap of the as-prepared t-Se nanorods using different chain lengths of the alkyl group in the Zinc dithiocarbamate precursors at 50 °C for 6 hours. (Bu = butyl; Et = ethyl; Pr = propyl; ^{i}Bu = isobutyl).

Table 3.2 Optical parameters and crystallite sizes of t-Se nanowires

Precursor	Deposition Temperature/ ^{o}C	Deposition time (hrs)	Band gap of nanoparticle (eV)	Particle size (nm)	
				U.V	XRD
$Zn(S_2CNEt_2)_2$: Se/$NaBH_4$	RT	4	3.85	1.81/2.83	-
		5	3.87	1.80/2.79	-
		6	3.48	2.06/3.52	-
$Zn(S_2CNEt_2)_2$: Se/$NaBH_4$	50	4	3.7	1.91/3.06	5.61
		5	3.8	1.84/2.90	3.65
		6	3.7	1.91/3.06	7.08
$Zn(S_2CNEt_2)_2$: Se/$NaBH_4$	70	4	2.86	2.74/8/22	6.14
		5	3.96	1.75/2.67	1.07
		6	3.83	1.82/2.85	6.12
$Zn(S_2CNPr_2)_2$: Se/$NaBH_4$	50	6	3.91	1.78/2.74	6.18
$Zn(S_2CNBu_2)_2$: Se/$NaBH_4$	50	6	3.70	1.90/3.06	2.00
$Zn(S_2CN^{i}Bu_2)_2$: Se/$NaBH_4$	50	6	3.83	1.82/2.85	5.10

Band gap of bulk t-Se = 1.74

Table 3.2 gives the optical parameters and crystallite sizes of the t-Se nanoparticle thin films formed at different temperatures, deposition times and with different precursors. The band gap of t-Se nanoparticle thin films increased from the bulk t-Se of 1.74 eV to the range 2.86 eV to 3.96 eV as the crystallite sizes changed to between 1.07 to 7.08 nm.

3.3.3 Tellurium nanorods

The reaction of toluene solution of zinc diethyldithiocarbamate with aqueous solution of NaHTe obtained by the borohydride reduction of tellurium powder yielded t-Te nanorods at the water-toluene interface. Rao *et al*., (2004) synthesized t-Te nanowires in water and indicated that the lateral dimensions of the 1-D structures formed depended on the nature of the seeds and can be varied by varying the initial reaction conditions. A likely reaction scheme is as follows:

$$4NaBH_4 + 2Te + 7H_2O \longrightarrow 2NaHTe + Na_2B_4O_7 + 14H_2 \quad \text{..... (3.8)}$$

$$Na_2B_4O_7 + 2NaHTe + 2Te + 5H_2O \longrightarrow 2Na_2Te + 4H_3BO_3 \quad \text{.....(3.9)}$$

$$Na_2Te + 2H_2O \longrightarrow 2a\text{-}Te + 2NaOH + H_2 \quad \text{.....(3.10)}$$

$$a\text{-}Te \longrightarrow t\text{-}Te \quad \text{.....} \quad (3.11)$$

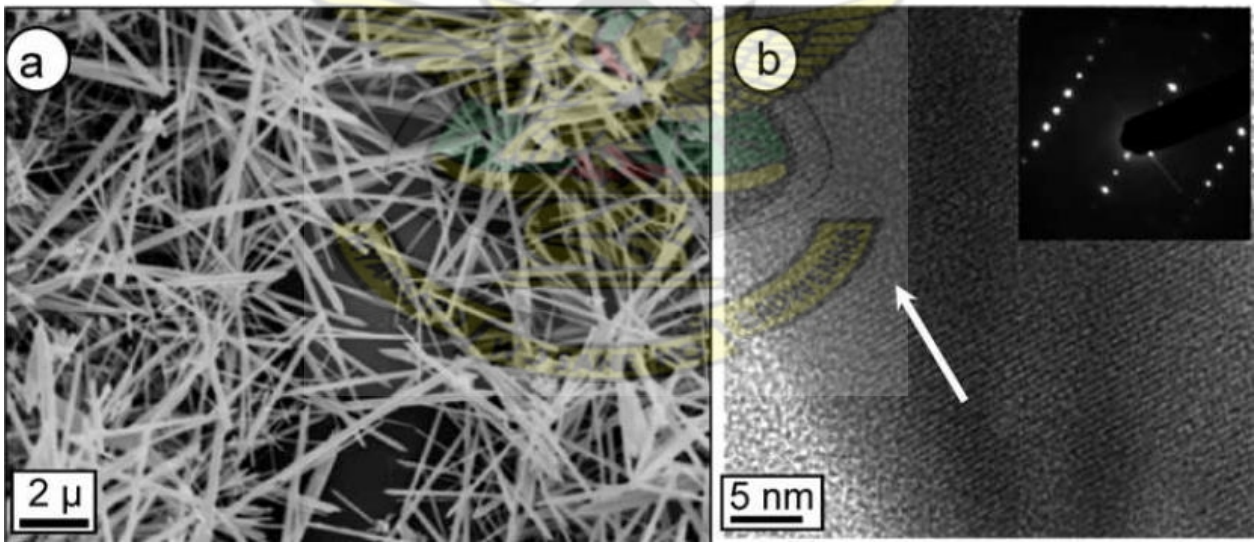

Figure 3.21. (a) SEM image of t-Te nanorods obtained from the reaction of 0.03 g of Te with $NaBH_4$ in 20 ml water. (b) HREM image of one of the nanorods showing (0 0 1) planes of hexagonal t-Te (inset shows the corresponding SAED pattern) (Gautam *et al.,* 2005)

Figure 3.21 shows a SEM image of the nanorods obtained and HREM image of one of the nanorods showing the (001) planes of hexagonal t-Te and the corresponding SAED pattern in such a preparation (Rao *et al*., 2004). The process involved addition of $NaBH_4$ to a container with Te powder in water upon heating leads to an aqueous solution of NaHTe. By appropriate control of the reaction conditions, different morphologies of the 1D nanostructures of Te have been achieved: (i) rods or wires, (ii) belts, (iii) tapered rods or whiskers, (iv) T-junctions and (v) Y-junctions. Figure 3.22 gives a Schematic process of formation of t-Te nanorods in solution.

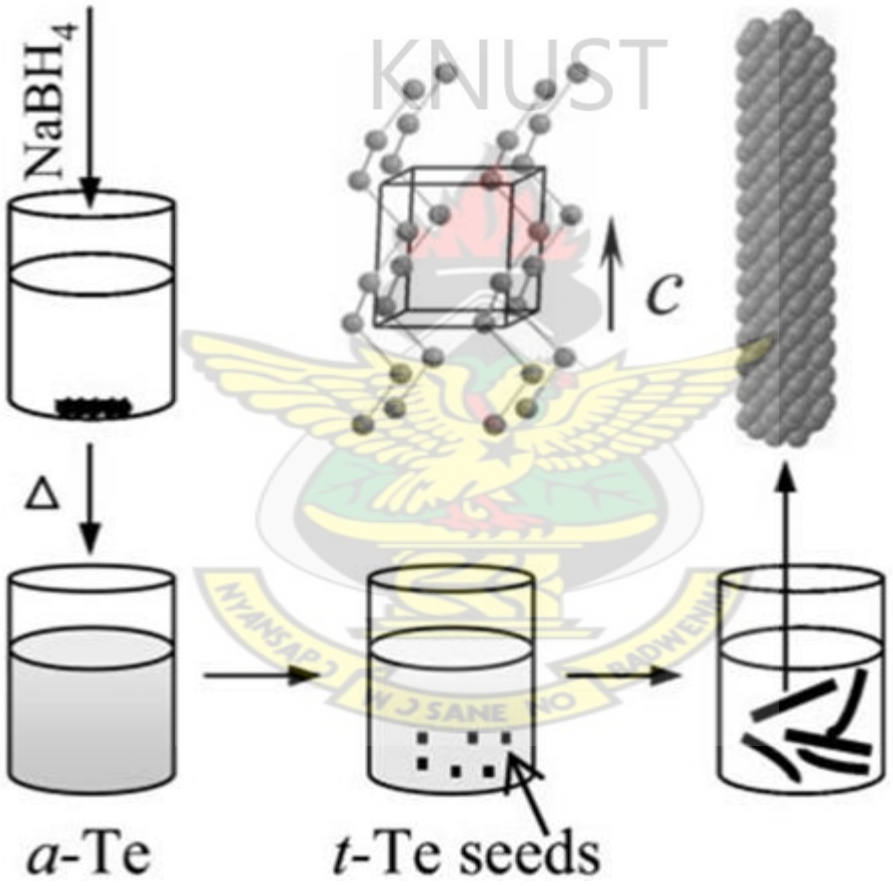

Figure. 3.22 Schematic process of formation of t-Te nanorods in solution (Gautam and Rao, 2004)

3.3.3.1 Structural characterization and morphology

Figures 3.22-3.24 show the XRD spectra taken from the t-Te nanowires. It can be seen that the positions of the diffraction peaks of the various samples are approximately the same. All the peaks of t-Te NWs in the XRD pattern can be indexed to the hexagonal phase of Te, whose unit cell constants are a = 0.4451 nm and c= 0.5904 nm, which is consistent with the literature data (JCPDS: card no. 36-1452).

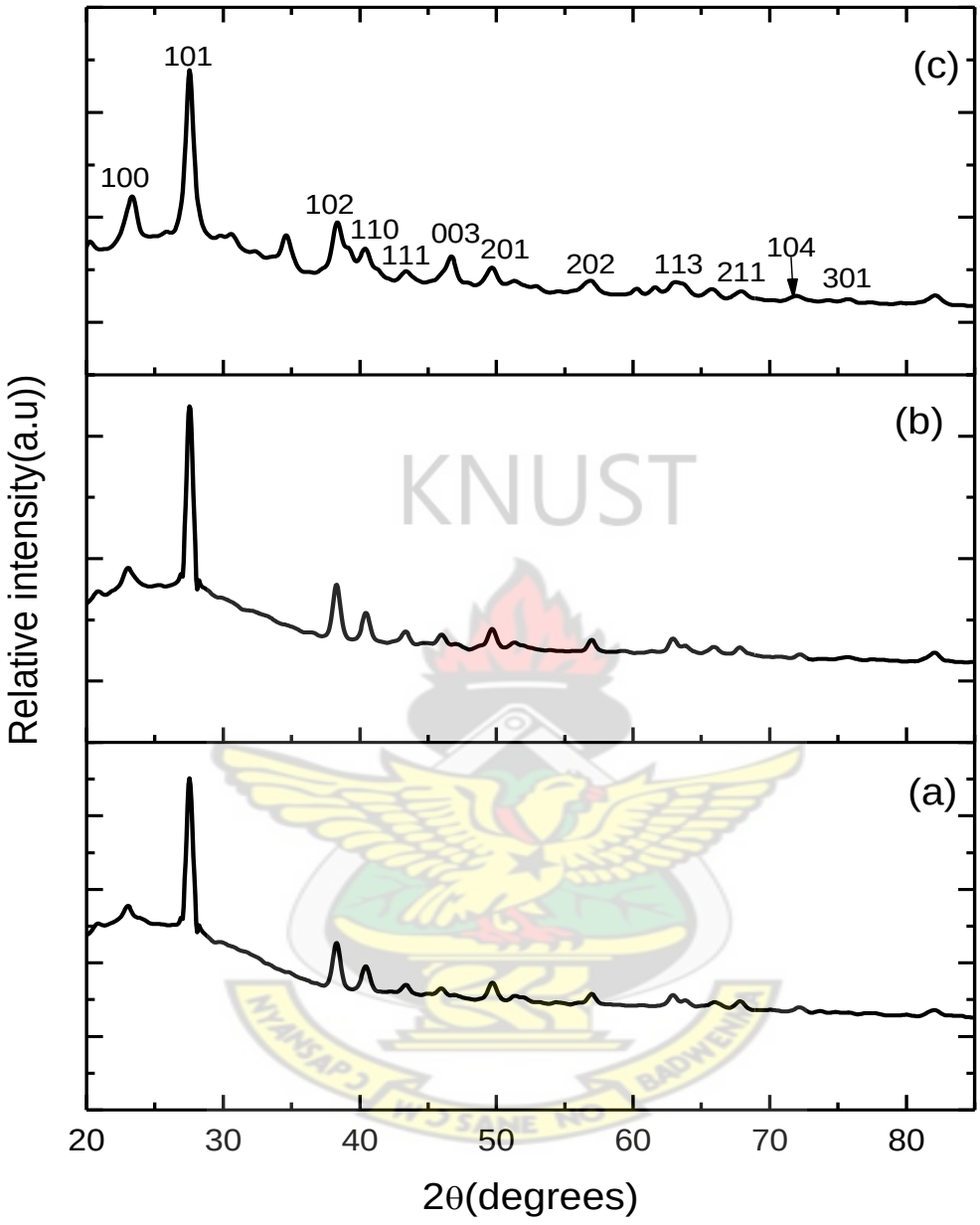

Figure 3.23: XRD of different as-prepared t-Te nanowires (a) for 4 hours (b) for 5 hours and (c) for 6 hours at 50 ºC.

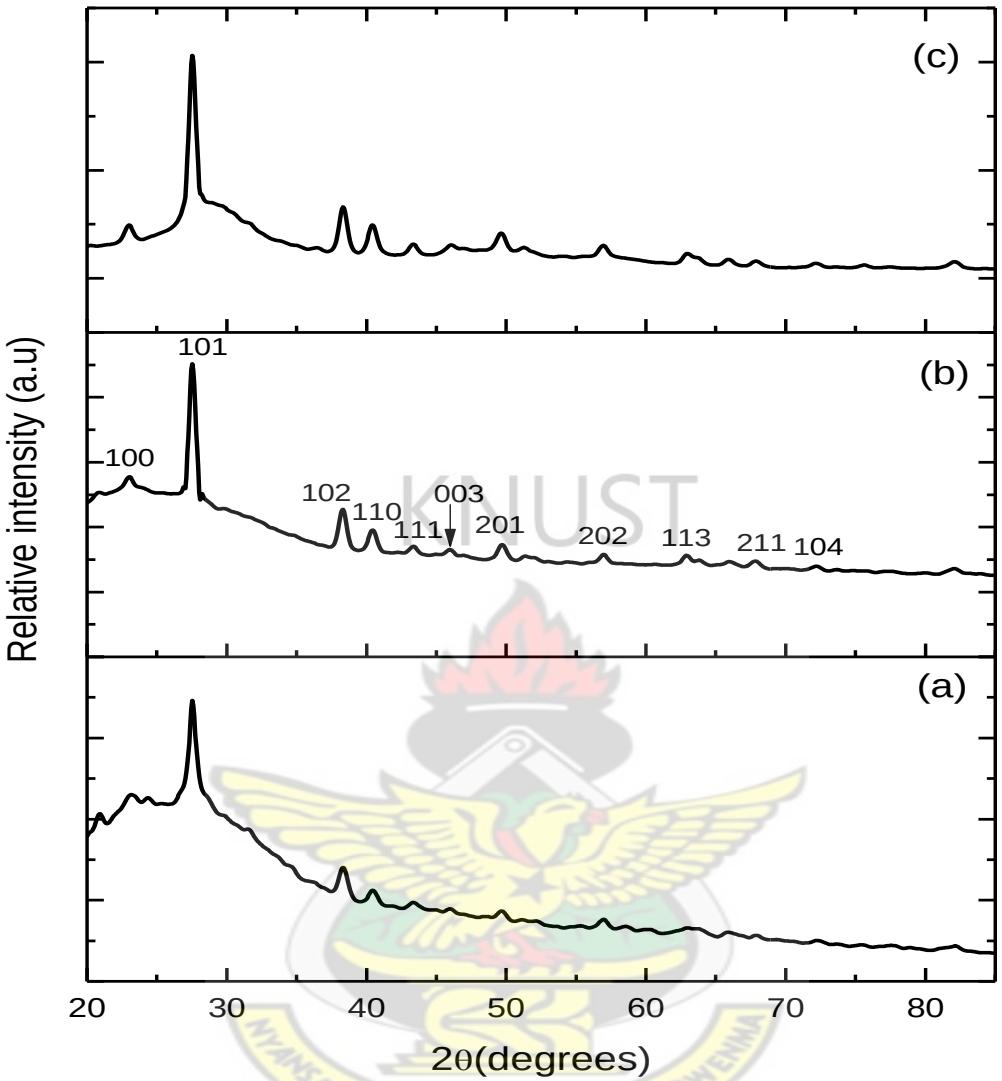

Figure 3.24: XRD of different as-prepared t-Te nanowires at (a) 50 ºC, (b) 60 ºC, and (c) 70 ºC, for 24 hours.

The XRD pattern show peaks whose intensities increase with increasing deposition time and temperature (Figures 3.23 and 3.24). This indicates increase in the crystallinity of the nanomaterial thin film with increase in deposition time and temperature. The hexagonal structures show orientations along the 101 planes.

The effect of the length of the alkyl chain length on the size of the crystallites and morphology of the t-Te nanorods was also investigated. The XRD diffractogram is shown in Figure 3.25 and the structural parameters given in Table 3.8.

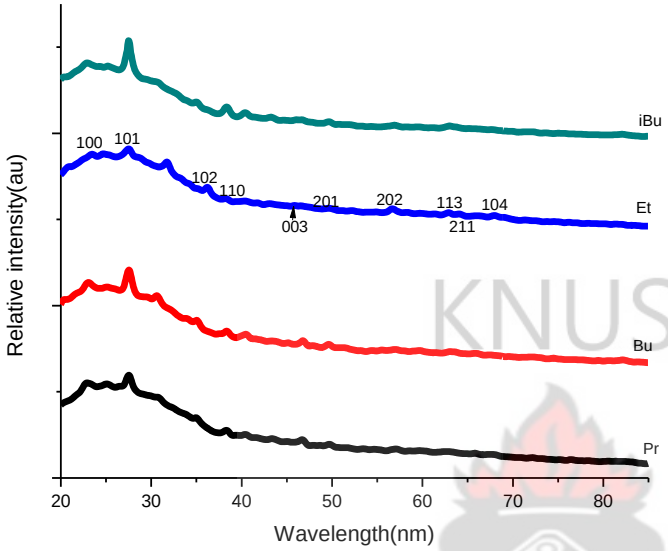

Figure 3.25: XRD of different as-prepared t-Te nanorods using different chain lengths of the alkyl group in the dithiocarbamate precursors and lead cupferronate precursor at 50 °C for 6 hours. (Et = ethyl; Pr = propyl; Bu = butyl; *i*Bu = isobutyl).

3.3.3.2 Optical analyses

The optical absorption spectra of the nanorods were measured using CARY 5000 UV-Vis-NIR spectrophotometer. The optical absorption spectra were measured at room temperature over a range of 400 to 1500 nm. The spectra of the nanorods show a broad band at 800 nm which is not observed in the spectrum of the bulk Te.

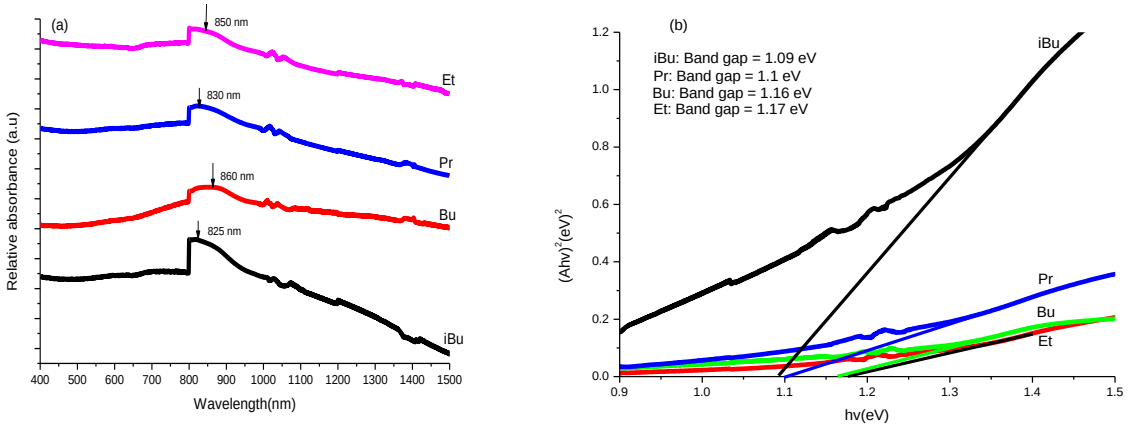

Figure 3.26: (a) Optical absorption spectra and (b) optical band gap of the as-prepared t-Te nanowires using different chain lengths of the alkyl group in the Zinc dithiocarbamate precursors at 50 °C for 6 hours. (Bu = butyl; Et = ethyl; Pr = propyl; ^{i}Bu = isobutyl).

The fundamental absorption corresponds to the electron excitation from the valence band to the conduction band and can be used to determine the optical band gap. The t-Te nanowires have been reported to possess two characteristic peaks: peak I and peak II. Peak I is due to the transition from π-bonding valence band (VB2) to the p-antibonding conduction band (CB1), and it appears in the range of 250-350 nm. Peak II is due to the transition from p-lone pair valence band (VB3) to the p-antibonding conduction band (CB1), and it appears around 600-850 nm (Lin *et al*., 2008; Sreeprasad *et al*., 2009; Rao and Gautama, 2004). Plots of the absorption spectra and plots of $(Ah\upsilon)^2$ versus hυ are given in Figure 3.26.

Table 3.3 Optical parameters and crystalline sizes of t-Te nanowires

Precursors	Deposition Temperature/°C	Deposition time (hrs)	Band gap of nanoparticle (eV)	Particle size (nm)	
				U.V	XRD
$Zn(S_2CNEt_2)_2$: Te/$NaBH_4$	50	4	3.9	0.69/2.22	
		5	3.85	0.71/2.26	
		6	3.6	0.76/2.52	
$Zn(S_2CNEt_2)_2$: Te/$NaBH_4$	50	5	1.17	-	5.70
$Zn(S_2CNPr_2)_2$: Te/$NaBH_4$	50	5	1.10	-	6.38
$Zn(S_2CNBu_2)_2$: Te/$NaBH_4$	50	5	1.16	-	6.74
$Zn(S_2CN^iBu_2)_2$: Te/$NaBH_4$	50	5	1.09	-	5.70

Band gap of bulk Te = 0.33 eV

3.4 Conclusions

ZnS, nanoparticles/thin films have been prepared at the water-toluene interface using sulphide produced from sulphur powder reduced with $NaBH_4$ and zinc diethyldithiocarbamate as zinc source. The ZnS prepared exhibited the cubic structure as confirmed by powder XRD. The characteristics of these nanoparticles/thin films prepared under these mild conditions compare favourably with other materials prepared by other methods under drastic conditions. However attempts to synthesize ZnSe and ZnTe using the same procedure resulted in the formation of t-Se and t-Te nanowires. The average crystallite sizes of the as-prepared nanoparticles at different temperatures, concentrations and deposition times ranged from 1.3 to 6.9 nm for ZnS, 2.0 to 7.1 nm for t-Se and 5.70 to 6.74 nm for t-Te. The dislocation densities ranged from 1.14 to 9.33 x 10^{17} lines/m for ZnS, 2.0 to 8.7 x 10^{17} lines/m for t-Se and 2.22 to 6.5 x 10^{17} lines/m for t-Te. The shape of the as-prepared nanoparticles at different temperatures was studied by SEM and gave morphologies from cubes to rods. The band gaps obtained for ZnS ranged from 3.6 to 3.88 eV, t-Se ranged from 2.86 to 3.91 eV and for t-Te from 1.09 to 1.17 eV. These show significant increases from the band gaps of the bulk materials.

3.5 References

Aquili, A. K. S., Ali, Z. & Maqsood, A. (2000). "Optical and structural properties of two-sourced evaporated ZnTe thin films," *Appl. Surf. Sci*., 167, 1-11.

Bellakhder, H., Outzourhit, A. & Ameziane, E. L. (2001). "Study of ZnTe thin films deposited by r.f. sputtering". *Thin Solid Films,* 382: 30-33.

Bose, D. N. & Bhunia, S. (1998). "Microwave synthesis, single crystal growth and characterization of ZnTe". *J. Cryst. Growth,* 186: 535-542.

Bozzini, B., Baker, M. A., Cavallotti, P. L., Cerri, E. & Lenardi, C. (2000). "Electrodeposition of ZnTe for Photovoltaic Cells". *Thin Solid Films,* 361-362; 388-395.

Brus, L. E. (1984). "The size dependence of the lowest excited electronic state". *J. Chem. Phys.,* 80: 4403-4409.

Catarina, A., Esteves, C. & Trinidale. T. (2002). "Synthetic studies on II/VI semiconductor quantum dots". *Curr. Opin. Solid State Mater. Sci.,* 6: 347-353.

Chin, P. T. K., Stouwdam, J. W. & Janssen, R. A. J. (2009). "Highly Luminescent Ultranarrow Mn-Doped ZnSe Nanowires". *NanoLett.* 9: 745-750.

Chu, C. C., Ng, T. B., Han, J., Hua, G. C., Gunshor, R. L., Ho, E., Warlick, E. L., Kolodziejski, L. A. & Nurmikko, A. V. (1996). "Reduction of structural defects in II-VI blue green laser diodes". *Appl. Phys. Lett.,* 69: 602-604.

Cozzoli, P. D., Manna, L., Curri, M. L., Kudera, S., Giannini, C., Striccoli, M. & Agostiano, A. (2005). "Shape and Phase Control of Colloidal ZnSe Nanocrystals". *Chem. Mater.,* 17: 1296-1306.

Dai, Q., Xiao, N., Ning, J., Li, C., Li, D., Zou, B., Yu, W. W., Kan, S., Chen, H., Liu B. & Zou, G. (2008). "Synthesis and mechanism of particle- and flower-shaped ZnSe nanocrystals". *J. Phys. Chem. C*, 112: 7567-7571.

Dai, S. Q., Xiao, N., Ning, J., Li, C., Li, D., Zou, B., Yu, W. W., Kan, S., Chen, H., Liu, B. & Zou, G. (2008). "Synthesis and mechanism of particle- and flower-shaped ZnSe nanocrystals: green chemical approaches toward green nanoproducts". *J. Phys. Chem. C*, 112: 7567-7571.

Davidson, W. L. (1948). "X-ray diffraction evidence for ZnS formation in zinc activated rubber vulcanizates". *Phys. Rev*., 74: 116-117.

Deutsch, T. F. (1973). "Absorption coefficient of infrared laser window materials". *J. Phys. Chem, Solids,* 34: 2091-2104.

Ding, J. X., Zapien, J. A., Chen, W. W., Lifshitz, Y. & Lee, S. T. (2004). "Room-temperature Single Nanoribbon Lasers". *Appl. Phys. Lett*. 85: 2361-2363.

Dong, A. G., Wang, F. D., Daulton, T. & Buhro, W. E. (2007). "Solution-liquid-solid (SLS) growth of ZnSe-ZnTe quantum wires having axial heterojunctions. *Nano Lett.* 7: 1308-1313.

Dryfe, R. A. W. (2006). "Modifying the liquid/liquid interface: pores, particles and deposition". *Phys. Chem. Chem. Phys.*, 16: 1869-1883.

Duan, H., Wang, D., Kurth, D. G. & Möhwald, H. (2004). "Directing self-assembly of nanoparticles at water/oil interfaces". *Angew. Chem., Int. Ed.,* 43: 5639-5642.

Erwin, S. C., Zu, L., Haftel, M. I., Efros, A. L., Kennedy, T. A. & Norris, D. J. (2005). "Doping Semiconductor Nanocrystals". *Nature*, 436: 91-94.

Fang X. & Zhang, L. (2006). "One-dimensional ZnS nanomaterials and nanostructures". *J. Mater. Sci. Technol*., 22: 721-736.

Fang, X.-S., Ye, C.-H., Zhang, L.-D., Wang, Y.-H. & Wu, Y.-C. (2005). "Temperature-Controlled Catalytic Growth of ZnS Nanostructures by the Evaporation of ZnS Nanopowders". *Adv. Funct. Mater.* 15: 63-68.

Fujita, S., Arai, S., Itoh, F. & Sokaguchi, T. (1975). "Electrical properties and injection luminescence in ZnSe-ZnTe heterojunctions prepared by liquid-phase epitaxy". *J. Appl. Phys*. 46: 3070-3075.

Gardner P. J. & Pang, P. (1988). "Thermodynamics of the zinc sulphide transformation, sphalerite → wurtzite, by modified entrainment". *J. Chem. Soc., Faraday Trans. 1*, 84: 1879-1887.

Gautam, U. K. & Rao, C. N. R. (2004). "Controlled synthesis of crystalline tellurium nanorods, nanowires, nanobelts and related structures by a self-seeding solution process". *J. Mater. Chem.*, 14: 2530-2535.

Gautam, U. K., Ghosh, M. & Rao, C. N. R. (2004). "Unipolar assembly of ZnO rods manifesting polarity-driven collective luminescence". *Langmuir,* 20: 10775-10778.

Gautam, U. K., Nath, M. & Rao, C. N. R. (2003). "New strategies for the synthesis of t-selenium nanorods and nanowires". *J. Mater. Chem*., 13: 2845-2847.

Gautam, U. K., Sardar, K., Deepak, F. L., Rao, C. N. R. (2005) "Soft chemical routes to semiconductor nanostructures". *Pramana- J. Phys*., 65(4): 549-564.

Gedanken, A. (2004). "Using sonochemistry for the fabrication of nanomaterials". *Ultrason Sonochem,* 11: 47-55.

Ghosh, S. C., Thanachayanont, C. & Dutta, J. (2004). "Studies on zinc sulphide nanoparticles for field emission devices". Proceedings of the First ECTI Annual Conference, Pattaya, Thailand, 145-148.

Ghosh, S. C., Thanachayanont, C. & Dutta, J. (2004). Studies on zinc sulphide nanoparticles for field emission devices, Proceedings of the First ECTI Annual Conference (ECTI-CON 2004), Pattaya, Thailand, 13-14: 145-148.

Green, M. & O'Brien, P. (1999). "Recent advances in the preparation of semiconductors as isolated nanometric particles: new routes to quantum dots". *Chem. Commun.,* 22: 2235-2241

Guinier, A. (1963). X-ray Diffraction in Crystals, Imperfect Crystals and Amorphous Bodies (Freeman, San Francisco, Calif., 1963), Chap. 2, 46.

Hines, M. A. & Guyot-Sionnest, P. (1998). "Bright UV-Blue Luminescent Colloidal ZnSe Nanocrystals". *J. Phys. Chem. B,* 10(2): 3655-3657.

Hu, J. S., Ren, L. L., Guo, Y. G., Liang, H. P., Cao, A. M., Wan, L. J., Bai, C. L. (2005). Mass production and high photocatalytic activity of ZnS nanoporous nanoparticles. *Angew. Chim. Inter. Edit.,* 44(8), 1269-1273.

Hu, J. S., Ren, L. L., Guo, Y.G., Liang, H. P., Cao, A. M., Wan, L. J., Bai, C. L. (2005). "Mass production and high photocatalytic activity of ZnS nanoporous nanoparticles". *Angew. Chem. Int. Ed*., 44(8): 1269-1273.

Huo, H. B., Dai, L., Xia, D. Y., Ran, G. Z., You, L. P., Zhang, B. R. & Qin, G. G. (2006). "Synthesis and optical properties of ZnTe single-crystalline nanowires". *J. Nanosci. Nanotechnol*. 6(4): 1182-1184

Janik, E., Sadowski, J., Dluzewski, P., Kret, S., Baczewski, L. T., Petroutchik, A., Lusakowska, E., Wrobel, J., Zaleszczyk, W., Karczewski, G., Wojtowicz, T. & Presz, A. (2006). "ZnTe nanowires grown on GaAs (100) substrates by molecular beam epitaxy". *Appl. Phys. Lett*. 89: 133-114.

Johnson, J. C., Yan, H. Q., Yang, P. D. & Saykally, R. J. (2003). "Optical Cavity Effects in ZnO Nanowire Lasers and Waveguides". *J. Phys. Chem. B*, 107: 8816-8828.

Kim, T. W., Lee, D. U., Cho, J., Lim, Y. S., Lee, J. Y. & Park, H. L. (1991). "Strain effects in $Cd_xZn_{1-x}Te$/ZnTe double quantum-wells". *J. Phys. Chem. Solids*, 60: 857-860.

Klayman D.L. & Griffin, T.S. (1973). "Reaction of selenium with sodium borohydride in protic solvents. A facile method for the introduction of selenium into organic molecule". *J. Am. Chem. Soc.* 95: 197-199.

Lan, C., Hong, K., Wang, W. & Wang, G. (2003). "Synthesis of ZnS nanorods by annealing precursors ZnS nanoparticles in NaCl flux". *Solid State Commun.* 125: 455-458.

Lan, C., Hong, K., Wang, W. & Wang, G. (2003). Synthesis of ZnS nanorods by annealing precursor ZnS nanoparticles in NaCl flux. *Solid State Commun.* 125: 455-458.

Lan, G-Y., Lin, Y. –W., Huang Y-F., Chang, H-T. (2007). "Synthesis and characterization of $Zn_xHg_{1-x}Se_yS_{1-y}$ quantum dots". *J. Mater. Chem.*, 17: 2661-2666.

Lee, D., Zucker, J. E., Johnson, A. M., Feldman, R. D., Austin & R. F. (1990). "High Quality ZnSe and ZnS Nanocrystals Formed by Activating Zinc Carboxylate Precursors". *Appl. Phys. Lett.* 57: 1132-1134.

Li, L. S., Pradhan, N., Wang, Y. & Peng, X., (2004). "High Quality ZnSe and ZnS Nanocrystals Formed by Activating Zinc Carboxylate Precursors". *Nano Lett.,* 4: 2261-2264.

Li, L., Yang, Y. M., Huang, X. H., Li, G. H. & Zhang, L. D. (2005). "Fabrication and electronic transport properties of Bi nanotube arrays". *J. Phys. Chem. B,* 109: 12394-12398.

Li, Y. D., Ding, Y. & Wang, Z. Y. (1999). A Novel Chemical Route to ZnTe Semiconductor Nanorods. *Adv. Mater*. 11(10): 847-850.

Lin, Y., Skaff, H., Emrick, T., Dinsmore, A. D. & Russell, T. P. (2003). "Nanoparticle assembly and transport at liquid-liquid interfaces". *Science,* 299: 226-229.

Lin, Z. H, Yang, Z. & Chang, H. T. (2008). "Preparation of Fluorescent Tellurium Nanowires at room temperature". *Cryst. Growth Des.* 8: 351-357.

Lu, B. S. W., Lee, I. & Wang, Z. L. (2001). "Synthesis and photoluminescence enhancement of Mn^{2+}doped ZnS nanocrystals". *J. Lumin.,* 92(1): 73-78.

Lu, S. W., Lee, B. I., Wang, Z. L., Tong, W., Wagner, B. K., Park, W. & Summers, C.J. (2001). "Synthesis and photoluminescence enhancement of Mn^{2+}-doped ZnS nanocrystals." *Journal of Luminescence,* 92(1-2): 73-78.

Masetti, E., Montecchi, M. & da Silva, M. P. (1993). "Analysis of the oxidation of polycrystalline zinc selenide by spectroscopic ellipsometry and photothermal deflection spectroscopy". *Thin solid Films,* 234(1-2): 557-560.

Mondal, A., Chaudhuri, S. & Pal, A. K. (1987). "Optical properties of ZnTe films". *Appl. Phys.* A. 43: 81-84.

Moore, D. & Wang, Z. L. (2006). "Growth of anisotropic one-dimensional ZnS nanostructures". *J. Mater. Chem.*, 16: 3898-3905.

More, D., Ding Y., Wang & Z. L. Wang, (2006). "Hierarchical Structured Nanohelices of ZnS". *Angew. Chem., Int. Ed.*, 45: 5150-5154.

Murray, C. B., Norris, D. J. & Bawendi, M. G., (1999). "Synthesis and characterization of nearly monodisperse CdE (E = sulphur, selenium, tellurium) semiconductor nanocrystallites". *J. Am. Chem Soc.*, 115: 8706-8715.

Nisho, M., Hayashida, H., Guo, Q. & Ogawa, H. (2001). "Effect of VI/II ratio upon photoluminescence properties of aluminium-doped ZnTe layers grown by MOVPE". *Appl. Surf. Sci.* 223: 169-170.

Norberg, N. S., Parks, G. L., Salley, G. M. & Gamelin, D. R. (2006). "Giant Excitonic Zeeman Splittings in Co^{2+}-doped ZnSe Quantum Dots". *J. Am. Chem. Soc.*, 128: 13195-13203.

Norris, D. J., Efros, A. L. & Erwin, S. C. (2008). "Doped Nanocrystals". *Science*, 31(9): 1776-1779.

Norris, D. J., Yao, N., Charnock, F. T. & Kennedy, T. A. (2001). "High-Quality Manganese-Doped ZnSe Nanocrystals". *Nano Lett.*,1: 3-7.

O'Brien P. & Nomura, P. (1995). "Single-molecule precursor chemistry for the deposition of chalcogenide (S or Se)-containing compound semiconductors by MOCVD and related methods of Metal Nanocrystals Formed at Aqueous-Organic Interfaces". *J. Phys. Chem. B*, 107: 7391-7399.

Panda, A. B., Acharya, S., Efrima, S. & Golan, Y. (2007). "Synthesis, Assembly and Optical Properties of Shape and Phase Controlled ZnSe Nanocrystals". *Langmuir,* 23: 765-770.

Platt, M., Dryfe, R. A. W. & Roberts, E. P. L. (2004). "Controlled deposition of nanoparticles at the liquid-liquid interface". *Electrochim. Acta,* 49: 3937-3945.

Pradhan N. & Peng, X. (2007). "Efficient and colour-tunable Mn-doped ZnSe nanocrystal emitters: control of optical performance via greener synthetic chemistry". *J. Am. Chem. Soc.,* 129: 3339-3347.

Pradhan, N., Battaglia, D. M., Liu, Y. & Peng, X. (2007). "Efficient, stable, small, and water-soluble doped ZnSe nanocrystal emitters as non-cadmium biomedical labels". *Nano Lett.* 7: 312-317.

Pradhan, N., Goorskey, D., Thessing, J. & Peng, X. (2005). "An Alternative of CdSe Nanocrystal Emitters: Pure and Tunable Impurity Emissions in ZnSe Nanocrystals". *J. Am. Chem. Soc.,* 127: 17586-17587.

Ramasamy, K., Nejo, A. O., Ziqubu, N., Rajasekhar, P. V. S. R., Nejo, A. A., Revaprasadu, N. & O'Brien, P. (2011). "A New Route to Lead Chalcogenide Nanocrystals". *Eur. J. Inorg. Chem.,* 33: 5196-5201.

Rao, C. N. R., Kulkarni, G. U., Agrawal, V. V., Gautam, U. K., Ghosh, M. & Tumkurkar, U. (2005). "Use of the Liquid-Liquid Interface for Generating Ultrathin Nanocrystalline Films of Metals, Chalcogenides, and Oxides". *J. Colloid Interface Sci.,* 289: 305-318.

Rao, C. N. R., Kulkarni, G. U., Thomas, P. J., Agrawal, V. V. & Saravanan, P. (2003). "Films of Metal Nanocrystals Formed at Aqueous-Organic Interfaces". *J. Phys. Chem. B,* 107: 7391-7395.

Reincke, F., Hickey, S. G., Kegel, W. K. & Vanmaekelbergh, D. (2004). "Highly Luminescent Water-Soluble CdTe Quantum Dots". *Angew. Chem., Int. Ed.* 43: 458-462.

Ruitao, L., Chuanbao, C., Yajun, G. & Hesun, Z. (2004). "Preparation of ZnS nanotubes via surfactant micelle-template inducing reaction". *J. Mater. Chem*, 39: 1575-1578.

Santangelo, S. A., Hinds, E. A., Vlaskin, V. A., Archer, P. I. & Gamelin, D. R. (2007). "Bimodal Bond-Length Distributions in Cobalt-Doped CdSe, ZnSe, and $Cd_{1-x}Zn_xSe$ Quantum Dots". *J. Am. Chem. Soc.*, 129: 3973-3978.

Schrier, J., Demchenko, D. O., Wang, L. W. & Alivisatos, A. P. (2007). "Optical properties of ZnO/ZnS and ZnO/ZnTe heterostructures for solar cell applications". *Nano Lett.* 7: 2377-2382.

Shen, H. B., Wang, H. Z., Li, X. M., Niu, J. Z., Wang, H., Chen, X., Li, L. S. (2009). "Phosphine-free synthesis of high quality ZnSe, ZnSe/ZnS, and Cu-, Mn-doped ZnSe nanocrystals". *Dalton Trans*. 47: 10534-10540.

Shen, H., Niu, J. Z., Wang, H., Li, X., Li, L. S. & Chen, X. (2010). "Size- and shape-controlled synthesis of ZnSe nanocrystals using SeO_2 as selenium precursor". *Dalton Trans*. 39: 11432-11438

Sreeprasad, T. S.; Samal, A. K.; Pradeep, T. (2009). "Tellurium Nanowire-Induced Room Temperature Conversion of Graphite Oxide to Leaf-like Graphenic Structures". *J. Phys. Chem. C*, 113: 1727-1737.

Stern A.E. & Kim K. (1981). "Thickness effect on the extended. X-ray absorption fine structure amplitude". *Phys. Rev.*, 23: 3781-3787.

Su, B., Fermin, D. J., Abid, J.-P., Eugster, N. & Girault, H. H. (2005). "Adsorption *and* Photoreactivity of CdSe Nanoparticles at Liquid-Liquid Interfaces". *J. Electroanal. Chem.,* 583: 241-247.

Tamarso, M. C. ed., (2002). II-VI Semiconductor Materials and their Applications, Taylor and Francis, New York.

Venkatachalam, S., Mangalaraj, D. & Narayandass, S. K. (2006). "Influence of substrate temperature on the structural, optical and electrical properties of zinc selenide (ZnSe) thin films". *J. Phys. D: Appl. Phys.*, 39: 4777-4782.

Wang, W., Germanenko, I. & El-Shell, M. S. (2002). "Room-temperature synthesis and characterization of nanocrystalline CdS, ZnS and $Cd_xZn_{1-x}S$". *Chem. Mater.,* 14: 3028-3033.

Warad, H. C., Ghosh, S. C., Hemtanon, B., Thanachayanont, C. & Dutta, J. (2005). Luminescent nanoparticles of Mn doped ZnS passivated with sodium hexametaphosphate. *Science and Technology of Advanced Materials*, 6: 296-301.

Wright, K. V., & J. D. Gale. 2004. "Interatomic potentials for the simulation of the zinc-blende and wurtzite forms of ZnS and CdS: Bulk structure, properties and phase stability". *Phys. Rev. B*, (70): 035211-1-035211-8.

Wu, Q., Litz, M. & Zhang, X. C. (1996). "Broadband detection capability of electro-optic field probes". *Appl. Phys. Lett*. 68, 2924-2926.

Xinhua, Z., Renguo, X., Ying, Z., Thomas, B. & Wolfgang, K. (2005). "High-Quality Violet-to Red-Emitting ZnSe/CdSe Core/Shell Nanocrystals". *Chem. Mater.,* 17: 4038-4042.

Yeh, C.Y., Lu, Z.W., Froyen, S. & Zunger, A. (1992). "Zinc blende wurtzite polytypism in semiconductors". *Phys. Rev. B,* 46: 10086-10097.

Yong, K., T., Sahoo, Y., Zeng, H., Swihart, M. T., Minter, J. R. & Prasad, P. N. (2007). Formation of ZnTe Nanowires by Oriented. Attachment. *Chem. Mater*. 19, 4108-4110.

Zhang, J., Chen, P. C., Shen, G. Z., He, J. B., Kumbhar, A., Zhou, C. W. & Fang, J. Y., (2008). "P-type field-effect transistors of single-crystal ZnTe nanobelts". *Angew. Chem. Int. Edn*., 47: 9469-9471.

Zingaro, R.A. and Cooper, W.C. (1974) "Selenium" Van Nostrand Reinhold, New York.

Ziqubu, N., Rasamy, K., Rajasekhar, P. V. S. R., Revaprasadu, N. & O'Brien. P. (2010). "Simple Route to Dots and Rods of PbTe Nanocrystals". *Chem Mater*., 22: 3817-3819.

Zu, L., Norris, D. J., Kennedy, K. T. A., Erwin, S. C. & Efros, A. L. (2006). "Impact of ripening on manganese-doped ZnSe nanocrystal". *Nano Lett.,* 6: 334-340.

CHAPTER FOUR

DEPOSITION OF CADMIUM CHALCOGENIDE NANOMATERIALS AT THE WATER-TOLUENE INTERFACE

This chapter describes the syntheses of Cadmium chalcogenide nanoparticles. The work was carried out at the School of Chemistry, and characterization of nanomaterials by XRD and SEM was performed in the School of Materials Science, The University of Manchester, UK.

Deposition of cadmium chalcogenide nanomaterials at the water/toluene interface

Abstract

Nanostructured thin films of CdE (E=S, Se,) have been prepared at the water-toluene interface by reacting toluene solutions of alkyidithiocarbamates/ cupferronates with aqueous chalcogenide ions obtained by the borohydride reduction of sulphur and selenium powder. The thin film deposits were characterized by powder X-ray crystallography, scanning electron microscopy and absorption spectroscopy. The influence of deposition conditions such as precursor concentrations, temperature as well as deposition times were studied. The reaction of toluene solution of cadmium cupferronate with aqueous solution of NaHS obtained by the borohydride reduction of sulphur powder yielded both cubic and hexagonal CdS nanomaterial at the water-toluene interface as shown by the X-ray diffraction measurements. The crystallite sizes obtained using Debye-Scherrer formula gave particle sizes ranging from 0.9 to 7.1 nm with dislocation densities ranging between 1.89 to 110 x 10^{17} lines/m for cubic CdS and 0.94 to 7.3 nm with dislocation densities ranging between 1.87 to 112.93 x 10^{17} lines/m for hexagonal CdS. The reaction of toluene solution of cadmium cupferronate with aqueous solution of NaHSe yielded hexagonal CdSe nanomaterial at the water-toluene interface. Calculation employing the Debye-Scherrer formula gave particle sizes ranging from 5.86 to 6.40 nm with dislocation densities ranging between 2.13 to 4.223 x 10^{17} lines/m. The band gaps obtained for CdS ranged from 3.69 to 3.98 eV, CdSe ranged from 3.7 to 4.05 eV.

4.1 Introduction

Colloidal chemistry approaches to the synthesis of nanocrystals of different II-VI and III-V semiconductor materials with narrow particle size distributions, high crystallinity, and size-dependent optical properties have been developed (Murray *et al*., 1993; Bowen Katari, 1994;

Vossmeyer *et al*., 1994; Rogach *et al*., 1996; Guzelian *et al*., 1996; Micic *et al*., 1997; Peng and Peng, 2001; Talapin *et al*., 2001, 2001).

Owing to the quantum confinement effect, semiconductor nanocrystals, especially the II–VI semiconductor nanocrystals, exhibit remarkable size-dependent optical properties (Alivisatos, 1996) which have attracted a great deal of attention in recent years for both fundamental research and technical applications such as light-emitting diodes (LED) (Colvin *et al*., 1994; Coe *et al*., 2002; Schlamp *et al*., 1997), solar cells (Huynh *et al*., 1999; 2002), lasers (Klimov *et al*., 2000) and biological markers (Bruchez *et al*.,1998; Chan and Nie, 1998; Zhang *et al*., 2003). In the past two decades, considerable effort has been made to synthesize high-quality semiconductor nanocrystals. Among the methods employed for synthesizing dot-shaped semiconductor nanocrystals, the organometallic approach (Murray *et al*., 1993; Peng, *et al*., 1998; Talapin *et al*., 2001) and its variations (Peng *et al*., 2002; Qu *et al*., 2001; Yu, *et al*., 2002; 2003) have proved the most popular, though other methods have also been very successful (Zhang *et al*., 2003; Vossmeyer *et al*., 1994; Cumberland *et al*., 2002; Talapin *et al*., 2002). For any applications based on the optical properties of nanocrystals, it is essential to use high quality nanocrystals. In principle, high quality nanocrystals should possess at least two characteristics, high emission colour purity and high photoluminescence quantum yield (PLQY). The colour purity of the emission is strongly dependent on the size distribution of the nanocrystals. The narrower the size distribution, the purer the colour of the emission light, which can be reflected by the narrow photoluminescence (PL) emission bandwidth and/or the narrow UV/Vis band-edge absorption bandwidth. The PLQY is very sensitive to the surface environment of the nanocrystals, and can be dramatically reduced by surface trap states (Qu and Peng, 2002). These surface trap states result from the dangling bonds and/or stacking faults of some of the surface atoms (Zhang *et al*., 2003; Qu and Peng, 2002; Doneg *et al*., 2002). Surface passivation with

suitable organic or inorganic materials and an increase of the crystallinity can effectively remove the surface trap states, and lead to a significant increase in the quantum yield.

Among the II–VI semiconductor nanocrystals, CdSe nanocrystals have been most extensively investigated, and their size and size distribution can be controlled, whereas relatively little work has been done on CdS nanocrystals. Recently, high quality CdS nanocrystals with a controllable size and a narrow size distribution were prepared successfully in a noncoordinating solvent (Yu *et al*., 2002). It was believed that maintaining a good balance between nucleation and growth by tuning the activities of the precursors was the key to this success. More recently, Pan *et al*. developed a two-phase approach to successfully synthesize highly luminescent and nearly monodisperse CdS nanocrystals (Pan *et al*., 2004). The reaction was carried out under mild conditions (at below 100 ^{o}C) with less toxic reagents than employed traditionally. The possible mechanism was based on slow nucleation and slow growth, which is definitely different from a mechanism based on fast nucleation and slow growth as reported previously. In fact, the two-phase approach, in which the reaction occurs at the interface of two liquid phases, was first applied to the synthesis of gold nanocrystals by Brust *et al* in 1994. Based on the work by Pan *et al*., (2004) a new two-phase approach to synthesize high quality CdS nanocrysals in an autoclave was developed. Compared with the earlier results, the CdS nanocrystals obtained by the new approach exhibited a narrower size distribution and a higher PLQY. Moreover, through a seeding-growth technique, tunable size CdS nanocrystals were obtained with PL peaks with a quite similar full width at half-maximum (FWHM = 18–22 nm) to those of the initial nanocrystal seed s throughout the whole controllable size range. In this study, cadmium myristate (CdM_2) and thiourea were used as cadmium source and sulphur source, respectively, and oleic acid (OA) was used as a ligand for stabilizing the nanocrystals. It was found that the resulting nanocrystals, without any size sorting, appeared to be comparable with the CdS nanocrystals reported previously.

CdSe nanocrystals have been synthesized in a trioctylphosphine oxide-trioctylphosphine (TOPO-TOP) (Murray *et al*., 1993; Bowen Katari *et al*., 1994) or hexadecylamine (HDA)-TOPO-TOP mixture (Talapin *et al*., 2001), and fractions of nanocrystals with narrow (~4 %) size distributions were carefully separated by a size-selective precipitation technique (Murray *et al*., 1993; Bowen Katari *et al*., 1994) and redissolved in toluene. In this chapter, the synthesis of CdS and CdSe nanomaterial/thin films at water-toluene interface at temperatures below 100 ^{o}C by the use of cadmium dialkylyldithiocarbamate/cupferronate ($Cd(dtc)_2$/$Cd(cup)_2$) as cadmium source and the borohydride reduction of Sulphur/Selenium/Tellurium as sulphide/selenide/telluride sources are reported.

4.2 Deposition of cadmium chalcogenide thin film nanomaterials

Briefly 30 ml of degassed water containing 0.1 mmol of NaHE (E= S, Se, Te) was transferred into a 100 ml beaker. 30 ml of toluene containing the 0.1mmol of the cadmium dialkyldithiocarbamate/cupferronate precursor was layered on top of the solution in the beaker. The reaction vessel was placed in an oven preheated to the desired temperature for 4 hours. The deposits formed at the interface were isolated by gently lifting the film from the interface onto glass substrates. The reaction was repeated by varying the reaction conditions such as temperature, time and the reacting species (details of the deposition are given in chapter 6 section 6.4). The reactions were carried out in a 100 ml beaker with the height of the liquid column at 4 cm.

4.3 Results and discussions

4.3.1 Cadmium sulphide

4.3.1.1 Structural characterization and morphology

The reaction of Cadmium cupferronate with aqueous solution of NaHS obtained by the borohydride reduction of sulphur powder at 50 ºC for 5 hours yielded cubic and hexagonal CdS nanomaterial at the water-toluene interface as shown by the X-ray diffraction measurements. Figure 4.1 show the XRD pattern of CdS film with reflections at 26.5º, 43.8º and 52.3º corresponding to 111, 220 and 311 respectively of the cubic CdS (ICDD 01-080-0021, cell constant a=5.618 Å) and reflections 25.37º , 41.26º and 49.0º corresponding to 002, 110 and 200 respectively of hexagonal CdS (ICDD 01-075-1545). The peak broadening at lower angle is more meaningful for the calculation of particle size therefore size of the nanocrystals has been calculated using Debye-Scherrer formula (Guinier, 1963) using (111), (220) and (311) reflections from the XRD pattern for the cubic CdS and (002), (110) and (200) reflections for the hexagonal CdS. The calculation gave particle sizes ranging from 0.9 to 7.1 nm with dislocation densities ranging between 1.89 to 110 x 10^{17} lines/m for cubic CdS and 0.94 to 7.3 nm with dislocation densities ranging between 1.87 to 112.93 x 10^{17} lines/m for hexagonal CdS.

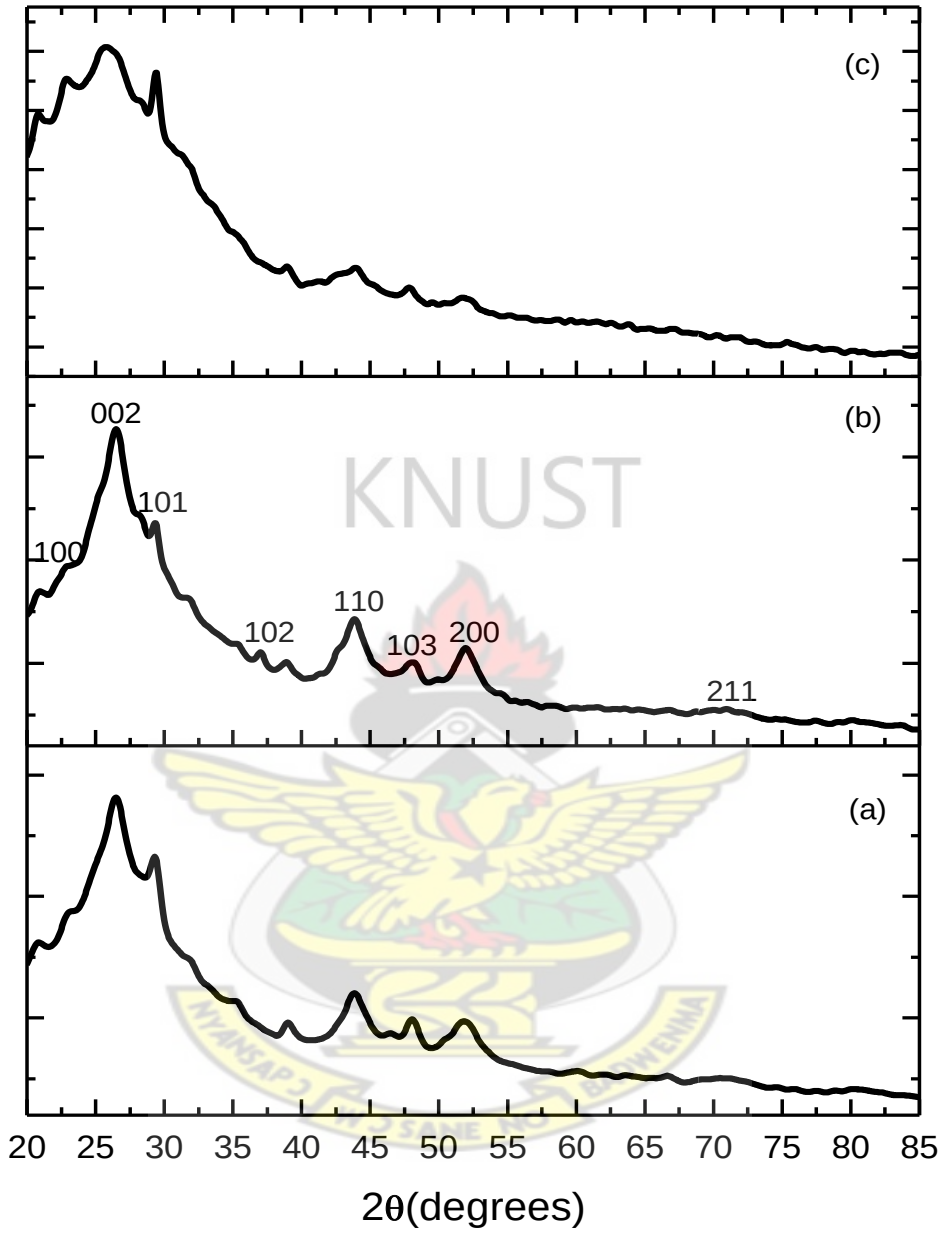

Figure 4.1: XRD of different as-prepared CdS samples (a) for 4 hours, (b) for 5 hours and (c) for 6 hours at 70 ^{o}C.

The SEM image of CdS nanomaterial formed at the water-toluene interface by reacting 30 ml of toluene solution of 0.1 mM copper cupferronate and 30 ml of 0.1 mM NaHS at 50 ^{o}C for 5 hours is shown in Figure 4.2.

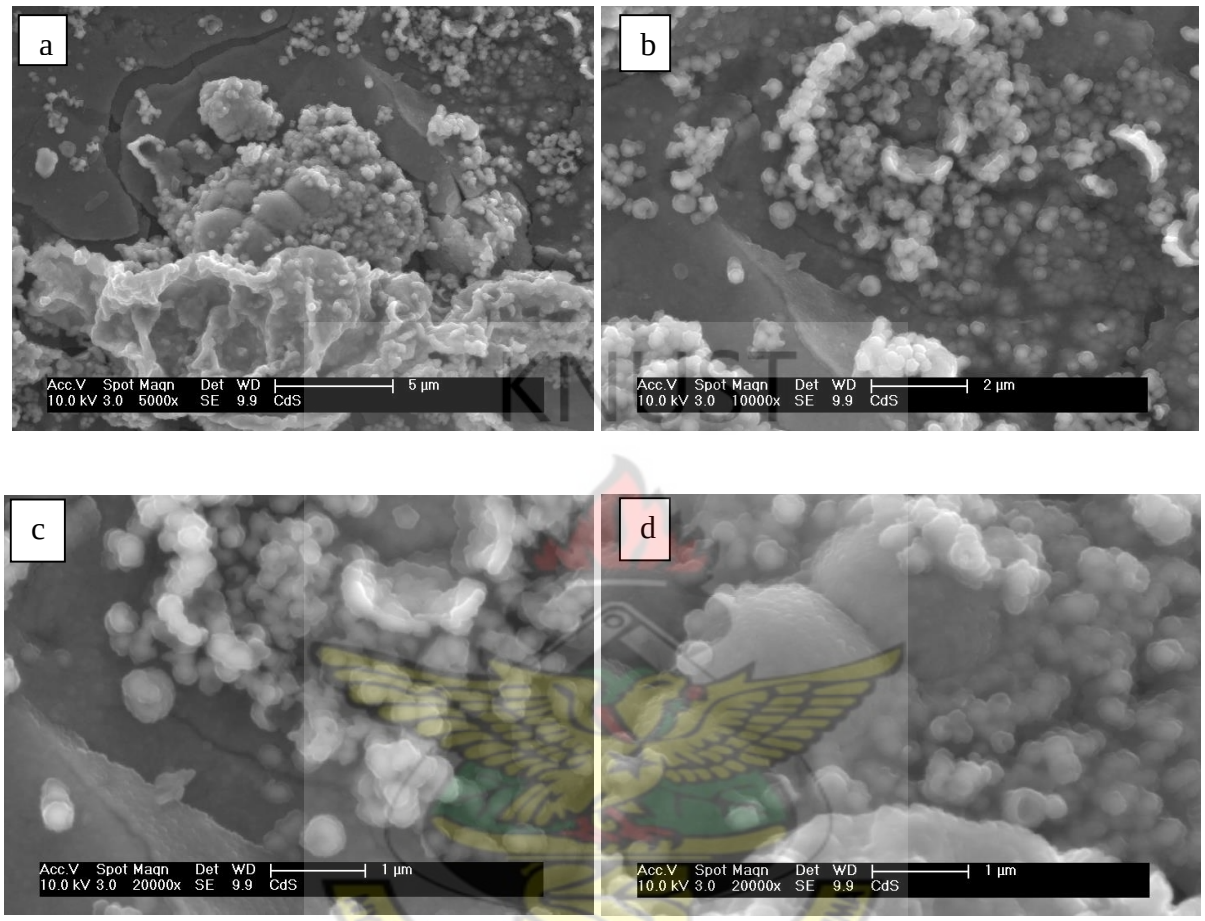

Figure 4.2: SEM image of CdS nanomaterial formed at the water-toluene interface by reacting 30 ml of toluene solution of 0.1 mM copper cupferronate and 30 ml of 0.1 mM NaHS at 50 ^{o}C for 5 hours at different magnifications (a-5000x, b-10000x, c-20000x and d-20000x).

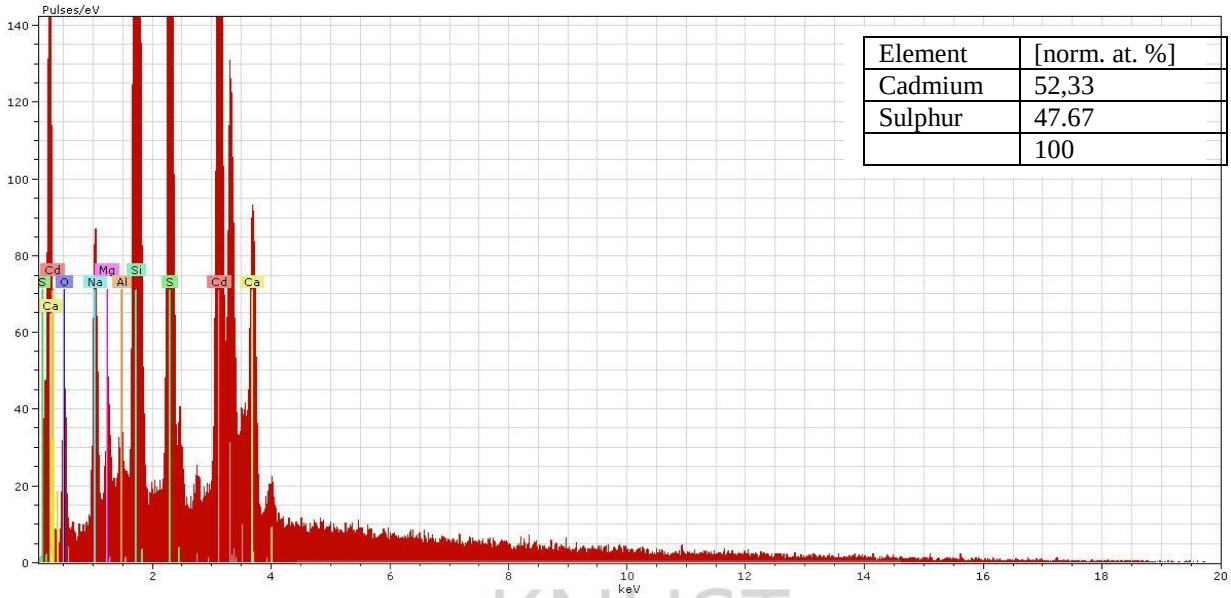

Element	[norm. at. %]
Cadmium	52,33
Sulphur	47.67
	100

Figure 4.3: EDAX image of CdS nanomaterial formed at the water-toluene interface by reacting 30 ml of toluene solution of 0.1 mM copper cupferronate and 30 ml of 0.1 mM NaHS at 50 ^{o}C for 5 hours

The Scanning electron microscopy (SEM) images of CdS nanomaterials/thin films formed at the water-toluene interface by reacting 30 ml of toluene solution of 0.1mM cadmium cupferronate and 30 ml of 0.56 mM NaHS for 5 hours at 50 ^{o}C are shown in Figure 4.2. The microstructure consisted of jagged platelets with long dimension around 1 μm and thickness around 10 nm. The platelets stack to form five to six layer tall stacks that extend across the entire area of the interface. The surface of the platelets seems rough. The energy dispersive X-ray analysis (EDAX) spectra shown in Figure 4.3 indicates the elemental composition of the nanomaterial/thin film formed at 50 ^{o}C for 5 hours in addition to those of the glass substrate respectively. Quantitative EDAX analysis of CdS nanomaterial formed at water-toluene interface also indicate that the CdS formed at 50 ^{o}C for 5 hours show slightly Cadmium rich (4.66%) in comparism with sulphur.

4.3.1.2 Optical analyses

The optical absorption spectra of the nanocrystals were measured using CARY 5000 UV-Vis-NIR spectrophotometer. The optical absorption spectra have been measured at room temperature over a range of 250 to 600 nm.

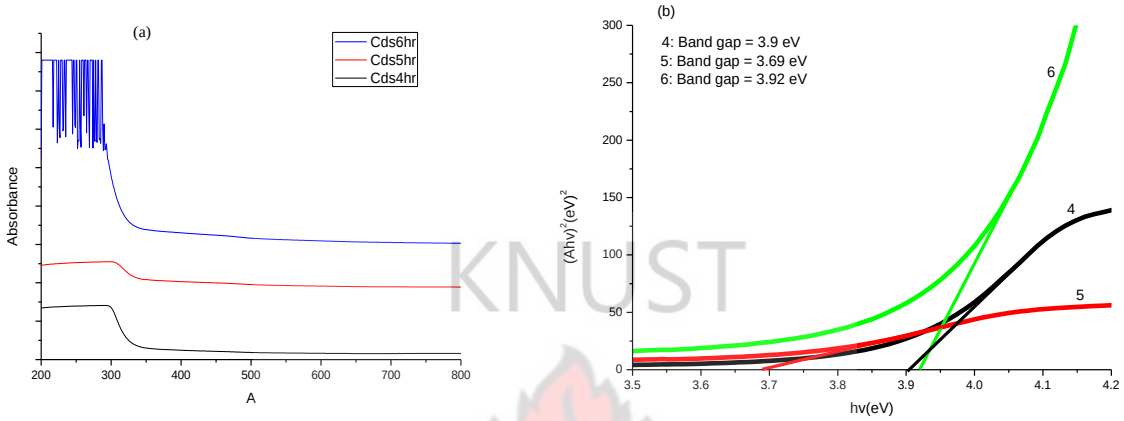

Figure 4.4: (a) Optical absorption spectra and (b) optical band gap of the as-prepared CdS samples for 4, 5 and 6 hours at 50 ^{o}C

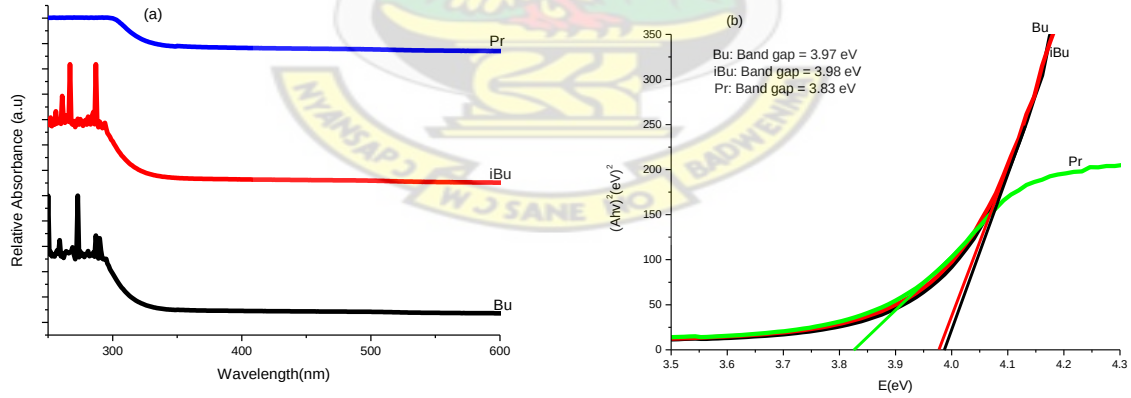

Figure 4.5: (a) Optical absorption spectra and (b) optical band gap of the as-prepared CdS samples using different chain lengths of the alkyl group (Et = ethyl; Bu – butyl; ^{i}Bu = isobutyl) for 6 hours at 70 ^{o}C.

The fundamental absorption corresponds to the electron excitation from the valence band to the conduction band and can be used to determine the optical band gap. The relationship between the absorbance (A) and the incident photon energy (hυ) is given by the Stern relationship of near-edge absorption (Stern and Kim, 1981):

$$A = [k(h\upsilon - E_g)]^{1/n}/h\upsilon$$

Where υ is the frequency, h is the constant, k is a constant and carries a value of either 1 or 4. The value of n is 1 for direct transition and 4 for indirect transition respectively. The optical band gap is determined by a plot of $(Ah\upsilon)^{2/n}$ as a function of hυ extrapolation of the line to the hυ axis where $(Ah\upsilon)^{2/n}$ is zero gives the band gap E_g. The plots of $(Ah\upsilon)^2$ versus hυ is a straight line indicating that CdS is a direct band gap material. The plots of $(Ah\upsilon)^2$ versus hυ for the different nanocrystallites obtained at 50 ^oC are given in the Figures 5.4b and 5.5b.

Generally, this wavelength of the maximum exciton absorption decreases as the particle size decreases as a result of quantum confinement of the photogenerated electron-hole pairs. The grain size of semiconductor particles can be determined using Brus equation (Brus, 1984) where E is the onset of absorption of the sample, E_g is the bulk band gap, R is the radius of the particle, m_e and m_h are the reduced masses of the conduction band electron and valence band hole in units of the electron mass, ε_0 is the vacuum permittivity and ε_{Ry} is the high-frequency dielectric constant. Estimation of particle size of the present CdS sample, using a value of 2.4 eV for E_g gave a values ranging from 2.48 to 2.82 nm. This is more than twice the value of the grain size obtained by XRD technique. It has been shown by a number of experimental studies that the equation for E cannot be expected to be quantitatively correct for very small particles.

Table 4.1 Optical parameters and crystallite sizes of the CdS nanoparticles

Precursors	Deposition Temperature/ ^{o}C	deposition time (hrs)	Band gap of nanoparticle (eV)	Particle size (nm)	
				UV	XRD
$Cd(Cup)_2$: $S/NaBH_4$	70	4	3.97	2.49	7.3
		5	3.69	2.82	3.9
		6	3.92	2.54	4.5
$Cd(S_2CNBu_2)_2$: $S/NaBH_4$	50	6	3.97	2.49	-
$Cd(S_2CN^{i}Bu_2)_2$: $S/NaBH_4$	50	6	3.98	2.48	-
$Cd(S_2CNPr_2)_2$: $S/NaBH_4$	50	6	3.83	2.64	-

Band gap of bulk CdS =2.42[a]/2.51[b] eV [a]Cubic; [b]Hexagonal,

4.3.2 Cadmium selenide

4.3.2.1 Structural characterization and morphology

The reaction of toluene solution of Cadmium cupferronate with aqueous solution of NaHSe for 4, 5 and 6 hours at room temperature, 50 ^{o}C and 70 ^{o}C yielded hexagonal CdSe nanomaterial at the water-toluene interface as shown by the X-ray diffraction measurements. Figures 5.6-5.8 show the XRD pattern of CdSe film with 23.5^{o}, 27.0^{o} and 48.8^{o} reflections corresponding to (100), (101) and (200) respectively of the hexagonal CdSe (ICDD 01-077-2307, cell constant a= b= 4.299 Å, c= 7.010 Å). The peak broadening at lower angle is more meaningful for the calculation of particle size therefore size of the nanocrystals has been calculated using Debye-Scherrer formula (Guinier, 1963) using (100), (002), (101) and (200) reflections from the XRD pattern. The calculation gave particle sizes ranging from 5.86 to 6.40 nm with dislocation densities ranging between 2.1295 to 4.2213 x 10^{17} lines/m (Table 4.5). Figure 4.9 and Table 4.4

show the XRD diffractogram and structural parameters respectively when selenosulphate was used as the seleniding source.

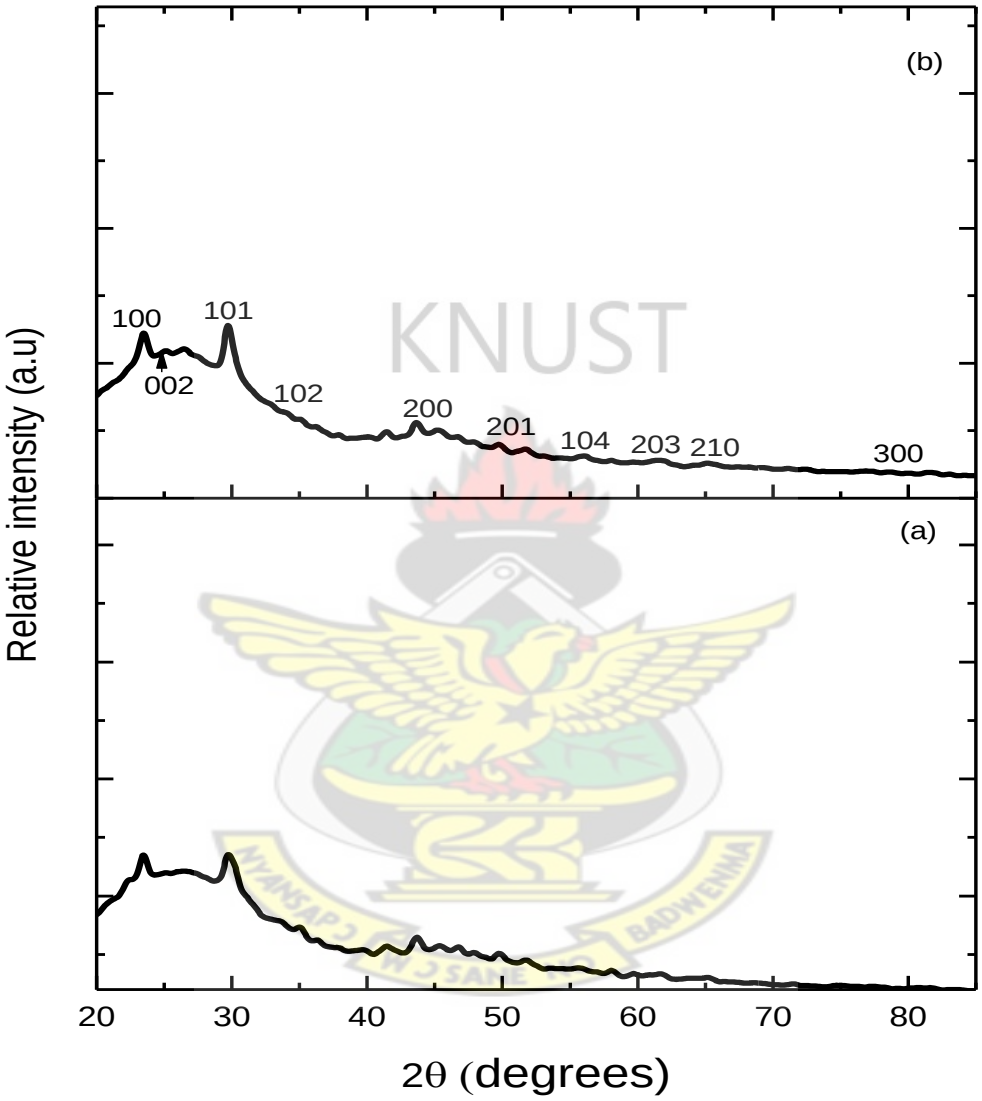

Figure 4.6: XRD of different as-prepared CdSe samples (a) for 4 hrs and (b) for 5 hours at room temperature using cadmium cupferronate precursors.

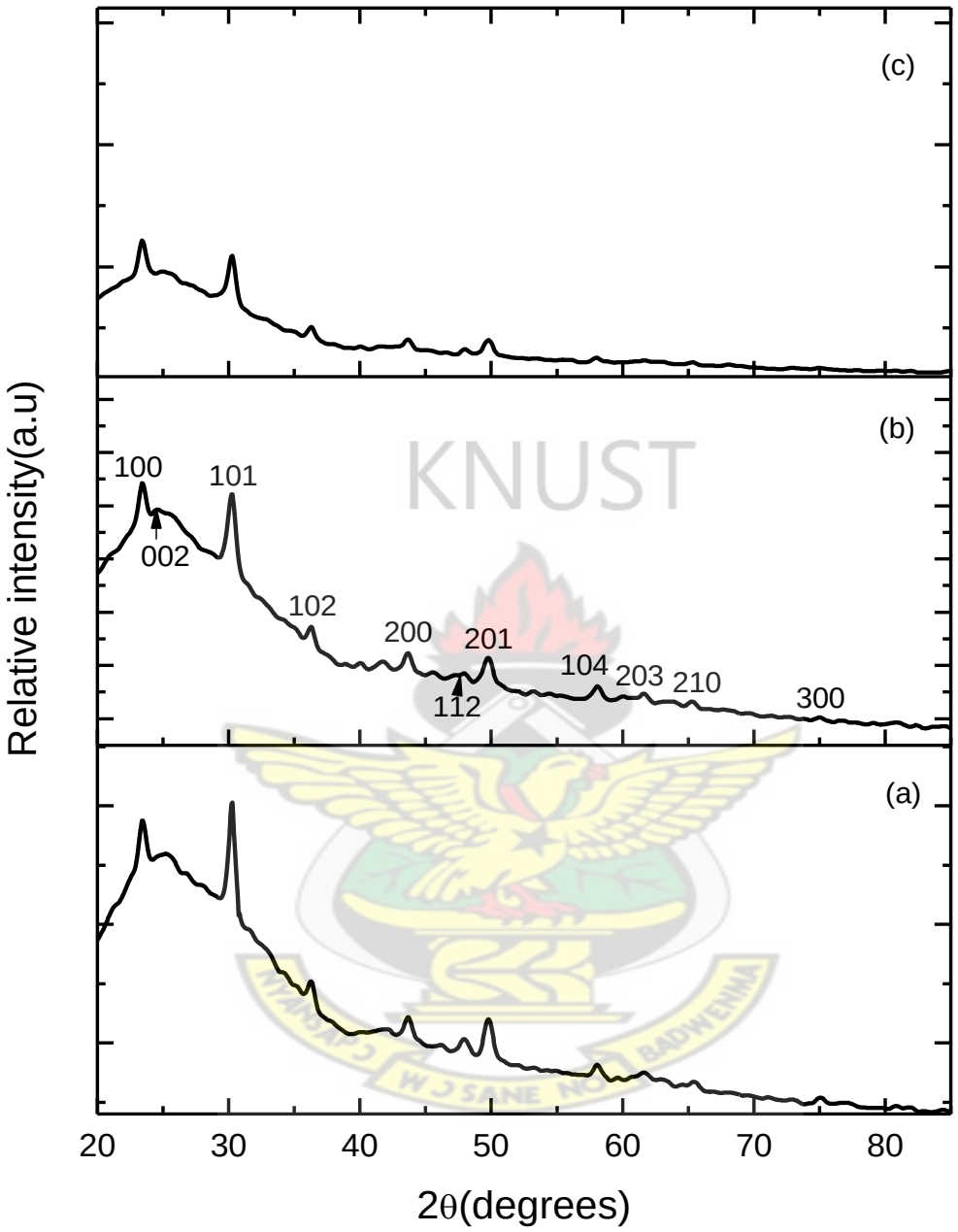

Figure 4.7: XRD of different as-prepared CdSe samples (a) for 4 hours, (b) for 5 hours and (c) for 6 hours at 50 ^{o}C using cadmium cupferronate precursors.

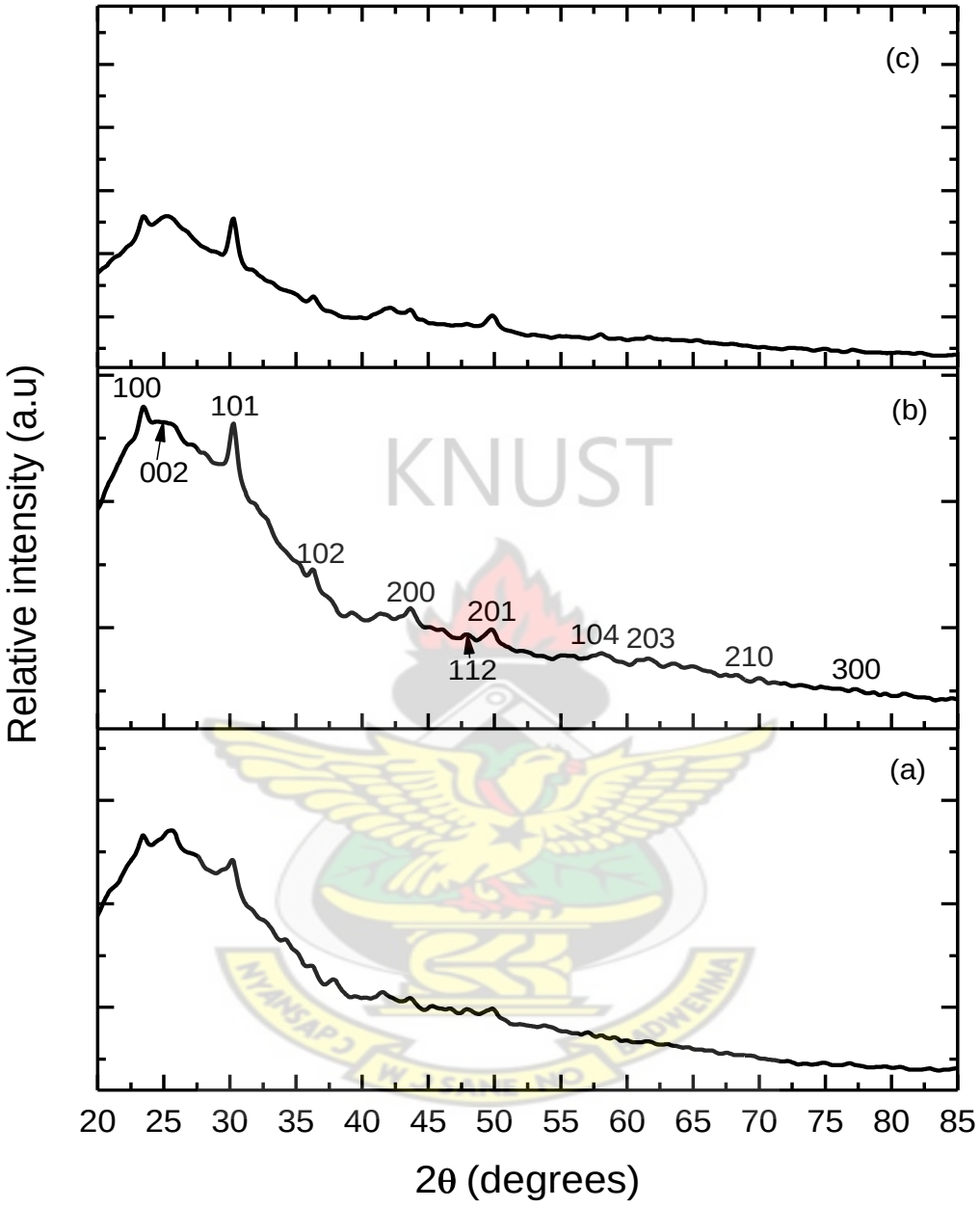

Figure 4.8: XRD of different as-prepared CdSe samples (a) for 4 hours, (b) for 5 hours and (c) for 6 hours at 70 ^{o}C using cadmium cupferronate precursors.

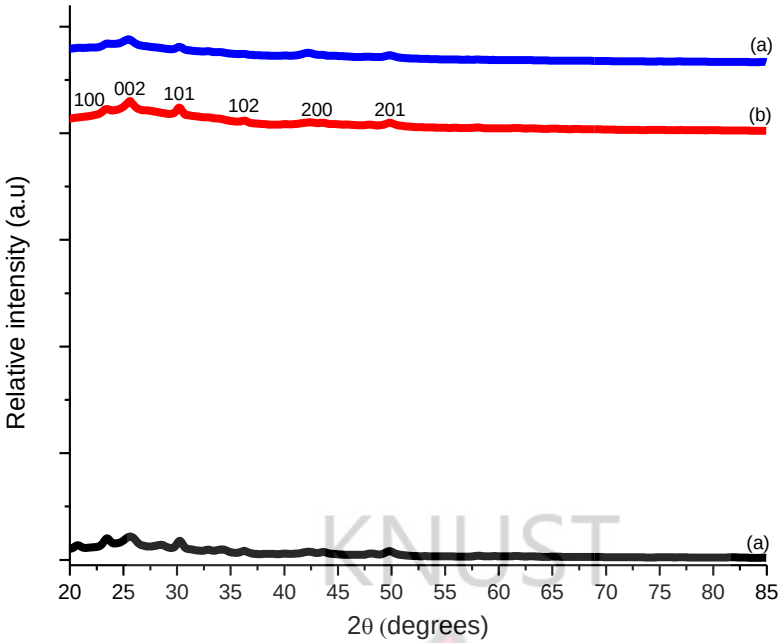

Figure 4.9: XRD of different as-prepared CdSe samples (a) for 8 hours, (b) for 10 hours and (c) for 12 hours at 50 ºC using selenosulphate as the seleniding source.

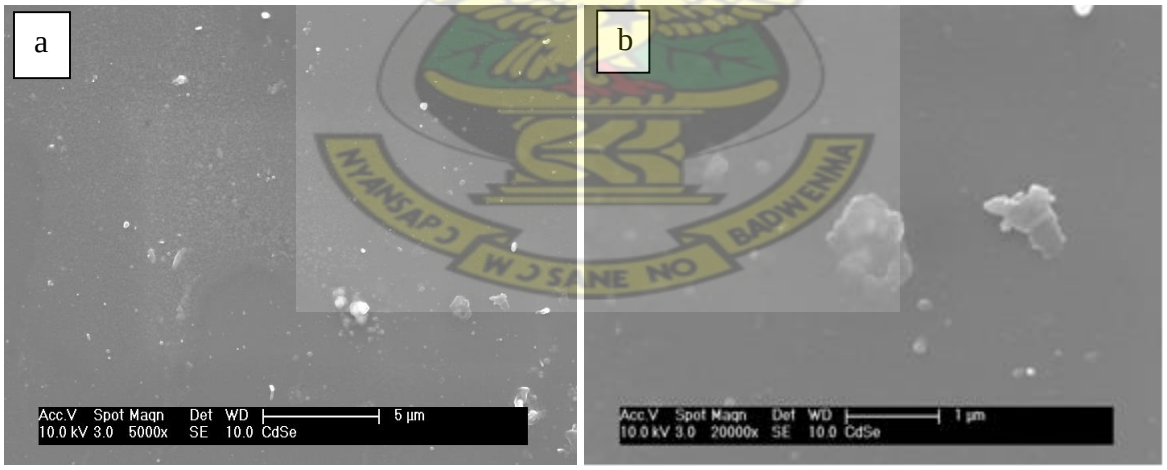

Figure 4.10: Scanning electron microscopy (SEM) image of CdSe nanomaterial formed at the water-toluene interface by reacting 30 ml of toluene solution of 0.1 mM Cadmium cupferronate and 30 ml of 0.1 mM NaHSe at 50 ºC for 5 hours at different magnifications (a-5000x and b-20000x).

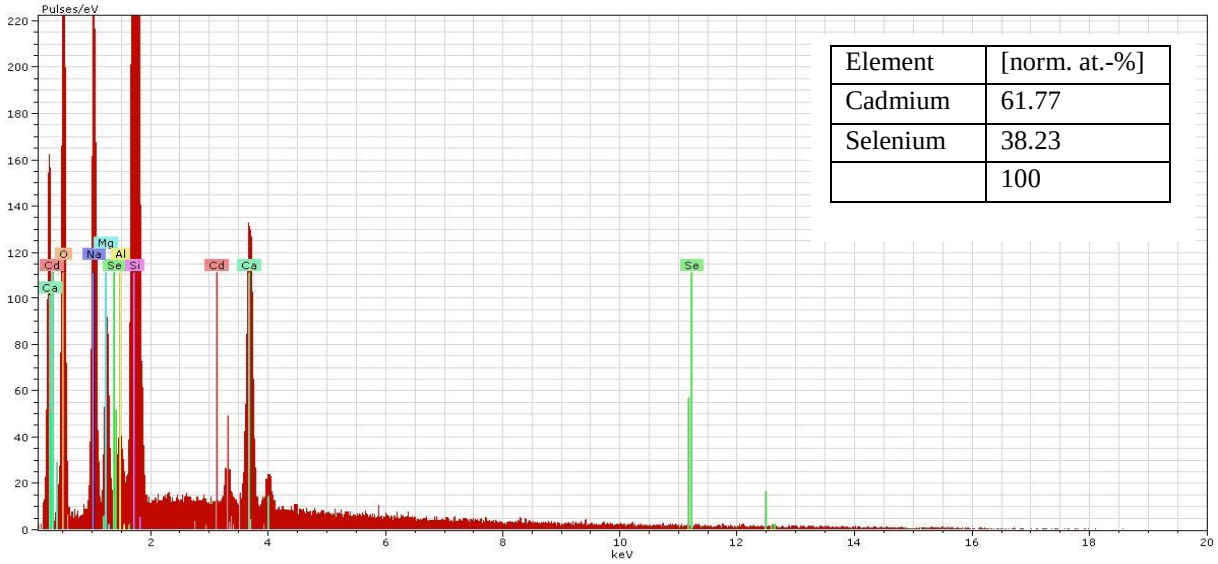

Figure 4.11: EDAX mapping of CdSe nanomaterial formed at the water-toluene interface by reacting 30 ml of toluene solution of 0.1 mM Cadmium cupferronate and 30 ml of 0.1 mM NaHSe.

The Scanning electron microscopy (SEM) images of CdSe thin film nanoparticles formed at the water-toluene interface by reacting toluene solution of Cadmium Cupferronate and aqueous solution of NaHSe obtained by the borohydride reduction of selenium powder for 5 hours at 50 ^{o}C is shown in Figure 4.10.

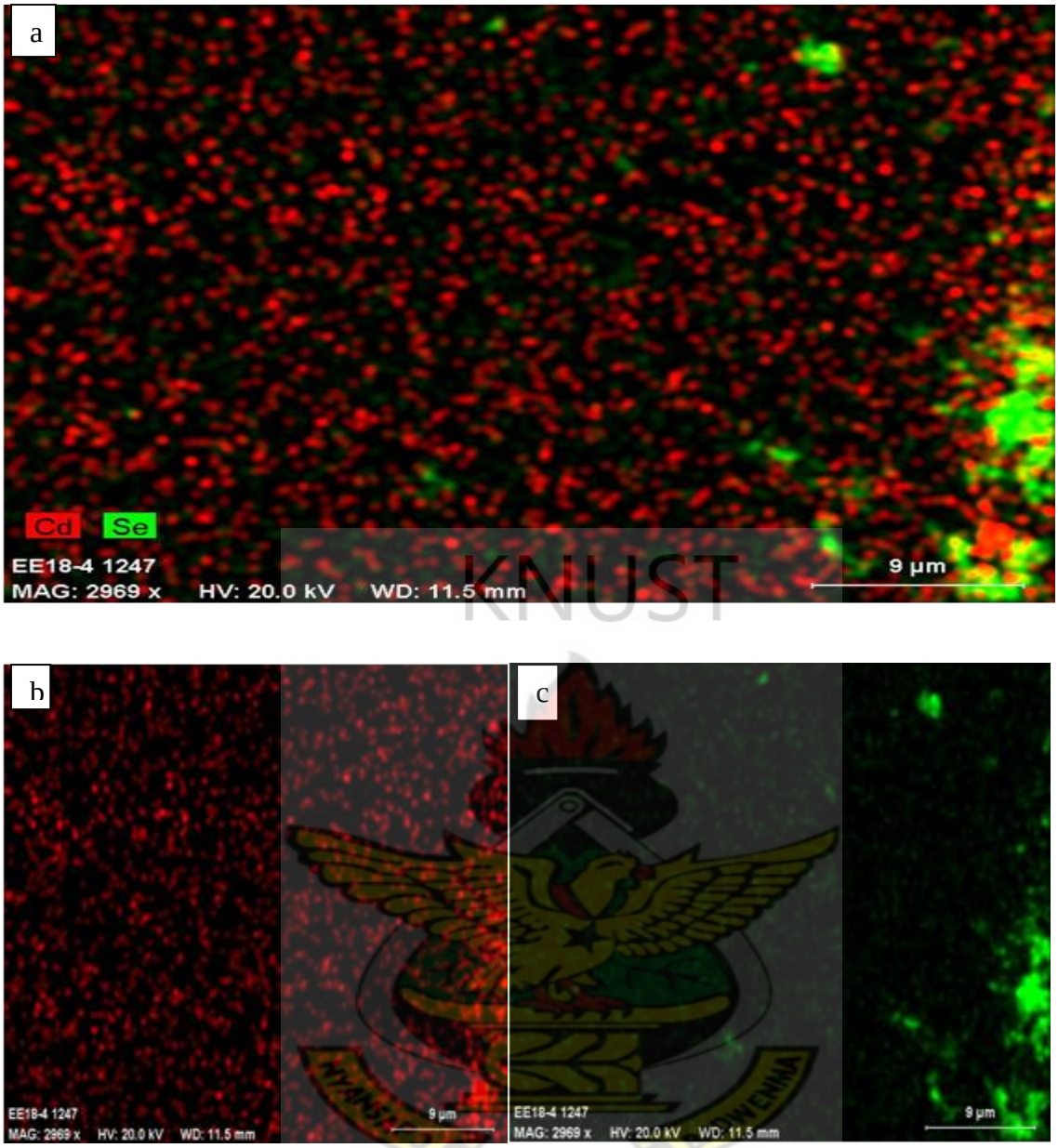

Figure 4.12: EDAX mapping of CdSe nanomaterial formed at the water-toluene interface by reacting 30 ml of toluene solution of 0.1 mM Cadmium cupferronate and 30 ml of 0.1 mM NaHSe at 50 ^{o}C for 5 hours: (a) shows distribution of Cd and Se, (b) shows Cd distribution and (c) shows Se distribution.

These images show the formation of some hexagonal structures. The energy dispersive X-ray analysis (EDAX) spectra shown in Figure 4.11 indicate the elemental composition of the

nanomaterial/thin film formed at 50 ^{o}C for 5 hours at water-toluene interface. The EDAX mapping is given in Figure 4.12.

4.3.2.2 Optical analyses

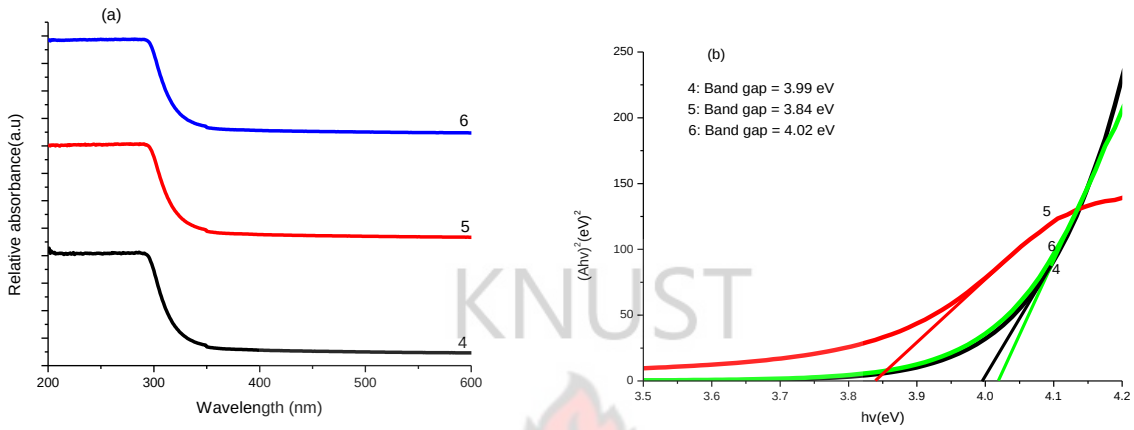

Figure 4.13: (a) Optical absorption spectra and (b) optical band gap of the as-prepared CdSe samples for 4, 5 and 6 hours at 50 ^{o}C.

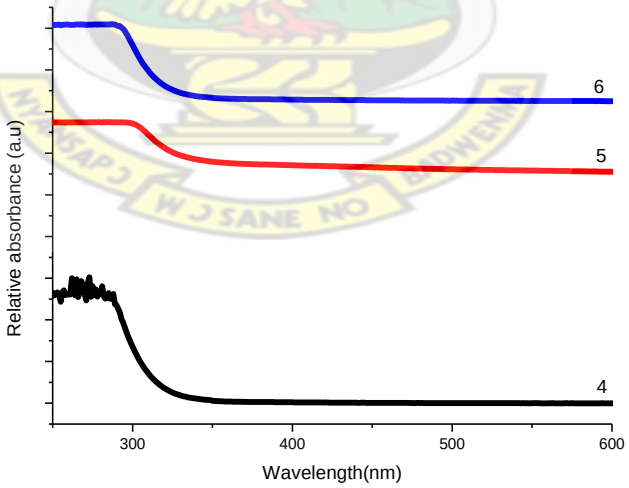

Figure 4.14: Absorption spectra of different as-prepared CdSe samples for 4 hours, for 5 hours and for 6 hours at 70 ^{o}C.

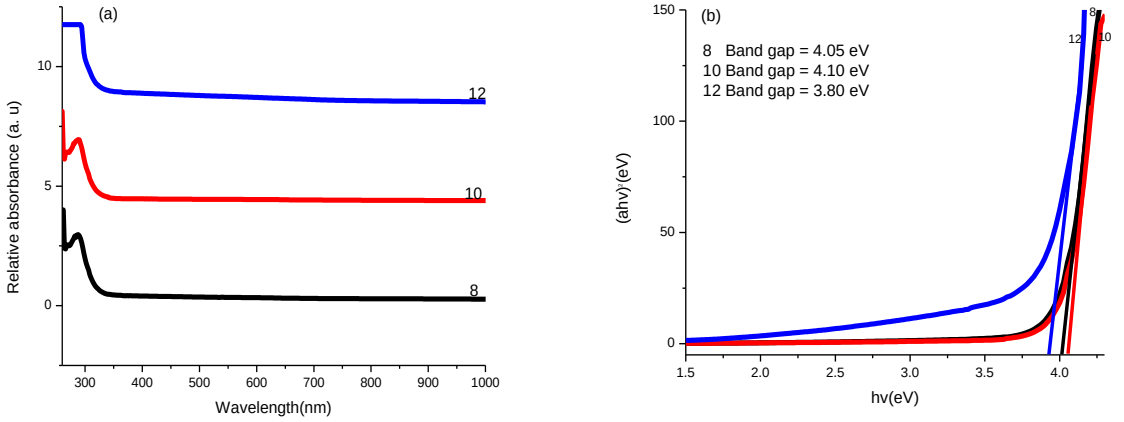

Figure 4.15: (a) Optical absorption spectra and (b) optical band gap of the as-prepared CdSe samples using sodium selenosulphate as selenide ion source for 8, 10 and 12 hours at 50 ^{o}C.

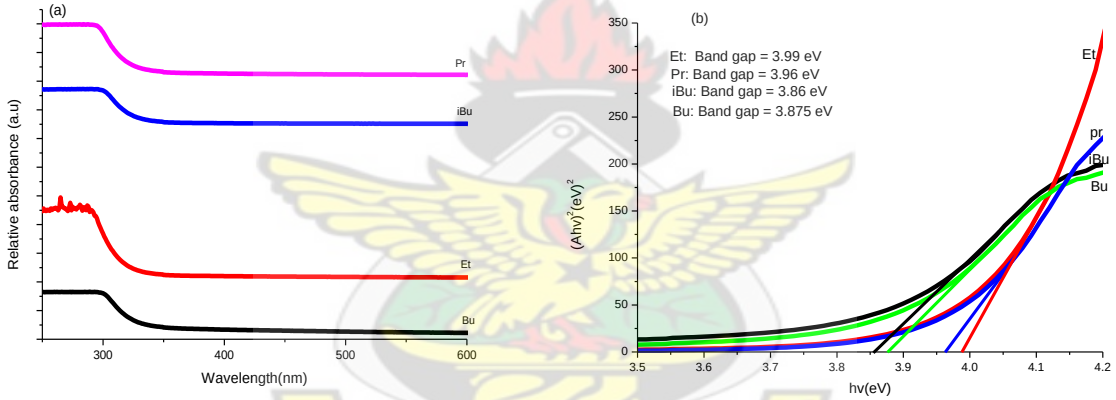

Figure 4.16: (a) Optical absorption spectra and (b) optical band gap of the as-prepared CdSe samples using different chain lengths of the alkyl group in the Cadmium dithiocarbamate precursor for 6 hours at 50 ^{o}C. (Et=ethyl; Pr = propyl; Bu = butyl; ^{i}Bu = isobutyl.

The optical absorption spectra have been measured at room temperature over a range of 250 to 600 nm using CARY 5000 UV-Vis-NIR spectrophotometer. The fundamental absorption corresponds to the electron excitation from the valence band to the conduction band and can be used to determine the optical band gap. The plots of $(Ah\upsilon)^2$ versus $h\upsilon$ for the different nanocrystallites obtained at 50 ^{o}C are given in the Figures 4.13 - 4.15. The grain size was also

estimated using a method proposed by Sarma and Sapra (2004). This method is based on high level theoretical calculations yield accurate estimates of size dependent shifts in band gap. Accordingly, the increase in band gap (ΔE_g) is given by:

$$\Delta E_g = \frac{1}{ad^2 + bd + c} \qquad (4.1)$$

Where, d is the diameter and a, b and c are material dependent constants. For CdSe, a= 0.0397, b = 0.1723 and c= 0.1111.

Table 4.2 Optical parameters and crystallite sizes of CdSe nanoparticles

Precursors	Deposition Temperature/ ^oC	Deposition time (hrs)	Band gap of nanoparticle (eV)	Particle size (nm)		
				U.V		XRD
				(a)	(b)	
$Cd(Cup)_2$: $Se/NaBH_4$	50	4	3.99	2.31	1.46	4.9
		5	3.84	2.42	1.49	5.8
		6	4.02	2.29	1.45	4.9
$Cd(Cup)_2$: $Se/NaBH_4$	70	4	3.9	2.38	1.62	5.9
		5	4.05	2.27	1.44	5.9
		6	3.7	2.54	1.68	6.4
$Cd(S_2CNPr_2)_2$: $Se/NaBH_4$	50	6	3.96	2.33	1.47	-
$Cd(S_2CNBu_2)_2$: $Se/NaBH_4$	50	6	3.87	2.40	1.50	-
$Cd(S_2CN^iBu_2)_2$: $Se/NaBH_4$	50	6	3.86	2.41	1.50	-
$Cd(S_2CNEt_2)_2$: $Se/NaBH_4$	50	6	3.99	2.31	1.46	-
$Cd(Cup)_2$: Selenosulphate	50	8	4.05	-	-	4.2
$Cd(Cup)_2$: Selenosulphate	50	10	4.10	-	-	6.4
$Cd(Cup)_2$: Selenosulphate	50	12	3.90	-	-	6.5

Band gap of bulk CdSe =1.70[c]/1.75[d] eV. [a]Calculated from the Brust relation, [b]calculated from Sarma and Sapra method; [c]Cubic; [d]Hexagonal.

4.4 Conclusions

Nanoparticles of CdS and CdSe have been synthesized at the water-toluene interface. The crystal structure and grain size of the particles were determined using XRD. UV-visible absorption spectrum showed a blue-shift indicating quantum confinement of charged particles. The average crystallite sizes of the as-prepared nanoparticles at different temperatures, concentrations and deposition times ranged from 0.9 to 7.1 nm for cubic CdS, 0.94 to 7.3 nm for hexagonal CdS and 5.9 to 6.4 nm for CdSe. The dislocation densities ranged from 2.89 to 110 x 10^{17} lines/m for cubic CdS, 1.87 to 112.93 x 10^{17} lines/m for hexagonal CdS and 2.12 to 4.22 x 10^{17} lines/m for CdSe. The band gaps obtained for CdS ranged from 3.69 to 3.98 eV, CdSe ranged from 3.7 to 4.05 eV. When selenosulphate was used as the seleniding source the crystallite sizes obtained ranged from4.1 to 6.4 nm with dislocation densities ranging from 2.4 to 5.7 x 10^{17} lines/m.

4.5 References

Alivisatos, P. (1996). "Semiconductor Clusters, Nanocrystals, and Quantum Dots". *Science*, 271: 933-937.

Bowen Katari, J. E., Colvin, V. L. & Alivisatos, A. P. (1994). "X-ray Photoelectron Spectroscopy of CdSe Nanocrystals with Applications to Studies of the Nanocrystal Surface". *J. Phys. Chem.,* 98: 4109-4117.

Bruchez Jr., M., Moronne, M., Gin, P., Weiss, S. & Alivisatos, A. P. (1998). "Semiconductor nanocrystals as fluorescent biological labels". *Science*, 28: 2013-2016.

Brus, L. E. (1984). "Semiconductor crystallites: The size dependence of the lowest excited electronic state". *J. Chem. Phys*., 80: 4403-4409.

Brust, M., Walker, M., Bethell, D., Schiffrin, D. J. & Whyman, R. (1994). "Synthesis of thiol derivatized gold nanoparticles in a 2-phase liquid-liquid system". *J. Chem. Soc. Chem. Commun.* 7: 801-802.

Chan, W. C. W. & Nie, S. M. (1998). "Quantum dot bioconjugates for ultrasensitive nonisotopic detection". *Science*, 281: 2016-2018.

Coe, S., Woo, W. K., Bawendi, M. G. & Bulovic, V. (2002). "Electroluminescence from single monolayers of nanocrystals in molecular organic devices". *Nature*, 420: 800-803.

Colvin, V. L., Schlamp, M. C. & Alivisatos, A. P. (1994). "Nanoparticles as Catalysts for Protein Fibrillation". *Nature*, 370: 354-357.

Cumberland, S. L., Hanif, K. M., Javier, A., Khitrov, G. A., Strouse, G. F., Woessner, S. M. & Yun, C. S. (2002). "Inorganic Clusters as Single-Source Precursors for Preparation of CdSe, ZnSe, and CdSe/ZnS Nanomaterials". *Chem. Mater.*, 14: 1576-1584.

Dmitri, V. T., Elena, V. S., Kornowski, A., Gaponik, N., Haase, M. Rogach, A. L. & Welle, H. (2001). "A New Approach to Crystallization of CdSe Nanoparticles into Ordered Three- Dimensional Superlattices". *Adv. Mater*., 13(24): 1868-1871.

Doneg, C. de M., Hickey, S. G., Wuister, S. F., Vanmaekelbergh, D. & Meijerik, A. (2003). "Single-step synthesis to control the photoluminescence quantum yield and size dispersion of CdSe nanocrystals". *J. Phys. Chem. B*, 107: 489-496.

Guzelian, A. A., Banin, U., Kadavanich, A. V., Peng, X. & Alivisatos, A. P. (1996). "Colloidal chemical synthesis and characterization of InAs nanocrystal quantum dots". *Appl. Phys. Lett*., 69: 1432-1434.

Huynh, W. U., Dittmer, J. J. & Alivisatos, A. P. (2002). "Hybrid nanorod-polymer solar cells". *Science*, 295: 2425-2427.

Huynh, W. U., Peng, X. G. & Alivisatos, A. P. (1999). "CdSe nanocrystal rods/poly(3-hexylthiophene) composite photovoltaic devices". *Adv. Mater.*, 11: 923–927.

Klimov, V. I., Mikhailovsky, A. A., Xu, S., Malko, A., Hollings-worth, J. A., Leatherdale, C. A., Eisler, H. J. & Bawendi, M. G. (2000). "Optical gain and stimulated emission in nanocrystal quantum dots". *Science*, 290: 314–317.

Micic, O. I., Cheong, H. M., Fu, H., Zunger, A., Sprague, J. R., Mascarenhas, A. & Nozik, A. J. (1997). "Size-dependent spectroscopy of InP quantum dots". *J. Phys. Chem. B*, 101: 4904-4912.

Murray, C. B., Kagan, C. R. & Bawendi, M. G., (1995). "Self-Organization of CdSe Nanocrystallites into 3-dimensional Quantum-Dot". *Science,* 270: 1335-1338.

Murray, C. B., Norris, D. J. & Bawendi, M. G. (1993). "Synthesis and Characterization of Nearly Monodisperse CdE (E = S, Se, Te) Semiconductor Nanocrystallites". *J. Am. Chem. Soc*., 115: 8706-8715.

Pan, D. C., Jiang, S. C., An, L. J. & Jiang, B. Z. (2004). "Controllable Synthesis of Highly Luminescent and Monodisperse CdS Nanocrystals by a Two-Phase Approach under Mild Conditions". *Adv. Mater.*, 16: 982-985

Pan, D. C., Wang, Q., Jiang, S. C., Ji, X. L. & An, L. J. (2005). "Synthesis of extremely small CdSe and highly luminescent CdSe/CdS core–shell nanocrystals via a novel two-phase thermal approach". *Adv. Mater,* 17: 176-178.

Peng, X. G., Wickham, J. & Alivisatos, A. P. (1998). "Kinetics of II-VI and III-V colloidal semiconductor nanocrystal growth: Focusing" of size distributions". *J. Am. Chem. Soc*., 120: 5343-5344.

Peng, Z. A. & Peng, X. G. (2001). "Formation of high-quality CdTe, CdSe, and CdS nanocrystals using CdO as precursor". *J. Am. Chem. Soc.,* 123: 183-184.

Peng, Z. A. & Peng, X. G. (2002). "Nearly monodisperse and shape-controlled CdSe nanocrystals using CdO as precursor". *J. Am. Chem. Soc.*, 124: 3343-3353.

Qu, L. H. & Peng, X. G. (2002). "Control of Photoluminescence Properties of CdSe Nanocrystals in Growth". *J. Am. Chem. Soc*., 124: 2049-2055.

Qu, L. H., Peng, Z. A. & Peng, X. G. (2001). "Alternative Routes Toward High Quality CdSe Nanocrystals". *Nano Lett*., 1: 333-337.

Rogach, A. L., Katsikas, L., Kornowski, A., Su, D., Eychmüller, A. & Weller, H. (1996). "Synthesis and Characterization of Thiol-Stabilized CdTe Nanocrystals". *Ber. Bunsenges. Phys. Chem.*, 100: 1772-1778.

Sapra, S. & Sarma, D. D. (2004). "Evolution of the electronic structure with size in II-VI semiconductor nanocrystals". *Phys. Rev. B*, 69: 125304-125307.

Schlamp, M. C., Peng, X. G. & Alivisatos, A. P. (1997). "Improved efficiencies in light emitting diodes made with CdSe.CdS.core/shell type nanocrystals and a semiconducting polymer". *J. Appl. Phys.*, 82: 5837-5842.

Talapin, D. V., Rogach , A. L., Shevchenko, E. V., Kornowski, A., Haase, M. & Weller, J. H. (2002). "Dynamic Distribution of Growth Rates within the Ensembles of Colloidal II-VI and III-V Semiconductor Nanocrystals as a Factor Governing their Photoluminescence Efficiency". *J. Am. Chem. Soc.*, 124: 578-5790.

Talapin, D. V., Rogach, A. L., Kornowski, A., Haase, M. & Weller, H. (2001). "Highly Luminescent Monodisperse CdSe and CdSe/ZnS Nanocrystals Synthesized in a Hexadecylamine – Trioctylphosphine Oxide – Trioctylphospine Mixture". *Nano Lett.*, 1: 207-211.

Vossmeyer, T., Katsikas, L., Giersig, M., Popovic, I. G., Diesner, K., Chemsedine, A., Eychmller, A. & Weller, H. (1994). "CdS Nanoclusters: Synthesis, Characterization, Size Dependent Oscillator Strength, Temperature Shift of the Excitonic Transition Energy, and Reversible Absorbance Shift". *J. Phys. Chem.*, 98: 7665-7673.

Weller, H. (1993). "Quantized Semiconductor Particles: A novel state of matter for materials science". *Adv. Mater.*, 5: 88-95.

Yu, W. W. & Peng, X. G. (2002). "Formation of high-quality CdS and other II-VI semiconductor nanocrystals in noncoordinating solvents: Tunable reactivity of monomers". *Angew. Chem . Int. Ed.,* 41: 2368–2371.

Yu, W. W., Wang, Y. A. & Peng, X. G. (2003). "Controlled CdTe nanocrystals: Ligand effects on monomers and nanocrystals". *Chem . Mater.* 15: 4300-4308.

Zhang, H., Wang, L. P., Xing, H. M., Hu, L. H., Yang, B. & Li, W. (2003). "Hydrothermal synthesis for high quality Cadet QDs". *Adv. Mater*., 15: 1712-1715.

Zheng, X., Feng, Y., Knoll, W. & Han, M. (2003). "Alloyed $Zn_xCd_{1-x}S$ nan crystals with highly narrow luminescence spectral width". *J. Am. Chem. Soc.*, 125: 13559-13563.

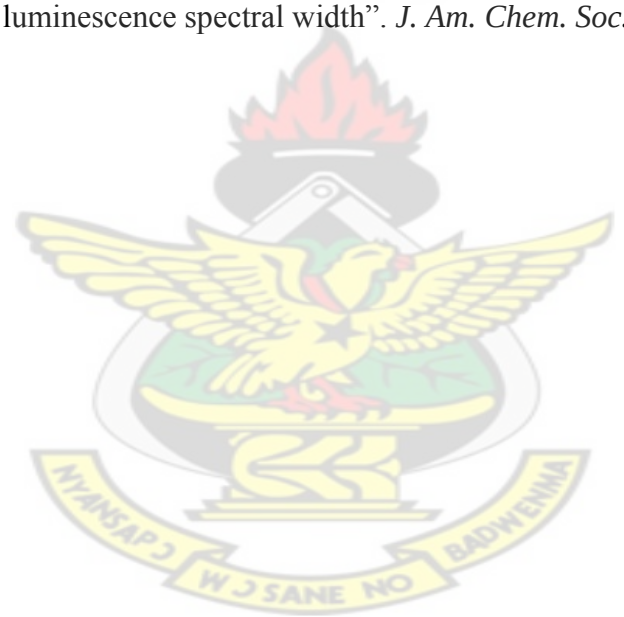

CHAPTER FIVE

DEPOSITION OF LEAD CHALCOGENIDE NANOMATERIALS AT WATER-TOLUENE INTERFACE

This chapter describes the syntheses of Lead chalcogenide nanoparticles. The work was carried out at the School of Chemistry, and characterization of nanomaterials nanowires by XRD and SEM was performed in the School of Materials Science, The University of Manchester, UK.

Deposition of lead chalcogenide nanomaterials at water-toluene interface

Abstract

Nanostructured thin films of PbE (E=S, Se, Te) have been prepared at the water-toluene interface by reacting toluene solutions of lead alkyldithiocarbamates/ cupferronates with aqueous chalcogenide ions obtained by the borohydride reduction of sulphur, selenium and tellurium powder. The thin film deposits were characterized by powder X-ray diffraction, scanning and transmission electron microscopy and absorption spectroscopy. The influence of deposition conditions such as precursor concentrations, temperature as well as deposition times were studied. At lower concentrations of the reacting species the films formed at the water-toluene interface consisted mainly of nanocrystals. However with increasing concentration as well as temperature thicker films were formed which were mostly single crystalline. All the materials prepared have the halite structure as confirmed by X-ray diffraction. The average crystallite sizes of the as-prepared nanoparticles at different temperatures, concentrations and deposition times ranged from 1.8 to 6.3 nm for PbS, 2.5 to 8.3 nm for PbSe and 3.9 to 6.3 nm for PbTe. The dislocation densities ranged from 2.2 to 31.4 x 10^{17} lines/m for PbS, 2.5 to 5.7 x 10^{17} lines/m for PbSe and 2.5 to 6.6 x 10^{17} lines/m for PbTe. The shape of the as-prepared nanoparticles at different temperatures was studied by SEM and gave morphologies from cubes to rods. The band gaps obtained for PbS ranged from 0.84 to 1.75 eV, PbSe ranged from 1.35 to 1.80 eV and 0.96 eV for PbTe. These show significant increases from the band gaps of the bulk materials of 0.41 eV, 0.29 eV and 0.27 eV for PbS, PbSe and PbTe respectively.

5.1 Introduction

The synthesis of materials with different morphologies not only facilitate the realization of constructing nanodevices using nanoscale building blocks, but also avail the applications of complex inorganic materials in optics, electronics, mechanical, magnetism and biology (Moore *et al.*, 2006, Xu *et al*., 2007). Remarkable progress has been made for the synthesis of inorganic materials including metal, metal oxide, sulphide and other minerals with complex structures (Chen and Ye, 2008). Among all kinds of fabrication strategy, solution phase synthesis has proved to be an effective way for controlling the morphology of the final products with low cost and large-scale production (Manna *et al.*, 2003).

Lead chalcogenides (PbE, E= S/Se/Te) are extremely important in both basic scientific studies and technological applications. Lead chalcogenide materials with critical dimensions of the order of nanometers have been of considerable interest of late both because of their unique physical and chemical properties and because of a perceived potential for use in a diverse range of applications (Alivisatos, 1996, Wang and Herron, 1991, Calvert, 1999, Hu *et al.*, 1999, Cheng *et al*., 2007). Such materials can be used in photovoltaic cells (Cui *et al.*, 2006), infrared detectors, (Qi *et al*., 2005) and thermoelectric devices (Harman *et al*., 2002). Lead chalcogenide nanocrystals exhibit a strong quantum size effect because of the large Bohr radii of both electron and holes [PbS (≈18 nm), PbSe and PbTe (≈46 nm)], which leads to a large confinement energy. Their critical dimensions, especially for selenide and telluride, are greater than in most II–VI and III–V semi-conductors (ZnSe, CdSe, CdS, InAs) (Wise, 2000). The stable and tunable emission of NIR-emitting lead chalcogenide quantum dots (QDs) make them suitable for applications in telecommunications (1300–1600 nm), bioimaging (near-IR tissue window 800 and 1100 nm) and solar cells (800–2000 nm) (McDonald *et al*., 2005).

The structures of lead chalcogenides can be viewed as a face-centred cubic (fcc) array of E^{2-} (E = S, Se, Te) anions with bulky cations Pb^{2+} occupying all the octahedral holes. Alternatively it can be viewed as a structure in which the anions occupy all the octahedral holes in an fcc array of Pb^{2+} ions. The coordination number is of each type of ion is 6, and the structure is said to have (6, 6)-coordination. The nature of bond between Pb and the chalcogenide has been studied extensively; some reports treat this bonding as ionic, others covalent and still other mixtures of both ionic and covalent. Notwithstanding, ionic bonding is considered more important and ionic characters decrease as the size of chalcogenide species increases (Khoklov, 2003; Alivisastos *et al*., 1998; Pantarotto *et al*., Ma *et al*., 2003). Important properties of bulk lead chalcogenide are given in Table 6.1 (Khoklov, 2003; Alivisastos *et al*., 1998; Pantarotto *et al*., Ma *et al*., 2003).

Table 5.1 Selected physical properties of lead chalcogenides (Khoklov, 2003; Alivisastos *et al*., 1998; Pantarotto *et al*., Ma *et al*., 2003).

Properties	PbS	PbSe	PbTe
Bohr radius bulk (nm)	18	46	46
Band gap (373) (eV)	0.41	0.29	0.27
Density (g/cm^3)	7.6	8.3	8.2
Dielectric constant	169	204	414
Structure	cubic	Cubic	Cubic
Lattice constant	5.936	6.124	6.460

Various morphologies of PbE nanocrystals have been reported, including spheres (Murray *et al*., 2001), cubes (Lu *et al*., 2005), rings (Cho, *et al*., 2005), tubes (Tong *et al*., 2006), wires (Wang *et al*., 1998, Afzaal and O'Brien, 2006), dendrites (Li *et al*., 2008), and sponge-like structures (Kerner *et al*., 2001). Several groups have reported the shape evolution of PbSe nanocrystals

from cubes to truncated octahedral (Cheng *et al*., 2009), spheres to cubes (Lee *et al*., 2002) and stars to cubes (Lu *et al*., 2005). Shape evolution for PbE can be affected by temperature, growth time, solvent and precursor delivery. The systematic tuning of the size and shape of nanocrystallites remains a key objective in realizing both functionality and assembly. The synthesis of such nanocrystals has involved methods that include sputtering (Jdanov *et al*., 2004), ultrasonic synthesis (Ge and Li, 2003), injection of a solution of a lead salt and trioctylphosphane chalcogenide (TOP-E, E = S, Se, Te) into a hot solvent (Cho *et al*., 2005; Kumar *et al*., 2009), thermolysis of single source precursors (Lee *et al*., 2002; Trindade *et al*., 1999; Akhtar *et al*., 2010; Trindade *et al*., 1997; Moloto *et al*., 2005; 2005; Berhanu *et al*., 2006), or hydrothermal synthesis (Berhanu *et al*., 2006). These methods generally involve high temperatures and/or quite difficult conditions such as high vacuum or high pressure or salt–solvent-mediated high temperature. Rhodes *et al*. demonstrated the triggered aggregation of PbS nanocrystals in a polymer matrix by changing the 1,2-ethanedithiol concentration-triggered assembly of network-like quantum dot (QD) structures (low concentration) and self-assembled more-ordered micrometer-sized crystals (high concentration) (Rhodes *et al*., 2011). The role of 1, 2-ethanedithiol in decreasing the aggregation as a result of decreasing inter-QD separation and the self-assembly as result of a rapid ligand-exchange process was suggested (Rhodes *et al*., 2011). The one-dimensional (1-D) structures from such processes are often polycrystalline and not well dispersed after separating from the template. Limited success has been re-ported in the growth of 1D PbTe by solution-based soft-templating approaches.

In a preliminary work, Ziqubu *et al*. (2010) have demonstrated a simple approach to controlled growth of low-dimension PbTe structures (spheres or rods) and extended the method to the synthesis of PbS and PbSe. The method involves the reaction of sulphur, selenium or tellurium powder with sodium borohydride ($NaBH_4$) to produce sulphide, selenide or telluride ions, followed by reaction with a lead salt.

Lead sulphide (galena) has been known as a distinct entity since antiquity (Pliny, 1991) and was one of the earliest materials to be used as a photodetector. Polycrystalline layers of PbS, which may be produced by chemical deposition or evaporation, find wide application in infrared detection (Elliot, 1981). PbS has a cubic (rock-salt type structure and, as with the other lead chalcogenides (PbSe, PbTe), the intrinsic band gap decreases with decreasing temperature, which is unusual in semiconductors (Elliot, 1981). The electronic band structure (Kohn *et al*., 1973) of PbS has been reported showing a minimum direct gap at the L point in the Brillouin zone. It is readily recognized in nature by its distinctive crystal habit as small cubes ({001} faceted) with the occasional occurrence of forms involving the expression of the (111) faces of the octahedron or tetrahedron and ready cleavage of the cubes along the (111) planes. The form of the crystal has attracted attention for well over 100 years (Buckley, 1951). After detailed calculations, Dowty (Dowty, 1976) has ranked the stability of faces in the order {100}, {111}, {110}, {113}, {210} and noted that this is not perfect, especially as regards the form {113} which is never observed (Stranski, 1928).

Indeed both natural and synthetic forms of PbS show only {100} or {111} facets (Rhodes *et al.*, 2011, Sunagawa, 1987, Garcia-ruiz, 1986). O'Brien *et al* (2010) have reported a simple method for the preparation of square based pyramids with {113} faces and {002} basal planes. These unique crystals have been formed by precipitation at the interface of toluene (lead containing) and water (sulphide containing) solutions.

As an important semiconductor with narrow band gap of 0.41 eV, lead sulphide has been extensively studied and employed in various applications such as IR photodetectors, solar absorbers, electro- and photoluminescence, sensors, and so on (Kumar *et al*., 2009, Warner, 2008). The synthesis of PbS with well-defined morphology has been achieved via a huge number of new methods (Xiu *et al*., 2008; Sun *et al*., 2009; Jana *et al*., 2009; Stavrinadis *et al*., 2008; Peng *et al*., 2008). Pyramidal PbS crystallites with high energy {113} facets were obtained at

the interface between toluene and water (O'Brien *et al*., 2008). PbS nanowire "pine trees" was fabricated using chemical vapour deposition method (Lau *et al*., 2009). The size dependent optical properties of PbS quantum dots have also been investigated thoroughly (Moreels *et al*., 2009). For the inevitable reaction with water vapour and other matters under ambient environment, PbS devices were usually coated with protective materials. Undoubtedly, the coating process not only increases the cost, but also requires additional apparatus.

Lead selenide (PbSe) is a leading material, because of its small band gap of (0.27 eV) and large bulk exciton Bohr radius (46 nm), which results in strong confinement of the electron-hole pair and large optical nonlinearity (Lifshitz *et al*., 2003). From a technological perspective, PbSe is a promising material in many applications, including laser materials (Cui *et al*., 2006), thermoelectric devices (Harman *et al*., 2002, Murray *et al*., 2001), near-infrared (near-IR) luminescence (Schaller *et al*., 2003), and IR detectors (Qi *et al*., 2005). The recently discovered phenomenon of the multiple exciton generation (MEG) effect in PbE (where E = S, Se, or Te) materials could lead to an entirely new paradigm for high-efficiency and low-cost solar cell technology (Elingson *et al*., 2005, Allan and Delerue, 2006, Nozik, 2008). The deposition of PbSe thin films have been reported by various methods, including molecular beam epitaxy (Zhao *et al*., 2008), electrodeposition (Shah and Holze, 2008), pulse laser deposition (Evstratov *et al*., 2001), and chemical bath deposition (Gorer *et al*., 1995). Reports on the growth of PbSe thin films by chemical vapor deposition (CVD) techniques are scarce (O'Brien *et al*., 2004, Bierman *et al*., 2007). An earlier report on the thermal decomposition (O'Brien *et al*., 2004) of $[Pb((SePiPr)_2N)_2]$, which is a precursor sufficiently volatile for low-pressure CVD, resulted in globular PbSe films. Later, hyperbranched structures of PbS and PbSe were reported by CVD from $PbCl_2$ and S/Se under hydrogen flow (Trindade *et al.*, 1999). The formation of PbSe in nanocrystalline form has been demonstrated by several methods including the decomposition of a single molecular precursor (Cheng *et al.*, 2009), polymer-assisted solvothermal method (Liu *et*

al., 2003), soft template routes (Das and Bhat, 1990), electrodeposition (Birdi, 1997), Aerosol-assisted chemical vapor deposition (AACVD) of PbSe films/crystals on glass and Si/SiO_2 (100) substrates from lead phosphonodiselenoato compounds ($Pb[Ph(RO)PSe_2]_2$, where R is a methyl group (Me) or an ethyl group (Et)) have been reported (Das and Bhat, 1990). Deposition on Si/SiO_2 (100) substrates leads to highly faceted PbSe micrometer- sized crystals with morphologies strongly influenced by growth temperatures.

PbTe is an important narrow band gap semiconductor material with a large excitonic Bohr radius (~46 nm). It can or could be used in optical switches, solar cells (Harman *et al.,* 2002; Hsu *et al.,* 2004), photodetectors (Wise, 2000), thermoelectrical applications, and electroluminescent devices (Sargent, 2005). Nano dimensional crystals of PbTe have been reported, as dendrites (McDonald *et al.,* 2005), sponge like structures (Lu *et al.,* 2004; Bakueva *et al.,* 2003; Steckel *et al.,* 2003), spheres (Tong *et al.,* 2006), and boxes (Hu *et al.,* 1999). Many groups have reported that nanodimensional lead chalcogenide crystals undergo shape evolution from spherical to polyhedral, cubic, or tetragonal structures with increasing size/reaction time (Li *et al.,* 2008). Dependence of the form of the final product on reaction temperature and the choice of capping ligand has also been noted (Cheng *et al.,* 2007). The synthesis of 1D PbTe nano structures is challenging (Kerner *et al.,* 2001). Rods can also show good thermoelectric Figures of merit (ZT) as compared to isotropic structures (Zou *et al.,* 2004).

There are only a few reports of synthesis of PbTe nanorods or nanotubes, which include hydrothermal, sonoelectrochemical, and template-assisted synthesis (Kerner *et al.,* 2001; Zou *et al.,* 2004; Lee *et al.,* 2002; Pietryga *et al.,* 2004; Jun *et al.,* 2005; Lee *et al.,* 2003; Lu *et al.,* 2005). However, these methods have limited success in the control overall shape and size. A completely new simple two-step colloidal method to synthesize single-crystal PbTe nano-spheres and -rods with control of size and shape has been reported by Purkayastha *et al.* (2008). Lead telluride was synthesized by the addition of an aqueous solution or suspension of a lead

salt (chloride, nitrate, or carbonate), to a freshly prepared NaHTe solution (The solid product of this reaction was isolated by centrifugation, dispersed into TOP and injected into hot hexadecylamine (HDA) at temperatures of 190, 230, or 270 °C and held at the same temperature for 2 or 4 hour. After being cooled to 50 °C, the PbTe nanoparticles were isolated by the addition of methanol to the reaction mixture.

5.1.2 Mechanism of formation of cubic or spherical nanocrystals

Factors that control the shapes of inorganic nanocrystals involve competition between thermodynamic and kinetic factors (Lee *et al*., 2003). According to this model, after the formation of a preferred crystalline-phase seed, the final morphology of the nanocrystals is mainly determined by the growth process through a balance between the kinetic growth and thermodynamic preference. At high temperature, the reaction is under thermodynamic control, and at low temperature/room temperature the reaction is under kinetic control (O'Brien *et al*., 2011). The form of the precipitate is remarkably dependent on reaction conditions. It has been reported that the shape of an inorganic nanoparticle is determined by the growth rates of different crystal planes (Hou *et al*., 2009; Cheon *et al*., 2003). The shape of a face-centre-cubic (fcc) nanoparticle is determined by the ratio (R) of the growth rates along (100) and (111) directions as shown in Figure 5.1. The surface energy of (111) plane is higher than (100) plane (Cheon *et al*., 2003). When the value of R is close to 0.58, cubes terminated by (100) plane will be produced and when the value approaches to 0.87 spherical nanoparticles will be formed (Hou, 2009; Lee, 2003). However, when R is above 1.73, one dimensional growth occurs producing rods or multi-pod structures. The cubic shape of PbS is reported to be more stable at higher temperature.

The intrinsic surface energy of the PbS (111) face is higher than that of the (100) face and growth rate of either these face determines the final shape of nanoparticles. Thus the shape of the PbS nanoparticles can be controlled by the manipulation of the growth time and temperature. As the

growth temperature increases, a correlation between an increase in intensity of the (200) peak and a decrease in the (111) peak emerges. A decrease in the relative intensity of (111) reflection indicates that growth along the (111) direction is taking place, thus promoting the formation of (100) facets. At lower growth temperature, the growth along the (100) direction increases, resulting in the elimination of the (100) facets and promoting the formation of (111) facets.

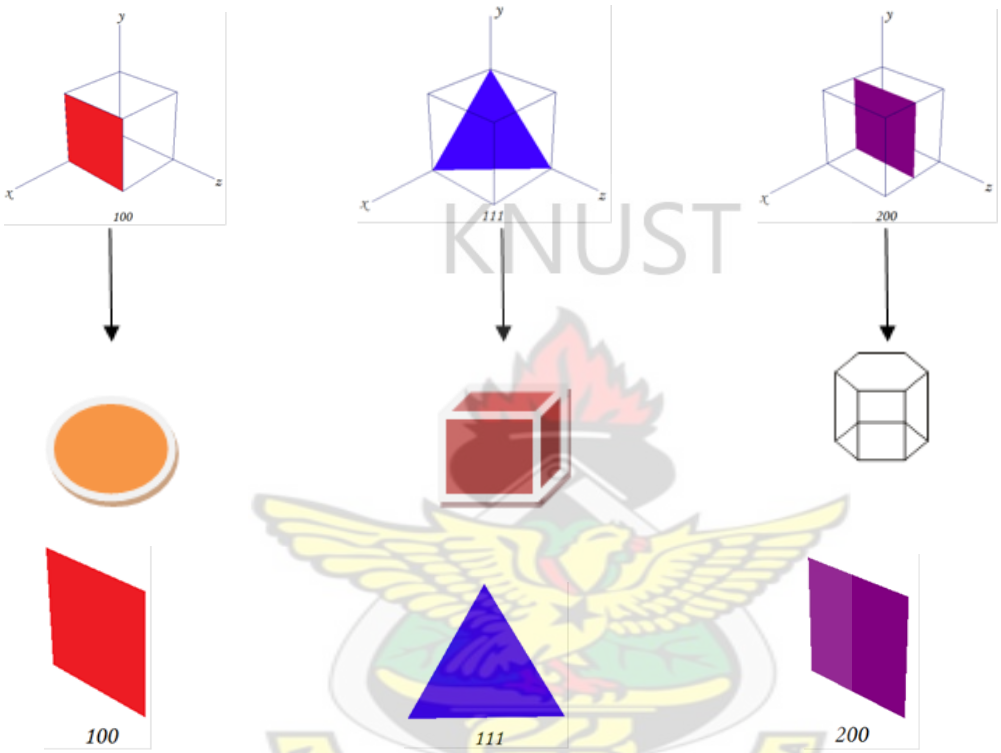

Figure 5.1: Lattice planes of PbS cubic crystal system, faster growth of (111) or (100) plane results in cubic or spherical shape PbS nanoparticles.

In this chapter, the synthesis of PbS, PbSe and PbTe nanomaterial/thin films at water-toluene interface at temperatures below 100 ^{o}C by the use of cadmium dialkylyldithiocarbamate/cupferronate ($Pb(dtc)_2$/$Pb(cup)_2$) as lead source and the borohydride reduction of Sulphur/Selenium/Tellurium as sulphide/selenide/telluride sources are being reported.

5.2 Deposition of lead chalcogenide thin film nanomaterials

Briefly 30 ml of degassed water containing 0.1 mmol of NaHE (E= S, Se, Te) was transferred into a 100 ml beaker. 30 ml of toluene containing the 0.1 mmol of the Lead dialkyldithiocarbamate/cupferronate precursor was layered on top of the solution in the beaker. The reaction vessel was placed in an oven preheated to the desired temperature for 4 hours. The deposits formed at the interface were isolated by gently lifting the film from the interface onto glass substrates. The reaction was repeated by varying the reaction conditions such as temperature, time and the reacting species (Details of the deposition are given in chapter 6 section 6.4).

5.3 Results and discussions

Nanoparticles of PbE were synthesized by the layering a toluene solution of lead diethyldithiocarbamate/lead cupferronate on top of a freshly prepared NaH(S/Se/Te) solution. Previous reports suggest that primary amines preferentially coordinate to the [111] facets of PbSe and PbS, which prevents the formation of cubes (Warner and Cao, 2008). In this work, however no such observation was made since the structures of the lead chalcogenide deposited adopted the cubic structure. It is believed that this route could make available materials in new forms with interesting properties as suggested by Burda *et al*., (2005) and Buhro *et al*., (2003), and provide further insight into classic problems of crystal growth.

5.3.1 Lead sulphide

5.3.1.1 Structural characterization and morphology

The powder X-ray diffraction pattern of the PbS nanoparticles synthesized at 50 °C and 70 °C for 4, 5 and 6 hours show the presence of the (111), (200) and (220) diffraction planes of the

cubic rock-salt structure of PbS films are characteristic of cubic PbS crystallites with the rock salt structure orientated along the (200) plane. Figures 5.2 and 5.3 show the XRD pattern of PbS nanoparticles/thin film with reflections corresponding to those of the cubic PbS (ICDD 01-080-0021, cell constant a=5.618 Å). Broadening of the diffraction peaks was observed implying that the size of the PbS particles were small. The peak broadening at lower angle is more meaningful for the calculation of particle size therefore size of the nanocrystals has been calculated using Debye-Scherrer formula (Guinier, 1963) using (200), (220) and (311) reflections from the XRD pattern. The calculation gave average particle sizes ranging from 2.34 to 6.74 nm with dislocation densities ranging from 2.2007 to 18.2628 x 10^{17} lines/m (Tables 5.2 and 5.3).

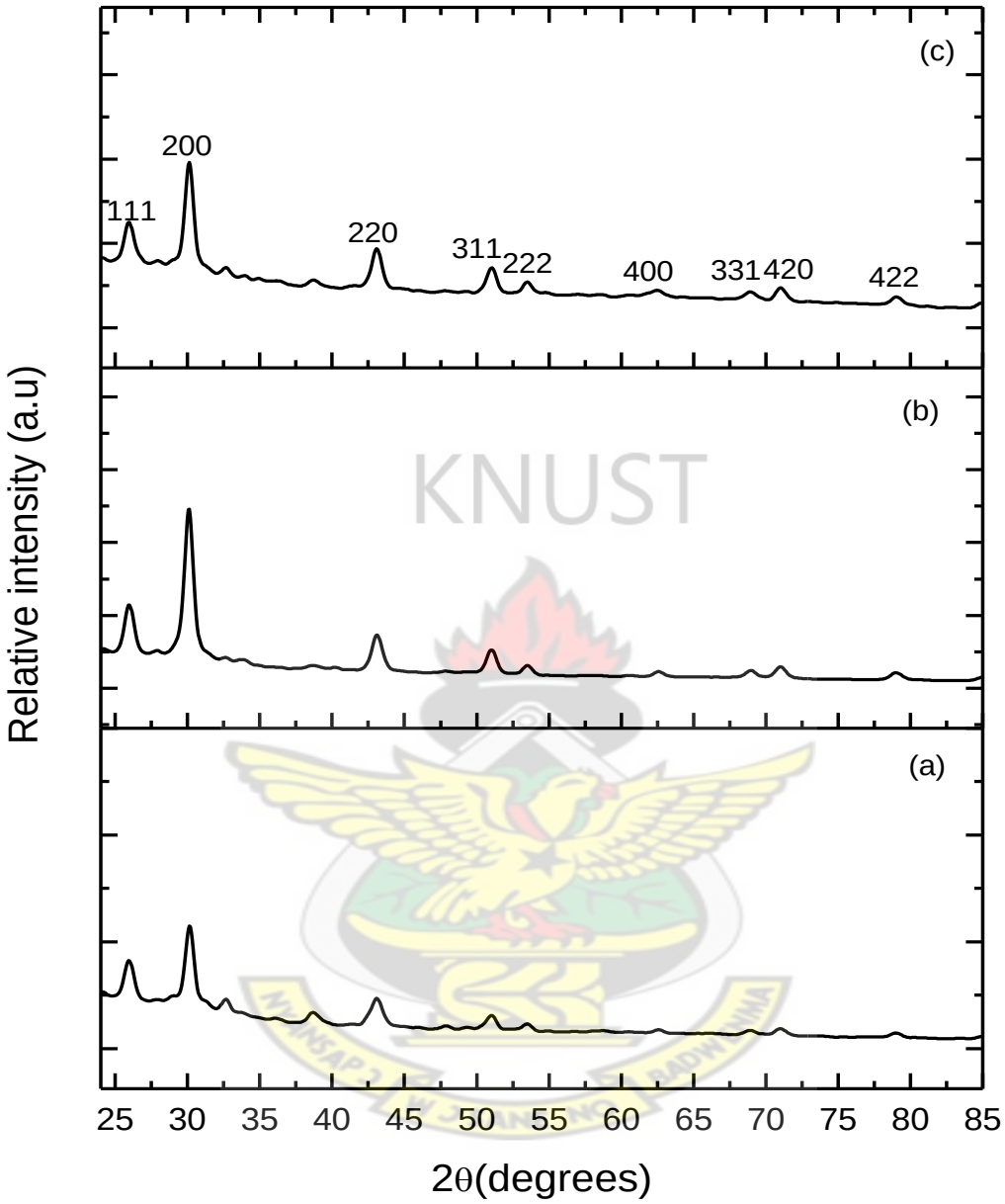

Figure 5.2: XRD of different as-prepared PbS samples (a) for 4 hours, (b) for 5 hours and (c) for 6 hours at 50 °C.

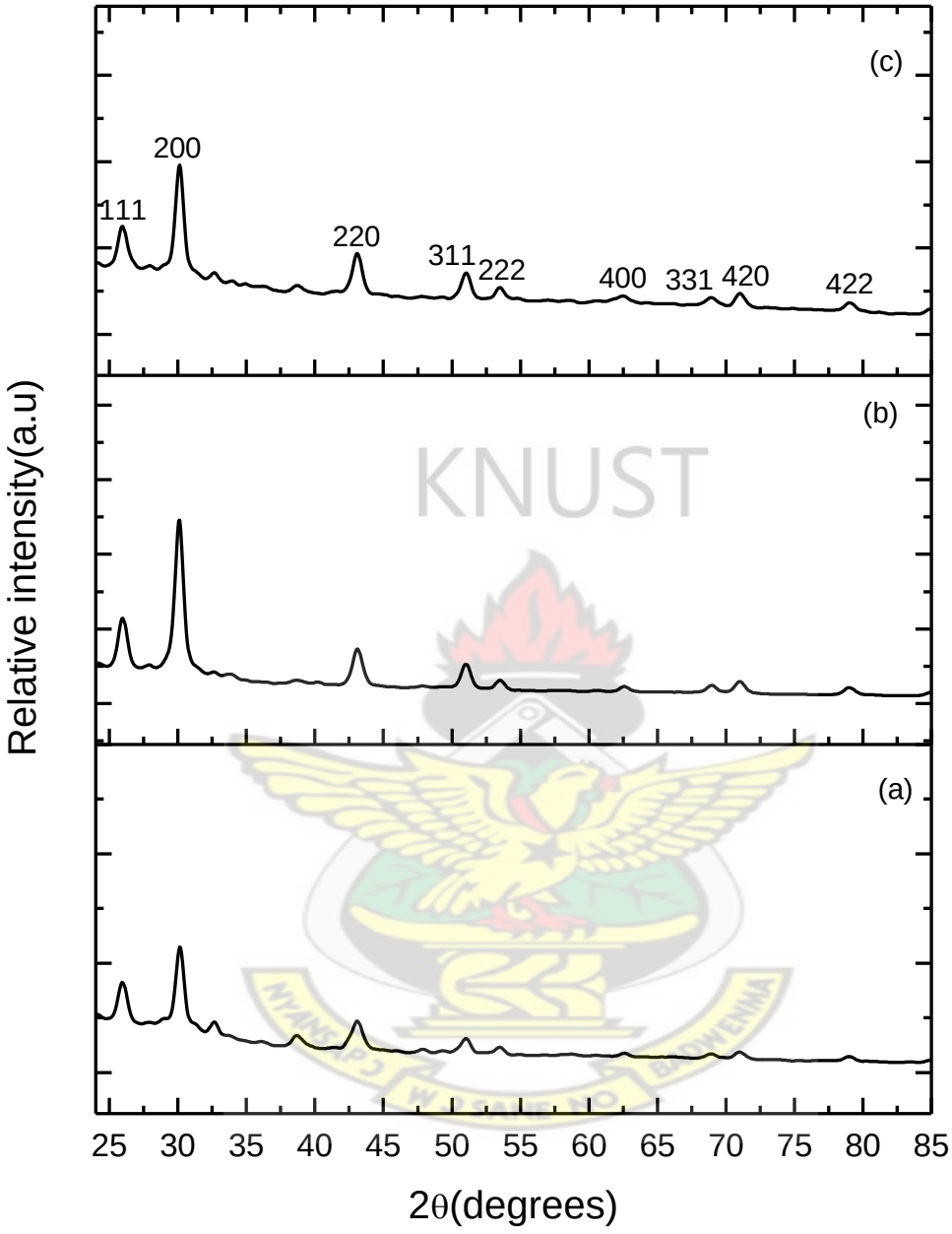

Figure 5.3: XRD of different as-prepared PbS samples (a) for 4 hours, (b) for 5 hours and (c) for 6 hours at 70 °C.

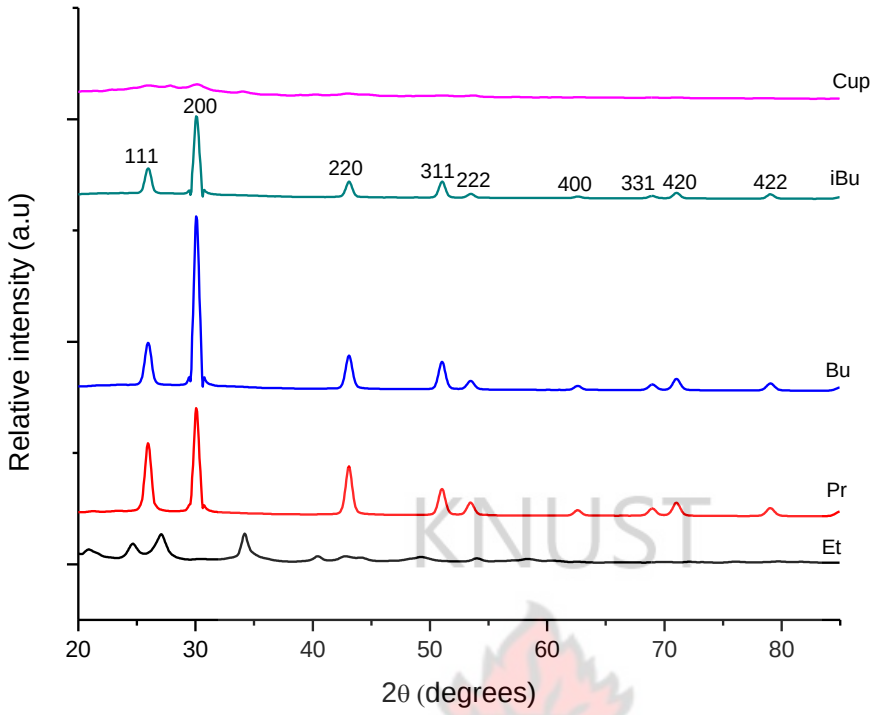

Figure 5.4: XRD of different as-prepared PbS samples using different chain lengths of the alkyl group in the dithiocarbamate precursors and lead cupferronate precursor at 50 °C for 6 hours. (Et = ethyl; Pr = propyl; Bu = butyl; ^{i}Bu = isobutyl; Cup = lead cupferronate).

The effect of the length of the alkyl chain length on the size of the crystallites and morphology of the nanoparticle was also investigated by varying the alkyl chain in the dithiocarbamate precursor. The XRD diffractogram is shown in Figure 5.4 and the structural parameters given in table 5.2. The crystallite sizes as calculated by the Debye-Scherrer relation increase with increasing chain length (i.e. from Et=ethyl through Pr= propyl to Bu= butyl). However there was a reduction in size from Bu to ^{i}Bu.The intensity of the diffraction peaks was observed to increase with increasing carbon chain length of the precursor (i.e. from ethyl to butyl). This implies that the PbS nanomaterial thin film formed become more crystalline with increasing carbon chain length of the dialkyldithiocarbamate precursor. However with the same number of carbon atoms

the intensity of the diffraction peak of the PbS nanomaterial was observed to decrease from the *n*-butyl to the *iso*-butyl isomer thus becoming less crystalline. In another experiment when lead cupferronate was used as the precursor under the same experimental conditions as the lead dialkyldithiocarbamate the thin film nanoparticle produced had crystallites with sizes and morphologies similar to those of the lead dialkyldithiocarbamate precursors. The intensity of the diffraction peaks was observed to increase with increasing carbon chain length of the precursor (i.e. from Et to Pr to Bu). Implying that the PbS nanoparticle thin film become more crystalline with increasing carbon chain length of the precursor. However with the isomeric precursors the intensity of the diffraction peaks was observed to decrease from the ^{n}Bu to ^{i}Bu isomers.

The scanning electron microscopy (SEM) images Figures 5.5 show two types of crystals i.e. both cubic and pyramidal crystallites. The compositional analysis of PbS was confirmed by energy-dispersive X-ray analysis (EDAX), as shown in Figure 5.6. The ratio between the lead and sulphide peaks should be nearly stoichiometric. From the graph it is noted that for a deposition time of 5 hours and deposition temperature of 50 °C, the atomic percentage of lead is 54.85 while that of sulphur is 45.12.

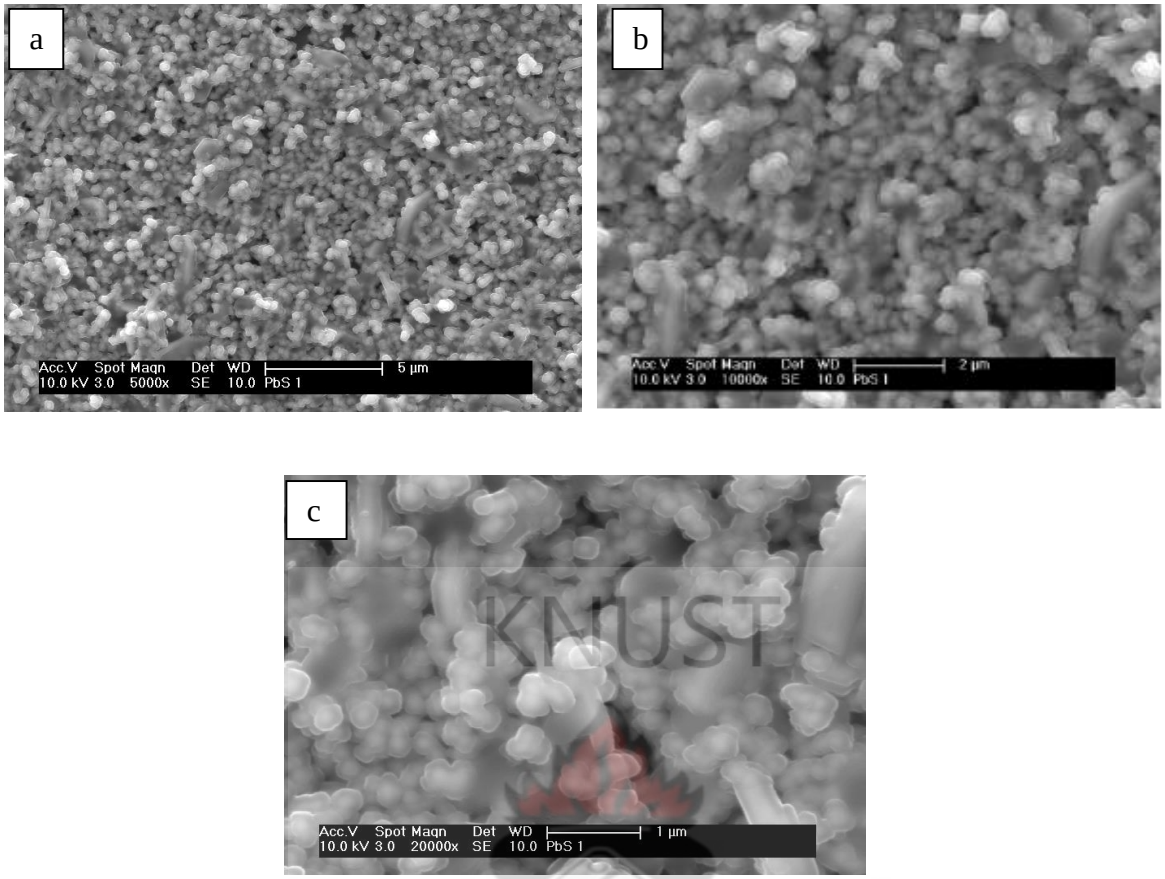

Figure 5.5: SEM image of different as-prepared PbS sample at 50 °C for 5 hours using lead cupferronate as precursor at different magnifications (a-5000x, b-10000x and c-20000x).

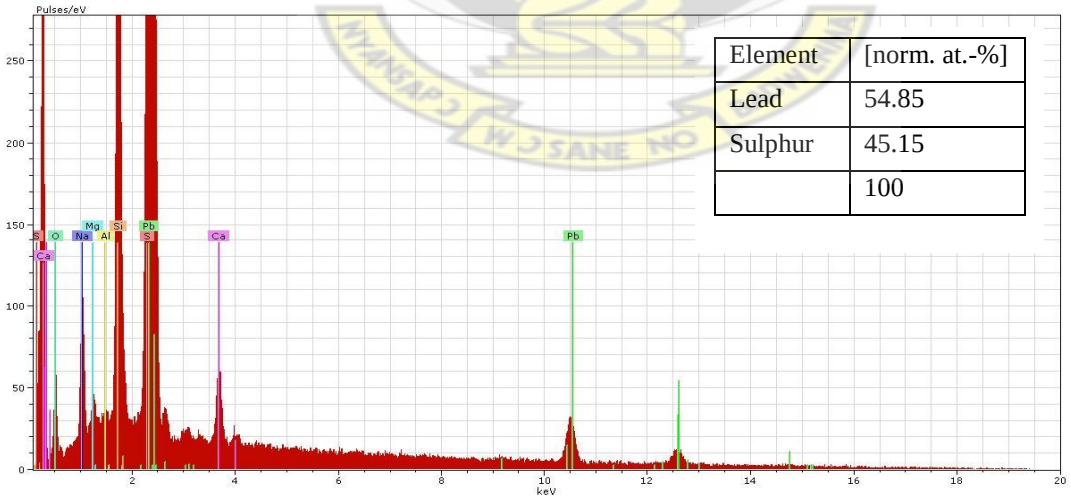

Element	[norm. at.-%]
Lead	54.85
Sulphur	45.15
	100

Figure 5.6: EDAX analysis of different as-prepared PbS sample at 50 °C for 5 hours using lead cupferronate as precursor.

5.3.1.2 Optical analyses

The optical absorption spectra of the nanocrystals were measured using CARY 5000 UV-Vis-NIR spectrophotometer. The optical absorption spectra have been measured at room temperature over a range of 500 to 1600 nm have been plotted in Figures 5.7 and 5.8. The fundamental absorption corresponds to the electron excitation from the valence band to the conduction band and can be used to determine the optical band gap. The relationship between the absorbance (A) and the incident photon energy (hυ) is given by the Stern relationship of near-edge absorption (Stern and Kim, 1981):

$$A = [k(h\upsilon - E_g)]^{1/n}/h\upsilon$$

Where υ is the frequency, h is the constant, k is a constant and carries a value of either 1 of 4. The value of n is 1 for direct transition and 4 for indirect transition. The optical band gap is determined by a plot of $(Ah\upsilon)^{2/n}$ as a function of hυ extrapolation of the line to the hυ axis where $(Ah\upsilon)^{2/n}$ is zero gives the band gap E_g. The plots of $(Ah\upsilon)^2$ versus hυ is a straight line indicating that PbS is a direct band gap material. The plots of $(Ah\upsilon)^2$ versus hυ for the different nanocrystallites obtained at 50 ºC are given in the Figure below:

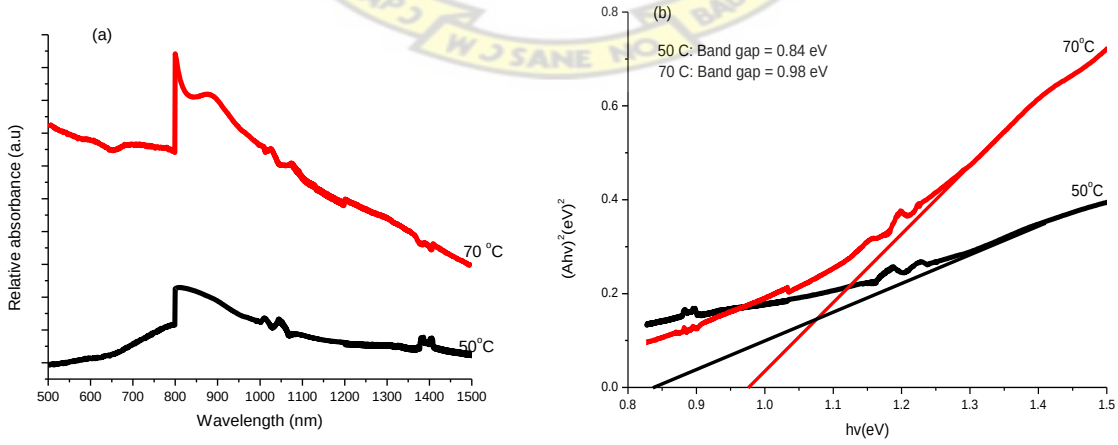

Figure 5.7: (a) Optical absorption spectra and (b) optical band gap of the as-prepared PbS samples (a) at 50 °C and (b) at 70 °C for 4 hours.

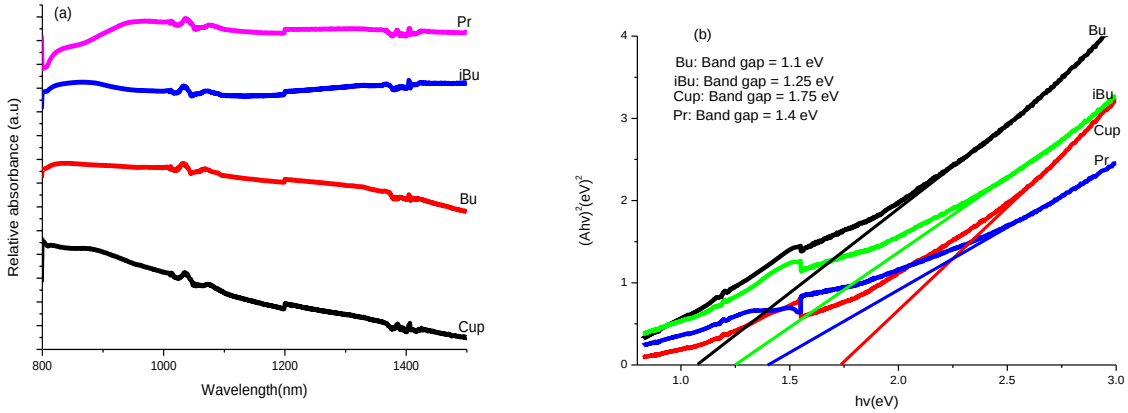

Figure 5.8: (a) Optical absorption spectra and (b) optical band gap of the as-prepared PbS samples using different chain lengths of the alkyl group in the dithiocarbamate precursors at 50 °C for 6 hours. (Pr = propyl; Bu = butyl; ^{i}Bu = isobutyl; Cup= lead cupferronate).

Table 5.2: Optical parameters and crystallite sizes of PbS nanoparticles

Precursors	Deposition Temperature/ ^{o}C	Deposition time (hrs)	Band gap of nanoparticle (eV)	Particle size (nm)	
				U.V	XRD
$Pb(cup)_2$: S/$NaBH_4$	50	4	-	-	5.80
		5	-	-	4.78
		6	0.84	4.04	2.34
$Pb(cup)_2$: S/$NaBH_4$	70	4	-	-	5.31
		5	-	-	5.28
		6	0.96	3.41	4.87
$Pb(S_2CNBu_2)_2$: S/$NaBH_4$	50	6	1.10	2.90	6.36
$Pb(S_2CN^{i}Bu_2)_2$: S/$NaBH_4$	50	6	1.25	2.51	5.84
$Pb(S_2CNPr_2)_2$: S/$NaBH_4$	50	6	1.40	2.21	6.27
$Pb(S_2CNEt_2)_2$: S/$NaBH_4$	50	6	-	-	6.74

Band gap of bulk PbS = 0.41 eV

Table 5.2 gives the optical parameters and crystallite sizes of the PbS nanoparticle thin films formed at different temperatures, deposition times and with different precursors. The band gap of PbS nanoparticle thin films increased from the bulk value of 0.41 eV to 0.84 and 0.96 eV when the crystallite size decreased beyond the Bohr exciton radius of 18 nm to 5.3 and 4.87 nm respectively when $Pb(cup)_2$ precursor was used for the deposition. However with the $Pb(S_2CNR_2)_2$ (R= Et, Pr, Bu and ^{i}Bu) precursors the band gap increased from the bulk value of

0.41 eV to the range 1.10 to 1.40 eV as the crystallite sizes changed to between 5.84 to 6.74 nm beyond the Bohr exciton radius of 18 nm. Due to the increased oscillator strength in these nanoparticles as a result of quantum confinement (Kung & Kung, 2004) these are expected to have higher quatum efficiencies in applications such as light emission. This is a direct consequence of the greater overlap between the electron and the hole wave functions upon size reduction. Thus making them good candidates for electronic and optical devices due to their reduced dimensions. In addition PbS and PbSe Nanoparticles present the multiple exciton generation phenomena (Alivisatos *et al*., 2002; Kung & Kung, 2004) and they can produce n excitons for each absorbed photon possessing an energy of at least 'n' multiples of the band gap energy (E_g) where n is an integer number (Li *et al*., 2009). This phenomenon is very interesting for solar cell devices.

5.3.2 Lead selenide

5.3.2.1 Structural characterization and morphology

Figures 5.9–5.11 show the XRD patterns nanoparticles/thin films formed at the water-toluene interface at room temperature, 50 °C and 70 °C for 4, 5 and 6 hours respectively. The XRD patterns can be assigned to the face-centred cubic phase of PbSe with a lattice constant of a = 6.124 Å. The major diffraction peaks at 25.0°, 29.1°, 41.7° and 49.4°, can be indexed to the (111), (200), (220) and (311) planes of cubic PbSe, which is consistent with values in the standard card (ICDD-78-1903). The preferred orientation was along the 200 plane and the intensity of the diffraction peaks increased with increasing deposition times. The calculated lattice constants given in are in good agreement with the literature value (a = 6.128A˚). The peak broadening at lower angle is more meaningful for the calculation of particle size therefore size of the nanocrystals has been calculated using Debye-Scherrer formula (Guinier, 1963) using (200), (220) and (311) reflection from the XRD pattern. The calculation gave particle sizes

ranging from 2.50 nm to 8.29 nm with dislocation densities ranging from 1.4558 to15.8223 x 10^{17} lines/m (Tables 6.4 and 6.5).

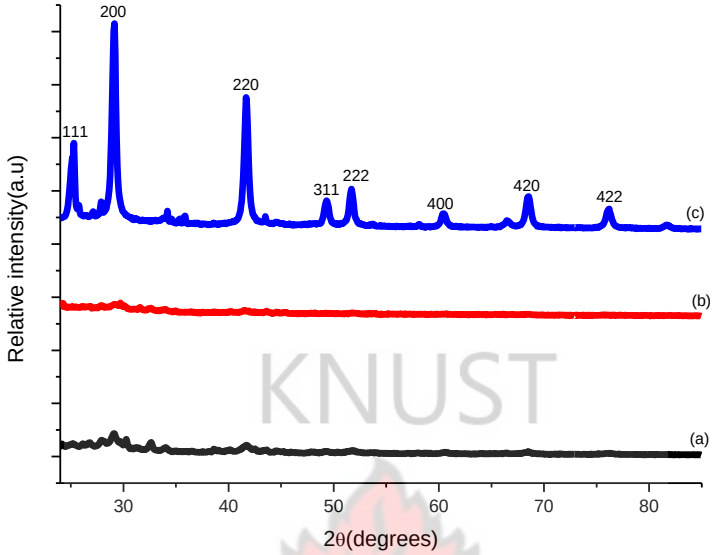

Figure 5.9: XRD of different as-prepared PbSe samples (a) for 4 hours, (b) for 5 hours and (c) 6 hours at 50 °C using lead cupferronate.

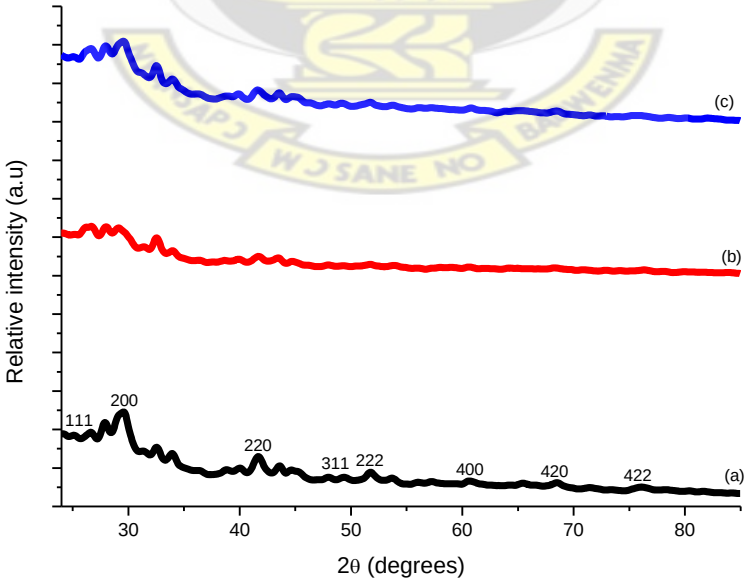

Figure 5.10: XRD of different as-prepared PbSe samples (a) for 4 hours, (b) for 5 hours and (c) 6 hours at 70 °C using lead cupferronate.

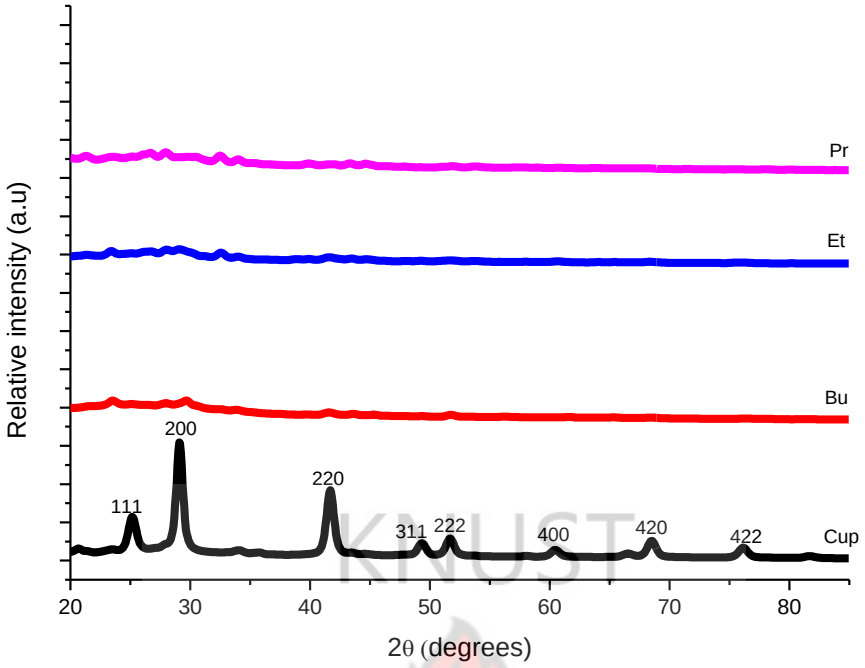

Figure 5.11: XRD of different as-prepared PbSe samples using different chain lengths of the alkyl group in the dithiocarbamate precursors and lead cupferronate precursor at 50 °C for 6 hours. (Et = ethyl; Pr = propyl; Bu = butyl; cup = lead cupferronate).

In another experiment when lead dialkyldithiocarbamate was used as the precursor under the same experimental conditions as the lead cupferronate the thin film nanoparticle produced had no clear cut morphologies and hence amorphous.

Scanning electron microscopy (SEM) studies were carried out to analyse the morphology of deposited materials. The SEM images shown in Figure 5.12 for compound deposited on glass for 5 hours at 50 °C indicates that the morphology of the PbSe thin films consisted predominantly of rods. It is also evident that the density of the particles increases as the growth temperature increases. The crystallites were scattered on the surface, which resulted in a discontinuous film. This may be a result from poor wetting between the PbSe crystallites and silicon substrate (Shandalov *et al.*, 2005).

The crystal morphology of PbSe crystals is dependent on the relative rates of growth in the (100) and (111) direction. The formation of octahedra suggests that the PbSe crystal growth is faster in the low-energy (100) direction (Houtepen *et al.,* 2006). The driving force behind the transformation from octahedrons to cubes may lie in the fact that the growth rate in the (111) direction is greater than that in the (100) direction (Petroski *et al.,* 1988, Dowty, 1976, O'Brien *et al.,* 2008). The highest growth temperature (70 °C) seems to shift crystal growth into a thermodynamic regime. These observations suggest that the growth of symmetric PbSe crystals is very sensitive to the deployed kinetic conditions in the system.

Studies to gain further insight into the mechanism of the transformation from octahedrons to cubic morphologies, have involved growth runs conducted for 5 and 10 min at 400 ^{o}C using compounds on Si/SiO_2 (100) substrates. The results indicate that after 5 min, small PbSe crystals that are truncated octahedron through their (111) facets clearly have a tendency to aggregate. The promotion of surface domains on neighbouring particles, to match up by sharing their (111) face, leads to an increase in lower-index planes and satisfies geometric criterion and dipole interactions on flow energy (Pacholski *et al.*, 2002, Korgel and Fitzmaurice, 1998, Lu *et al.*, 2004, Tang *et al.*, 2006, Harfenist *et al.*, 1997, Wang, 1998, Cho *et al.*, 2005). The evolution of truncated cubes involves the cuboctahedral seed growing along the (111) plane at a higher growth rate than that of the (100) plane. The compositional analysis of PbSe was confirmed by energy-dispersive X-ray analysis (EDAX), as shown in Figure 5.13. The ratio between the lead and selenide peaks should be nearly stoichiometric. From the graph it is noted that for a deposition time of 5 hours and deposition temperature of 50 °C, the atomic percentage of lead is 52.35 while that of sulphur is 47.65.

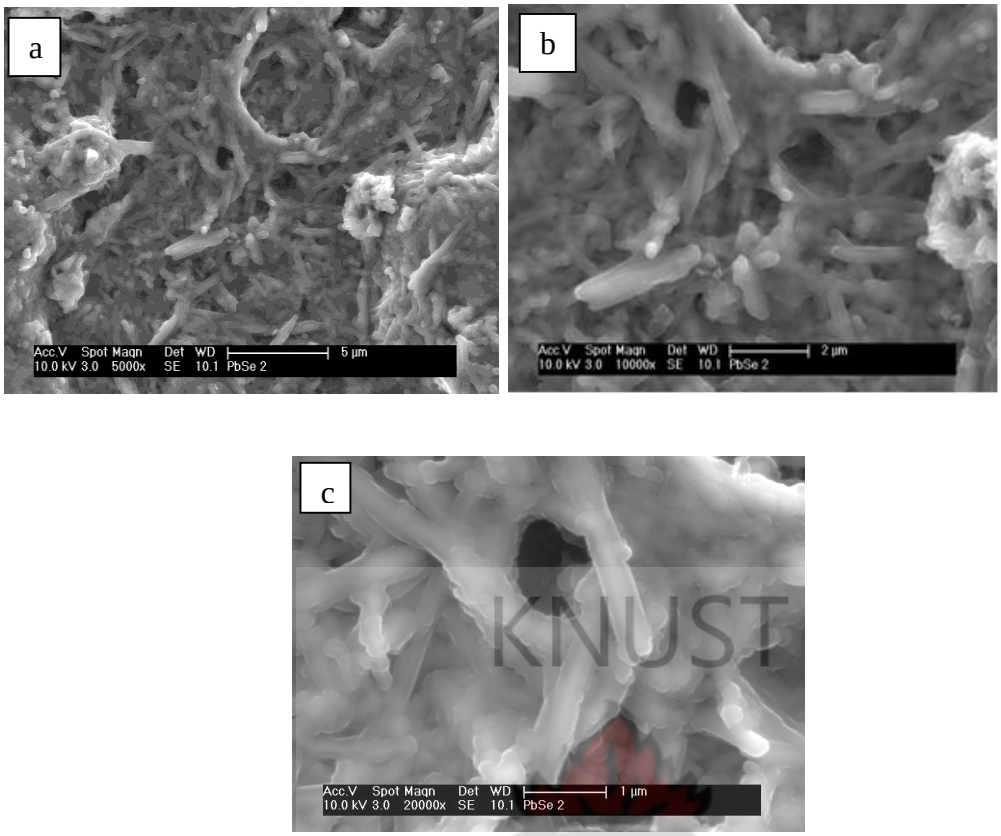

Figure 5.12: SEM image of PbSe deposited at 50 °C for 5 hours using lead cupferronate as precursor at different magnifications (a-5000x, b-10000x and c-20000x)

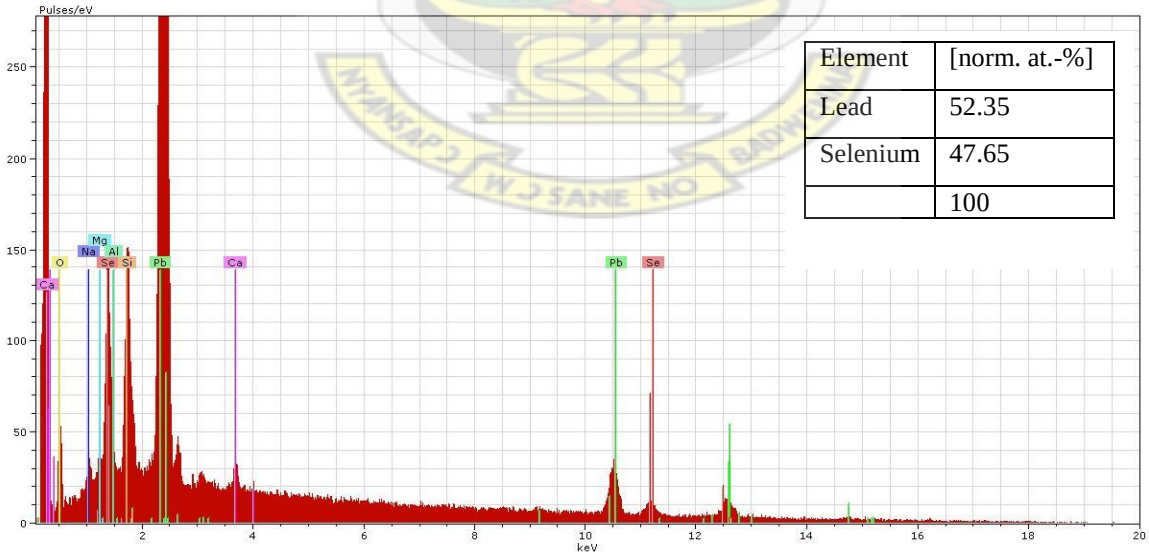

Element	[norm. at.-%]
Lead	52.35
Selenium	47.65
	100

Figure 5.13: EDAX spectra of PbSe deposited at 50 °C for 5 hours using lead cupferronate as precursor

5.3.2.2 Optical analyses

The optical absorption spectra of the nanocrystals were measured using CARY 5000 UV-Vis-NIR spectrophotometer. The optical absorption spectra have been measured at room temperature over a range of 400 to 1600 nm. The fundamental absorption corresponds to the electron excitation from the valence band to the conduction band and can be used to determine the optical band gap. The plots of $(Ah\upsilon)^2$ versus $h\upsilon$ for the different nanocrystallites obtained at 50 ^oC are given in the Figure below:

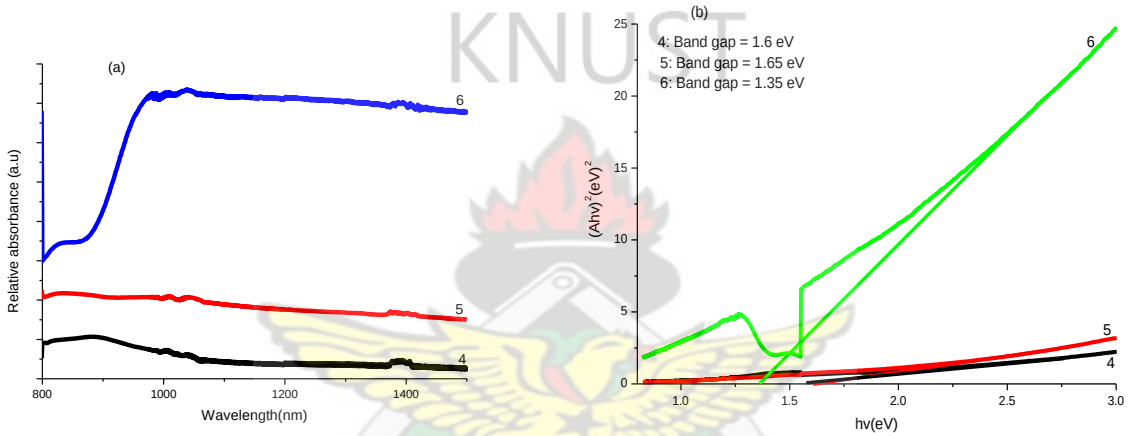

Figure 5.14: (a) Optical absorption spectra and (b) optical band gap of the as-prepared PbSe samples for 4, 5 and 6 hours at 50 °C.

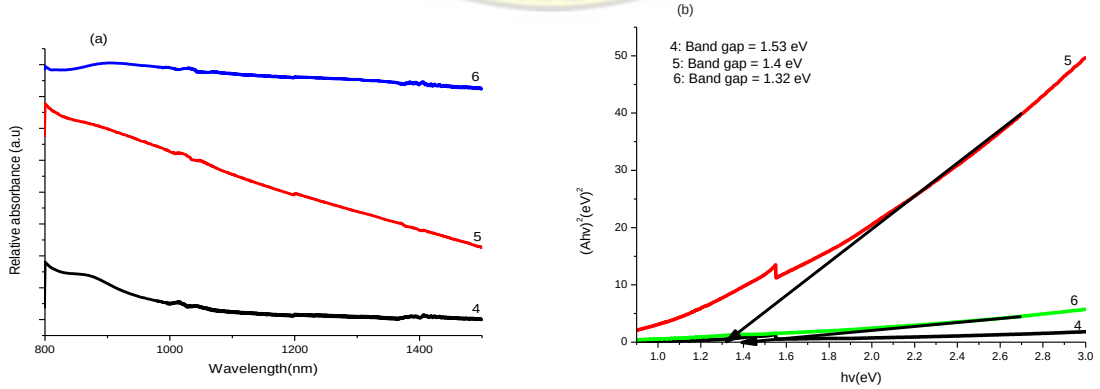

Figure 5.15: (a) Optical absorption spectra and (b) optical band gap of the as-prepared PbSe samples for 4, 5 and 6 hours at 70 °C.

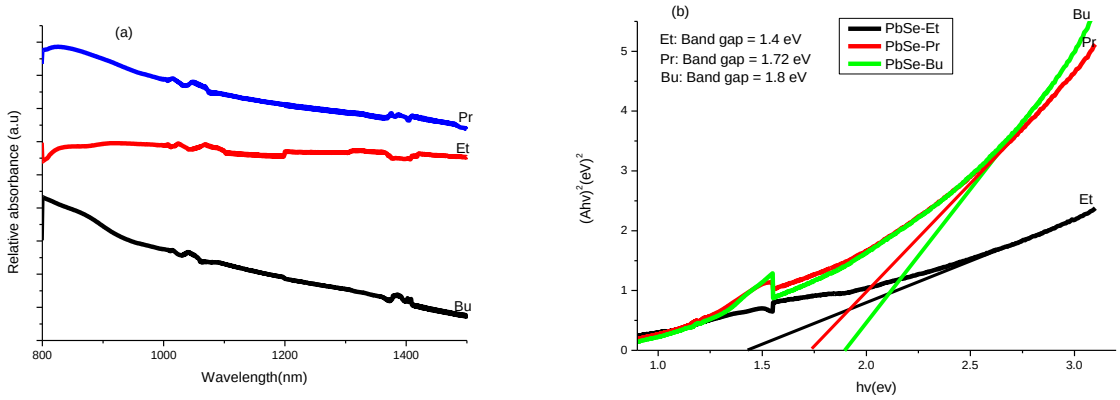

Figure 5.16: (a) Optical absorption spectra and (b) optical band gap of the as-prepared PbSe samples using different chain length of the alkyl group at 50 °C for 6 hours. (Bu = butyl; Et = ethyl; Pr = propyl)

Table 5.3 Optical parameters and crystallite sizes of PbSe nanoparticles

Precursors	Deposition Temperature/ ^{o}C	Deposition time (hrs)	Band gap of nanoparticle (eV)	Particle size (nm)	
				U.V	XRD
$Pb(cup)_2$: $Se/NaBH_4$	50	4	1.50	1.18	4.21
		5	1.65	1.23	4.53
		6	1.35	1.17	6.22
$Pb(cup)_2$: $Se/NaBH_4$	70	4	1.53	1.21	5.28
		5	1.40	1.16	6.21
		4	1.32	1.27	6.36
$Pb(S_2CNBu_2)_2$: $Se/NaBH_4$	50	6	1.80	1.21	2.51
$Pb(S_2CNPr_2)_2$: $Se/NaBH_4$	50	6	1.72	1.22	7.19
$Pb(S_2CNEt_2)_2$: $Se/NaBH_4$	50	6	1.40	1.18	8.29

Band gap of bulk PbSe = 0.29 eV

Table 5.3 gives the optical parameters and crystallite sizes of the PbSe nanoparticle thin films formed at different temperatures, deposition times and with different precursors. The band gap of PbSe nanoparticle thin films increased from the bulk value of 0.41 eV to the range 1.35 eV to 1.80 eV as the crystallite sizes changed to between 2.51 to 8.29 nm lower than the Bohr exciton radius of 18 nm.

5.3.3 Lead telluride

5.3.3.1 Structural characterization and morphology

In experiments using lead diethyldithiocabamate and tellurium, the type of PbTe nanocrystal obtained at different temperatures and reaction times varied as illustrated in Figure 5.1. This lead source gave distinct and interesting results as with the other soluble salts only spherical particles were obtained.

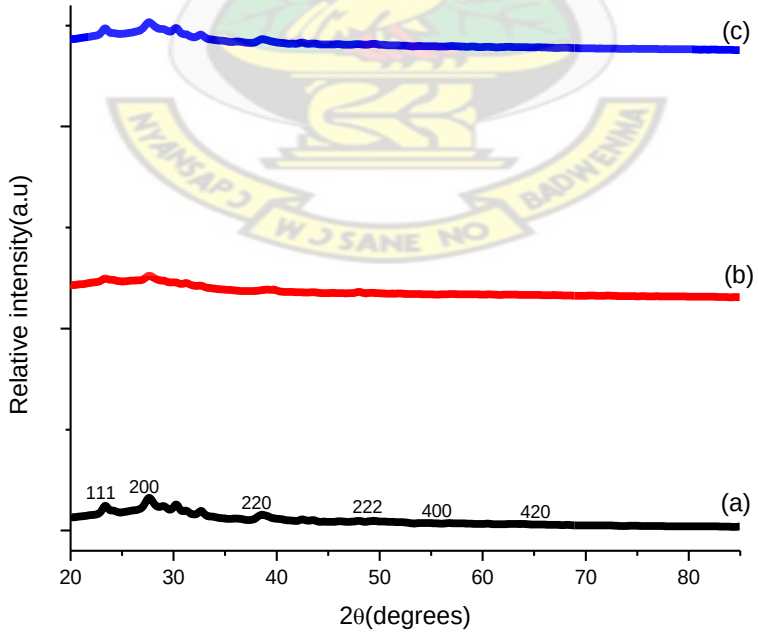

Figure 5.17: XRD of different as-prepared PbTe samples (a) for 4 hours, (b) for 5 hours and (c) 6 hours at 50 °C using lead cupferronate.

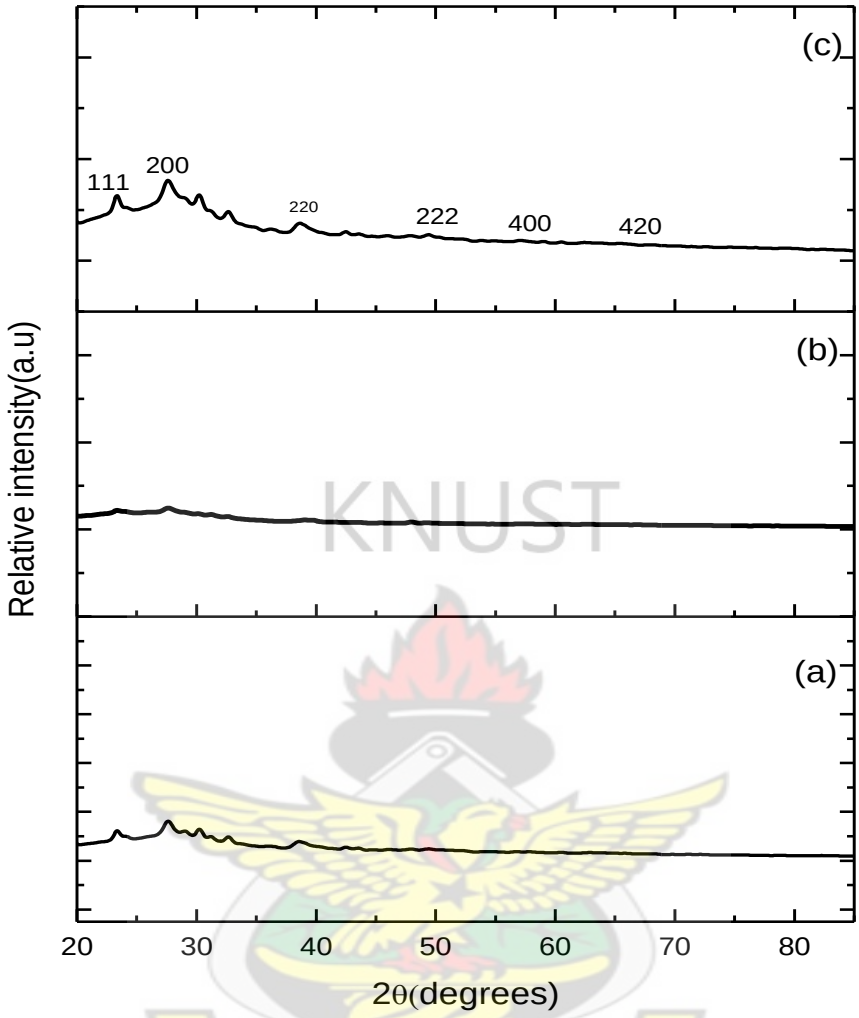

Figure 5.18: XRD of different as-prepared PbTe samples (a) at 50 °C, (b) at 60 °C and (c) at 70 °C for 6 hours using lead cupferronate.

In the halite structured lead chalcogenides, the formation of rods in which cubic symmetry is broken is really quite a common phenomenon. Close to spherical nanoparticles are minimum surface energy structures with no obvious facets. The growth rates on different facets in the system are dominated by surface energy. For halite type crystals the {111} face with high surface energy grows faster than the lower-surface- energy {100} face. Once an anisotropic structure

has started to form, it is easy for this to propagate into a rod. The crystallinity of the spheres and rods prepared has been confirmed by powder X-ray diffraction (PXRD) indicating all are halite (fcc, space group Fm3m) Figures 5.17 and 5.18. The major diffraction peaks are indexed as (200), (220), (222), (420), and (422) of cubic PbTe (ICDD no. 08-0028). The presence of oxides of Pb and Te is expected, as no special precautions to exclude oxygen were taken. The predominance of PbTe (as also by PXRD) suggests that any oxide is likely to be only on the surface and with a thickness less than the Pb 4f and Te 3d electron escape depths (< 2 nm).

5.3.3.2 Optical analyses

The optical absorption spectra of the nanocrystals were measured at room temperature over a range of 500 to 1600 nm using CARY 5000 UV-Vis-NIR spectrophotometer. The spectrum and the plots of $(Ah\upsilon)^2$ versus $h\upsilon$ for the different nanocrystallites obtained at 50 ^oC are given in the Figure 5.19.

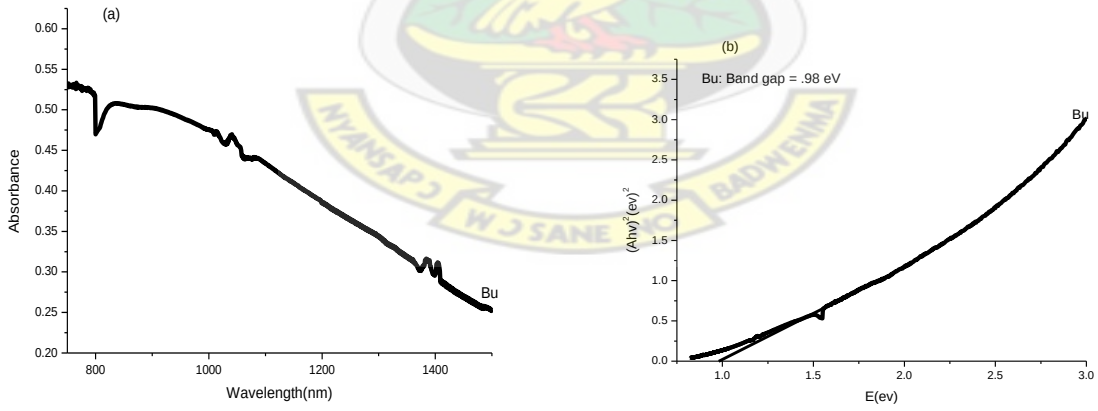

Figure 5.19: (a) Optical absorption spectra and (b) optical band gap of the as-prepared PbTe samples for 6 hours at 50 °C using lead cupferronate as precursor.

Table 5.4 Optical parameters and crystallite sizes of PbTe nanoparticles

Precursor	Deposition Temperature/^{o}C	deposition time (hrs)	Band gap of nanoparticle (eV)	Particle size (nm)	
				U.V	XRD
$Pb(Cup)_2$: $Te/NaBH_4$	50	6	0.96	3.16	5.27
$Pb(Cup)_2$: $Te/NaBH_4$	60	6	-	-	3.88
$Pb(Cup)_2$: $Te/NaBH_4$	70	6	-	-	4.25
$Pb(S_2CNBu_2)_2$: $Te/NaBH_4$	50	6	-	-	6.33

Band gap of bulk PbTe = 0.27 eV

Table 5.4 gives the optical parameters and crystallite sizes of the PbSe nanoparticle thin films formed at different temperatures, deposition times and with different precursors. The band gap of PbSe nanoparticle thin films formed at a temperature of 50 ^{o}C and deposition time of 6 hours of increased from the bulk value of 0.41 eV to 0.96 eV as the crystallite size changed to 5.27 nm lower than the Bohr exciton radius of 18 nm.

5.4 Conclusions

High-quality nanocrystals of PbS, PbSe and PbTe have been prepared by a simple route by using sulphide/selenide/telluride produced from sulphur/selenium/tellurium powder reduced with $NaBH_4$. All the materials prepared have the halite structure as confirmed by powder XRD. The average crystallite sizes of the as-prepared nanoparticles at different temperatures, concentrations and deposition times ranged from 1.8 to 6.3 nm for PbS, 2.5 to 8.3 nm for PbSe and 3.9 to 6.3 nm for PbTe. The dislocation densities ranged from 2.2 to 31.4 x 10^{17} lines/m for

PbS, 2.5 to 5.7 x 10^{17} lines/m for PbSe and 2.5 to 6.6 x 10^{17} lines/m for PbTe. The shape of the as-prepared nanoparticles at different temperatures was studied by SEM and gave morphologies from cubes to rods. The band gaps obtained for PbS ranged from 0.84 to 1.75 eV, PbSe ranged from 1.35 to 1.80 eV and 0.96 eV for PbTe. These show significant increases from the band gaps of the bulk materials of 0.41 eV, 0.29 eV and 0.27 eV for PbS, PbSe and PbTe respectively. However these are to be expected considering the large deviations from the bulk exciton radii of the bulk materials of 18 nm, 46 nm and ~46 nm for PbS, PbSe and PbTe respectively.

5.5 References

Afzaal, M. & O'Brien, P. (2006). "Silica coated PbS nanowires". *J. Mater. Chem.,* 16: 1113-1115.

Afzaal, M., Ellwood, K., Pickett, N. L., O'Brien, P., Raftery, J. & Waters, J. J. (2004). "The synthesis, X-ray structures and CVD studies of some group 11 complexes of iminobis(diisopropylphosphine selenides) and their use in the deposition of I/III/VI photovoltaic materials". *Mater Chem.,* 14: 1310-1315.

Akhtar, J., Malik, M. A., O'Brien, P. & Helliwell, M. (2010). "Controlled synthesis of PbS nanoparticles and the deposition of thin films by Aerosol-Assisted Chemical Vapour Deposition (AACVD)". *J. Mater. Chem.,* 20: 6116-6124.

Alivisatos, A. P. (1996). "Semiconductor Clusters, Nanocrystals, and Quantum Dots". *Science,* 271: 933-937.

Alivisatos, A.P., Bruchez, M., Moronne, J. M., Gin, P., Weiss, S. (1998). Semiconductor. Nanocrystals as Fluorescent Biological Labels. *Science*. 281: 2013-2016.

Alivisatos, A.P., Huynh, W. U., Dittmer, I. J. (2002). Hybrid nanorod polymer Solar cells. *Science,* 295, 2425-2427.

Allan, G. & Delerue, C. (2006). "Role of impact ionization in multiple exciton generation in PbSe nanocrystals". *Phys. Rev.* B, 73(20): 205423-205425.

Bakueva, L., Musikhin, S., Hines, M. A., Chang, T. W. F., Tzolov, M., Scholes, G. D. & Sargent, E. H. (2003). "Size-tunable infrared (1000-1600 nm) electroluminescence from PbS quantum-dot nanocrystals in a semiconducting polymer". *Appl. Phys. Lett.,* 82: 2895-2997.

Berhanu, D., Govender, K., Boyle, D. S., Archbold, M., Halliday, D. P. & O'Brien, P. (2006). "A novel soft hydrothermal (SHY) route to crystalline PbS and CdS nanoparticles exhibiting diverse morphologies". *Chem. Commun*., 45: 4709-4711.

Bierman, M. J., Lau, Y. K. A. & Jin, S. (2007). "Hyperbranched PbS and PbSe Nanowires and the Effect of Hydrogen Gas on Their Synthesis". *Nano Lett*., 7: 2907-2912.

Birdi, K. S., Ed. (1997). Handbook of Surface and Colloid Chemistry, CRC Press: New York.

Bruchez, M., J., Moronne, M., Gin, P., Weiss, S., Alivisatos, A. P. (1998). Semiconductor nanocrystals as fluorescent biological labels. *Science*. 25: 2013-2016.

Buckley, H. E. (1951). Crystal Growth, John Wiley: New York.

Buhro, W. E. & Colvin, V. L. (2003). "Semiconductor nanocrystals - Shape matters". *Nat. Mater.* 2: 138-139.

Burda, C., Chen, X. B., Narayanan, R. & El-Sayed, M. A. (2005). "Chemistry and properties of nanocrystals of different shapes". *Chem. Re*v., 105(4): 1025-1102.

Calvert, P. (1999). "Nanotube composites: A recipe for strength". *Nature*, 399: 210-211.

Chen, D. & Ye, J. H. (2008). "Hierarchical WO_3 Hollow Shells: Dendrite, Sphere and Dumbbell and Their Photocatalytic Properties". *Adv. Funct. Mater,* 18: 1922-1928.

Cheng, C. W., Xu, G. Y., Zhang, H. Q. & Luo, Y. (2007). "Fabricating ZnO Nanorods Sensor for Chemical Gas Detection at Room Temperature". *J. Nanosci. Nanotechnol.* 7: 4439-4442.

Cheng, C., Hu, G. & Zhang, H. (2009). "Facile solvothermal synthesis of nanostructured PbSe with anisotropic shape: Nanocubes, submicrometer cubes and truncated octahedron". *J. Cryst. Growth*, 311: 1285-1290.

Cho, K. S., Talapin, D. V., Gaschler, W. & Murray, C. B. (2005). "Designing PbSe nanowires and nanorings through oriented attachment of nanoparticles". *J. Am. Chem. Soc*., 127: 7140-7147.

Cui, D., Xu, J., Zhu, T., Paradee, G., Ashok, S. & Gerhold, M. (2006). "Harvest of near infrared light in PbSe nanocrystal-polymer hybrid photovoltaic cells". *Appl. Phys. Lett*. 88: 183111-183113.

Davies, J. T. & Wiggill, J. B. (1960). "Diffusion across the oil/water interface". *Proc. R. Soc. London, Ser. A*, 255: 277-291.

Dowty, E. (1976). "Crystal structure and crystal growth: I. The influence of internal structure on morphology". *Am. Miner*., 61: 448-449.

Elingson, R. J., Beard, M. C., Johnson, J. C., Shabaev, A. & Efros, A. L. (2005). "Highly efficient multiple exciton generation in colloidal PbSe and PbS quantum dots". *Nano Lett*. 5: 865-871.

Elliot, C. T. (1981). In Handbook on Semiconductors, vo1.4 (Ed. T. S. Moss), North-Holland, Amsterdam, 727.

Evstratov, I. Y., Kalaev, V. V., Zhmakin, A. I., Makarov, Y. N., Abramov, A. G., Ivanov, N. G., Smirnov, E. M., Dornberger, E., Virbulis, J., Tomzig, E. & Ammon, W. V. (2001). "The impact of nitrogen on the defect aggregation in silicon". *J. Cryst. Growth*, 230: 22-29.

Fan, D. B., Thomas, J. P. & O'Brien, P. (2008). "Pyramidal Lead Sulphide Crystallites with High Energy {113} Facets". *J. Am. Chem. Soc.*, 130: 10892-10894.

Garcia-ruiz, J. M. (1986). "Growth history of PbS single crystals at room temperature". *J. Cryst. Growth*, 75: 441-453.

Gorer, S., Albu-Yaron, A. & Hodes, G. (1995). "Quantum Size Effects in Chemically Deposited, Nanocrystalline Lead Selenide Films". *Chem. Mater*, 7: 1243-1256.

Harman, T. C., Taylor, P. J., Walsh, M. P. & Laforge, B. E. (2002). "Quantum dot superlattice thermoelectric materials and devices". *Science*, 297: 2229-2232.

Hou, Y., Kondoh, H. & Ohta, T. (2009). "PbS Cubes with Pyramidal Pits: An Example of Etching Growth". *Cryst. Growth Des.* 9: 3119-3123.

Houtepen, A. J., Koole, R., Vanmaekelbergh, D., Meeldijk, J. & Hickey, S. G. (2006). "The hidden role of acetate in the PbSe nanocrystal synthesis". *J. Am. Chem. Soc.*, 128: 6792-6793.

Hsu, K. F., Loo, S., Guo, F., Chen, W. J., Dyck, S., Usher, C., Hogan, T., Polychroniadis, E. K. & Kanatzidis, M. G. (2004). *Science*, 303, 818.

Hu, J., Odom, T. W. & Lieber, C. M. (1999). "Chemistry and Physics in One-Dimension: Synthesis and Properties of Nanowires and Nanotubes". *Acc. Chem. Res.*, 32: 435-445.

Jana, S., Goswami, S., Nandy, S. & Chattopadhyay, K. K. (2009). "Synthesis of tetrapod like PbS microcrystals by hydrothermal route and its optical Characterization". *J. Alloys Compd.* 481: 806-810.

Jun, Y. W., Lee, J. H., Choi, J. S. & Cheon, J. (2005). "Chemical design of nanoparticle probes for high-performance magnetic resonance imaging". *J. Phys. Chem. B,* 109(31): 14795-14806.

Kalyanikutty, K. P. & Rao, C. N. R. (2008). "The Liquid–Liquid Interface as a Medium to Generate Nanocrystalline Films of Inorganic Materials". *Acc. Chem. Res.*, 41: 489-499.

Kerner, R., Palchik, O. & Gedanken, A. (2001). "A Comparative Study". *Chem. Mater.*, 13: 1413-1419.

Khoklov, D. (2003). "Lead Chalcogenides: Physics and Applications Optoelectronic Properties of Semiconductors and Superlattices". *Taylor & Francis*, 18: 231-235.

Klayman, D. L. & Griffin, T. S. (1973). "Reaction of selenium with sodium borohydride in protic solvents. A facile method for the introduction of selenium into organic molecule". *J. Am. Chem. Soc*., 95: 197-199.

Kohn, S. E., Yu, F. Y., Petroff, Y., Shen. Y. R., Tsang, Y. & Cohen, M. L. (1973). "Electronic band structure and optical properties of PbTe, PbSe and PbS". *Phys. Rev. B,* 8: 1477-1488.

Korgel, B. A. & Fitzmaurice, D. (1998). "Self-Assembly of Silver Nanocrystals into Two-Dimensional Nanowire Arrays". *Adv. Mater*., 10: 661-665.

Kumar, D., Agarwal, G., Tripathi, B., Vyas, D. & Kulshrestha, V. (2009). "Characterization of PbS nanoparticles synthesized by chemical bath deposition". *J. Alloys Compd*. 484: 463-466.

Kumar, U., Sharma, S. N., Singh, S., Kar, M., Singh, V. N., Mehta, B. R. & Kakar, R. (2009). "Size- and shape-controlled synthesis and properties of colloidal PbSe nanocrystals". *Mater. Chem. Phys.*, 113: 107-114.

Kung, H. H. & Kung, M. C. (2004). Catalytic amonolysis of epoxide by alumina prepared from ammine-protected Al precursor. *Catalysis Today*, 97, 219-224.

Lau, A. Y. K., Chernak, D. J., Bierman, M. J. & Jin, S. (2009). "Formation of PbS Nanowire Pine Trees Driven by Screw Dislocations". *J. Am. Chem. Soc.* 131: 16461-16471.

Lee, S. M., Cho, S. N., Cheon, J. (2003). "Anisotropic shape control of colloidal inorganic nanocrystals". *Adv. Mater*., 15: 441-444.

Lee, S. M., Jun, Y. W., Cho, S. N. & Cheon, J. (2002). "Single-crystalline star-shaped nanocrystals and their evolution: programming the geometry of nano-building blocks". *J. Am. Chem. Soc*., 124: 11244-11245.

Li, G. R., Yao, C. Z., Lu, X. H., Zheng, F. L., Feng, Z. P., Yu, X. L., Su, C. Y. & Tong, Y. X. (2008). "Facile and efficient electrochemical synthesis of PbTe dendritic structures". *Chem. Mater*., 20: 3306-3314.

Li, S. L., Wang, H. Z., Xu, W. W., Si, H. L., Tao, X. J., Lou, S., Du, Z. & Li, S. (2009). "Synthesis and assembly of monodisperse spherical Cu_2S nanocrystals". *Journal of Colloidal and Surface Science*, 330: 483-487.

Lifshitz, E., Bashouti, M., Kloper, V., Kigel, A., Eisen, M. S. & Berger, S. (2003). "Synthesis and Characterization of PbSe Quantum Wires, Multipods, Quantum Rods, and Cubes". *Nano Lett.*, 3: 857-862.

Lin, Y., Skaff, H., Emrick, T., Dinsmore, A. D & Russell, T. P (2003). "Nanoparticles at Liquid-Liquid Interfaces: Assembly, Displacement and Transport". *Science*, 299: 226-229.

Liu, Y. F., Cao, J. B., Zeng, J. H., Li, C., Qian, Y. T. & Zhang, S. Y. (2003). *Eur. J. Inorg. Chem*., 4: 644-647.

Lu, W. G., Fan, J. Y., Stokes, K. L. & Lin, J. (2004). "Shape evolution and self-assembly of monodisperse PbTe nanocrystals". *J. Am. Chem. Soc*., 126: 11798-11799.

Lu, W. G., Fang, J. Y., Ding, Y. & Wang, Z. L. (2005). "Formation of PbSe nanocrystals: A growth toward nanocubes". *J. Phys. Chem. B*., 109: 19219-19222.

Lu, W., Gao, P., Jian, W. B., Wang, Z. L. & Fang, J. (2004). "Perfect Orientation Ordered in-Situ One-Dimensional Self-Assembly of Mn-Doped PbSe Nanocrystals". *J. Am. Chem. Soc*., 126: 14816-14821.

Ma, J., Wong, H., Kong, L. B. & Peng, K. W. (2003). "Biomimetic processing of nanocrystallite bioactive apatite coating on titanium". *Nanotech*. 14: 619-623.

Ma, J., Wong, H., Kong, L. B. & Peng, K.W. (2003). "Biomimetic processing of nanocrystallite bioactive apatite coating on titanium". *Nanotech*, 14: 619-623.

Manna, L., Milliron, D. J., Meisel, A., Scher, E. C. & Alivisatos, A. P. (2003). "Controlled growth of tetrapod-branched inorganic nanocrystals". *Nat. Mater*., 2: 382-385.

McDonald, S. A., Konstantatos, G., Zhang, S. G., Cyr, P. W., Klem, E. J. D., Levina, L. & Sargent, E. H. (2005). "Solution-processed PbS quantum dot infrared photodetectors and photovoltaics". *Nat. Mater*., 4: 138-142.

Moloto, M. J., Revaprasadu, N., Kolawole, G. A., O'Brien, P. & Malik, M. A. (2005). "The synthesis and characterization of Cu_xS_y and PbS nanoparticles from alkylthiourea lead and copper complexes". *S. Afr. J. Sci.,* 101: 463-465.

Moloto, S. N., Revaprasadu, N., Christian, P. & O'Brien, P. (2005). "Cadmium and Lead Thiosemicarbazide Complexes: Precursors for the Synthesis of CdS Nanorods and PbS nanoparticles in Chemistry of nanomaterial Synthesis and Processing". *Materials Res. Soc. Symp Proc,* 879E, Z7.4, 6.

Moore, D., Ding, Y. & Wang, Z. L. (2006). "Hierarchical Structured Nanohelices of ZnS". *Angew. Chem. Int. Ed*. 45: 5150-5154.

Moreels, I., Lambert, K., Smeets, D., Muynck, D. D., Nollet, T., Martins, J. C., Vanhaecke, F., Vantomme, A., Delerue, C., Allan, G. & Hens, Z. (2009). "Size-dependent optical properties of colloidal PbS quantum dots". *ACS Nano*., 3: 3023-3030.

Murray, C. B., Sun, S., Gaschler, W., Doyle, H., Betley, T. A., Kagan, C. R. (2001). "Colloidal synthesis of nanocrystals and nanocrystal superlattices". *Betley and CR Kagan, IBM J. Res. Dev.,* 45(1): 47-56.

Nozik, A. (2008). "Multiple exciton generation in semiconductor quantum dots". *J. Chem. Phys. Lett*., 457: 3-11.

O'Brien, P. & Nomura, R. (1995). "Single-molecule precursor chemistry for the deposition of chalcogenide (S or Se)-containing compound semiconductors by MOCVD and related methods". *J. Mater. Chem*., 5: 1761-1773.

O'Brien, P., Ahmad, K., Afzaal, M., Hua, G. & Woollins, J. D. (2010). "Morphological Evolution of PbSe Crystals via the CVD Route". *Chem. Mater*., 22(16): 4619-4624.

O'Brien, P., Thomas, P. J. & Fan, D. B. (2008). "Pyramidal Lead Sulfide Crystallites with High Energy {113} Facets". *J. Am. Chem. Soc.*, 130: 10892-10894.

O'Brien, P., Ziqubu, N., Ramasamy, K., Rajasekhar, P. V. S. R. & Revaprasadu, N. (2010). "Simple Route to Dots and Rods of PbTe Nanocrystals". *Chem. Mater*., 22: 3817-3819

Pacholski, C., Kornowski, A. & Weller, H. (2002). "Self-assembly of ZnO: from nanodots to nanorods". *Angew. Chem., Int. Ed*., 41: 1188-1191.

Pantaro, D., Partidos, C. D., Hoebeke, J., Brown, F., Kramer, E., Briand, J. P., Muller, S., Prato, M. & Pantarotto, A. (2003). *Chem. Biol*., 10: 961-966.

Pantarotto, D., Tarotto, D., Partidos, C. D., Hoebeke, J., Brown, F., Kramer, E., Briand, J. P., Muller, S., Prato, M. & Pantarotto, (2003). "A: Immunization with peptide-functionalized carbon nanotubes enhances virus-specific neutralizing antibody responses". *Chem. Biol*., 10: 961-966.

Peng, Z. P., Jiang, Y. S., Song, Y. H., Wang, C. & Zhang, H., (2008). "Morphology control of nanoscale PbS particles in a polyol process". *J. Chem. Mater*. 20: 3153-3162.

Petroski, J. M., Wang, Z. L., Green, T. C. & El-Sayed, M. A. (1998). "Kinetically controlled growth and shape formation mechanism of platinum nanoparticles". *J. Phys. Chem. B*, 102: 3316-3320.

Pietryga, J. M., Schaller, R. D., Werder, D., Stewart, M. H., Klimov, V. I. & Hollingsworth, J. A. (2004). "Pushing the band gap envelope: Mid-infrared emitting colloidal PbSe quantum dots". *J. Am. Chem. Soc*., 126: 11752-11753.

Pliny, N. H., 77 AD, Vol. 34, p 173. (b) Pliny the elder. Natural History a Selection, Penguin: London, 1991.

Purkayastha, A., Yan, Q., Gandhi, D. D., Li, H., Pattanaik, G., Borac-Tasiuc, T., Ravishankar, N. & Ramanath, G. (2008). "Ratio Single-Crystal Lead Telluride Nanorods". *Chem. Mater*. 20: 4791-4793.

Qi, D., Fischbein, M., Drndic, M. & Selmic, S. (2005). "Efficient polymer-nanocrystal quantum-dot photodetectors". *Appl. Phys. Lett.*, 86: 093103-093113.

Ramasamy, K., Nejo, A. O., Ziqubu, N., Rajasekhar, P. V. S. R., Nejo, A. A., Revaprasadu, N. & O'Brien, P. (2011). "A New Route to Lead Chalcogenide Nanocrystals". *Eur. J. Inorg. Chem.*, 33: 5196-5201.

Rao, C. N. R., Kulkarni, G. U., Agrawal, V. V., Gautam, U. K., Ghosh, M. & Tumkurkar, U. (2005). "Use of the Liquid-Liquid Interface for Generating Ultrathin Nanocrystalline Films of Metals, Chalcogenides, and Oxides". *J. Colloid Interface Sci.*, 289(2): 305-318.

Reincke, F., Kegel, W. K., Zhang, H., Nolte, M., Wang, D., Vanmaekelbergh, D. & Möhwald, H. (2006). "Understanding the self-assembly of charged nanoparticles at the water/oil interface". *Phys. Chem. Chem. Phys.*, 8: 3828-3835.

Rhodes, R., O'Brien, P. & Saunders, B. R. (2011). "Triggered aggregation of PbS nanocrystal dispersions, towards directing the morphology of hybrid polymer films using a removable bilinker ligand". *J. Colloid Interface Sci*., 358: 151-159.

Sargent, E. H. (2005). Infrared Quantum Dots. *Adv. Mater*., 17: 515-522.

Schaller, R. D., Petruska, M. A. P. & Klimov, V. I. (2003). "Tunable near-infrared optical gain and amplified spontaneous emission using PbSe nanocrystals". *J. Phys. Chem. B*, 107: 13765-13768.

Shah, A. A. & Holze, R. (2008). "Spectroelectrochemistry of two Layered Composites of Polyaniline and Poly(o-aminophenol)". *Electrochim. Acta,* 53: 4642-4653.

Shandalov, M. & Golan, Y. (2005). "Microstructure and Morphology Evolution in Chemical Solution Deposited Semiconductor Films". *Eur. Phys. J. Appl. Phys*., 31: 27-30.

Stavrinadis, A., Beal, R., Smith, J. M., Assender, H. E. & Watt, A. A. R. (2008). "Direct Formation of PbS Nanorods in a Conjugated Polymer". *Adv. Mater*. 20: 3105-3109.

Steckel, J. S., Coe-Sullivan, S., Bulovic, V. & Bawendi, M. G. (2003). "1.3 μm to 1.55 μm Tunable Electroluminescence from PbSe Quantum Dots Embedded within an Organic Device". *Adv. Mater*., 15: 1862-1866.

Stranski, I. N. (1928). "On the theory of crystal growth". *Z. Phys. Chem,* 136: 259-278.

Sun, L. F., Bao, L., Hyun, B. R., Bartnik, A. C., Zhong, Y. W, Reed, J. C., Pang, D. W., Abruna, H. D., Malliaras, G. G. & Wise, F. W. (2009). "Electrogenerated Chemiluminescence from PbS Quantum Dots". *Nano Lett.* 9: 789-793.

Sunagawa, I. (1987). Morphology of Crystals Part A, Terra Scientific and Kulwer Academic: Dordrecht.

Tang, Z. Y., Zhang, Z. L., Wang, Y., Glotzer, S. C. & Kotov, N. A. (2006). "Self-Assembly of CdTe Nanocrystals into Free-Floating Sheets". *Science,* 314: 274-278.

Tong, H., Zhu, Y. J., Yang, L. X., Li, L. & Zang, L. (2006). "Lead chalcogenide nanotubes synthesized by biomolecule-assisted self-assembly of nanocrystals at room temperature". *Angew Chem. Int. Ed*., 45: 7739-7742.

Trindade, T., Monteiro, O. C., O'Brien, P. & Motevalli, M. (1999). "Synthesis of PbSe nanocrystallites using a single-source method. The X-ray crystal structure of lead *(*II*)* diethyldiselenocarbamate". *Polyhedron,* 18: 1171-1175.

Trindade, T., O'Brien, P., Zhang, X.-M. & Motevalli, M. (1997). "Synthesis of PbS nanocrystals using a novel single molecule precursor approach: X-ray single crystal structure of $Pb(S_2CNEtPr^i)_2$". *J. Mater. Chem.,* 7: 1011-1016.

Wang, W. Z., Geng, Y., Qian, Y. T., Ji, M. R. & Liu, X. M. (1998). "A Novel Pathway to PbSe Nanowires at Room Temperature". *Adv. Mater.,* 10: 1479-1481.

Wang, Y. & Herron, N. J. (1991). "Nanometer-sized semiconductor clusters*:* materials *synthesis, quantum* size effects, *and* photophysical properties". *Phys. Chem.,* 95: 525-532.

Wang, Z. L. (1998). "Structural Analysis of Self-Assembling Nanocrystal Superlattices". *Adv. Mater*. 10: 13-30.

Warner, J. H. (2008). "Self-Assembly of Ligand-Free PbS Nanocrystals into Nanorods and Their Nanosculpturing by Electron-Beam Irradiation". *Adv*. *Mater*. 20: 784-787.

Warner, J. H., Cao, H. (2008). "Shape Control of PbS Nanocrystals Using Multiple Surfactants". *Nanotechnology*, 19(30), 305605.

Wise, F. W. (2000). "Lead salt quantum dots: the limit of strong quantum confinement". *Acc. Chem. Res*., 33: 773-780.

Xiu, Z. L., Liu, S. W., Yu, J. X., Xu, F. X., Yu, W. N. & Feng, G. J. (2008). Sonochemical synthesis of PbS nanorods. *J. Alloys Compd*. 457(1-2): 9-11.

Xu, F., Zhang, P., Navrotsky, A., Yuan, Z. Y., Ren, T. Z., Halasa, M. & Su, B. L. (2007). "Hierarchically Assembled Porous ZnO Nanoparticles: Synthesis, Surface Energy, and Photocatalytic Activity". *Chem. Mater.,* 19: 5680-5686.

Zhao, F., Mukherjee, S., Ma, J., Li, D., Elizondo, S. L. & Shi, Z. (2008). "Influence of oxygen passivation on optical properties of PbSe thin films". *Appl. Phys. Lett.,* 92: 211110-211112.

Ziqubu, N., Ramasamy, K., Rajasekhar, P. V. S. R., Revaprasadu, N. & O'Brien, P. (2010). "Simple Route to Dots and Rods of PbTe Nanocrystals". *Chem. Mater.,* 22(13): 3817-3819.

Zou, G. F., Liu, Z. P., Wang, D. B., Jiang, C. L. & Qian, Y. T. (2004). "Selected-control solvothermal synthesis of nanoscale hollow spheres and single-crystal tubes of PbTe". *Eur. J. Inorg. Chem.,* 22: 4521-4524.

CHAPTER SIX

EXPERIMENTAL METHODS AND TECHNIQUES

This chapter deals with the synthesis of the metal *bis*-(dithiocarbamate) and metal cupferronate precursors and characterization by elemental analysis, FTIR, and NMR. The synthetic procedures of nanocrystals and characterization techniques XRD, SEM and TEM have also been described. All synthetic work is carried out at the School of Chemistry, The University of Manchester, UK, in lab. 7.23.

6.1 Synthesis and characterization of precursors and nanoparticles/thin films

All reagents were purchased from Sigma-Aldrich and used as received. ^{1}H NMR spectra were obtained using a Brucker AC 400 FT-NMR spectrometer. Mass spectra were recorded on a Kratos concept 15 instrument. Infrared spectra were obtained on a single reflectance ATR instrument (4000-400 cm^{-1}). Elemental analysis was perfomed by the University of Manchester Micro-analytical facility.

X-ray diffraction studies were performed on a Brucker AXS D8 diffractometer using Cu-Kα radiation with wavelength of 1.54 nm, accelerating voltage set at 40 kV and a 40 mA flux. The samples were mounted flat and scanned between 20 to 80° in a step of 0.05 with a count rate of 7 Sec. Scanning electron microscopy, SEM was applied to investigate the morphology and this was performed using Philips XL 30 FEG analyser at 20 kV. The sample for SEM analysis was prepared by attaching the glass substrates with the nanomaterials deposited on them to aluminium stumps. They were then carbon coated with a GATAN MODEL 682 PRECISION ETCHING COATING SYSTEM. Energy dispersive X-ray analysis EDAX was carried out by the camera connected to the Philips XL 30 FEG microscope. The nano/microstructures of the ZnS, ZnSe and ZnTe products were further observed by transmission electron microscopy, TEM

with the C200 with an accelerating voltage of 200 kV. The samples used for the TEM observations were prepared by dispersing the nanoparticles in absolute ethanol followed by ultrasonic vibration for 10 minutes and then placing a drop of dispersion on to a Cu grid coated with a layer of amorphous carbon. Absorbance measurements were taken using CARY 5000 UV-Vis-NIR spectrophotometer.

6.2 Methods of syntheses

6.2.1 Synthesis of zinc dithiocarbamates

6.2.1.1 Zinc diethyldithiocarbamate

The zinc diethyldithiocarbamate was prepared using methods reported previously (O'Brien and Nomura, 1995). Briefly, $Zn(S_2CNEt_2)_2$ was prepared by adding 1.128 ml diethylamine and 0.65 ml carbon disulfide to a stirred 40 ml methanol solution of 0.42 g sodium hydroxide. The solution was then cooled to 4 ^oC using an ice bath and a 40 ml methanol solution of 0.746 g of zinc chloride was added dropwise resulting in precipitation of the dithiocarbamate as a white solid. The crude product was purified by re-crystallizing from toluene. The resulting white zinc bis-(diethyldithiocarbamate) was subjected to elemental analysis, FT-IR spectroscopic analysis, ^1H NMR analysis, and powder X-ray analysis. The elemental analysis gave the following results: Found (Calculated) [$C_8H_{20}S_2C_2N_2Zn$]: C (%) 33.30 (33.2), H (%) 5.71 (5.6), N (%) 7.63 (7.7), S (%) 35.44 (35.4), Zn (%) 18.24 (18.0). IR cm^{-1}: 2983 υ (C–H), 1502 υ (C–N), 995 υ (C–S). Figures A1 and B1 show the powder X-ray diffractogram and FT-IR spectrum respectfully of the zinc *bis*-(diethyldithiocarbamate)

6.2.1.2 Zinc dipropyldithiocarbamate

The procedure was the same as described above but this time dipropylamine was used. The elemental analysis gave the following results: Found (Calculated) [$C_8H_{20}S_2C_2N_2Zn$]: C (%) 40.24 (40.2), H (%) 6.96 (6.8), N (%) 6.70 (6.7), S (%) 30.82 (30.6), Zn (%) 15.53 (15.7). IR cm^{-1}: 2961 υ (C–H), 1460 υ (C–N), 968 υ (C–S). Figure B2 shows the FT-IR spectrum of the zinc *bis*-(dipropyldithiocarbamate).

6.2.1.3 Zinc diisopropyldithiocarbamate

The procedure was the same as described above but this time diisopropylamine was used. The elemental analysis gave the following results: Found (Calculated) [$C_8H_{20}S_2C_2N_2Zn$]: C (%) 10.31 (40.2), H (%) 3.62 (6.8), N (%) 1.21 (6.7), S (%) 14.30 (30.6), Zn (%) 36.07 (15.7).

6.2.1.4 Zinc dibutyldithiocarbamate

The procedure was the same as described above but this time dibutylamine was used. The elemental analysis gave the following results: Found (Calculated) [$C_8H_{20}S_2C_2N_2Zn$]: C (%) 45.58 (45.6), H (%) 7.87 (7.7), N (%) 5.86 (5.9), S (%) 26.94 (27.0), Zn (%) 13.1 (13.8). IR cm^{-1}: 2956 υ (C–H), 1457 υ (C–N), 934 υ (C–S). Figure B3 shows the FT-IR spectrum of the zinc *bis*-(dibutyldithiocarbamate)

6.2.1.5 Zinc diisobutyldithiocarbamate

The procedure was the same as described above but this time diisobutylamine was used. The elemental analysis gave the following results: Found (Calculated) [$C_8H_{20}S_2C_2N_2Zn$]: C (%) 33.90 (45.6), H (%) 6.34 (7.7), N (%) 4.41 (5.9), S (%) 22.42 (27.0), Zn (%) 29.67 (13.8).

6.2.1.6 Zinc ethylhexyldithiocarbamate

The procedure was the same as described above but this time ethylhexylamine was used. The elemental analysis gave the following results: Found (Calculated) [$C_8H_{20}S_2C_2N_2Zn$]: C (%) 45.53 (45.6), H (%) 7.94 (7.7), N (%) 5.97 (5.9), S (%) 27.03 (27.0), Zn (%) 13.59 (13.8). IR cm^{-1}: 2930 υ (C–H), 1492 υ (C–N), 951 υ (C–S). Figure B4 shows the FT-IR spectrum of the zinc *bis*-(diethylhexyldithiocarbamate).

6.2.2 Synthesis of copper dithiocarbamates

6.2.2.1 Copper diethyldithiocarbamate

The copper diethyldithiocarbamate was prepared using methods reported previously (O'Brien and Nomura, 1995). Briefly, $Cu(S_2CNEt_2)_2$ was prepared by adding 1.128 ml diethylamine and 0.65 ml carbon disulfide to a stirred 40 ml methanol solution of 0.42 g sodium hydroxide. The solution was then cooled to 4 ^oC using an ice bath and a 40 ml methanol solution of 1g copper nitrate was added dropwise resulting in precipitation of the dithiocarbamate as a white solid. The crude product was purified by re-crystallizing from toluene. The resulting white copper bis-(diethyldithiocarbamate) was subjected to elemental analysis, FT-IR spectroscopic analysis, Proton NMR analysis and powder X-ray analysis. The elemental analysis gave the following results: Found (Calculated) [$C_8H_{20}S_2C_2N_2Cu$]: C (%) 32.59 (33.4), H (%) 5.49 (5.6), N (%) 7.65 (7.8), S (%) 35.59 (35.6), Cu (%) 16.88 (17.6). IR cm^{-1}: 2982 υ (C–H), 1502 υ (C–N), 995 υ (C–S). Figures A2 and B5 show the powder X-ray diffractogram and FT-IR spectrum of the copper *bis*-(diethyldithiocarbamate).

6.2.2.2 Copper dipropyldithiocarbamate

The procedure was the same as described above but this time dipropylamine was used. The elemental analysis gave the following results: Found (Calculated) [$C_8H_{20}S_2C_2N_2Cu$]: C (%) 39.96 (40.42), H (%) 6.46 (6.79), N (%) 6.49 (6.74), S (%) 31.02 (30.77), Cu (%) 15.06 (15.29). IR cm^{-1}: 2958 υ (C–H), 1483 υ (C–N), 979 υ (C–S). Figure B6 shows the FT-IR spectrum of the zinc *bis*-(dipropyldithiocarbamate)

6.2.2.3 Copper diisopropyldithiocarbamate

The procedure was the same as described above but this time diisopropylamine was used. The elemental analysis gave the following results: Found (Calculated) [$C_8H_{20}S_2C_2N_2Cu$]: C (%) 30.56 (40.42), H (%) 4.85 (6.79), N (%) 4.10 (6.74), S (%) 33.20 (30.77), Cu (%) 22.58 (15.29). IR cm^{-1}: 2968 υ (C–H), 1488 υ (C–N), 1035 υ (C–S). Figure B7 shows the FT-IR spectrum of the zinc *bis*-(diisopropyldithiocarbamate)

6.2.2.4 Copper dibutyldithiocarbamate

The procedure was the same as described above but this time dibutylamine was used. The elemental analysis gave the following results: Found (Calculated) [$C_8H_{20}S_2C_2N_2Cu$]: C (%) 46.05 (45.79), H (%) 8.42 (7.69), N (%) 5.92 (5.94), S (%) 27.37 (27.11), Cu (%) 12.52 (13.47). IR cm^{-1}: 2951 υ (C–H), 1491 υ (C–N), 967 υ (C–S). Figure B8 shows the FT-IR spectrum of the copper *bis*-(dibutyldithiocarbamate)

6.2.2.5 Copper diisobutyldithiocarbamate

The procedure was the same as described above but this time diisobutylamine was used. The elemental analysis gave the following results: Found (Calculated) [$C_8H_{20}S_2C_2N_2Cu$]: C (%) 46.03 (45.79), H (%) 7.32 (7.69), N (%) 5.89 (5.94), S (%) 27.03 (27.11), Cu (%) 12.48 (13.47).

IR cm^{-1}: 2958 υ (C–H), 1499 υ (C–N), 982 υ (C–S). Figure B9 shows the FT-IR spectrum of the copper *bis*-(diisobutyldithiocarbamate).

6.2.2.6 Copper ethylhexyldithiocarbamate

The procedure was the same as described above but this time ethylhexylamine was used. The elemental analysis gave the following results: Found (Calculated) [$C_8H_{20}S_2C_2N_2Cu$]: C (%) 43.53 (45.79), H (%) 7.34 (7.69), N (%) 5.74 (5.94), S (%) 23.49 (27.11), Cu (%) 17.83 (13.47). IR cm^{-1}: 2955 υ (C–H), 1456 υ (C–N), 928 υ (C–S). Figure B10 shows the FT-IR spectrum of the copper *bis*-(ethylhexyldithiocarbamate).

6.2.3 Synthesis of cadmium dithiocarbamates

6.2.3.1 Cadmium diethyldithiocarbamate

The cadmium diethyldithiocarbamate was prepared using methods reported previously (O'Brien and Nomura, 1995). Briefly, $Cd(S_2CNEt_2)_2$ was prepared by adding 1.128 ml diethylamine and 0.65 ml carbon disulfide to a stirred 40 ml methanol solution of 0.42 g sodium hydroxide. The solution was then cooled to 4 ^oC using an ice bath and a 40 ml methanol solution of 1g Cadmium chloride was added dropwise resulting in precipitation of the dithiocarbamate as a white solid. The crude product was purified by re-crystallizing from toluene. The resulting yellow Cadmium bis-(diethyldithiocarbamate) was subjected to elemental analysis, FT-IR spectroscopic analysis, ^1H NMR analysis, and powder X-ray analysis. The elemental analysis gave the following results: Found (Calculated) [$C_8H_{20}S_2C_2N_2Cd$]: C (%) 29.34 (29.4), H (%) 4.89 (4.9), N (%) 6.74 (6.9), S (%) 31.20 (31.4), Cd (%) 26.26 (27.5). IR cm^{-1}: 2974 υ (C–H), 1495 υ (C–N), 985 υ (C–S). Figures A4 and B11 show the powder X-ray diffractogram and FT-IR spectrum respectfully of the cadmium *bis*-(diethyldithiocarbamate)

6.2.3.2 Cadmium dipropyldithiocarbamate

The procedure was the same as described above but this time dipropylamine was used. The elemental analysis gave the following results: Found (Calculated) [$C_8H_{20}S_2C_2N_2Cd$]: C (%) 36.47 (36.2), H (%) 5.71 (6.1), N (%) 5.98 (6.0), S (%) 27.68 (27.53), Cd (%) 23.94 (24.2). IR cm^{-1}: 2957 υ (C–H), 1491 υ (C–N), 967 υ (C–S). Figure B12 show the FT-IR spectrum of the cadmium *bis*-(dipropyldithiocarbamate).

6.2.3.3 Cadmium dibutyldithiocarbamate

The procedure was the same as described above but this time dibutylamine was used. The elemental analysis gave the following results: Found (Calculated) [$C_8H_{20}S_2C_2N_2Cd$]: C (%) 40.96 (41.49), H (%) 6.61 (6.97), N (%) 5.20 (5.38), S (%) 24.33 (24.57), Cd (%) 19.72 (21.59). IR cm^{-1}: 2957 υ (C–H), 1490 υ (C–N), 950 υ (C–S). Figure B13 shows the FT-IR spectrum of the cadmium *bis*-(dibutyldithiocarbamate).

6.2.3.4 Cadmium diisobutyldithiocarbamate

The procedure was the same as described above but this time diisobutylamine was used. The elemental analysis gave the following results: Found (Calculated) [$C_8H_{20}S_2C_2N_2Cd$]: C (%) 41.97 (41.49), H (%) 7.29 (6.97), N (%) 5.28 (5.38), S (%) 24.69 (24.57), Cd (%) 21.00 (21.59). IR cm^{-1}: 2958 υ (C–H), 1488 υ (C–N), 978 υ (C–S). Figure B14 shows the FT-IR spectrum of the cadmium *bis*-(diisobutyldithiocarbamate).

6.2.3.5 Cadmium ethylhexyldithiocarbamate

The procedure was the same as described above but this time ethylhexylamine was used. The elemental analysis gave the following results: Found (Calculated) [$C_8H_{20}S_2C_2N_2Cd$]: C (%) 27.67 (41.49), H (%) 4.80 (6.97), N (%) 3.37 (5.38), S (%) 23.70 (24.57), Cd (%) 41.17(21.59).

IR cm^{-1}: 2956 υ (C–H), 1461 υ (C–N), 932 υ (C–S). Figure B15 shows the FT-IR spectrum of the cadmium *bis*-(diethylhexyldithiocarbamate).

6.2.4 Synthesis of lead dithiocarbamates

6.2.4.1 Lead diethylthiocarbamate

The lead diethylthiocarbamate was prepared using methods reported previously (O'Brien and Nomura, 1995). Briefly, $Pb(S_2CNEt_2)_2$ was prepared by adding 1.128 ml diethylamine and 0.65 ml carbon disulfide to a stirred 40 ml methanol solution of 0.42 g sodium hydroxide. The solution was then cooled to 4 ºC using an ice bath and a 40 ml methanol solution of 1g lead acetate was added dropwise resulting in precipitation of the dithiocarbamate as a white solid. The crude product was purified by re-crystallizing from toluene. The resulting white lead bis-(diethyldithiocarbamate) was subjected to elemental analysis, FT-IR spectroscopic analysis, Proton NMR analysis and powder X-ray analysis. The elemental analysis gave the following results: Found (Calculated) [$C_8H_{20}S_2C_2N_2Pb$]: C (%) 24.12 (23.84), H (%) 3.92 (4.00), N (%) 5.47 (5.6), S (%) 25.54 (25.4), Pb (%) 40.67 (41.2). IR cm^{-1}: 2962 υ (C–H), 1479 υ (C–N), 980 υ (C–S). Figures A5 and B16 show the powder X-ray diffractogram and FT-IR spectrum respectively of the lead *bis*-(diethyldithiocarbamate).

6.2.4.2 Lead dipropyldithiocarbamate

The procedure was the same as described above but this time dipropylamine was used. The elemental analysis gave the following results: Found (Calculated) [$C_8H_{20}S_2C_2N_2Pb$]: C (%) 30.0 (30.04), H (%) 5.01 (5.05), N (%) 4.90 (5.01), S (%) 22.92 (22.87), Pb (%) 35.62 (37.05). IR cm^{-1}: 2956 υ (C–H), 1475 υ (C–N), 1009 υ (C–S). Figure B17 shows the FT-IR spectrum of the lead *bis*-(dipropyldithiocarbamate).

6.2.4.3 Lead diisopropyldithiocarbamate

The procedure was the same as described above but this time diisopropylamine was used. The elemental analysis gave the following results: Found (Calculated) [$C_8H_{20}S_2C_2N_2Pb$]: C (%) 12.53 (30.04), H (%) 2.40 (5.05), N (%) 0.25 (5.01), S (%) 26.16 (22.87), Pb (%) 37.32 (37.05). IR cm^{-1}: 2963 υ (C–H), 1430 υ (C–N), 1013 υ (C–S). Figure B18 shows the FT-IR spectrum of the lead *bis*-(diisopropyldithiocarbamate).

6.2.4.4 Lead dibutyldithiocarbamate

The procedure was the same as described above but this time dibutylamine was used. The elemental analysis gave the following results: Found (Calculated) [$C_8H_{20}S_2C_2N_2Pb$]: C (%) 35.27 (35.1), H (%) 6.07 (5.90), N (%) 4.55 (4.55), S (%) 20.80 (20.78), Pb (%) 33.56 (33.67). IR cm^{-1}: 2955 υ (C–H), 1474 υ (C–N), 949 υ (C–S). Figure B19 shows the FT-IR spectrum of the lead *bis*-(dibutyldithiocarbamate).

6.2.4.5 Lead diisobutyldithiocarbamate

The procedure was the same as described above but this time diisobutylamine was used. The elemental analysis gave the following results: Found (Calculated) [$C_8H_{20}S_2C_2N_2Pb$]: C (%) 35.36 (35.1), H (%) 6.07 (5.90), N (%) 4.40 (4.55), S (%) 20.80 (20.78), Pb (%) 31.59 (33.67). IR cm^{-1}: 2953 υ (C–H), 1472 υ (C–N), 973 υ (C–S). Figure B20 shows the FT-IR spectrum of the lead *bis*-(diisobutyldithiocarbamate).

6.3.1 Synthesis of zinc cupferronates

The zinc cupferronate was prepared using methods reported previously (Kalyanikutty *et al.*, 2007). Briefly, $Zn(cup)_2$ was prepared by solubulizing 1.5 g of cupferron in 60 ml of distilled water and cooled to 0 °C in an ice bath. 5.51 mM of Zinc chloride was dissolved in 25 ml of distilled water and cooled to 0 °C in an ice bath. The solubulized cupferron solution was added to the ice cold zinc chloride solution dropwise with vigorous stirring. The precipitate of zinc cupferronate was filtered washed with 2.5% ammonia solution followed by distilled water to remove excess cupferron and then dried. The precipitate was characterized by chemical analysis which yielded the following: Found (calculated) C % 39.86 (42.4), H % 3.33(3.0), N % 17.61 % (16.5) %, Zn % 18.22 (19.3). IR cm^{-1}: 1461 υ (C–N), 1337 υ (N–N), 1220 υ (N–O), 928 υ (ring vibration), 755 υ (C–H-ring). Figure B21 shows the FT-IR spectrum of the zinc cupferronate.

6.3.2 Synthesis of copper cupferronates

The procedure was the same as described above but this time a copper nitrate was used. The elemental analysis gave the following results: Found (calculated) C % 43.01 (42.7), H % 2.84 (3.0), N % 16.55 % (16.6) %, Cu % 17.83 (18.8). IR cm^{-1}: 1463 υ (C–N), 1352 υ (N–N), 1200 υ (N–O), 931 υ (ring vibration), 760 υ (C–H-ring). Figures A5 and B22 show the powder X-ray diffractogram and FT-IR spectrum of the copper cupferronate.

6.3.3 Synthesis of cadmium cupferronates

The procedure was the same as described above but this time a cadmium Chloride was used,: Found (calculated) C % 36.58 (37.3), H % 2.75 (2.6), N % 14.34 % (14.6) %, Cd % 28.23 (29.1). IR cm^{-1}: 1462 υ (C–N), 1363 υ (N–N), 1229 υ (N–O), 921 υ (ring vibration), 745 υ (C–H-ring). Figure B23 shows the FT-IR spectrum of the cadmium cupferronate.

6.3.4 Synthesis of lead cupferronates

The procedure was the same as described above but this time a lead acetate was used Found (calculated) C % 28.40 (29.9), H % 2.0 (2.1), N % 10.79 % (11.6) %, Pb % 45.08 (43.1). IR cm^{-1}: 1461 υ (C–N), 1333 υ (N–N), 1275 υ (N–O), 910 υ (ring vibration), 756 υ (C–H-ring). Figure B24 shows the FT-IR spectrum of the lead cupferronate.

6.3.5 Synthesis of sodium selenosulphate

Sodium selenosulphate was prepared utilizing a method reported previously (Gorer and Hodes, 1994; Singh *et al*., 2011). A 50 ml aqueous dispersion containing 1 g Se powder (0.0127 mol) and 10 g (0.079 mol) sodium sulphite was heated under reflux in a round bottomed flask at 70 ^{o}C for 24 hours to obtain a nearly clear reddish solution. The solution was cooled to room temperatuire and a small quantity of insoluble particles filtered off to obtain a solution of sodium selenosulphate.

6.4 Deposition of nanomaterial/thin films

6.4.1 Deposition of nanomaterial/thin films with borohydride reduced chalcogenides

0.212 mmol of Sodium borohydride (8.0 mg) was dissolved in 1 ml ultrapure water in a 20 ml glass vial, and then 0.101mmol of selenium powder (7.99 mg) was added. The vial was sealed quickly with parafilm having a small hole allowing air circulation between flask and atmosphere, and then was placed in an ice bath. A rapid reaction evolved hydrogen in the flask. Approximately 30 minutes later, the black selenium powder disappeared completely and NaHSe was formed (Klayman and Griffin, 1973; Lan *et al*., 2007; Chen *et al.*, 2000). The resulting clear aqueous solution was transferred carefully, using a syringe, into 30 ml of degassed water in a

100 ml beaker. 30 ml of toluene containing 0.10 mM of precursor was gradually layered on top of the selenium solution in the beaker. The same procedure was employed for tellurium powder.

For the metal sulphide films the procedure was slightly different. i.e. Sodium borohydride 0.0303 g (0.80 mM) was dissolved in 1 ml of ethanol in a 20 ml glass vial, and then 0.0198772 g (0.62 mmols) of sulphur powder was added. The resulting clear aqueous solution was transferred carefully, using a syringe, into 30 ml of degassed water in a 100 ml beaker. 30 ml of toluene containing 0.10 mM of precursor was gradually layered on top of the selenium solution in the beaker.

The deposits at the interface were isolated by gently lifting the film from the interface using the glass substrates. Depositions at different temperatures were carried out by placing the reaction vessel in an oven preheated to the desired temperature. The reactions were carried out in a 100 ml beaker, with the height of the liquid columns at 4 cm. The deposition occur by via a metathesis reaction as shown by equations (iia) and (iib) below.

(i) $4NaBH_4 + 2E + 7H_2O \rightarrow 2NaHE + Na_2B_4O_7 + 14H_2$

(iia) $2NaHE + M(dtc)_2 \rightarrow ME + 2Na(dtc) + H_2E$

(iib) $2NaHE + M(cup)_2 \rightarrow ME + 2Na(cup) + H_2E$

Where E = S/Se/Te ; M = Zn/Cu/Cd/Pb

6.4.2 Deposition of nanomaterial/thin films using Sodium selenosulphate

Metal selenide nanomaterial/thin films were prepared by layering 30 ml of toluene containing 0.10 mM of metal cupferronate/dialkyldithiocarbamate precursor over 30 ml of freshly prepared solution of sodium selenosulphate whose pH was adjusted to below 10 using aqueous KOH in the beaker. The beaker containing the liquids was introduced into an oven held at 50 ^oC and left

undisturbed for 8 hours. At the end of this time a brown film was found adhered to the interface of the two liquids. The interfacial deposits transferred intact to glass substrates by contact transfer. Prior to the transfer, the organic layer at the top was gently decanted.

6.5 Characterization techniques

6.5.1 X-ray diffraction

The principles of X-ray diffraction are based on the theory of X-ray crystallography, which were first proposed by Max von Laue in 1912, and published in 1913 (von Laue,1913), as a result of experiments aimed at studying the interaction of X-rays with single crystals. Von Laue was awarded the Nobel Prize for physics in 1914 as a result of this work. Based on these early experiments, in 1919, Hull (Hull, 1919) presented a paper entitled "A New Method of Chemical Analysis", in which he described the fundamental concepts of modern X-ray diffraction, and was able to state: "….*every crystalline substance gives a pattern; the same substance always gives the same pattern; and in a mixture of substances each produces its pattern independently of the others*". The X-ray diffraction pattern of any individual substance is therefore like a precise fingerprint of that substance, and also, these precise fingerprints can be readily identified even in complex mixtures of compounds. XRD techniques are therefore ideally suited to the identification and characterisation of 'unknown' powders. Furthermore, with suitable instruments, since the usual sample preparation technique for powder samples involves packing the sample into a holder to provide a flat surface, the technique is also directly applicable to the precise analysis of thin films and corrosion deposits.

The operating principles of a modern XRD machine are still based on the fundamental experiments reported by von Laue (von Laue,1913) in 1913, and the first practical X-Ray diffraction apparatus was described by Davey (Davey,1921) in 1921. When X-rays interact with

any solid material, the resultant scattered beams can 'add together' in a few directions, and thereby reinforce each other to yield diffraction. Diffraction therefore occurs when the scattered waves are moving 'in phase' with each other. This phenomenon is termed 'constructive interference', and therefore the degree of regularity of the material is responsible for the diffraction of the beams, and the diffraction pattern generated by any substance is therefore absolutely characteristic of, and specific to that compound. The fact that the material must possess a regular periodic structure as a fundamental prerequisite in causing constructive interference, means that X-ray diffraction only occurs with, and can only be applied to, crystalline substances. A full discussion of the theory of X-ray diffraction is beyond the scope of this Section introduction, but a brief summary of the essential operating principles and theory will be given. There are several recent comprehensive reviews available in the literatures which give a full account of the theory and operating principles of X-ray diffraction techniques (Warren, 1990; Chung and Smith, 1999). In addition, several extensive reviews are available that discuss fully the specific applications of XRD techniques in the area of materials science, and also to the identification of deposit layers and powders (Pecharsky and Zavalij, 2005; Suryanarayana and Norton, 1998).

As stated above, XRD techniques are only applicable to crystalline materials. A crystal can be defined as comprised of a regular repeated array of identical lattice points which can be atoms, ions or molecules. The lattice is effectively infinite. The smallest unit of the crystal structure, which reflects the overall shape of the crystal, is called the unit cell. There are only seven basic shapes of unit cell, and these form the seven essential crystal systems, which are: cubic, tetragonal, orthorhombic, hexagonal, monoclinic, rhombohedral (trigonal) and triclinic. Note that only these seven basic shapes can exist, since there are only seven ways in which atoms etc. can be packed together to form a space filling lattice. However, sometimes, extra lattice points occur, for example when there may be an atom in the centre of a face or in the centre of the unit

cell. When these extra lattice points are combined with the seven crystal systems, this results in 14 possible Bravais lattices. All crystalline materials fall into one of these groups, although they can be of different sizes and can have different aspect ratios within the constraints of symmetry. The full symmetry of a crystal lattice is described by the space cell, which relates the symmetry of the unit cell to those around it. There are 230 space groups.

Since crystals consist of lots of unit cells packed together to form a regular array, it will be evident that there will be planes of atoms, called lattice planes that exist at the basic structural level. The spacing of these lattice planes are called *d*-planes, and these spacings are measured in Ångstroms (10^{-10} m). The process of X-ray diffraction actually measures these *d*-spacings, and from this information it is possible to determine the size and shape of the crystal, and in turn; the crystal structure is determined by the composition of the material. This information therefore allows a precise identification of the material, usually by comparing any diffraction pattern that is obtained for a particular substance with a library or data-base of known patterns.

A coherent beam of monochromatic X-rays of known wavelength is required for XRD analysis. Striking a pure anode of a particular metal with high-energy electrons in a sealed vacuum tube generates X-rays that may be used for X-ray diffraction. The wavelengths of the X-rays produced are dependent on the anode material of the X-ray tube. Most X-ray tubes used for X-ray diffraction of inorganic materials use a copper anode, although a cobalt anode is used mainly for ferrous samples. The X-ray spectrum produced by any tube consists of two parts; these are the continuous radiation, which is unwanted, and the characteristic lines. It is the strongest characteristic line, the K_α, which is used for X-ray diffraction, and all other unwanted lines and radiation are usually removed using filters, or a device known as a monochromator. The K_α line for X-rays generated from a copper anode is 1.54 Å. X-rays are normally characterised by their wavelength or their energy which can be connected by the following relation:

$E = h\,c\,f$ …… (6.1)

Where: E = the energy; h = the Planck's constant (6.62559 x 10-27erg sec); c = the velocity of light (3 x 10^{10} cm/sec); λ = the wavelength.

Following the above discussion and for ease of explanation; X-rays can be considered as a beam of particles called photons, and each photon has its particular energy which can be calculated according to the following relation:

$E = h \times f$ …… (6.2)

Where: f = the frequency of the wave.

A main component of a typical X-ray diffraction instrument, commonly called a Diffractometer, are shown in Figure 6.2. The essential parts of a diffractometer consist of only five main parts: X-ray tube used to generate the X-ray beam; the 'primary optics' between the X-ray tube and the sample, which consists of a tube mainly containing a series of slits that regulates the area of the sample being irradiated; the sample holder; the 'secondary optics' between the sample and the detector, which consists primarily of a set of receiving slits that control resolution, together with a curved crystal monochromator; the detector.

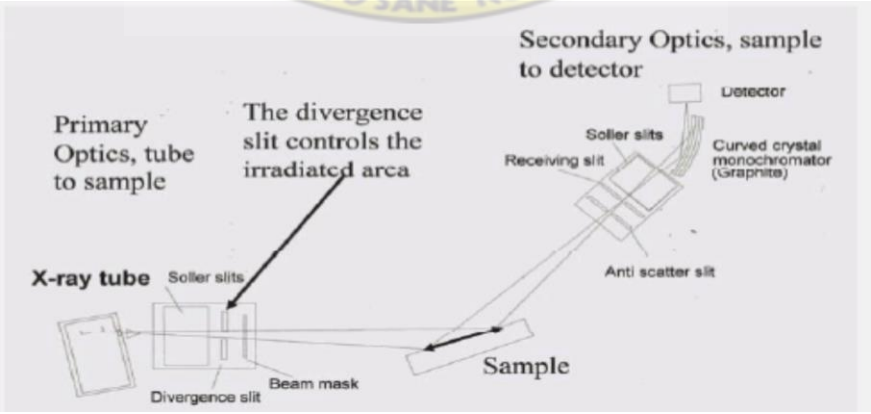

Figure 6.1 Diffractometer (Davey, 1921)

During operation, the sample is irradiated by the X-ray beam, and the detector is then moved through a specific angle: *2θ*, known as the Bragg angle, whilst continuously collecting the X-ray diffraction pattern. The Bragg angle is given by Bragg's Law, which describes the angle at which a beam of X-rays of a particular wavelength diffracts from a crystalline surface. Bragg's Law is as follows:

$\lambda = 2d \sin\theta$ …… (6.3)

Where: θ = Bragg angle; λ = is the incident wavelength; *d* = is the spacing between different planes, as atoms in any crystal materials are arranged in a specific way to form various planes and the spacing between such planes can be used to calculate the wavelength. This relationship is illustrated diagrammatically in Figure 6.2.

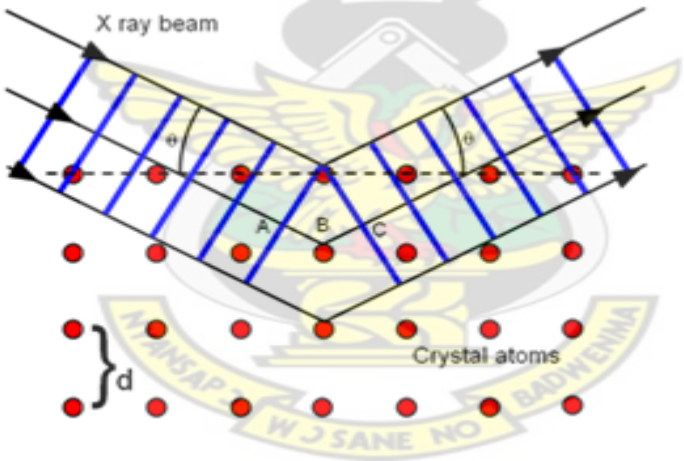

Figure 6.2: A schematic diagram for the Bragg's Law

Based on Bragg's law (Equation 6.3), we can measure the Bragg angle (2θ). This is the position of the Bragg reflection, or peak. Then, since we know the wavelength (λ), of the X-rays, we can then calculate the *d*-spacing (the distance between different planes in the crystal) from Bragg's Law. The *d*-spacing is characteristic of the compound under investigation and the calculated

values of the *d*-spacing can be matched against a data bank that is stored digitally in the hard-drive of the XRD machine (currently approximately 120,000 compounds – this will be discussed later). The diffraction results are in the form of a unique series of reflections, which form the diffraction pattern. Consequently, the exact composition of any compounds can be identified. A typical X-ray diffraction pattern is in the form of a graph, with a series of peaks (the actual diffraction pattern), with the horizontal axis being 2θ, or twice the Bragg angle; and the vertical axis is the intensity, or the X-ray count measured by the detector, which is a function of the crystal structure and the orientation of the crystallites. Note that in reality, although the diffraction pattern is given as a 2-dimentional graph, the radiation diffracted by any sample is in the form of cones, known as Debye Cones. To analyse a thin layer the angle of incidence of the incoming X-radiation must be fixed at a low angle, typically around 3º, sometimes referred to as ω, so that it skims through the top layer and does not penetrate into the substrate. Also, different X-ray optics must be used, the sample must also be flat, and quite large (ideally > 5.0 mm across). Once obtained and stored, diffraction patterns are compared with known patterns held in a database known as the Powder Diffraction Data Base (PDF), this currently holds over 120,000 entries, gathered over the last 50 years!.

6.5.2 Scanning electron microscopy (SEM) and energy-dispersive X-ray analysis (EDAX)

6.5.2.1 Introduction

The technique of Scanning Electron Microscopy (SEM) was employed in this study to obtain images of the morphology the as-deposited nanomaterials. The associated analytical facility of Energy Dispersive X-ray (EDAX) analysis was used to identify and quantify the elemental composition of the as-deposited nanomaterials. It should be noted, that these different techniques are essentially part of one instrument: the EDAX facility (basically an X-ray detector and associated software) is incorporated intimately as part of the SEM itself, and cannot function

without the operation of the SEM, since the generation of the analytical X-ray signal is dependent on the interaction between the incident electron beam and the sample in the SEM. Note also that the acronyms EDAX and EDS (Energy Dispersive Spectrometer) are often used interchangeably in place of EDAX by different instrument manufacturers but are essentially the same technique. Therefore, collectively, these techniques (SEM and EDAX) were considered one of the major procedures that were used to conduct this research. A brief description and discussion of the operating principles and capabilities respectively of these essential techniques is given in the following Sections. Both Goldstein *et al*., (2002) and Echlin (2009) have recently given a comprehensive account of the theory, operating principles and capabilities of SEM and EDAX.

6.5.2.2 Basic principles of scanning electron microscopy (SEM)

A microscope is an instrument that allows images to be obtained of a sample at magnifications greater than 30 times life-size (the term 'macro' is applied to instruments that image at magnifications from 5 X to 30 X). Since the recent development of new innovative instruments such as the Atomic force microscope (AFM) and the acoustic microscope, the older definitions of a microscope as being based on instruments that utilize optical systems (either light-rays or electron beams) for imaging at magnification above 30X are no longer applicable. There are three main types of electron microscope, these are: the Scanning electron microscope (SEM), the Transmission electron microscope (TEM) and instruments that have a dual function capability: – the Scanning-transmission electron microscope (STEM). Only the SEM will be discussed here. Essentially, in a Scanning electron microscope, a beam of electrons is generated by an electron gun in a high vacuum column, at an accelerating voltage of between 1.0 to 30 kV, but usually within the range 5.0 kV to 20 kV, then collimated into a coherent beam, using a system of electromagnetic coils or lenses; then passed down through the main electron gun column into the specimen chamber, where it is focused into a fine spot, then scanned rapidly

over the surface of the sample. Two processes then occur simultaneously: secondary electrons are emitted from the sample as a result of ionization processes, and in addition, some electrons from the primary beam (generated by the electron gun), are reflected or 'bounced back' from the sample as a result of interactions with the nuclei of the elements of the sample. These latter electrons are termed 'backscattered electrons' or the BSE signal. Both types of electrons are then collected separately by a specific type of electron detector, and the resulting signals are then processed, amplified and displayed to give an image which can then either be viewed and/or stored digitally. Secondary electron detectors are normally a combined scintillator and photo-multiplier system, known as an Everhart-Thornley detector which is mounted to one side of the specimen stage; whilst most modern BSE detectors are a compact semiconductor design and mounted directly onto the final electron objective of the microscope (i.e. immediately above the sample). Generally, secondary electron (SE) images are used to give high resolution images of the sample surfaces as three-dimensional surface topography, with good depth of field; whilst BSE images can provide useful analytical information about the sample, since the electrons from the primary beam that are backscattered have interacted with the atoms of the sample. BSE images at 8 kV give good 'orientation contrast', whilst BSE images at 20 kV give atomic number contrast, since the intensity of the BSE signal is strongly related to the atomic number (Z) of the specimen, the BSE images can provide information about the elemental composition in the sample surface, or the near-surface region (~ 1.0 to 2.0 μm). Figure 6.18 illustrates schematically the main SEM instrument that was used throughout this study.

There are several types of SEM instrument available, which vary either in terms of the type of electron gun used to produce the primary beam of electrons, or in either/both the type of vacuum system and electron detector used to collect the emitted/reflected electrons. There are three types of electron gun in common use – two of these are 'thermionic'; i.e. where electrons are generated as a result of emission through heat – most typically by a heated (to ~ 2000 – 2700 K) thin (~

100 μm diameter) tungsten wire or filament formed into a 'hairpin' shape, which emits electrons and these are attracted and channelled by a charged anode, then passed through an electron optics system of electromagnetic coils to give a coherent beam of electrons. The second type of thermionic electron gun is a lanthanum hexaboride (LaB_6) type, which also operates on a 'thermal' principle to emit electrons, but is much more efficient than a basic heated filament. The third and most efficient type of electron producing source is a Field Emission Gun (FEG) type, which consists of a very sharp tungsten tip situated adjacent to a high electric field (a highly charged anode) and electrons then 'tunnel' out of the tip. Such a system is not 'thermal' (although most currently available FEG guns also heat the tungsten tip to improve efficiency) and is extremely efficient since the energy distribution of a FEG system is much narrower than the two 'thermal' filament types. Although the filaments in thermal electron guns are cheap to replace, they have low brightness, a limited lifetime (~150 hours) and large energy spread. In contrast, a FEG tip will last for about 2 years of constant operation, but costs around three thousand pounds. Most of the SEM investigations in this study were undertaken using a FEI (Phillips) XL-30 FEG SEM (Figure 6.3).

One disadvantage of most SEM instruments, is that the electron gun (especially a FEG – tip) must always operate in an extremely high vacuum, and any specimen being examined must be electrically conductive in order to allow electrons from the primary beam to flow to earth, and hence avoid the build-up of regions of 'charge' on the surface of the sample, which results in severe degradation of the image. About 15 years ago, a new type of SEM instrument known as an Environmental SEM or ESEM became readily available, that allowed non-conductive samples to be directly imaged in an SEM, without the need to first coat them with a thin film of sputtered or evaporated metal (usually gold or platinum) or carbon. Apart from the fact that sputtered metal coatings are approximately 7.0 to 25 nm thick, they severely restrict the use of EDAX analysis. The ESEM was originally developed with the main aim of being able to examine

non-conductive biological samples whilst still hydrated, and without the risk of producing imaging artefacts caused by critical point drying or other sample preparation techniques. A full account of the development of ESEM instruments has been given by Danilatos (1990).

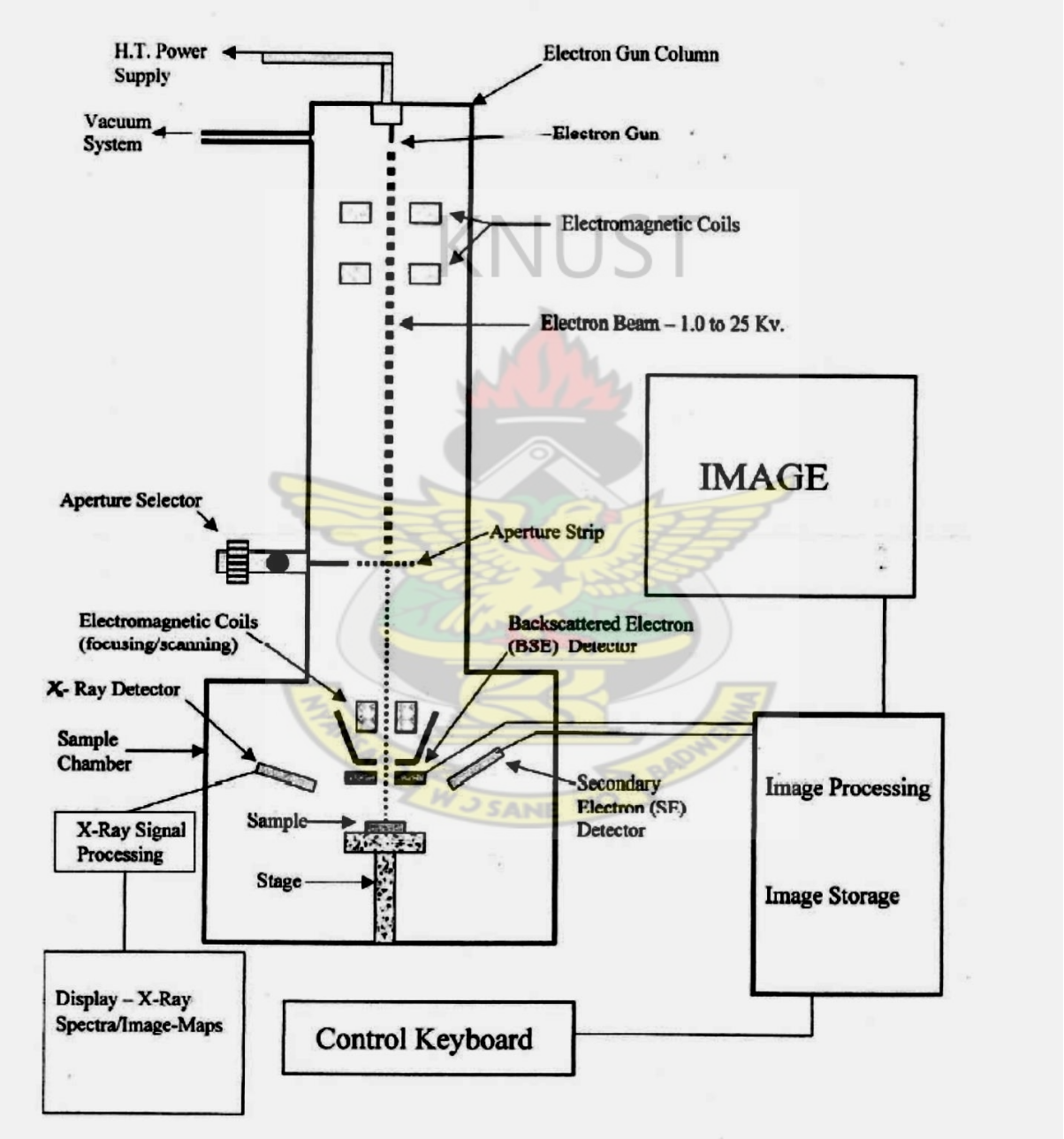

Figure 6.3: Schematic diagram of scanning electron SEM) microscopy

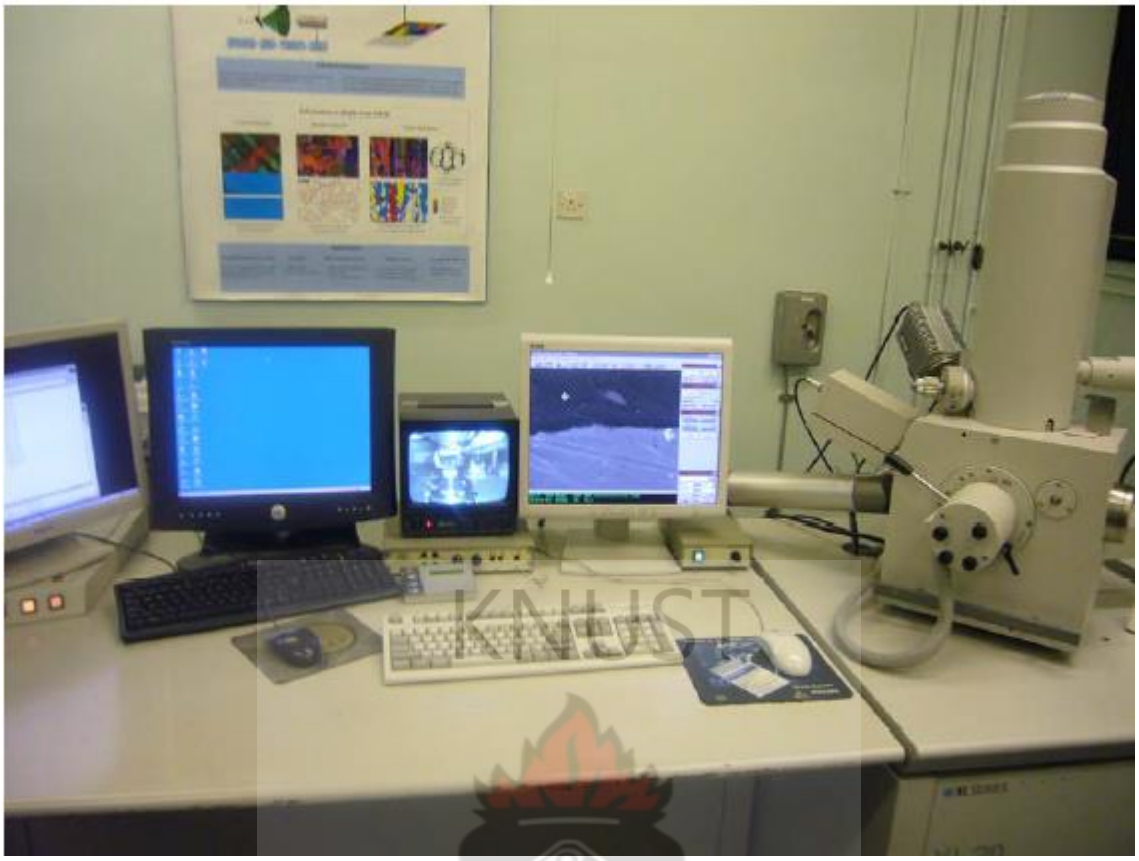

Figure 6.4 Photograph of FEI XL 30 FEGSEM

Both an ESEM, and the more recently available variant of the ESEM known as a Variable Pressure SEM or VPSEM are able to eliminate the high vacuum requirements of the SEM by separating the vacuum environment in the specimen chamber from the high vacuum environment in the main column and electron gun region. In a typical ESEM (or VPSEM), two pressure limiting apertures (PLAs) separate the specimen chamber from the electron gun column. All the regions are separately pumped, and this gives a graduated vacuum from 10 Torr in the specimen chamber, to 10^{-8} Torr in the column and 10^{-10} Torr in the electron gun emission chamber. By using an electrically cooled (Peltier) stage, water can be maintained in the liquid state within the specimen chamber. The presence of gas in the specimen chamber produces two important effects, these are induced intrinsic signal amplification, and charge neutralisation. Secondary electrons emitted by the sample accelerate within the detector field as imposed by the detector.

They then collide with gas molecules. These collisions result in ionization of the gas, creating positive ions and also additional secondary electrons called environmental secondary electrons. The continuous repetition of this process results in a proportional cascade amplification of the original secondary electron signals that are strong enough to be detected. The positive ions are attracted to the sample surface as negative charge accumulates from the beam on the (in the case of a non-conductor) insulated specimen surface. This is how the positive ions effectively suppress charging artefacts. The elimination of charging allows the imaging of non-conductive samples in their natural uncoated state, with a free choice of accelerating voltages. A very recent comprehensive discussion of the operating principles and capabilities of the ESEM has been given by Stokes (2008).

Most new dedicated ESEM instruments image using a new type of secondary electron detector, known as a Gaseous secondary electron detector or GSED, whose main function is to collect secondary electrons for imaging, but eliminate the 'noise' forming electrons. Goldstein, *et al.*, (2002) have given a detailed description of the available types of SEM instruments and their capabilities. Depending on the type of instrument, SEM instruments are capable of providing images of sample surfaces at magnifications up to (realistically) around 250,000 X, and with an achievable resolution of around 1.0 nm. However, this would be under ideal operating conditions, using a high vacuum FEG instrument, and with an optimum sample type. It should be noted, that the term 'magnification' has little meaning, since it is possible to generate images with 'false' magnification, whereby the image of the sample is made larger, but with no additional increase in the amount of information contained therein. The term 'resolution' is now used to describe the main operating capability of any microscope, and is defined as the minimum distance between two separate features on the specimen, that any instrument is capable of defining/imaging, such that the image that is obtained shows the two features as being separate. The particular FEG-SEM (FEI XL30) mainly used in this Study has a resolution of around 1.8

nm and had an associated RONTEC EDAX system which was utilised as the primary analytical facility.

6.5.2.3 Energy dispersive X-ray analysis (EDAX)

One of the consequences of the bombardment of any material with a high energy electron beam is the production of X-rays, whose wavelength depends on the nature and characteristics of the elements that are present in the specimen. In basic terms, the X-rays arise when an inner shell electron of an atom within the sample surface region is sufficiently excited by the primary electron beam of the SEM, to leave the atom entirely or go into a higher un-occupied energy level. The space created by the excited electron is filled by another electron which drops from a higher energy level and emits an X-ray photon of energy equal to the energy lost by the electron falling between the two atomic shells. These X-rays are collected by a detector and separated on the basis of their energy. This is the principle of Energy dispersive X-ray Analysis (EDAX) which is most often associated with Scanning electron microscopy. Note that some X-ray based analytical instruments are capable of separating X-rays on the basis of wavelength, and are hence known as Wavelength-Dispersive X-ray analysis or WDX systems. The EDAX technique can be considered as the most versatile system for the analytical micro characterisation of materials.

All EDAX systems can function in various different operating modes, depending on the type of analysis that is required. The first type of operating mode, is known as 'spectrometer' mode, whereby the instruments functions as a basic spectrometer, and provides a full spectra and quantitative data regarding all the elements that are present either over the whole area of the sample being scanned (and imaged) by the SEM electron beam, or within a pre-defined small area or spot. Note that the accelerating voltage of the SEM electron beam must be sufficiently high enough to be able to detect the elements that it is desired to detect. Usually, the accelerating voltage must be at least twice as high as the particular energy of the individual electron shell (i.e.

K, L, *etc.*) of the atom of the specific element being analysed. For example the 'K' shell peak for the element iron (Fe) is 6.4 keV, which would require a minimum accelerating voltage of 13.0 kV for effective detection. Note that for some heavier elements, it is impractical to use the 'K' energy shell peak for analysis, since the accelerating voltage required would be far too high, and therefore the EDAX system performs the analysis using a peak from a lower energy shell (L or M). As an example, the KA (= K_α) peak for gold (Au) is 68.8 keV, which would require an accelerating voltage of around 140 kV for effective detection and therefore the 'L' shell peak at 9.7 keV (which requires an SEM accelerating voltage of 20 kV for effective detection) is used. However, it should also be noted, that since EDAX analysis usually requires fairly high accelerating voltages to be employed, this creates a minimum 'interaction volume' at the sample surface; i.e. the specific region where beam/atom interactions occur that generate X-rays, as a result of beam penetration. This is usually a minimum of around 2 – 3 μm. Care must therefore be taken when using the 'spot' analysis facility at high magnifications, even at a magnification of 25,000 X, the spot analysis area is actually about 25% of the area of the sample being examined. The other main EDAX operating mode is known as 'imaging mode' and involves two further operating functions viz 'mapping' mode and 'line scan' mode. In mapping mode, the EDAX system shows the distribution of several selected elements as a series of coloured dot maps, either singly, or overlaid on the corresponding SEM image. In line scan mode, a secondary electron image is first obtained, then a line is drawn on the image, and several elements are selected as required. The EDAX system then gives a graph with coloured plots corresponding to each selected element, of relative percentages of all the elements along the selected line. Once the analysis is completed, it is then possible to read off the precise relative percentages of all the elements along the line with an accuracy of 2 - 3 μm. A full account of X-ray analysis in the SEM using EDAX has been given by Lyman, *et al.*, (1990) and Goldstein, *et al.*, (2002). As

indicated previously, an FEI XL 30 FEGSEM fitted with integrated EDAX analysis system was used in this work.

6.5.2.4 Sample preparation for SEM and EDAX

When a sample is being examined in a high vacuum SEM, the surface of the sample receives electrons from the primary beam and loses electrons by either secondary emission or backscatter. Therefore, the specimen may have either a net loss or gain of electrons and will charge up positively or negatively. Any such charging effects are undesirable, and may cause image brightness, beam distortion and loss of resolution. Charging effects can be minimized or eliminated either by the use of an electrically conducting specimen that is able to maintain a constant zero potential by means of electron flow through the specimen stub and stage to earth, or by coating the sample with a conducting film such as carbon or gold which will prevent the build-up of charge. A thorough account of sample preparation techniques for SEM has recently been given by Echlin (2009). In this study all samples were carbon coated with a GATAN MODEL 682 PRECISION ETCHING COATING SYSTEM since the gold coating would have given a significant 'false' peak, and would also completely prevent a true elemental map being obtained. A coating thickness reference chart was used to estimate that samples were coated with carbon to a thickness of approximately 5.0 to 8.0 nm. All SEM/EDAX results presented in the following Chapters were obtained from prepared samples examined using a FEI XL 30 FEGSEM, with attached RONTEC EDAX system running Quantax Esprit 1.8 analytical software. In the Results Sections of the experimental Chapters the SEM photomicrographs of the samples are presented as secondary electron (SE) images, recorded digitally (as TIFF files), which give optimum image quality to show surface topography with good depth of field (in contrast to backscattered electron [BSE] images). The results of the EDAX analysis are given either as results from the EDAX system operating in Spectra Mode (SM) or Imaging Mode (IM).

Data from the Spectra Mode results are shown as a series of spectrum peaks, that identify all the elements within a sample, and these results are usually shown with the corresponding quantification data, usually as an Excel Table, which gives the relative percentages of all the elements present at the sample surface, expressed either as Wt. % or At No %.

The analyses performed using the Imaging Mode of the EDAX facility were carried out using the system operating in either Electron Mapping Mode or Line Scan Mode. The Electron Mapping Mode indicates the occurrence and distribution of selected elements over the sample surface; either singly, or in combination, and/or overlaid over the corresponding secondary electron image. The Line Scan Mode shows the quantitative variation in the relative percentages of several selected elements over a pre-determined line on the sample surface, and is a very sensitive quantitative technique. To ensure that all results obtained could be directly comparable, the same SEM instrument operating parameters (accelerating voltage [20KV], spot size, working distance [WD] *etc.*), were maintained for all imaging and EDAX studies, for all samples. Note that due to occasional problems with the SEM to EDAX system communication software, the real WD was sometimes not displayed in the EDAX images. In addition, to further maintain consistency in the SEM and EDAX results, and to allow precise comparisons to be made between SEM micrographs obtained for different samples, secondary images were usually recorded for the same selected range of instrument magnifications, for each sample, throughout the study. These magnifications were mainly: 500X, 1000X, 2000X and 5000X. These magnifications correspond to the scale bars given on the SEM images of 50.0 μm, 20.0 μm, 10.0 μm and 5.0 μm respectively. The magnifications referred to throughout the text and Figure legends refer to the instrument magnification setting only, and do not give the actual real magnifications of the images as presented in this Report.

6.5.3 Transmission electron microscopy (TEM) / selected area diffraction (SAD)

In a transmission electron microscope (TEM), a thin specimen is irradiated with a high-energy electron beam (usually in the range of 100 to 200 keV). The beam is focused by magnetic lenses. The first few lenses before the specimen permit variation of the illumination aperture and the size of the illuminated area. The electron intensity distribution of the beam after interaction with the specimen is imaged onto a fluorescent screen by the objective lens and the post-objective lens system. Images are recorded by a digital charged couple device (CCD) camera or, alternatively, with an electron sensitive photographic emulsion (which is chemically developed as in light photography). Contrast in the image arises either by absorption of electrons scattered through angles larger than the lens aperture (scattering contrast) or by interference between the scattered and incident wave at the image point (phase contrast). Information obtained from phase contrast is ultimately limited by lens aberrations and the limited coherence of the electron beam. The typical limit in a modern TEM is in the 0.2 to 0.4 nm range.

In addition to imaging information, a TEM is also capable of providing transmission electron diffraction data. This is done quite simply by changing the post objective lens settings so that, rather than projecting the objective-lens image they project the electron intensity in the objective back-focal plane. Many modern TEMs are also capable of forming small electron probes (5 nm or less), allowing diffraction information from nano-scale areas – so-called nano-beam diffraction. Production of characteristic X-rays (arising from excitation of inner atomic shells) is limited essentially to the illuminated area, since beam broadening is typically small for a thin sample. Detection of these X-rays allows for qualitative or semi-quantitative elemental analysis at the nano-scale.

Any modern TEM that can form a small electron probe may also be configured as a scanning TEM (STEM) simply by adding the capability of beam rastering together with appropriate

detectors. This STEM configuration is often available on TEMs with field emission sources. STEM mode is convenient for analytical work (X-ray analysis or energy-loss spectroscopy) since the rastered image can be recorded almost simultaneously with the analytical signal without altering the illumination optics.

Typical applications involve microstructure and nanostructure size and morphology determination and Phase identification at the nano-scale. Double-tilt sample holders permit crystallographic studies, including defect analysis (dislocations, stacking faults, etc.). Chemical information can also be discerned from emission of characteristic X-rays (energy dispersive spectroscopy of X-rays, or EDAX). Chemical information is also discerned from ionization edges in the electron energy loss spectrum (EELS). Formation of small electron probe allows diffraction, EDAX, or EELS at the nano-scale cross-section analysis (layer thickness, interface quality).

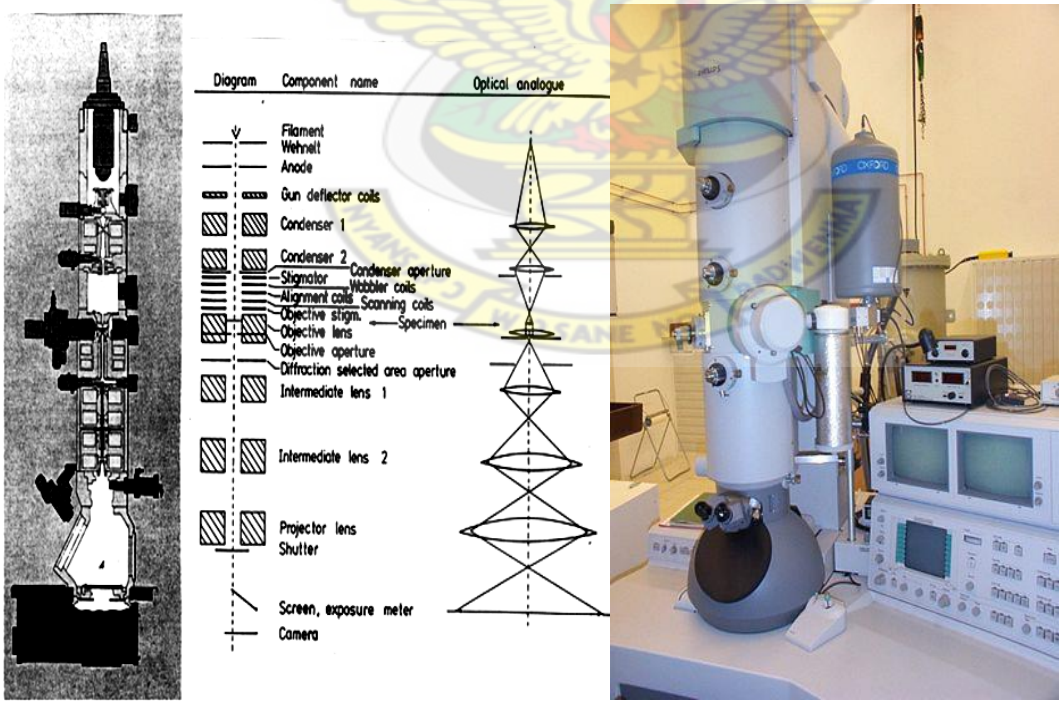

Figure 6.5: A schematic diagram of transmission electron microscope (TEM)

6.5.4 UV-Visible absorption spectroscopy

Optical spectroscopy has been widely used for the characterization of nanomaterials. The absorption and emission spectra determine the electronic structures of atoms, ions, molecules or crystals through exciting electrons from the ground to excited states (absorption) and relaxing from the excited to ground states (emission). The characteristic lines observed in the absorption and emission spectra of nearly isolated atoms and ions due to transitions between quantum levels are extremely sharp. As a result, their wavelengths or photon energies can be determined with great accuracy. The lines are characteristic of a particular atom or ion and can be used for identification purposes. Molecular Spectra, while usually less sharp than atomic spectra, are also relatively sharp. Positions of spectral lines can be determined with sufficient accuracy to verify the electronic structure of molecules.

In solids the large degeneracy of the atomic levels is split by interactions into quasi-continuous bands (valence and conduction bands), and makes their optical spectra rather broad. The energy difference between the highest lying valence (the highest occupied molecular orbital, HOMO) and the lowest lying conduction band (the lowest unoccupied molecular orbital, LUMO) bands are designated as the fundamental gap. Penetration depths of electromagnetic radiation are of the order of 50 nm through most of the optical spectrum (visible light). That makes this technique readily applicable for the characterization of nanostructures and nanomaterials. In this work, UV-vis spectra were recorded using a Cary 5000 Uv-Vis-NIR spectrophotometer. A lamp produces a beam of light which hits a prism and splits into its component wavelengths. The prism is rotated so that only a specific wavelength of light reaches the exit aperture, before interacting with the sample. A detector then measures the transmittance and absorbance of the sample. Transmittance light passes through the sample and hits the detector, while absorbance is a

measure of the light absorbed by the sample. The detector senses the light being transmitted through the sample and converts the information to a digital display.

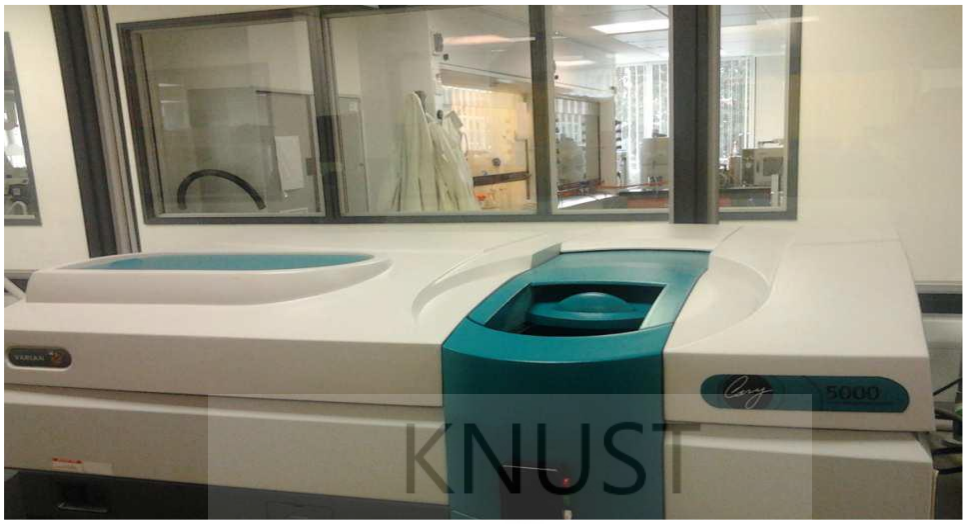

Figure 6.6 Photograph of Cary 5000 Uv-Vis-NIR- spectrometer.

6.5.5 Elemental analyses

6.5.5.1 Determination of C/H/N/S - elemental analyser

The determination of C/H/N/S was performed using the Carbo Erba EA 1108 Elemental Analyser. The technique used for the determination of C, H, N and C, H, N, S is based on the quantitative "dynamic flash combustion" method. In this method the samples are held in a thin container/ placed inside the auto-sampler drum where they are purged with a continuous flow of helium and then dropped at pre-set intervals into a vertical quartz tube maintained at 1020 ^{o}C (combustion reactor). When the samples are dropped inside the furnace, the helium stream is temporary enriched with pure oxygen and sample and its container melt and the tin promotes a violent reaction (flush combustion) in a temporary enriched atmosphere of oxygen. Under those favourable conditions even thermally resistant substances are completely oxidized. Quantitative combustion is then achieved by passing the mixture of gases over a catalyst layer. The mixture

plug of combustion gases is then passed over copper to remove the excess of oxygen and to reduce the nitrogen oxides to elemental nitrogen. The resulting mixture is directed to the chromatographic column (Porapak PQS) where the individual components are separated and eluted as nitrogen (N_2), carbon dioxide (CO_2), water and sulphur dioxide (SO_2) with the help of a Thermal conductivity detector whose signal feeds a potentiometric recorder or an integrator or the automatic workstation known as EAGER 200. The instrument is calibrated with the analysis of standard compounds using K factors calculation or using the linear regression method incorporated in the EAGER 200 workstation.

6.5.5.2 Fourier transform infrared spectroscopy (FTIR)

Molecules and crystals can be thought of as systems of balls (atoms or ions) that are connected by springs (chemical bonds). These systems can be set into vibration, and vibrate with frequencies determined by the mass of the balls (atomic weight) and by the stiffness of the springs (bond lengths). The mechanical molecular and crystal vibrations are at very high frequencies ranging from 10 to 1014 kHz (3 - 300 µm wavelength), which is in the infrared (IR) regions of the electromagnetic spectrum.

The oscillations induced by certain vibrational frequencies provide a means for matter to couple with an impinging beam of infrared electromagnetic radiation and exchange energy with it when the frequencies are in resonance. These absorption frequencies represent excitations of vibrations of the chemical bonds and thus are specific to the type of bond and the group of atoms involved in the vibration. In the infrared experiment, the intensity of a beam of infrared radiation is measured before and after it interacts with the sample as a function of light frequency. A plot of the relative intensity versus the frequency gives the "infrared spectrum". A familiar term "FTIR" refers to Fourier Transform Infrared Spectroscopy when the intensity - time output or the interferometer is subjected to Fourier transform to convert it to the familiar infrared spectrum

(intensity-frequency). The identities, surrounding environments or atomic arrangement, and concentrations of the chemical bonds that are present in the sample can therefore be determined.

6.5.5.3 Metal content/inductively coupled plasma-optical emission spectroscopy (ICP-OES)

The quantitative analysis of metals content in samples (precursors) is performed using inductively coupled plasma-optical emission spectroscopy (ICP-OES). The equipment used is a Fissons instrument horizon model. Atomic emission spectroscopy is a process in which the light emitted by excited atoms or ions is measured. If sufficient thermal or electrical energy is available to excite a free atom or ion to an unstable energy state, then light is emitted, consisting of certain wavelengths which are characteristic to each element. The thermal energy source is provided by an argon plasma which is the basis of the ICP-OES technique. In ICP, the sample is heated to around 8,000 K in an argon plasma which is formed by the interaction between a rapidly oscillating magnetic field (RF field) and ionized argon gas – this occurs in the ICP torch. The sample solution is aspirated via a nebulizer and spray–chamber and enters the plasma as an aerosol up through the centre of the ICP torch. Here, it forms an atomic vapour to a high proportion of the atoms being raised to a high energy level because of the temperature in the plasma. The emitted radiation is focused onto the spectrometer where the signal intensity and wavelength are measured. Samples are introduced into the ICP-OES instrument in the form of aqueous solution. Because most samples are solids that are generally not water soluble, wet acid digestion is required. Samples and standard reference materials are accurately weighed into glass digestion tubes- normally 4 standards are prepared to cover a suitable concentration range, an appropriate amount of sample is weighed to ensure it will fit within this range, this is calculated from the expected percentage value. The samples and standards are then acid digested in a fume cupboard – the actual acids and heating temperature used depends on the nature of the sample and the elements present within it. After digestion the samples and standards are quantitatively

transferred to volumetric flasks, and are now ready to run on the ICP instrument. The emission in the plasma will vary proportionately according to the concentration of element in the solution. So first the range of standards prepared is run on the ICP to generate a calibration curve, i.e. a graph of emission signal versus concentration of element. The sample is then also run and the emission signal is directly converted into a concentration value using the stored calibration curve.

6.6 References

Arumugam, P., Patra, D., Samanta, B., Agasti, S. S., Subramani, C. & Rotello, V. M. (2008). "Self-Assembly and Cross-linking of FePt Nanoparticles at Planar and Colloidal Liquid-Liquid Interfaces" *J. Am. Chem. Soc.*, 130: 10046-10047.

Asuri, P., Karajanagi, S. S., Dordick, J. S., & Kane, R. S. (2006). "Directed assembly of carbon nanotubes at liquid-liquid interfaces: Nanoscale conveyors for interfacial biocatalysis". *J. Am. Chem. Soc.* 128: 1046-1047.

Chung, F. H., Smith, D. K. (1999). Industrial Applications of X-Ray Diffraction. Marcel Dekker Pub., 1006.

Danilatos, G. D. (1990). Foundations of Environmental Scanning Electron Microscopy. In: Characterization of Materials". *Springer Verlag*, 713.

Davey, W. P. (1921). "A New X-Ray Diffraction Apparatus". *J. Op. Soc. Am*. 5: 479-492.

Echlin, P. (2009). Handbook of Sample Preparation for Scanning Electron Microscopy and X- Electron Microscopy (VP-ESEM). John Wiley and Son Ltd. 221.

Goldstein, J., Newbury, D. E., Joy, D. C., Lyman, C. E., Echlin, P., Lifshin, E. L., Sawyer, C., Michael, J. R. (2002). Scanning Electron Microscopy and X-Ray Microanalysis. Springer.

Gorer, S., Hodes, G. (1994). Quantum size effects in the study of chemical solution deposition mechanisms of semiconductor films. *J. Phys. Chem*. 98; 5338-5346.

Hawkes, P.W. (1989). Advances in electronics and electron physics. Academic Press, Inc., San Diego, 73: 233.

Hu, L. F., Ma, R., Ozawa, T. C. & Sasaki, T. (2009). "An universal approach for the self-assembly of ... at a toluene/water interface". *Angew. Chem., Int. Ed*., 48: 3846-3849.

Hu, L. F., Ma, R., Ozawa, T. C. & Sasaki, T. (2010). "Synthesis of a Solid Solution Series of Layered $Eu_xGd_{1-x}(OH)_{2.5}$ Cl $0.5{\cdot}0.9H_2O$ and Its Transformation into $(Eu_xGd_{1-x})_2O_3$ with Enhanced Photoluminescence Properties". *Inorg. Chem*., 49(6): 2960-2968.

Hu, L. F., Ma, R., Ozawa, T. C., Geng, F., Iyi, N. & Sasaki, T. (2008). "Oriented Monolayer Film of Gd_2O_3:0.05Eu Crystallites: Quasi-Topotactic Transformation of the Hydroxide Film and Drastic Enhancement of Photoluminescence Properties". *Chem. Commun*., 40: 4897-4899.

Kalyanikutty, K. P., Gautam, U. K., and Rao, C. N. K. (2007). "Ultra-Thin crystalline Films of CdSe and CuSe formed at the Organic-aqueous Interface." *J. Nanosci and Nanotechnol.* 7, 6, 1916-1922.

Klayman, D. L. & Griffin, T. S. (1973). "Reaction of selenium with sodium borohydride in protic solvents. A facile method for the introduction of selenium into organic molecules". *J. Am Chem. Soc*., 95: 197-199.

Lan, G. Y., Lin, Y. W., Huang, Y. F. & Chang, H. T. (2007). "Photo-assisted synthesis of highly fluorescent ZnSe quantum dots in aqueous solution". *J. Mater. Chem*., 17: 2661-2666.

Li, Y. J., Huang, W. J. & Sun, S. G. (2006). "A universal approach for the self-assembly of hydrophilic nanoparticles into ordered monolayer films at a toluene/water interface". *Angew. Chem., Int. Ed*., 45: 2537-2539.

Matsui, J., Iko, M., Inokuma, N., Orikasa, H., Kyotani, T. & Miyashita, T. (2006). "Simple Fabrication of Carbon Nanotube Monolayer Film". *Chem. Lett*., 35: 42-43.

Matsui, J., Yamamoto, K. & Miyashita, T. (2009). "Assembly of untreated single-walled *carbon* nanotubes at a liquid–liquid interface". *Carbon*, 47: 1444-1450.

Matsui, J., Yamamoto, K., Inokuma, N., Orikasa, H., Kyotani, T. & Miyashita, T. (2007). "Fabrication of densely packed multi-walled carbon nanotube ultrathin films using a liquid-liquid interface". *J. Mater. Chem*., 17: 3806-3811.

Matsui, J., Yamamoto, K., Inokuma, N., Orikasa, H., Kyotani, T. & Miyashita, T. (2008). "Multi-Walled Carbon Nanotube Ultrathin Film Using a Liquid-Liquid Interface: Effect of Alcohol Type to the Film Property". *Mol. Cryst. Liq. Cryst*., 491: 9-13.

O'Brien, P. & Nomura, R. (1995). "Single-molecule precursor chemistry for the deposition of chalcogenide (S or Se)-containing compound semiconductors by MOCVD and related methods". *J. Mater. Chem*., 5: 1761-1773.

Park, Y.-K., Yoo, S.-H. & Park, S. (2007). "Assembly of Highly Ordered Nanoparticle Monolayers at a Water/Hexane Interface". *Langmuir*, 23: 10505-10510.

Park, Y.-K., Yoo, S.-H. & Park, S. (2008). "Three-dimensional Pt-coated Au nanoparticle arrays: applications for electrocatalysis and surface-enhanced Raman scattering". *Langmuir*, 24: 4370-4375.

Pecharsky, V. K., Zavalij, P. Y. (2005). "Fundamentals of powder diffraction and structural characterization of materials". Springer, 713.

Shi, H.-Y., Hu, B., Yu, X.-C., Zhao, R.-L., Ren, X.-F., Liu, S.-L., Liu, J.-W., Feng, M., Xu, A.-W. & Yu, S.-H. (2010). "Ordering of Disordered Nanowires: Spontaneous

Formation of Highly Aligned, Ultralong Ag Nanowire Films at Oil–Water–Air Interface". *Adv. Funct. Mater*. 20(6): 958-964.

Singh, S., Guleria, A., Rath, M. C., Singh, A. K., Adhikari, S. and Sarkar, S. K. (2011). "Electron beam induced synthesis of CdSe nanomaterials: Tuning of shapes from rods to cubes. Materials Letters, 65(12): 1815-1818.

Stokes, D. J. (2008). *Principles and Practice of Variable Pressure/Environmental Scanning Electron Microscopy (VP-ESEM)*. John Wiley & Sons, Ltd, UK.

Suryanarayana C., Norton, M. G. (1998). X-Ray Diffraction: A Practical Approach. Plenum Publishing Corporation, New York.

Von Laue, M. (1913). "X-ray interference". *Phy. J*., 14(22-23): 1075-1079.

Warren, B. E. (1990). X-Ray Diffraction (2nd Edition). Dover Publication, New York.

Yun, S., Oh, M. K., Kim, S. K. & Park, S. (2009). "Linker-molecule-free gold nanorod films*:* effect of nanorod size on surface enhanced Raman scattering". *J. Phys. Chem. C*, 113: 13551-13557.

Yun, S., Park, Y.-K., Kim, S. K. & Park, S. (2007). "Linker-Molecule-Free Gold Nanorod Layer- by-Layer Films for Surface-Enhanced Raman Scattering". *Anal. Chem*., 79: 8584-8589.

Zhang, Y., Shen, Y., Kuehner, D., Wu, S., Su, Z., Ye, S. & Niu, L. (2008). "Directing single-walled carbon nanotubes to self-assemble at water/oil interfaces and facilitate electron transfer". *Chem. Commun*., 36: 4273-4275.

CHAPTER SEVEN: OUTLOOK AND CONCLUSION

In this thesis deposition of Copper, Zinc, cadmium and Lead Chalcogenide nanomaterials/thin films have been described. Section 7.1 contains a short summary of the research work. The results and conclusions drawn from this research work are described in section 7.2. Based on these conclusions, an outlook to future research is provided in section 7.3.

7.1 Summary

Metal chalcogenides, ME (M= Cu, Zn, Cd, Pb; E=S, Se, Te) are important semiconductor materials which have found many applications in optoelectronics and solar cell technology. Metal chalcogenides as thin films and nanocrystals have received considerable interest in low cost photovoltaics devices. The work described in this thesis deals with the exploitation of the unique properties pertaining at the water/toluene interface for the preparation of these materials at temperatures below 100 ^{o}C. In the first part of this work a series of metal dithiocarbamate complexes were prepared with variations of the carbon chains from two to four and characterized. In addition metal cupferronates were also prepared and characterized.

Although the self-assembly of colloidal particles at a curved fluid interface has been reported for about 100 years, the self-assembly at a flat fluid interface to be functional films is just a burgeoning field. Compared with previous solution-based self-assembly routes, the advantages for this self-assembly strategy are evident in their universality, simplicity and high efficiency, the high quality of the as-assembled film. Multilayer nanofilms can be obtained by this interfacial self-assembly through a multiple deposition procedures.

Table 7.1 Summary of the properties of the prepared nanomaterials/thin films

Nanoparticle	Precursor	Chalcogenide	Observed morphology	Average crystallite size/ nm	Bulk Band gap/eV	Nanomaterial Band gap/eV
ZnS	$Zn(S_2CNEt_2)_2$	Sulphur	Cubic	2.2	3.68	3.7
	$Zn(S_2CNPr_2)_2$			6.8		3.84
	$Zn(S_2CNBu_2)_2$			6.8		3.92
	$Zn(S_2CN^iBu_2)_2$			5.1		3.93
ZnSe/t-Se	$Zn(S_2CNEt_2)_2$	Selenium	Hexagonal	3.7	2.70	3.7
	$Zn(S_2CNPr_2)_2$			6.2		3.91
	$Zn(S_2CNBu_2)_2$			5.2		3.70
	$Zn(S_2CN^iBu_2)_2$			6.1		3.83
ZnTe/t-Te	$Zn(S_2CNEt_2)_2$	Tellurium	Hexagonal	4.1	0.33	1.17
	$Zn(S_2CNPr_2)_2$			6.4		1.10
	$Zn(S_2CNBu_2)_2$			6.7		1.16
	$Zn(S_2CN^iBu_2)_2$			5.7		1.09
CuS	$Cu(cup)_2$	Sulphur	Hexagonal	3.8	1.75	3.8
CuSe	$Cu(cup)_2$	Selenium	Hexagonal	5.6	2.0/2.8	3.7
CuSe	$Cu(cup)_2$	Selenosulphate	Hexagonal	1.3	-	
CuTe	$Cu(cup)_2$	Tellurium	Hexagonal		1.5[a]	
CdS	$Cd(cup)_2$	Sulphur	Cubic	5.2	2.42	3.86
CdS	$Cd(cup)_2$	Sulphur	Hexagonal	5.0	2.51	3.86
CdSe	$Cd(cup)_2$	Selenium	Hexagonal	5.9	1.75	3.9
CdSe	$Cd(cup)_2$	Selenosulphate	Hexagonal	3.6	1.75	3.9
PbS	$Pb(cup)_2$	Sulphur	Cubic	3.9	0.41	0.9

	$Pb(S_2CNEt_2)_2$			6.7		
	$Pb(S_2CNPr_2)_2$			6.3		1.4
	$Pb(S_2CNBu_2)_2$			6.4		1.1
	$Pb(S_2CN^iBu_2)_2$			5.8		1.3
PbSe	$Pb(cup)_2$	Selenium	Cubic	5.5	0.27	1.46
	$Pb(S_2CNEt_2)_2$			8.3		1.4
	$Pb(S_2CNPr_2)_2$			7.2		1.7
	$Pb(S_2CNBu_2)_2$			2.5		1.8
PbTe	$Pb(cup)_2$	Tellurium	Cubic	2.7	0.29	0.96
	$Pb(S_2CNBu_2)_2$			6.3		

[a]Reported by Synco-Davis (2004).

7.2 Conclusion

A number of metal dithiocarbamato and metal cupferronates have been synthesized and used as precursors for the deposition of binary chalcogenide nanomaterial/thin films of Copper, Zinc, Cadmium and Lead at the water/toluene interface. For the first time the assembly of semiconductor nanocrystalline thin film at water-toluene interface has been carried out successfully with borohydride reduction of chalcogen powders as sources of chalcogenide ions. This procedure has yielded single crystalline films as against polycrystalline films. Hitherto defects and grain boundaries in polycrystalline films had led to the creation of trap states that act as carrier scattering centers, thus reducing the carrier mobility and transparency of the films. UV-visible spectra indicated that the nanocrystals forming the films interact strongly with each other with tangible red shift of the surface plasmon band. Varying the concentration, temperature, deposition times and the precursors have influenced the optical properties and morphology of the thin films.

The average crystallite sizes of the as-prepared copper nanoparticles at different temperatures, concentrations and deposition times ranged from 3.4 to 4.3 nm for CuS, 5.1 to 5.7 nm for CuSe and 1.4 to 4.5 nm for CuTe. The band gaps obtained for CuS ranged from 3.6 to 3.9 eV and CuSe ranged from 3.53 to 3.96 eV.

The average crystallite sizes of the as-prepared zinc sulphide nanoparticles at different temperatures, concentrations and deposition times ranged from 2.2 to 6.8 nm and band gap ranging from 3.7 to 3.93 eV. Attempts to deposit ZnSe and ZnTe nanocrystal thin films at the toluene –water interface rather yielded predominantly t-Se and t-Te respectively. The average crystallite sizes ranged from 3.7 to 6.2 nm for t-Se and 4.1 to 6.7 nm. The band gap of t-Se ranged from 3.7 to 3.91 eV and that of t-Te ranged from 1.09 to 1.17 eV. Yesu Thangam *et al* (2012) have reported of the synthesis of ZnS nanoparticle with a band gap as high as 5.48 eV and particle size of 1.57 nm and absorption peak at 227 nm. Panthan and Lokhande (2003) have also reported the synthesis of ZnS nanomaterials with band gap of 2.2 eV.

The average crystallite sizes of the as-prepared cadmium nanoparticles at different temperatures, concentrations and deposition times ranged from 0.9 to 7.1 nm for cubic CdS, 0.94 to 7.3 nm for hexagonal CdS and 5.9 to 6.4 nm for CdSe. The band gaps obtained for CdS ranged from 3.69 to 3.98 eV, CdSe ranged from 3.7 to 4.05 eV. When selenosulphate was used as the seleniding source the crystallite sizes obtained ranged from 4.1 to 6.4 nm. Nanostructured CdSe deposits with a mixture of hexagonal and cubic phases are formed at room temperature, 50 ^{o}C and 70 ^{o}C. Good quality PbS, PbSe and PbSe NCs with narrow size distribution absorbing in visible/near IR region were obtained. The diameters of PbS, PbSe and PbTe crystallites ranged from 3.9-6.4 nm, 2.5-8.3 nm and 2.7-6.3 nm respectively. Experiments have shown that by carefully controlling the conditions of reactions leads to lead chalcogenide nanocrystals with well-defined shapes, and band gaps can be tuned between 0.9 - 1.4 eV for PbS, 1.40 - 1.8 eV for PbSe and 0.9 eV for PbTe NCs.

7.3 Outlook

The synthetic work described in this thesis on different classes of compounds can be extended to other metals. In addition it could be employed for the controlled synthesis of compositionally tunable binary and ternary nanomaterials of different morphologies. It is hoped that the oil–water interfacial self-assembly, the state-of-the-art synthesis of nanoparticle thin films and nanomaterials presented in this thesis can provide the necessary background and principles of this exciting self-assembly with low-cost and high efficiency. And more importantly, it is hoped that this thesis can lead to more work by the candidate to prepare novel and functional nanomaterial thin films and also help younger researchers seeking new directions to find interesting topics in this burgeoning field, to push the development of oil–water self-assembly strategy in fundamental and practical applications together.

7.4 References

Panthan, H. M. and Lokhande, C.D. (2003). In 14th AGM and Symposium on Novel Polymeric Materials.

Synco-Davies, M. (2004). In Proc. 19th European Photovoltaic Solar Energy Conf., Paris, 6.

Yesu Thangam, Y., Anita, R., Kavitha, B. (2012). Novel method to synthesize and characterize Zinc Sulphide. *Int. Journal of Applied Sciences and Engineering Research*, 1, 2.

APPENDIX A

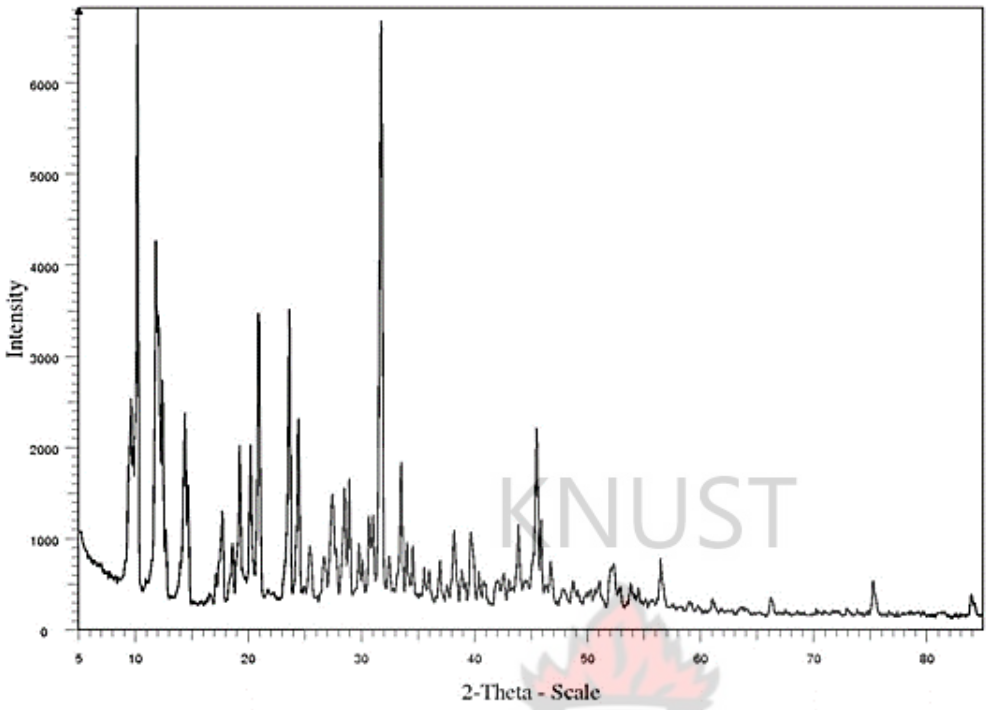

Figure A1: X-ray diffractogram of zinc diethyl dithiocarbamate ($Zn(S_2CNEt_2)_2$ precursor.

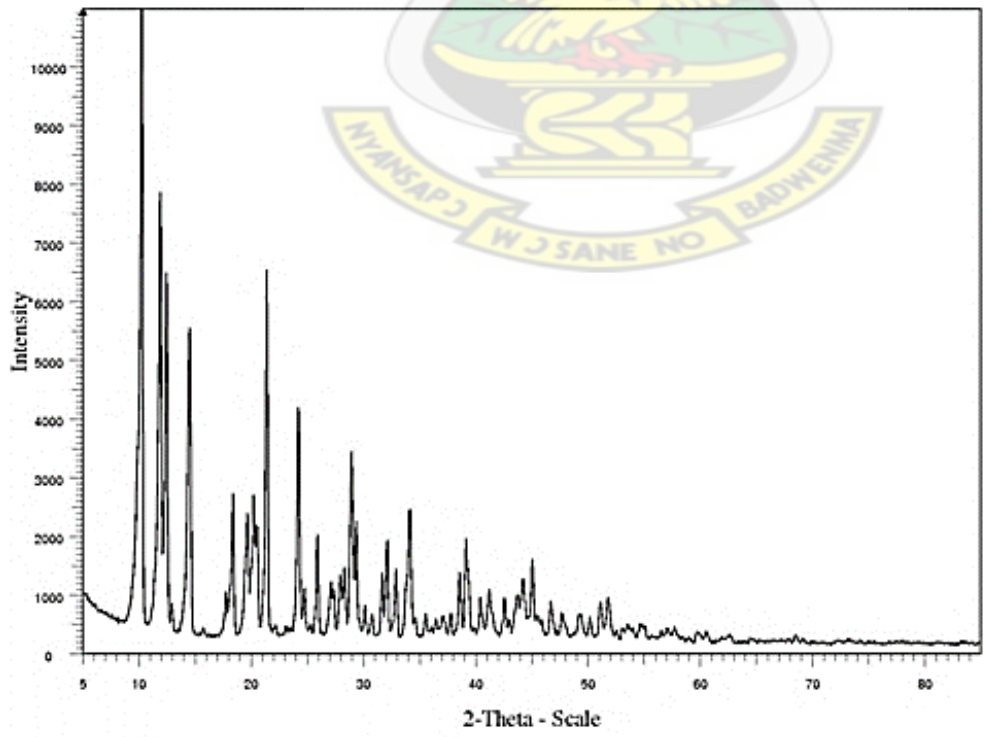

Figure A2: X-ray diffractogram of copper diethyldithiocarbamate ($Cu(S_2CNEt_2)_2$ precursor.

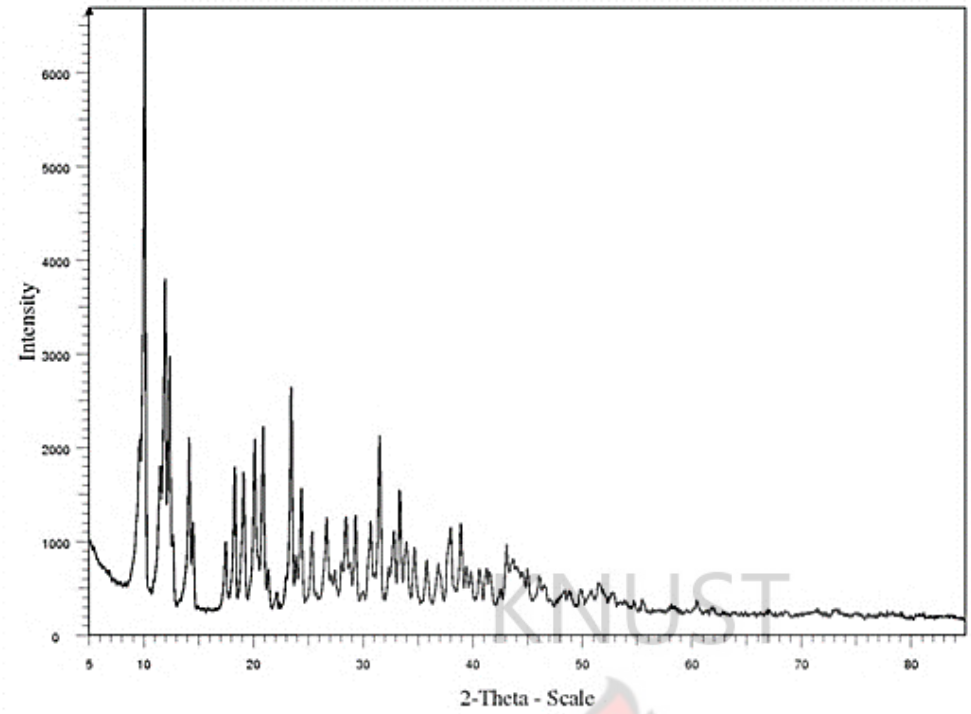

Figure A3: X-ray diffractogram of cadmium diethyldithiocarbamate ($Cd(S_2CNEt_2)_2$) precursor.

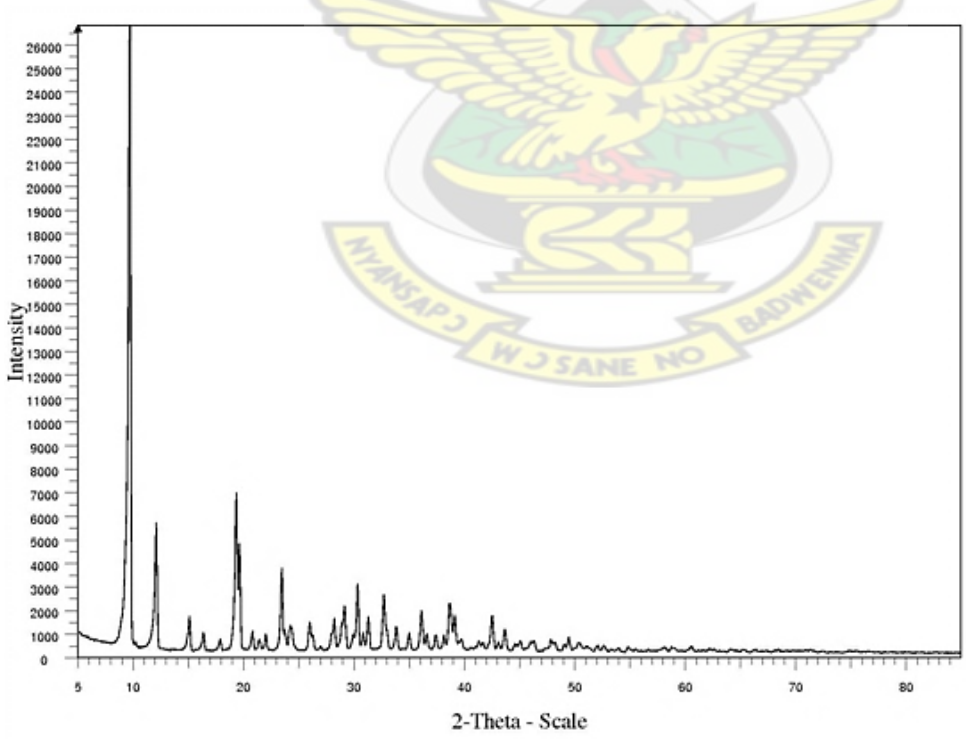

Figure A4: X-ray diffractogram of lead diethyldithiocarbamate ($Pb(S_2CNEt_2)_2$) precursor.

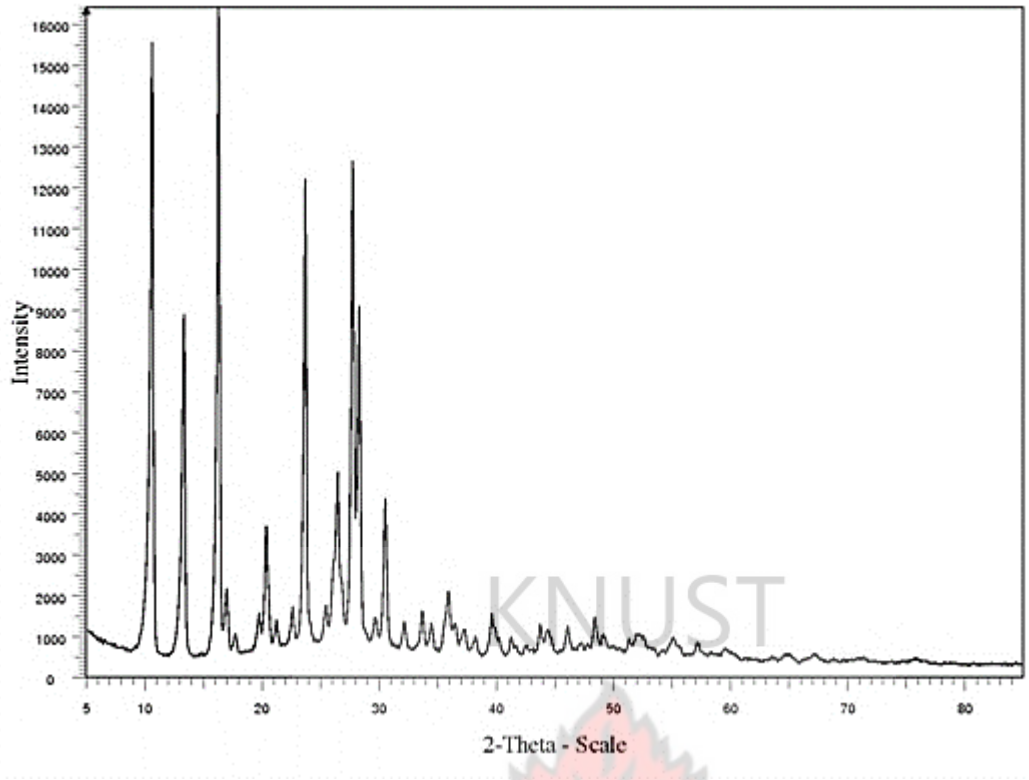

Figure A5: X-ray diffractogram of the copper cupferronate ($Cu(cup)_{2)}$ precursor

APPENDIX B

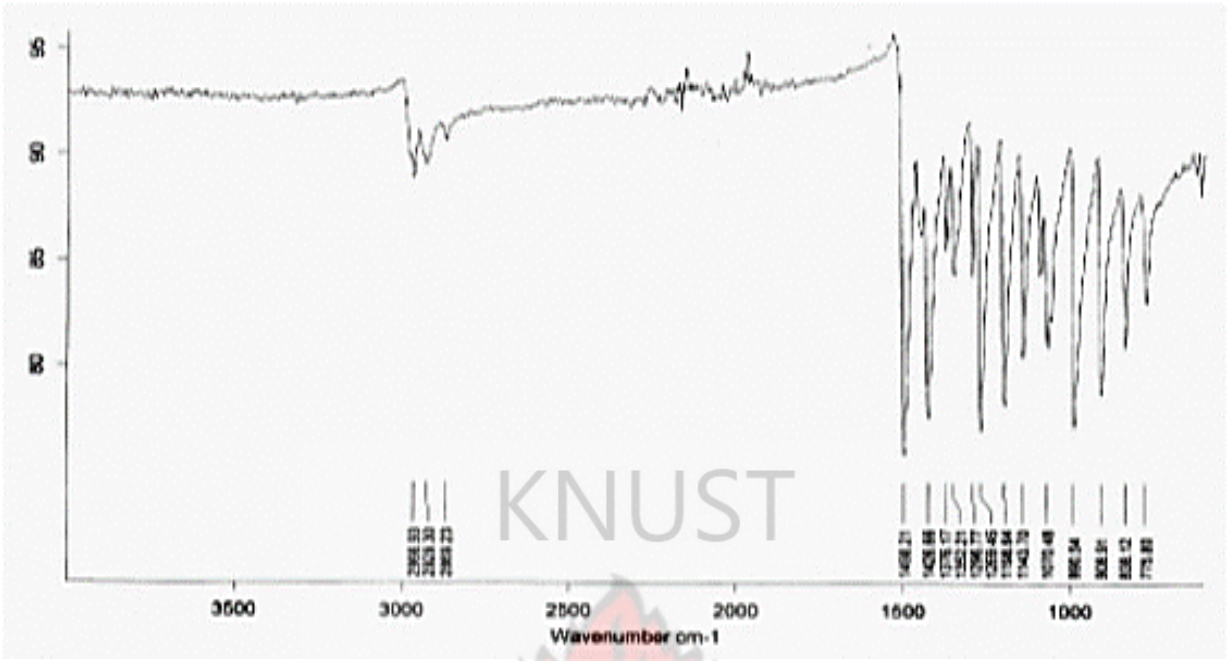

Figure B1: FT-IR Spectra for zinc diethyldithiocarbamate ($Zn(S_2CNEt_2)_2$)

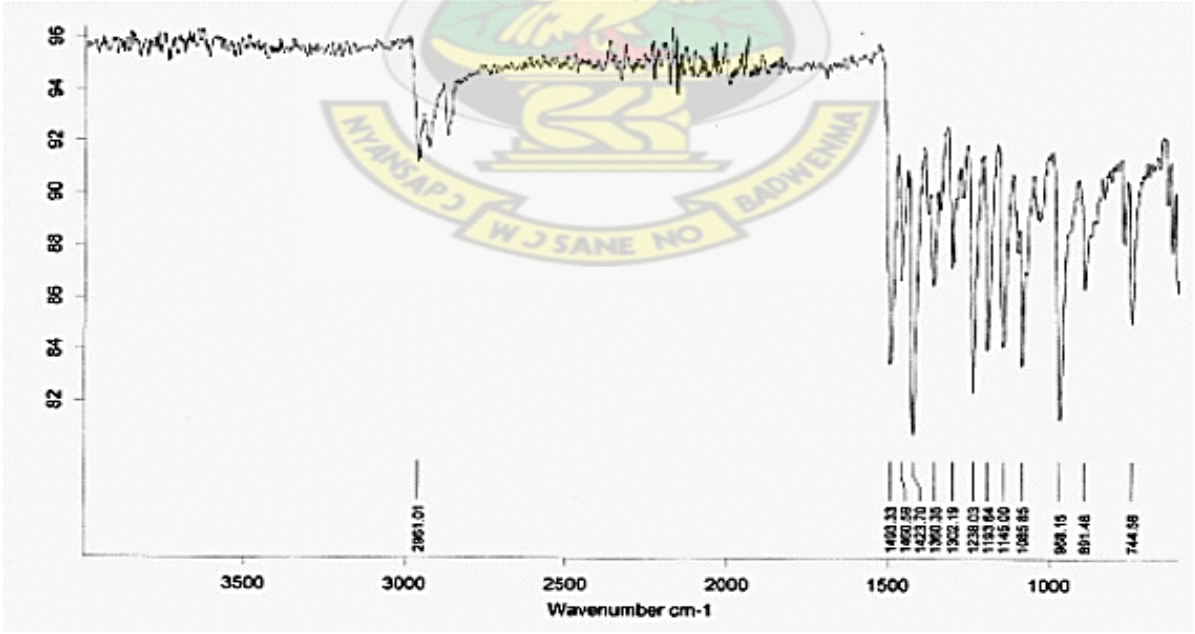

Figure B2: FT-IR Spectra for zinc dipropyldithiocarbamate ($Zn(S_2CNPr_2)_2$)

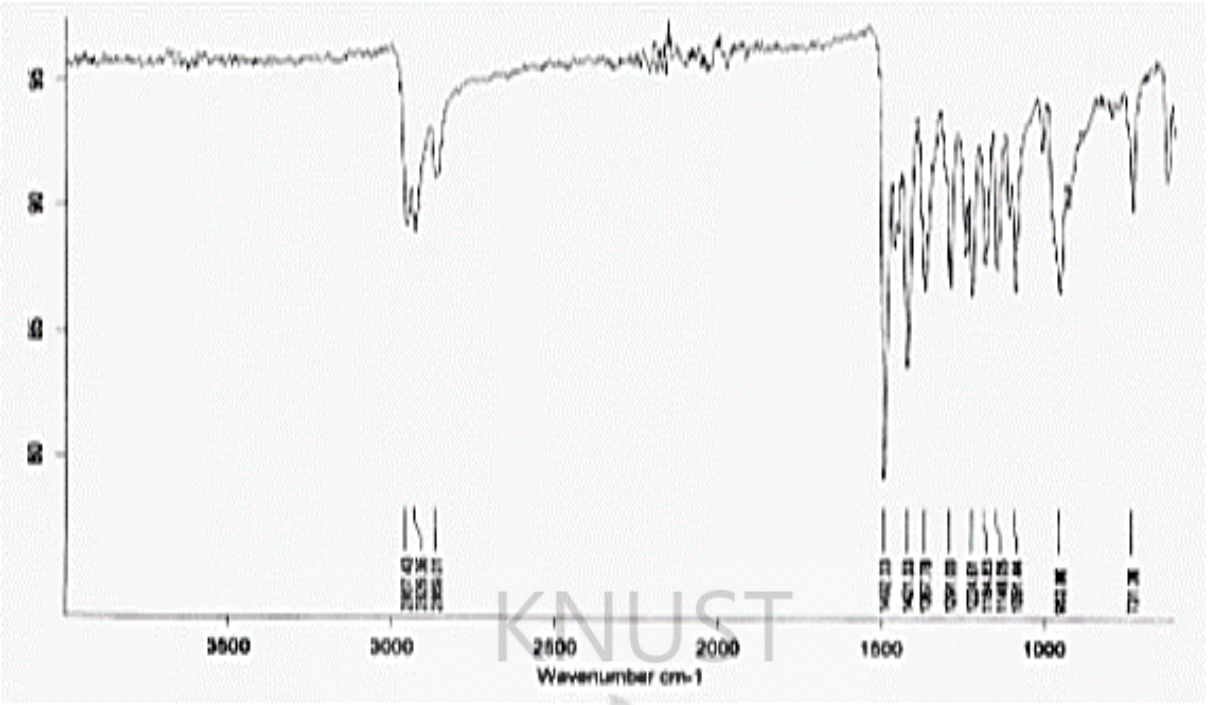

Figure B3: FT-IR Spectra for zinc dibutyldithiocarbamate ($Zn(S_2CNBu_2)_2$)

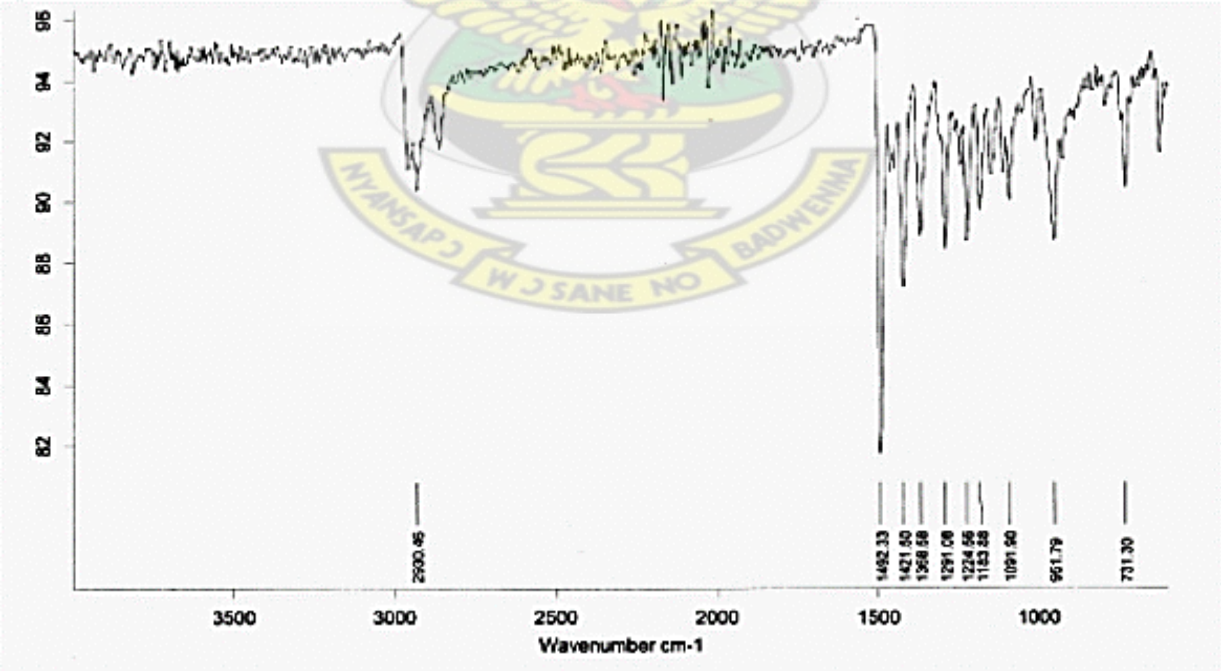

Figure B4: FT-IR Spectra for zinc ethylhexyldithiocarbamate ($Zn(S_2CNEtHex)_2$)

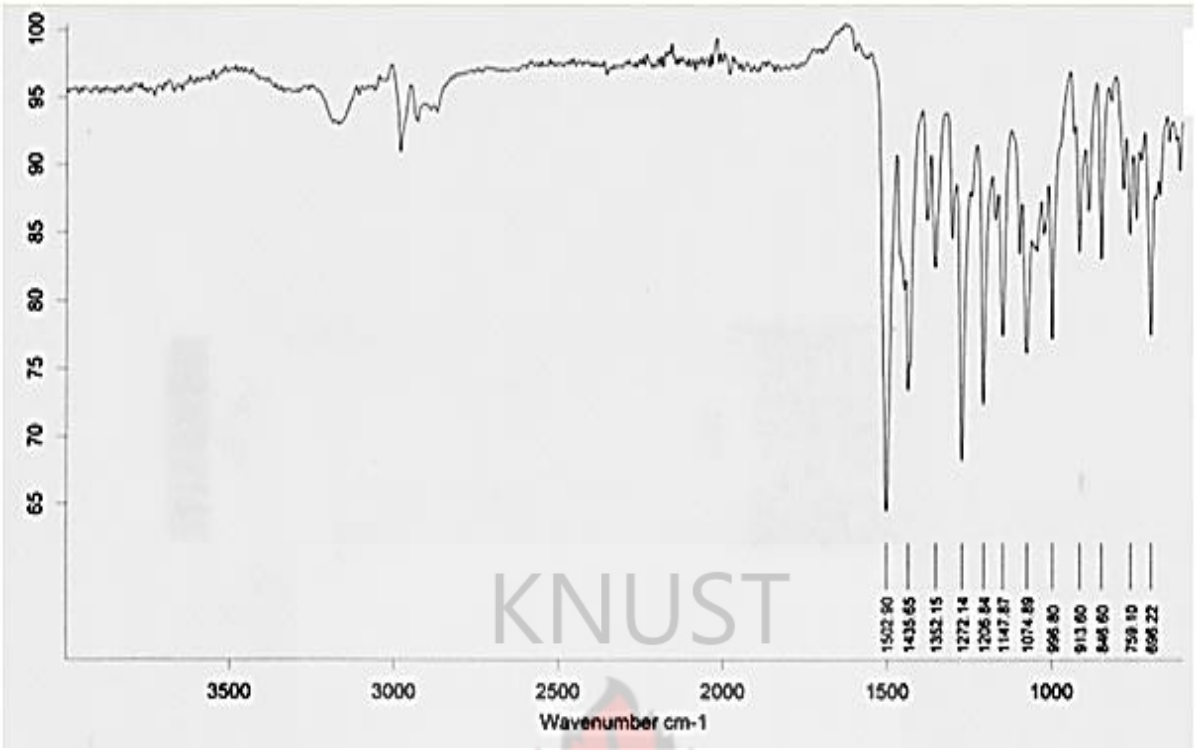

Figure B5: FT-IR Spectra for copper diethyldithiocarbamate $Cu(S_2CNEt_2)_2$

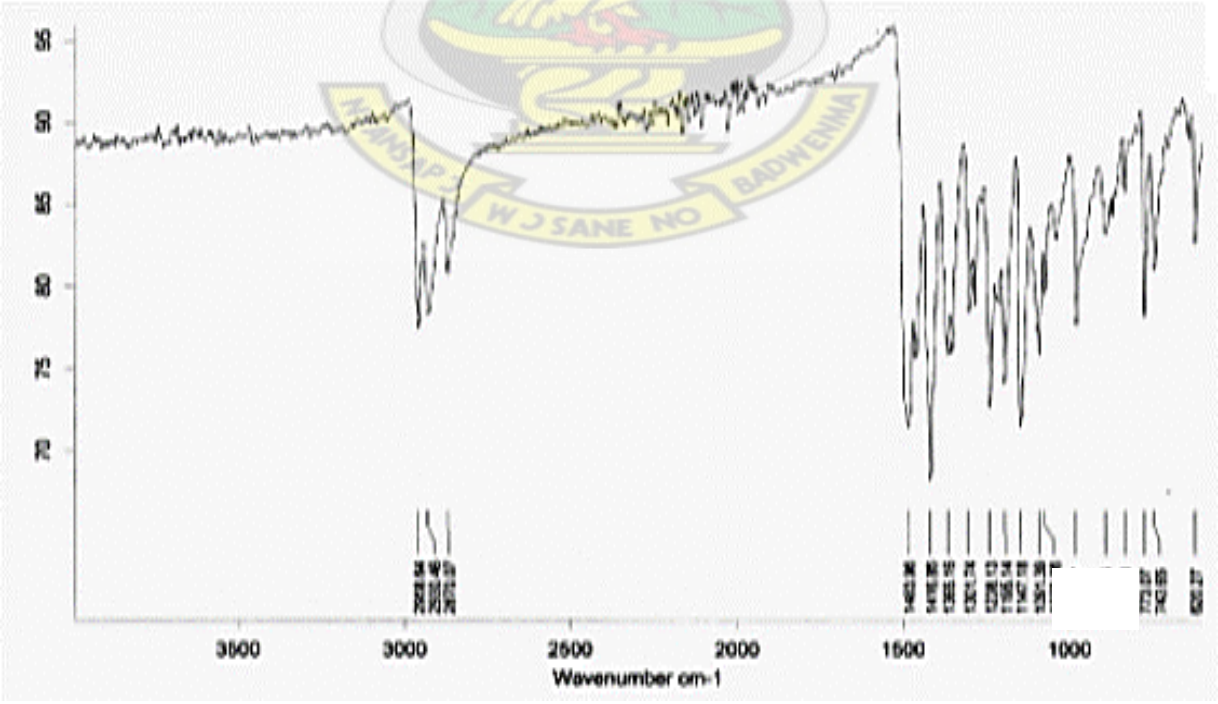

Figure B6: FT-IR Spectra for copper dipropyldithiocarbamate($Cu(S_2CNPr_2)_2$)

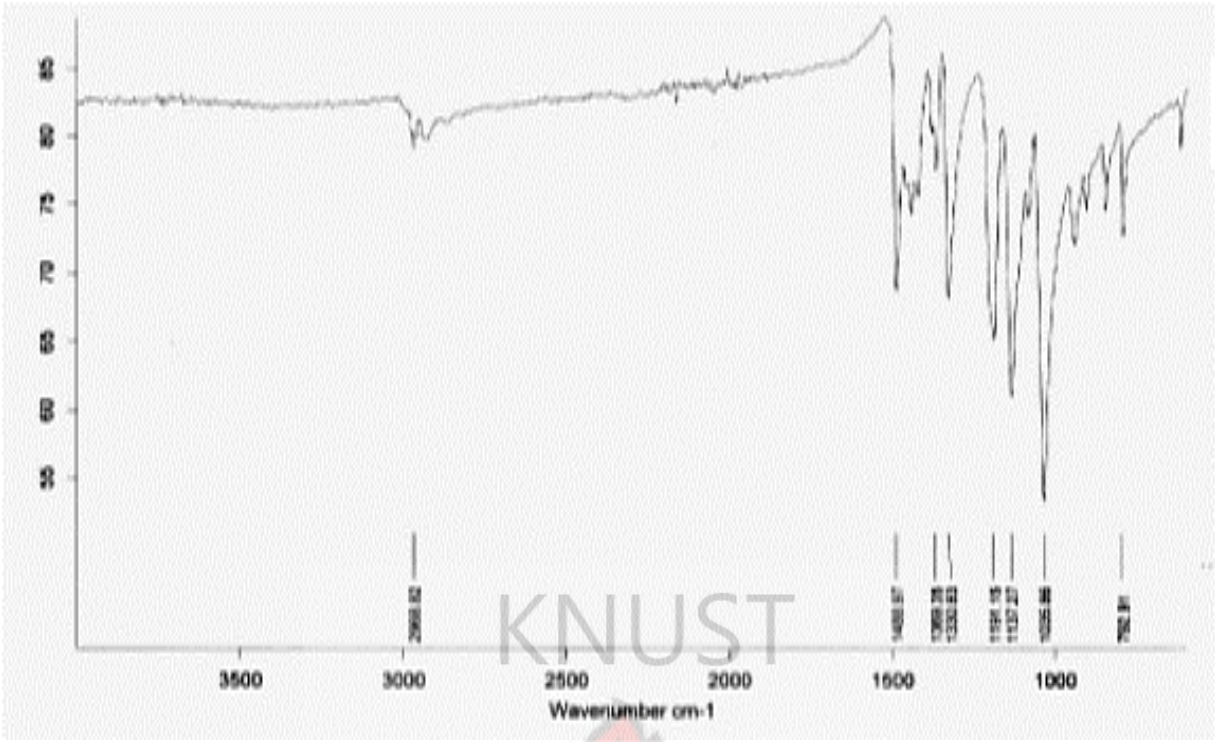

Figure B7: FT-IR Spectra for copper diisopropyldithiocarbamate ($Cu(S_2CN^iPr_2)_2$

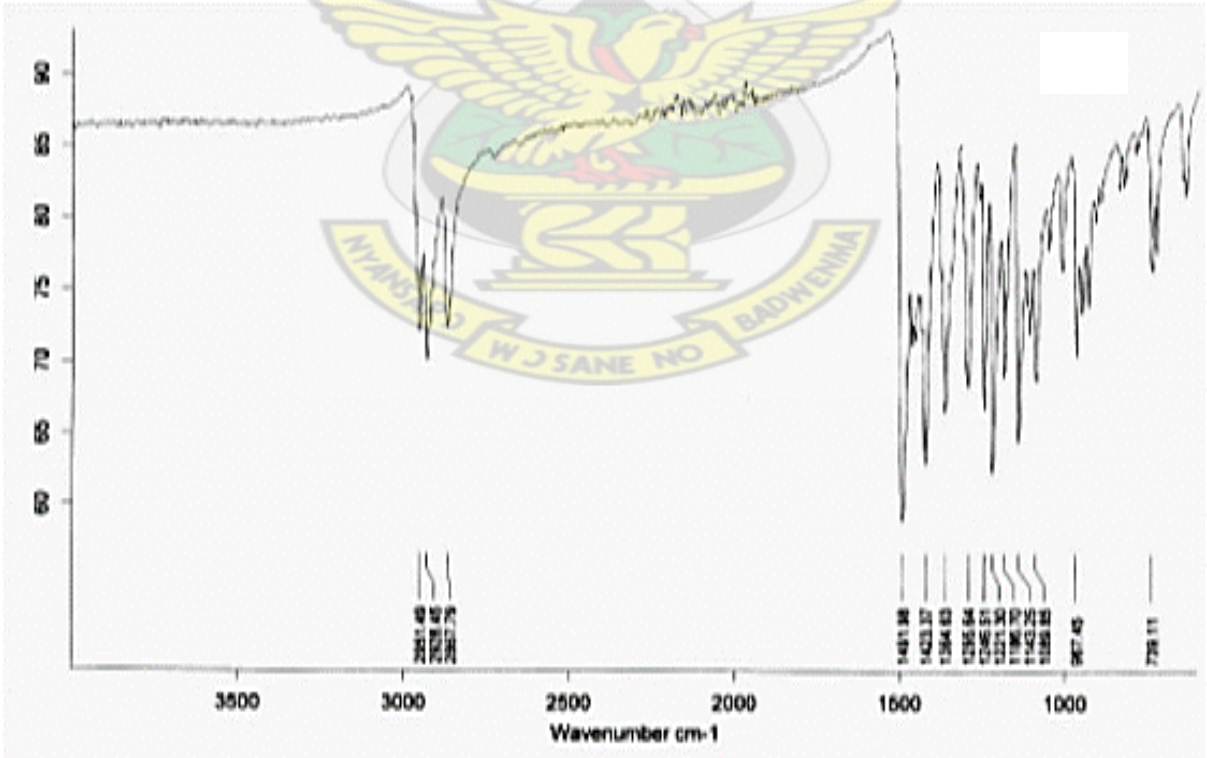

Figure B8: FT-IR Spectra for copper dibutyldithiocarbamate ($Cu(S_2CNBu_2)_2$)

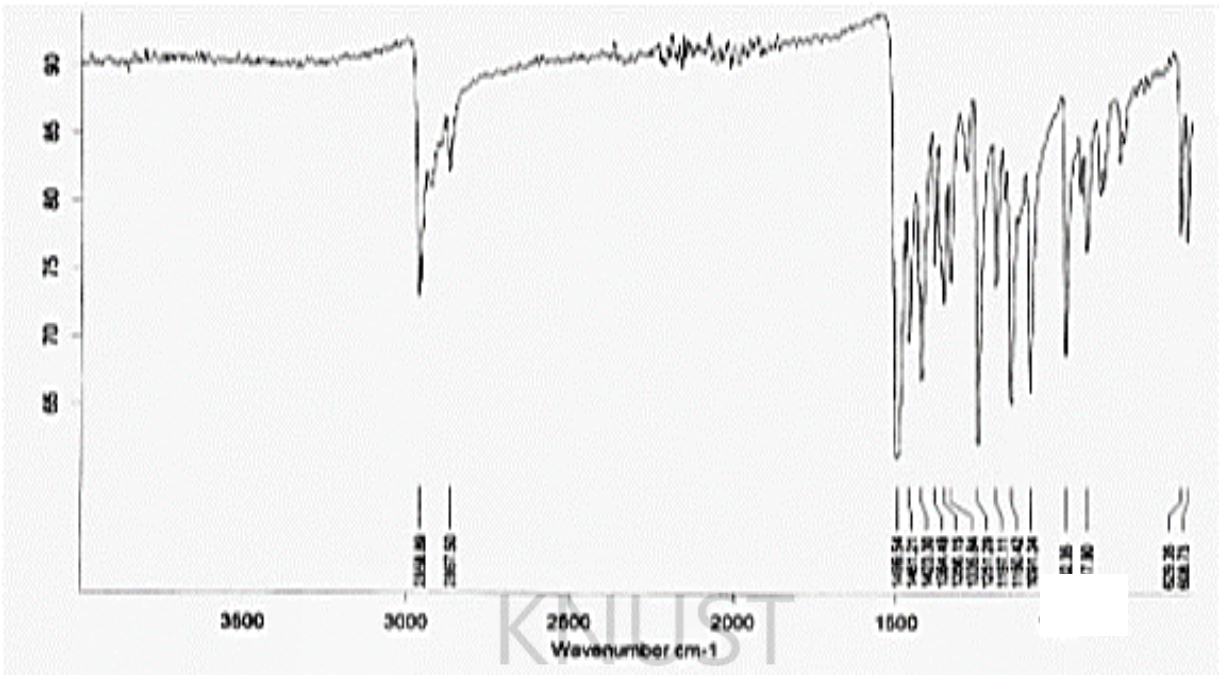

Figure B9: FT-IR Spectra for copper diisobutyldithiocarbamate ($Cu(S_2CN^iBu_2)_2$)

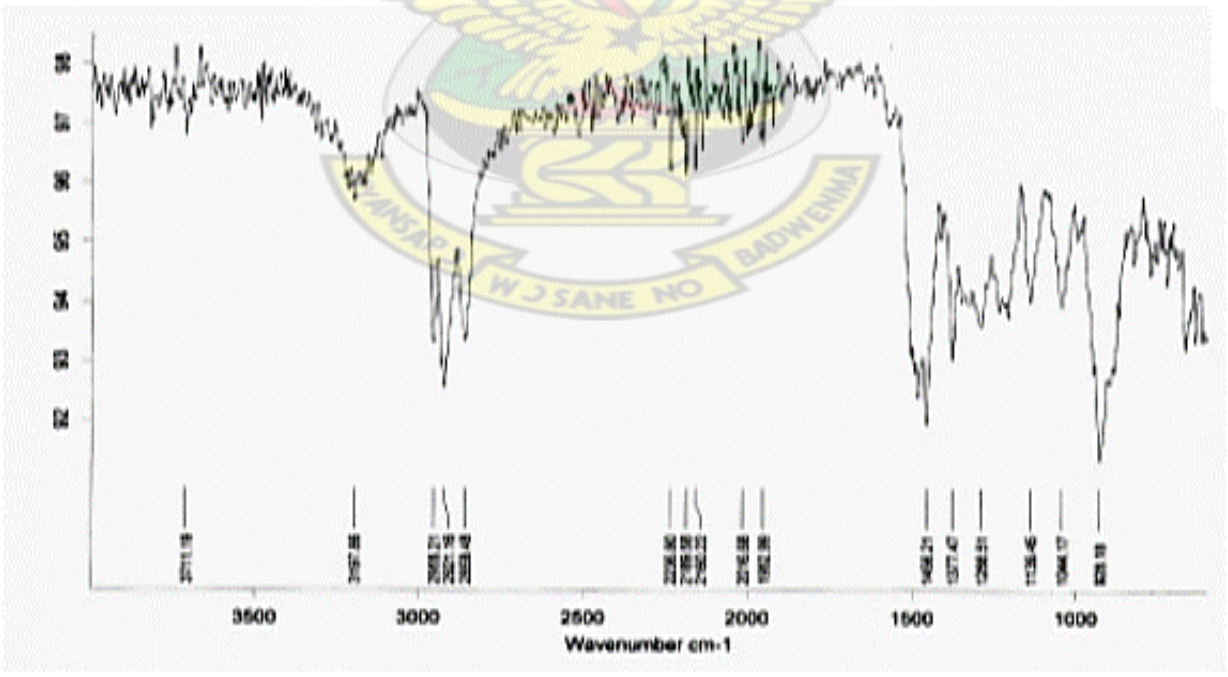

Figure B10: FT-IR Spectra for copper ethexyldithiocarbamate ($Cu(S_2CNEtHex)_2$)

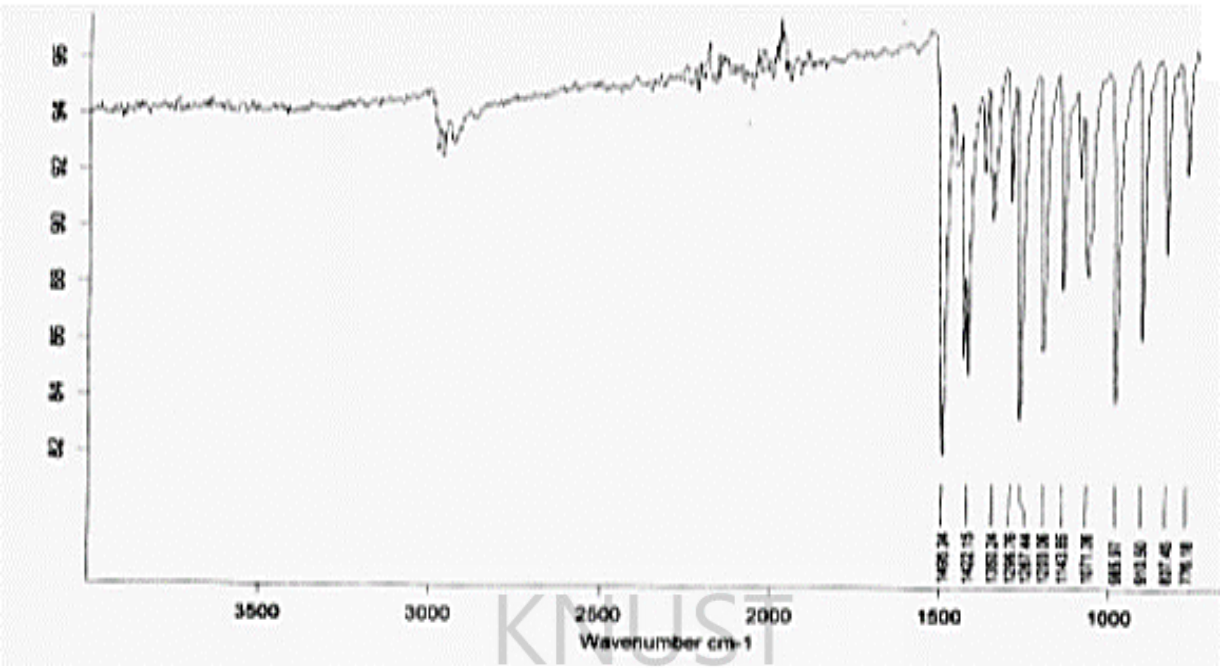

Figure B11: FT-IR Spectra for cadmium diethyldithiocarbamate ($Cd(S_2CNEt_2)_2$)

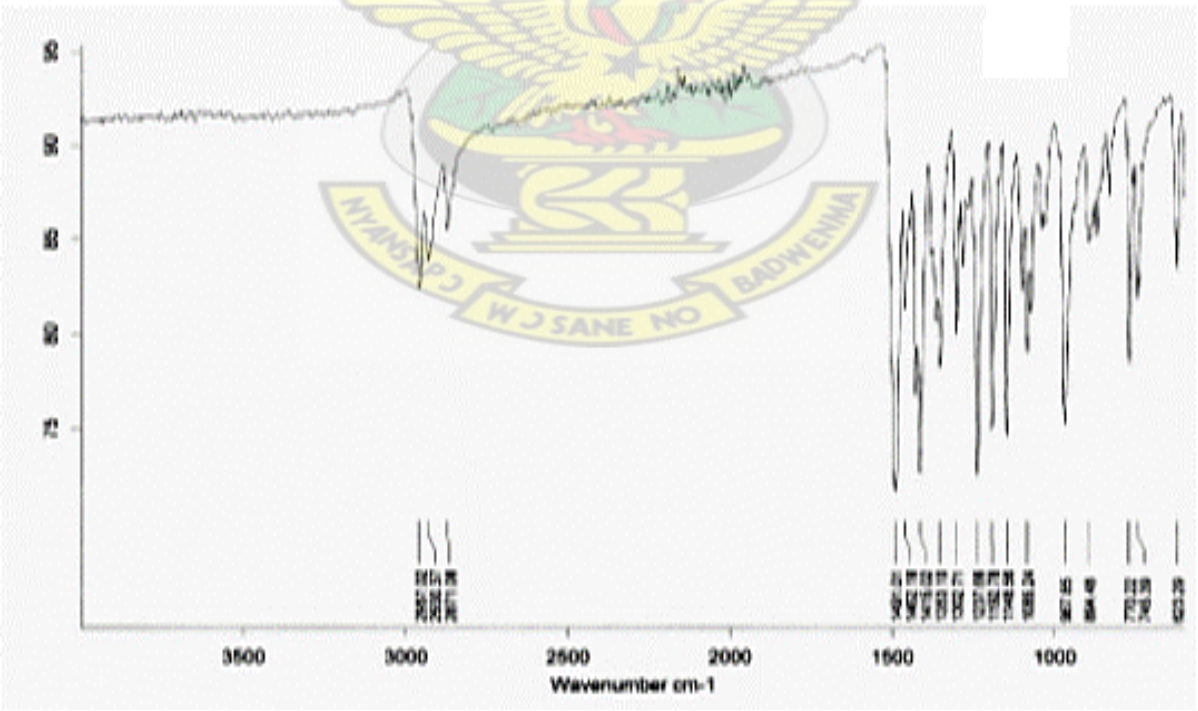

Figure B12: FT-IR Spectra for cadmium dipropyldithiocarbamate ($Cd(S_2CNPr_2)_2$)

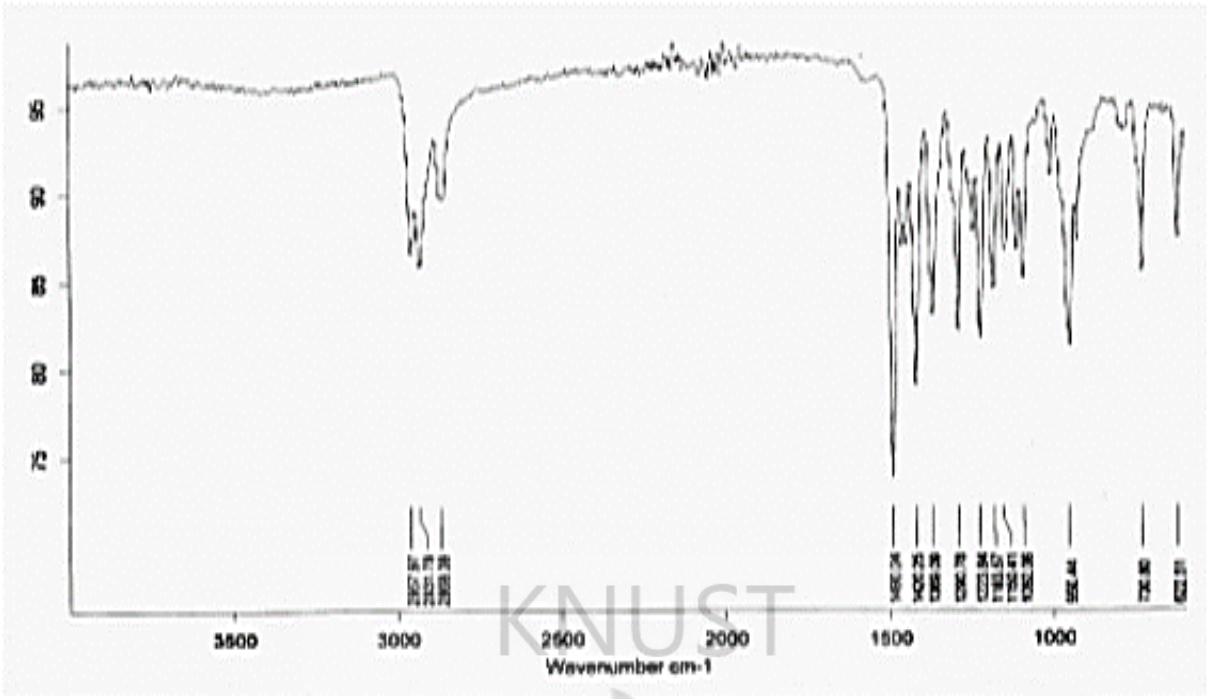

Figure B13: FT-IR Spectra for cadmium dibutyldithiocarbamate ($Cd(S_2CNBu_2)_2$)

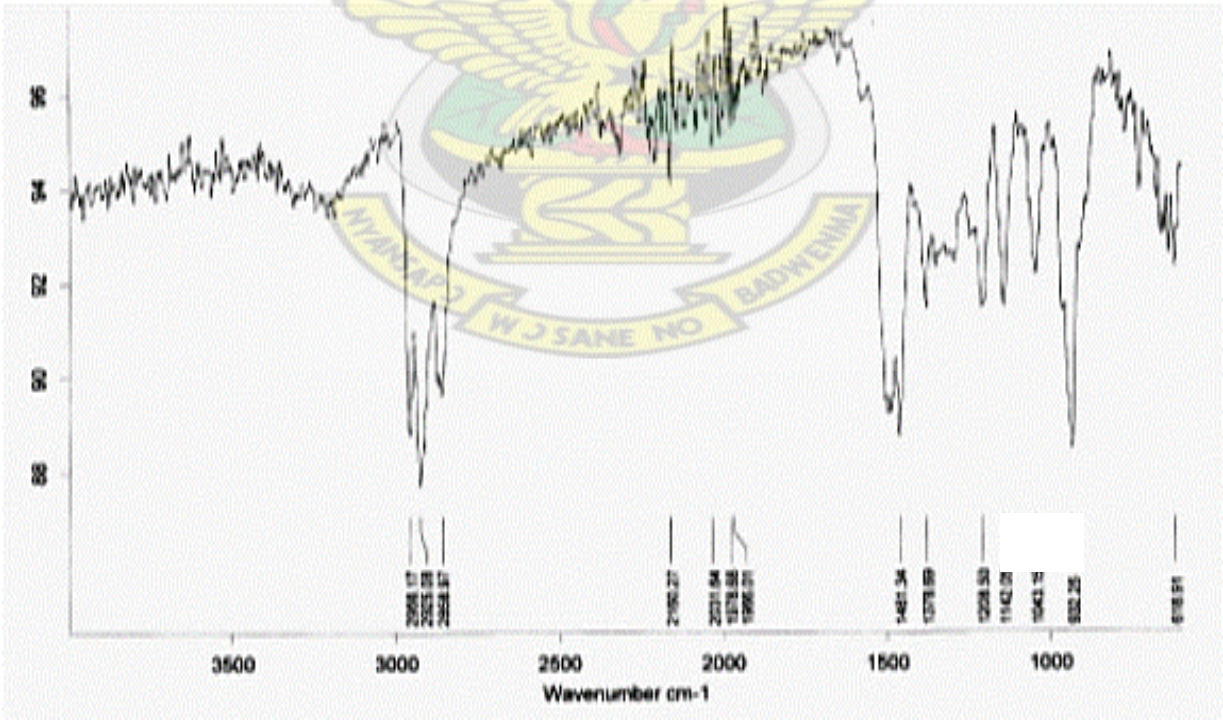

Figure B14: FT-IR Spectra for cadmium diisobutyldithiocarbamate ($Cd(S_2CN^iBu_2)_2$)

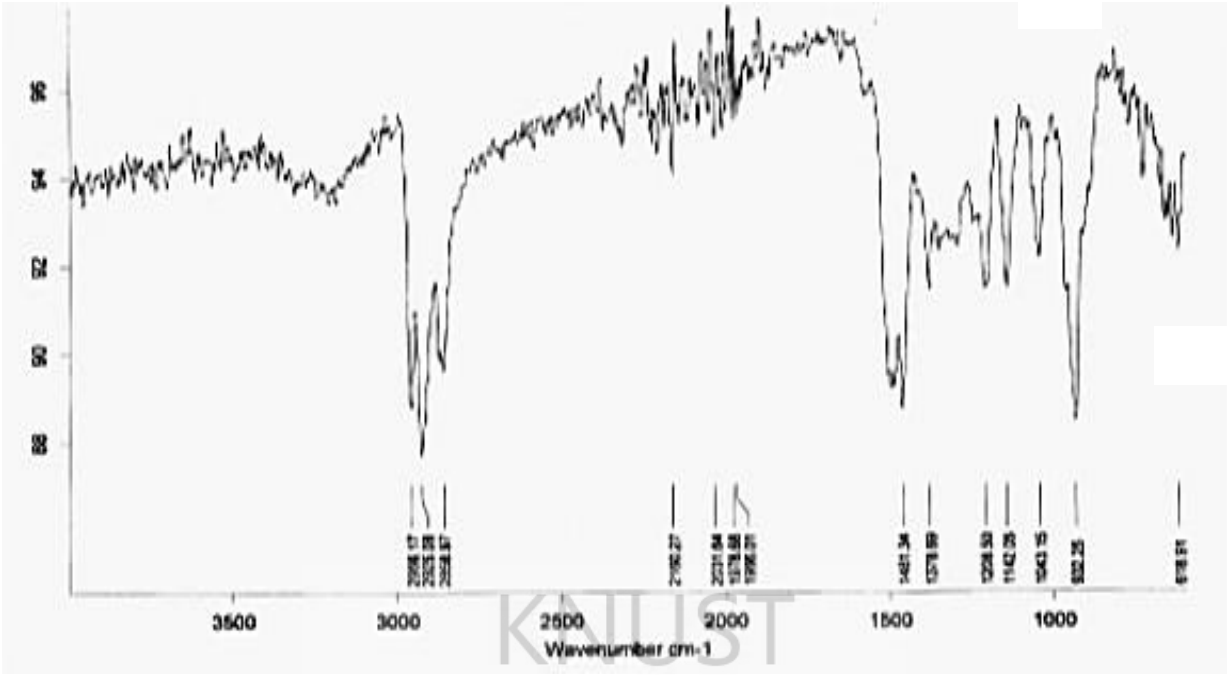

Figure B15: FT-IR Spectra for cadmium ethylhexyldithiocarbamate ($Cd(S_2CNEtHex)_2$)

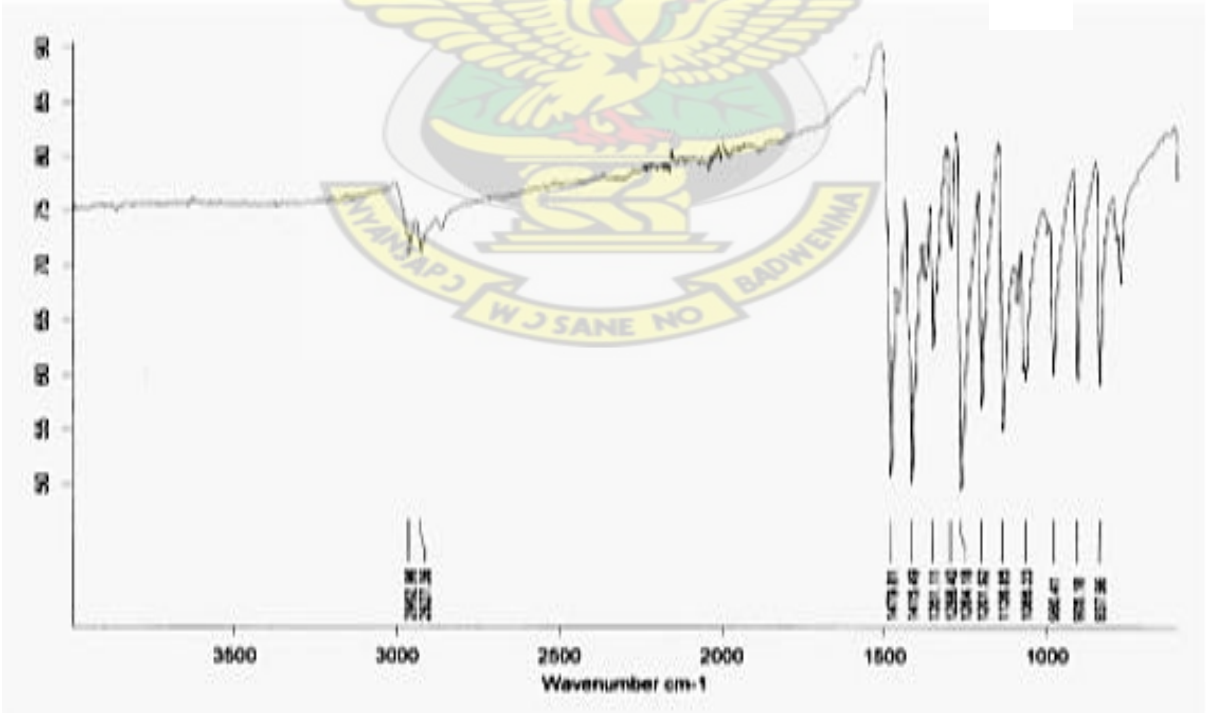

Figure B16: FT-IR Spectra for lead diethyldithiocarbamate ($Pb(S_2CNEt_2)_2$)

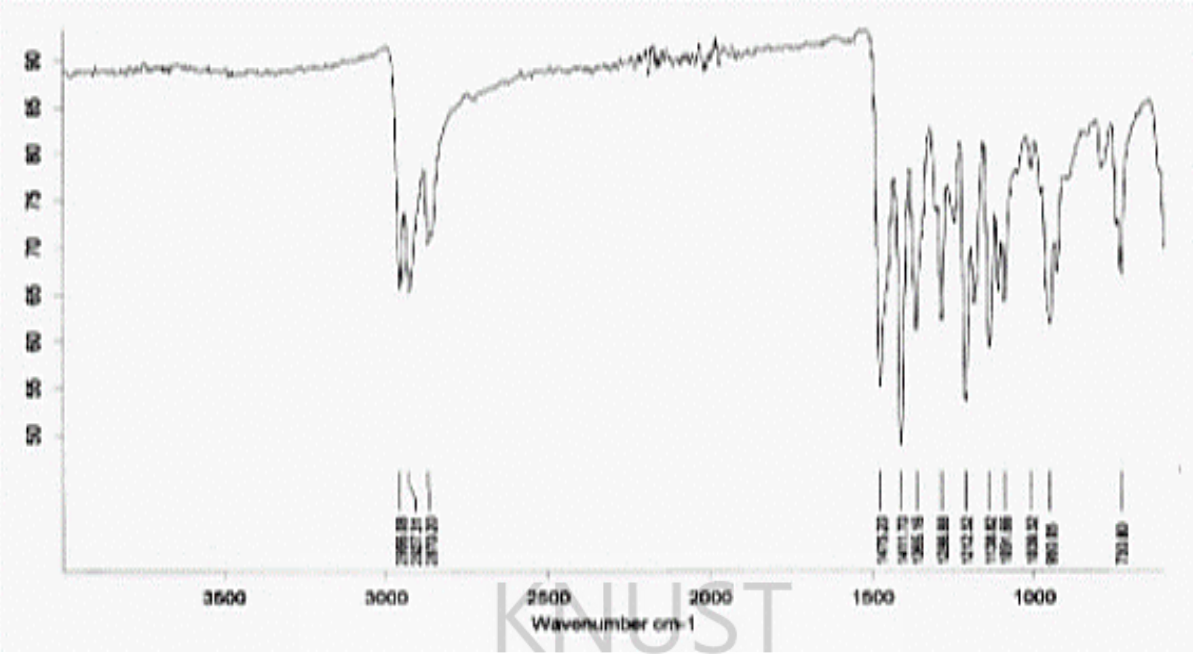

Figure B17: FT-IR Spectra for lead dipropyldithiocarbamate ($Pb(S_2CNPr_2)_2$)

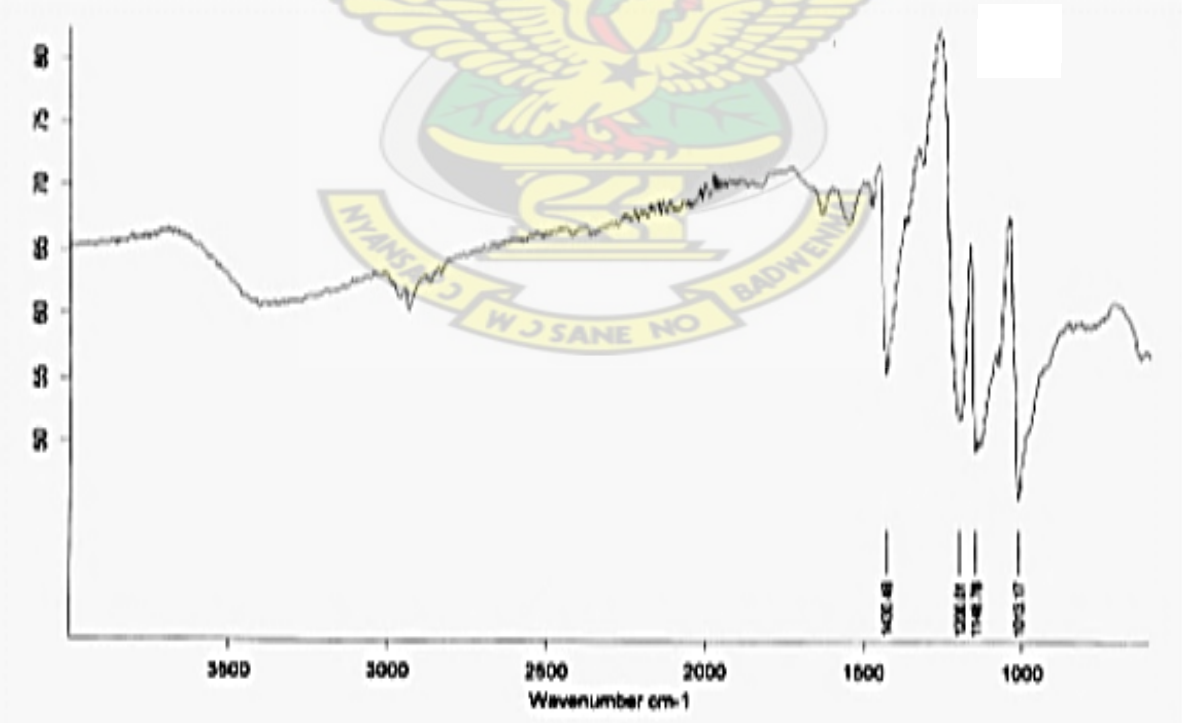

Figure B18: FT-IR Spectra for lead diisopropyldithiocarbamate ($Pb(S_2CN^iPr_2)_2$)

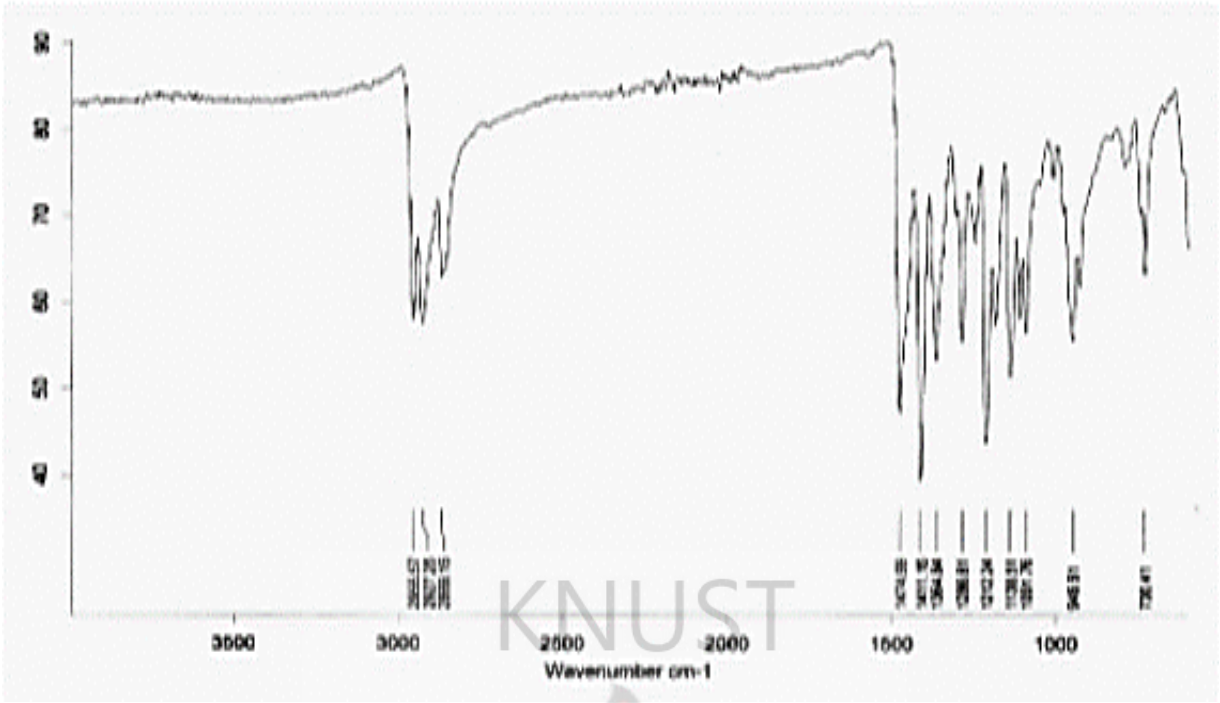

Figure B19: FT-IR Spectra for lead dibutyldithiocarbamate ($Pb(S_2CNBu_2)_2$)

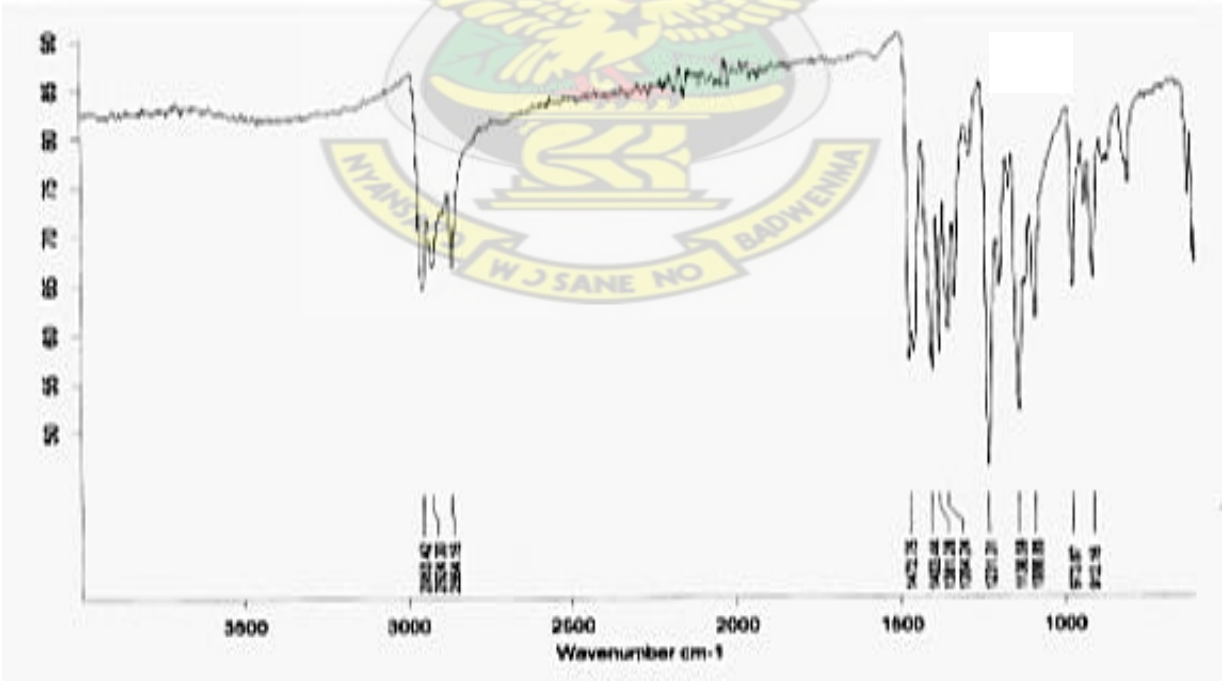

Figure B20: FT-IR Spectra for lead diisobutyldithiocarbamate ($Pb(S_2CN^iBu_2)_2$)

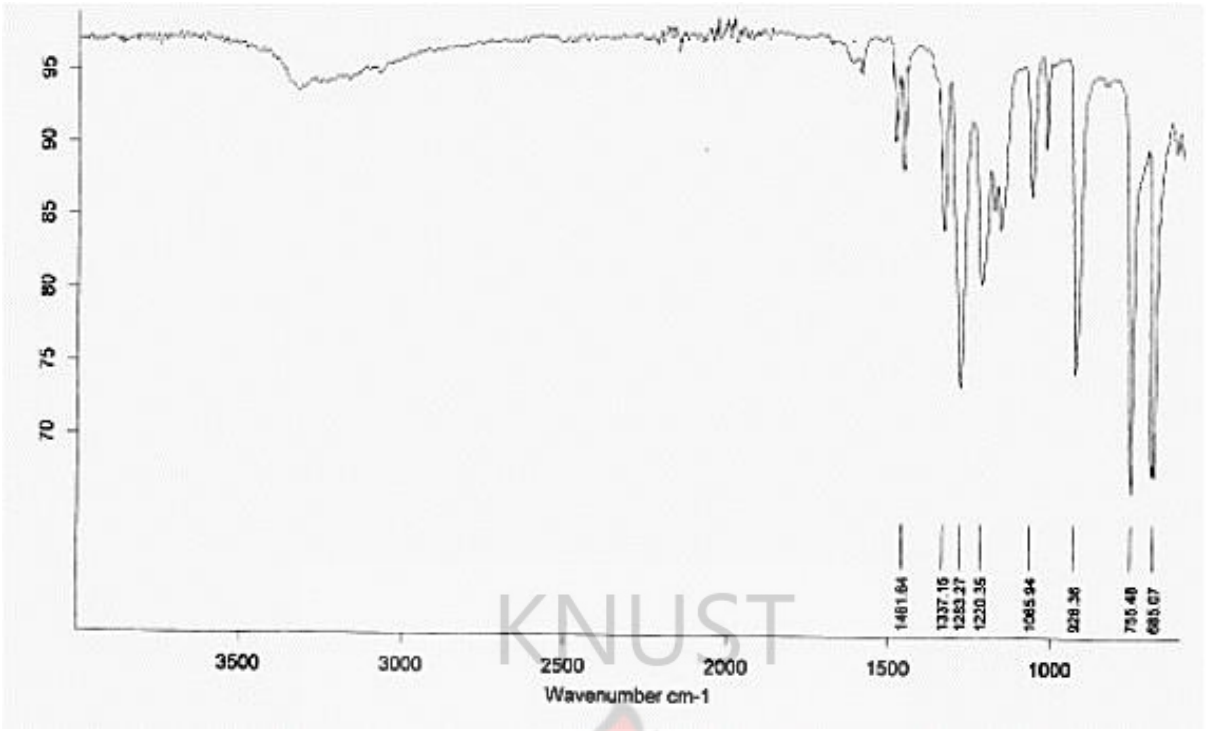

Figure B21: FT-IR Spectra for zinc cupferronate ($Zn(cup)_2$)

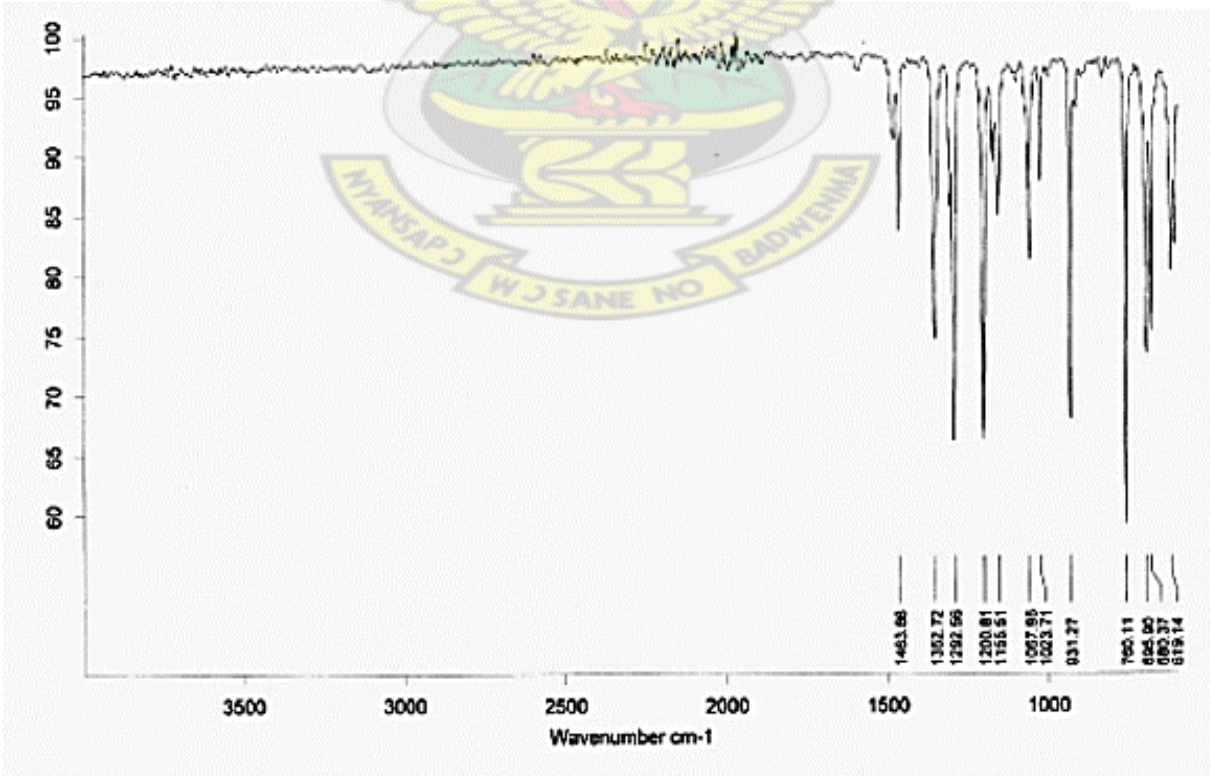

Figure B22: FT-IR Spectra for copper cupferronate (Cu(cup)2)

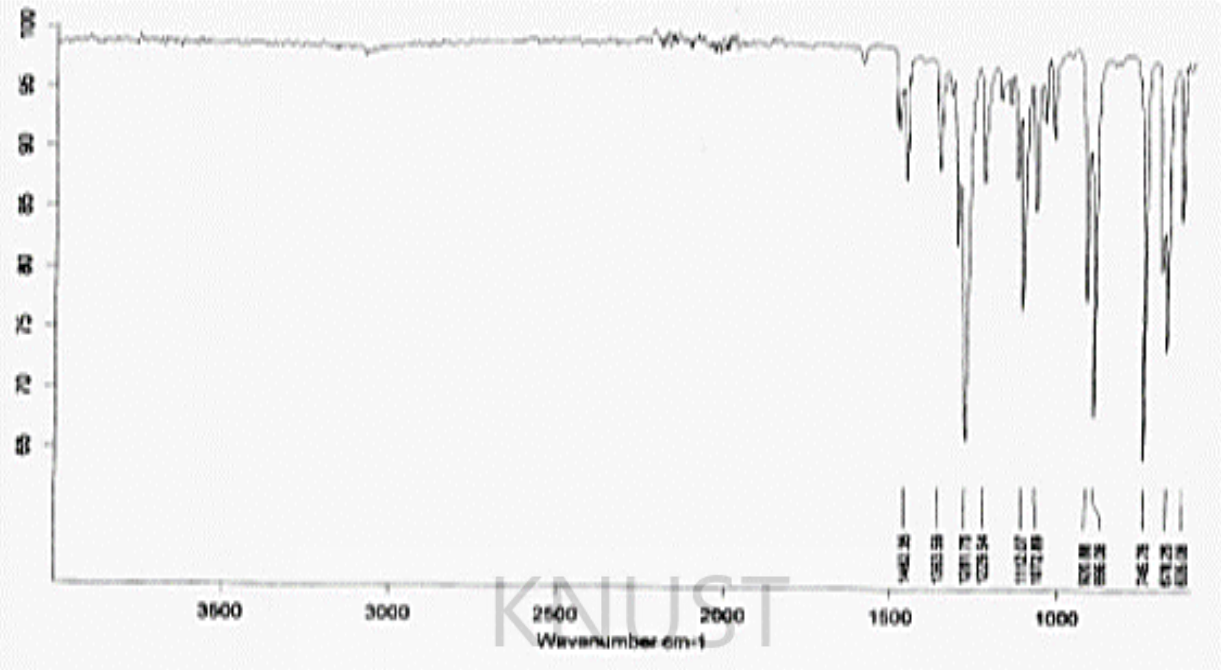

Figure B23: FT-IR Spectra for cadmium cupferronate ($Cd(cup)_2$)

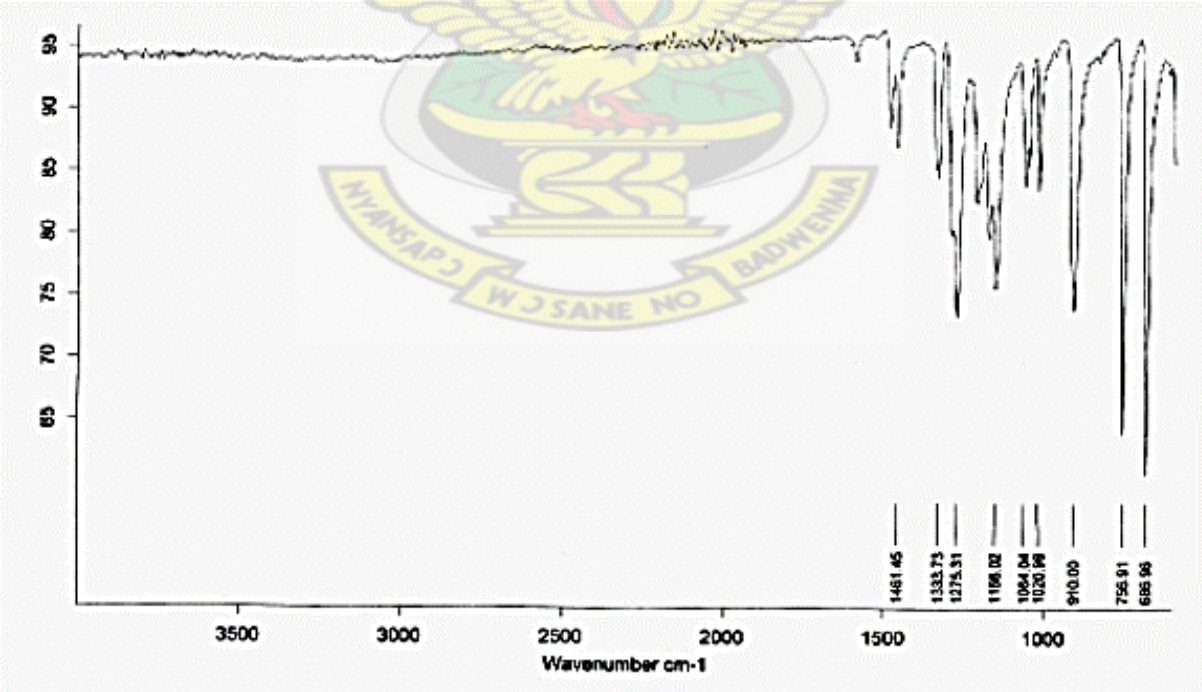

Figure B24: FT-IR Spectra for lead cupferronate ($Pb(cup)_2$)